

# Metal Ion Based Probes for Imaging

Dissertation

With the aim of achieving a doctoral degree at the Faculty of Mathematics, Informatics and Natural Sciences Department of the Universität Hamburg

Submitted by

Master of Science

Stephanie Besztejan

geb. Schruhl

from Hamburg

Hamburg, March 2016



Die vorliegende Arbeit wurde im Zeitraum von November 2011 bis August 2015 in der Arbeitsgruppe von Prof. Dr. Andrea Rentmeister im Fachbereich Chemie, Institut für Biochemie und Molekularbiologie an der Universität Hamburg durchgeführt.

1. Gutachter Prof. Dr. Andrea Rentmeister

2. Gutachter Prof. Dr. Alf Mews



## Publications

Parts of this work were published in

- Keskin, S. and Besztejan S. *et al.* Visualization of Multimerization and Self-Assembly of DNA- Functionalized Gold Nanoparticles Using In-Liquid Transmission Electron Microscopy. *J Phys Chem Lett.* (2015). doi:10.1021/acs.jpcllett.5b02075  
Shared first authorship

Further publications are in preparation

- Besztejan S. and Keskin S. *et al.* In-liquid Transmission Electron Microscopy to Visualize Cellular Dynamics in Live Cells  
Submitted, shared first authorship
- Besztejan S. *et al.* DNA-Gold Nanoparticle Probes for RNA Detection in Northern Blots  
In preparation
- Besztejan S. and Rentmeister A Engineering of Aequorin variants with improved Sm<sup>3+</sup> affinity  
In preparation

In the following bachelor theses methods and results were described that were achieved under my guidance:

- Fabian Bockholt (2012), Analyzing gold nanoparticles internalized in Mammalian cells using capillary electrophoresis
- Simon Dörner (2013), Gold nanoparticiles and their influence on the enzymatic nucleic acid synthesis
- Franziska Böwer (2014), Metal Ion Promiscuity of Aequorin – Production and Characterization of Aequorin Variants



All things are possible for one who believes

Mark 9:23





Dedicated to

Rianti, Detlef, Daniel and René



## Table of Content

Table of Content .....	I
Abstract.....	VI
List of Figures .....	VIII
List of Tables .....	XII
List of Abbreviations .....	XIV
1 Introduction .....	1
1.1 Microscopy Techniques .....	1
1.1.1 Fluorescence Microscopy .....	2
1.1.2 Electron Microscopy .....	5
1.2 Probes for Microscopy.....	9
1.2.1 Fluorescent Probes .....	9
1.2.2 Aequorin as a Potential Bimodal Probe .....	14
1.2.3 Scattering Probes.....	23
1.3 Mutagenesis Techniques for Protein Engineering.....	27
1.3.1 QuikChange®.....	28
1.3.2 Megaprimer Whole Plasmid PCR.....	28
1.3.3 NNK Libraries .....	28
1.3.4 Error Prone PCR .....	29
1.4 Iterative Saturation Mutagenesis – Combinatorial Active Site Saturation Test .....	29
1.5 Endocytosis and the Prostate Specific Membrane Antigen.....	31
1.6 Morphological Changes During Mammalian Cell Adhesion .....	34
2 Aim of This Work .....	36
3 Results .....	37
3.1 In-liquid TEM Experiments .....	37
3.1.1 Gold Nanoparticles for In-Liquid-TEM Imaging .....	37
3.1.2 Mammalian Cells in In-Liquid TEM.....	47
3.1.3 Imaging of Cellular Dynamics in PC3 Cells.....	51

3.1.4	Visualization of Anti-PSMA-Aptamer Functionalized Gold Nanoparticles in LNCaP Cells Using In-Liquid TEM.....	53
3.2	Engineering of Aequorin Variants with Improved $\text{Sm}^{3+}$ Binding Affinity as Potential Bimodal Probe for Light and Electron Microscopy .....	59
3.2.1	Saturation Mutagenesis for an Improved Aequorin .....	63
3.2.2	Engineering of Aequorin using Rational Design .....	76
3.2.3	Aequorin in TEM.....	98
3.2.4	Intracellular Application of TS A123W S125E in Mammalian Cell Culture .....	101
3.3	Combination of In-liquid TEM and Aequorin as a TEM Probe .....	105
4	Discussion.....	107
4.1	In-liquid TEM Experiments .....	107
4.1.1	Visualization of Hybridized DNA-Gold Nanoparticles .....	107
4.1.2	In-liquid TEM of Mammalian Cells.....	109
4.2	Engineering of Aequorin Variants with Improved $\text{Sm}^{3+}$ Binding Affinity Towards a Bimodal Probe for Light and Electron Microscopy .....	114
4.2.1	Saturation Mutagenesis for an Improved Aequorin Variant.....	114
4.2.2	Engineering of Aequorin using Rational Design .....	117
4.2.3	Contrasting Ability of TS A123W S125E in TEM.....	125
4.2.4	Intracellular Application of TS A123W S125E as Probe in Mammalian Cells .....	127
4.3	Combination of In-liquid TEM and Aequorin as a TEM Probe .....	130
5	Outlook.....	131
5.1	Experiments using In-liquid TEM.....	131
5.2	Aequorin as a Bimodal Probe for Electron and Light Microscopy .....	134
6	Summary .....	137
7	Zusammenfassung.....	139
8	Materials.....	143
8.1	Chemicals .....	143
8.2	Buffer, Media and Solutions.....	143
8.3	Gold Nanoparticles .....	146
8.4	Oligonucleotides .....	146

8.5	Enzymes and Proteins.....	148
8.6	Commercially Available Kits and Columns.....	148
8.7	Nucleotides.....	149
8.8	Antibodies.....	149
8.9	Bacteria.....	149
8.10	Plasmids.....	150
8.11	Mammalian Cells.....	150
8.12	Software.....	151
9	Methods.....	152
9.1	General Molecular Biological Methods.....	152
9.1.1	Polymerase Chain Reaction.....	152
9.1.2	Sequencing.....	154
9.1.3	Gel Electrophoresis.....	154
9.1.4	Detection of DNA or RNA in gel Electrophoresis.....	155
9.1.5	Second Strand Synthesis.....	155
9.1.6	<i>In vitro</i> Synthesis of RNA.....	155
9.2	Protein Biochemistry Methods.....	157
9.2.1	Discontinuous Tris Tricine PAA gel Electrophoresis.....	157
9.2.2	Visualization of Proteins in Tris Tricine Gels with Coomassie Blue.....	157
9.2.3	Immunoblot.....	157
9.2.4	Protein Concentration Determination Using Bradford Assay.....	158
9.3	General Microbiological Methods.....	159
9.3.1	Transformation of <i>E. coli</i> Cells.....	159
9.3.2	Overnight Culture.....	159
9.3.3	Preparation of Plasmid DNA.....	159
9.4	Cell culture.....	160
9.4.1	Cultivation of Prostate Cancer 3 Cells.....	160
9.4.2	Cultivation of LNCaP Cells.....	160

9.4.3	Transfection of PC3 Cells.....	160
9.4.4	Immunofluorescence Sample Preparation .....	160
9.4.5	Sample Preparation for GF-AAS Elemental Analysis for Samarium .....	161
9.5	Microscopy.....	161
9.5.1	Fluorescence Confocal Light Microscopy.....	161
9.5.2	Electron Microscopy .....	161
9.6	Gold Nanoparticles for Imaging .....	162
9.6.1	Coupling of Oligonucleotides to Gold Nanoparticles .....	162
9.6.2	Dynamic Light Scattering .....	162
9.6.3	Surface Plasmon Resonance Scan .....	162
9.6.4	Dot Blot and Northern Blot .....	163
9.6.5	Preparing the Nanofluidic Cell Samples and TEM Acquisition.....	163
9.7	Aequorin as a Bimodal Probe for Electron and Fluorescence Light Microscopy.....	164
9.7.1	Cloning of Amino Acid libraries using MEGAWHOP PCR .....	164
9.7.2	High-Throughput Screening for Luminescence Activity.....	164
9.7.3	Site-directed Mutagenesis.....	164
9.7.4	Protein Production .....	164
9.7.5	Protein Purification using ÄKTA.....	165
9.7.6	Luminescence Activity Assay .....	165
9.7.7	Determination of EC <sub>50</sub> Values .....	165
9.7.8	Determination of Half-lives .....	166
9.7.9	Emission Wavelength Scan .....	166
9.7.10	CD Spectroscopy .....	166
9.7.11	MALDI-MS .....	166
9.7.12	Isothermal Titration Calorimetry.....	167
9.7.13	Conventional TEM of Immobilized TS A123W S125E .....	167
10	References.....	168
11	Appendix.....	177
11.1	Disposal.....	177

11.2	List of used Chemicals according to GHS .....	178
11.3	Plasmid sequences .....	180
11.4	Table of all tested AQ variants .....	201
11.5	Overview of the Modeled Variant Structures .....	203
12	Acknowledgements .....	204
13	Curriculum vitae .....	207
14	Eidesstattliche Erklärung .....	208

## Abstract

In the framework of this thesis, metal ions were used for two different approaches for the application as bimodal probes for light and electron microscopy.

Gold nanoparticles (AuNPs) were used in the first strategy to establish in-liquid TEM. The AuNPs were used to image DNA-hybridization. Moreover, mammalian cells were imaged using in-liquid TEM. Subcellular structures such as nucleus, nucleoli, and cell membranes were visible without additional staining or sample preparation. It was also possible to perform live cell imaging of prostate cancer cells (PC3 and LNCaP) using in-liquid TEM. Dynamics of subcellular structures could be observed. Ribonucleotide-functionalized AuNPs were also used for live cell imaging.

The second approach used  $\text{Sm}^{3+}$  ions and the enzyme aequorin (AQ). AQ was engineered towards a bimodal probe for light and electron microscopy. The enzyme emits light upon metal ion binding. The natural metal ion inducing luminescence is  $\text{Ca}^{2+}$ . The engineering yielded a new variant TS A123W S125E that had 40-fold improved affinity for  $\text{Sm}^{3+}$  compared to the parental thermostabilized AQ TS. The  $\text{Ca}^{2+}$  affinity decreased 30-fold.

Binding of  $\text{Sm}^{3+}$  of the new variant TS A123W S125E could induce contrast in conventional TEM analysis. Additionally it showed luminescence in cell tests with PC3 cells for both  $\text{Sm}^{3+}$  and  $\text{Ca}^{2+}$ .





## List of Figures

Figure 1: Light path in a confocal light microscope, schematic overview. ....	3
Figure 2: Light pathways for TIRF and two-photon microscopy. ....	4
Figure 3: Scheme of available electron microscopy techniques. ....	6
Figure 4: Schematic overview of a silicon nitride chamber for in-liquid TEM not drawn to scale. ....	8
Figure 5: Stokes shift. ....	10
Figure 6: Jablonski energy diagram. ....	10
Figure 7: Variety of GFP proteins reproduced of R. Tsien's Nobel Prize lecture 2008. ....	14
Figure 8: Reconstitution of Apoaequorin to Aequorin. ....	15
Figure 9: Reaction of coelenterazine to coelenteramide. ....	16
Figure 10: Schematic drawing of an EF-hand motif. ....	18
Figure 11: Protein structure of AQ according to PDB 1SL8. ....	19
Figure 12: CTZ cavity of Aequorin. ....	20
Figure 13: Interaction of the amino acid residues of AQ with CTZ. ....	20
Figure 14: Beam path and principle of contrast in electron microscopy. ....	23
Figure 15: Scheme of iterative saturation mutagenesis with four randomization sites. ....	30
Figure 16: Scheme of defined regions (A-E) within a distance of 10 Å from the active site for CASTing. ....	31
Figure 17: Schematic overview of the three main endocytosis pathways. ....	31
Figure 18: Scheme of clathrin-mediated and non-clathrin mediated endocytosis of a receptor. ..	34
Figure 19: Morphological changes of a cell during adhesion to a surface. ....	35
Figure 20: Schematic overview of the two strategies to image clathrin mediated endocytosis in real time. ....	36
Figure 21: Schematic overview of multimerization for DNA1-AuNP and DNA2-AuNP with Hyb-DNA and the control DNA. ....	38
Figure 22: Characterization of functionalized DNA coated AuNPs. ....	39
Figure 23: Monitoring the hybridization of DNA1-AuNP and DNA2-AuNP with Hyb-DNA and controls <i>in vitro</i> via UV-vis spectroscopy. ....	40
Figure 24: Multimerization of DNA-AuNPs upon hybridization of ssDNA. ....	41
Figure 25: Schematic drawing of a DNA1- and DNA2-AuNP dimer (not drawn to scale). ....	42
Figure 26: 2D analysis of a multimer's motion. ....	43
Figure 27: Time sequential formation of DNA-AuNP clusters at higher electron doses. ....	44
Figure 28: AuNP clusters in motion. ....	45
Figure 29: 3D configurations of two clusters along with the projections on x-y axes. ....	46
Figure 30: Schematic overview of sample preparation for in-liquid TEM measurements. ....	47

Figure 31: In-liquid TEM micrographs of unstained human PC3 cells.....	50
Figure 32: Light microscopy images of the silicon nitride viewing areas of nanofluidic cells seeded with PC3 cells.....	51
Figure 33: In-liquid TEM imaging of living PC3 cells without any contrasting agents. ....	52
Figure 34: Characterization of anti-PSMA-AuNPs and analysis of their internalization into LNCaP cells.....	55
Figure 35: In-liquid TEM image of LNCaP cells targeted with anti-PSMA-AuNPs. ....	57
Figure 36: Promiscuous luminescence triggering of AQ wt.....	60
Figure 37: Luminescence activity of known low Ca <sup>2+</sup> affinity AQ variants triggered with Ca <sup>2+</sup> and Sm <sup>3+</sup> .....	61
Figure 38: Schematic overview of the site-directed and saturation mutagenesis performed on EF-hand motif 2 in AQ TS. ....	62
Figure 39: Protein structure of AQ with bound Ca <sup>2+</sup> (pdb dataset 1SL8). ....	63
Figure 40: Results of saturation mutagenesis at position 12 of EF hand motif 2 in AQ TS. ....	65
Figure 41: Results of saturation mutagenesis at position 11 of EF hand motif 2 in AQ TS. ....	67
Figure 42 Results of saturation mutagenesis at position 7 (A123) of EF hand motif 2 in LAAQ	69
Figure 43: Results of saturation mutagenesis at position 5 of EF hand motif 2.....	71
Figure 44: Results of saturation mutagenesis at position 3 of EF hand motif 2.....	72
Figure 45: Results of saturation mutagenesis at position 1 of EF hand motif 2.....	74
Figure 46: Results of the saturation mutagenesis. ....	75
Figure 47: Characterization of variants at position 7 EF-hand motif 2 after site-directed mutagenesis .....	77
Figure 48: Characterization of variants TS S125D and TS S125E.....	79
Figure 49: Modeled structure of TS S125G and TS S125R.....	80
Figure 50: Characterization of AQ TS variants with double substitutions at position 7 and 9 of EF-hand motif 2.....	81
Figure 51: ITC measurements of AQ TS and TS A123W S125E with CaCl <sub>2</sub> and SmCl <sub>3</sub> . ....	84
Figure 52: Luminescence curves of TS A123W S125E tested with 8 CTZ analogues in combination with Sm <sup>3+</sup> and Ca <sup>2+</sup> .....	86
Figure 53: Normalized Sm <sup>3+</sup> /Ca <sup>2+</sup> luminescence ratios of TS A123W S125E and CTZ analogues in relation to AQ TS with CTZ native.....	87
Figure 54: Molar ellipticity measured by CD spectroscopy of AQ TS and TS A123W S125E.....	88
Figure 55: Characterization of AQ variants with combined substitutions of rational design and saturation mutagenesis.....	90

Figure 56: Schematic overview of the tested variants. The best substitutions (TS A123W S125E) in different variants are highlighted blue. Already known substitutions in literature are depicted in grey (D119A and E128G). The number of tested colonies is given in brackets.....	92
Figure 57: Characterization of AQ variants with substitutions at position 7 and 9 in EF-hand motif 3 and in combination with EF-hand motif 2. ....	94
Figure 58: Characterization of EF-hand motif 1 variants.....	95
Figure 59: Variants including substitutions at position 7 and 9 in EF-hand motif 1, 2 and 3 and CTZ analogues.....	97
Figure 60: Luminescence assay of immobilized AQ enzymes on anti-His <sub>6</sub> AuNPs.....	98
Figure 61: TEM images of aequorin immobilized on 14 nm anti-His <sub>6</sub> AuNPs. ....	99
Figure 62: EDX analysis of TS A123W S125E (left) and Pumilio (right) immobilized on anti-His <sub>6</sub> AuNPs after incubation with SmCl <sub>3</sub> .....	100
Figure 63: Internalization of Sm <sup>3+</sup> into PC3 and LNCaP cells analyzed via GF-AAS.....	101
Figure 64: Analysis of AQ production in PC3 cell lysate after transfection. ....	102
Figure 65: Luminescence assay of transfected PC3 cells with AQ wt and TS A123W S125E after 24 h transfection.....	103
Figure 66: In-liquid TEM of fixed HEK293T cells transfected with TS A123W S125E.....	106



## List of Tables

Table 1: Common used organic fluorescent dyes and some parameters (Abcam, 2014). .....	12
Table 2: Overview of CTZ analogs according to Shimomura et al.(Shimomura et al., 1988, 1993; Shimomura, 1991) .....	21
Table 3: Diameter of AuNPs during functionalization measured via DLS. ....	54
Table 4: Overview of the CV values for AQ TS and LAAQ in the HTS.....	63
Table 5: $K_d$ values calculated from ITC measurements of AQ TS and TS A123W S125E.....	85
Table 6: Characterization of TS D119A A123W S125E, TS A123W S125E D127R, and TS D119A A123W S125E D127R. ....	91
Table 7: buffer, media and solutions for microbiological methods. ....	143
Table 8: Buffers and solutions for molecular biological experiments.....	144
Table 9: buffers and solutions used for protein biochemical methods .....	144
Table 10: Media and solutions for cell culture experiments .....	145
Table 11: Oligonucleotides used in this work.....	146
Table 12: Enzymes and proteins used in this work. ....	148
Table 13: Commercially available kits and columns .....	148
Table 14: Nucleotides used in this work.....	149
Table 15: Antibodies used in the experiments.....	149
Table 16: All bacteria used in the work .....	149
Table 17: List of used plasmids in this work.....	150
Table 18: Mammalian cells used for cell experiments. ....	150
Table 19: Software used in this worl for data processing and analysis. ....	151
Table 20: Schematic reaction mix for PCR with Phusion Polymerase .....	152
Table 21: Schematic temperature program for a PCR with Phusion.....	152
Table 22: Schematic reaction mix for PCR with Phusion Polymerase .....	153
Table 23: Schematic temperature program for a PCR with Phusion.....	153
Table 24: Schematic reaction mix for a colony PCR (6 samples) with FirePol.....	154
Table 25: Schematic temperature program for a colony PCR with FirePol .....	154
Table 26: Composition of an denat. PAA.....	155
Table 27: Schematic reaction mix for a colony PCR (100 $\mu$ L) with FirePol.....	156
Table 28: discontinuous 10% tris tricine PAA gels for protein analysis.....	157
Table 29: List of used Chemical according to GHS.....	178



**List of Abbreviations**

2'-F	2'-desoxy-2'-Fluor
3'-	3'-end of an oligonucleotide
5'-	5'-end of an oligonucleotide
a.u.	Arbitrary units
AEX	Anion exchange chromatography

## Amino acids

Ala (A)	Alanin
Arg (R)	Arginine
Asn (N)	Asparagine
Asp (D)	Aspartic acid
Cys (C)	Cysteine
Gln (Q)	Glutamine
Glu (E)	Glutamic acid
Gly (G)	Glycine
His (H)	Histidine
Ile (I)	Isoleucine
Leu (L)	Leucine
Lys (K)	Lysine
Met (M)	Methionine
Phe (F)	Phenylalanine
Pro (P)	Proline
Ser (S)	Serine
Thr (T)	Threonine
Trp (W)	Tryptophan
Tyr (Y)	Tyrosine
Val (V)	Valine
AP	Alkaline phosphatase
AP2	Accessory protein 2
APS	Ammonium persulfate
AQ	Aequorin



AQ TS	Thermostabilized aequorin
a.u.	Arbitrary unit
AuNPs	Gold nanoparticles
BCIP	5-Bromo-4-chloro-3-indolyl phosphate
bp	Base pair
BSA	Bovine serum albumin
CASTing	Combinatorial active site saturation test
CCV	Clathrin coated vesicles
CD	Circular dichroism
CLSM	Confocal laser scanning microscopy
CME	Clathrin mediated endocytosis
CMV	Cytomegalovirus
CT	Computer tomography
CTZ	Coelenterazine
CV	Coefficient of Variation
Da	Dalton
ddH <sub>2</sub> O	Bidest. water
DEAE	Diethylethanolamine
DLS	Dynamic Light Scattering
DMF	<i>N,N</i> -Dimethylformamide
DNA	Desoxyribonucleic acid
dNTPs	Mix of
dGTP	deoxyguanosine triphosphate
dTTP	deoxythymidine triphosphate
dATP	deoxyadenosine triphosphate
dCTP	deoxycytidine triphosphate
ds	Double strand
DTT	Dithiothreitol
<i>E. coli</i>	Escherichia coli
EC <sub>50</sub>	Half maximal effective concentration
EDTA	Ethylenediaminetetraacetic acid
EGTA	Eethylene glycol tetraacetic acid
EDX	Energy-dispersive X-ray spectroscopy

EGFP	Enhanced Green fluorescent protein
EM	Electron microscopy
$\epsilon$	Extinction coefficient
ESEM	Environmental scanning electron microscopy
<i>et al.</i>	<i>et altera</i>
EtBr	Ethidium bromide
FLM	Fluorescence light microscopy
GCP II	Glutamate carboxypeptidase II
GF-AAS	Graphite furnace atomic absorption spectrometry
GFP	Green fluorescent protein
HA	Hemagglutinin
HEPES	4-(2-hydroxyethyl)-1-piperazineethanesulfonic acid
His <sub>6</sub> -tag	Hexa-Histidine Tag
HTS	High-throughput screening
IMAC	Immobilized metal affinity chromatography
IPTG	Isopropyl $\beta$ -D-1-thiogalactopyranoside
ITC	Isothermal titration calorimetry
$K_d$	Dissociation constant
LAAQ	Low affinity aequorin
LB	Luria-Bertani
$\lambda_{Em}$	Emission wavelength
LBT	Lanthanide binding tag
$L_{max}$	Maximal luminescence
LNCaP	Androgen-sensitive human prostate adenocarcinoma cells
LPCVD	Low pressure chemical vapor deposition
LSM	Laser scanning Microscopy
MEGAWHOP	Megaprimer Whole Plasmid
MiniSOG	Mini Singlet Oxygen Generator
MRI	Magnetic resonance imaging
MTF	Modulation transfer functions
NAALDase I	<i>N</i> -acetyl-L-aspartyl-L-glutamate peptidase I (or NAAG peptidase)
NBT	Nitro blue tetrazolium chloride

NNK	Corresponding codon of an amino acid that allows in position 1 and 2 of the codon all four bases G, T, A and C (N), while on position 3 only pyrimidines G or T (K) can be inserted.
Norm.	Normalized
nt	Nucleotide
NTA	Nitrilotriacetic acid
OD	Optical density
PAA	Polyacrylamide
PAGE	Polyacrylamide gel electrophoresis
PC3	Prostate cancer cells
PCR	Polymerase chain reaction
PFA	Paraformaldehyde
PSMA	Prostate specific membrane antigen
QY	Quantum yield
ReAsH	Biarsenical labeling tag
REGAE	Relativistic electron gun for atomic exploration
Rel.	Relative
RNA	Ribonucleic acid
RT	Room temperature
SDS	Sodium lauryl sulfate
SELEX	Systematic evolution of ligands by exponential enrichment
SEM	Scanning electron microscopy
SiN	Silicon nitride
SiO	Silicon oxide
SOB	Super Optimal Broth
SOC	Super Optimal broth with Catabolite repression
SPR	Surface plasmon resonance
ss	Single stranded
STED	Stimulated Emission Depletion Microscope
STORM	Stochastic optical reconstruction microscopy
$t_{1/2}$	Half life
TAE	Tris-acetate-EDTA
<i>Taq</i>	<i>Thermus aquaticus</i>

XVIII | List of Abbreviations

TB	Terrific broth
TEM	Transmission electron microscopy
TEMED	<i>N,N,N',N'</i> -Tetramethylethylenediamine
TIRF	Total internal reflection fluorescence
T <sub>M</sub>	Melting temperature
Tris	Tris(hydroxymethyl)aminomethane
U	unit
UV-vis	UV- and visible light
<i>v/v</i>	Volume/volume
<i>w/v</i>	Weight/volume
<i>wt</i>	Wild type
YFP	Yellow fluorescent protein
YT	Yeast extract, tryptone





## 1 Introduction

Life itself is a highly dynamic process that undergoes many changes in different amount of times. In order to understand the mechanisms of life on the level of cells and molecules, different microscopy techniques have been established that magnify the scene. Powerful light and electron sources have been used to explore many of these mechanisms, like endocytosis, cell adhesion, and others we know today. Although we gained knowledge over the past decades, there is still a huge number of processes we do not fully understand, as we cannot resolve these processes with current conventional light microscopy. Microscopy techniques that can achieve the required nanometer resolution to explore this processes use electron sources. Here there limitation is that *in situ* imaging is rather difficult for biological samples. In order to address and visualize these processes, new bimodal microscopy techniques combining the benefits of overviewing light microscopy and high-resolution electron microscopy have been developed (Kukulski et al., 2011). Therefore, bimodal probes are necessary. These probes should ideally allow visualizing the area in fluorescence microscopy and having a more detailed look using electron microscopy.

This thesis is about the development of such new bimodal probes and the advantages of latest developments in electron microscopy towards imaging of biological specimens in their native state.

### 1.1 Microscopy Techniques

With the development of specialized microscopy techniques, it was possible to give first insights into intracellular dynamics like endocytosis, infection by virus particles, bacteria, etc. These findings helped to understand many cellular processes and functions and to postulate models of them.

In general, there are two major classes of microscopy techniques:

- Light microscopy: especially fluorescence light microscopy (FLM),
- Electron microscopy (EM).

FLM and EM use approaches very different from each other to produce an image of a sample. EM is known to be limited to fixed, stained, mainly dehydrated and thin cross sections, due to the low contrast of the atomic composition of biological specimens. EM uses the interaction of atoms with electrons to create an image. Fluorescence microscopy needs fluorescent dyes or proteins to image a sample. The discovery of the green fluorescent protein (GFP) (1962 Shimomura) opened a wide field of genetically encoded probes (Shimomura et al., 1962a). Until

today, the proteins of the GFP superfamily are still the state of the art approaches for fluorescent microscopy.

This chapter will give an overview about different microscopy techniques in general.

### 1.1.1 Fluorescence Microscopy

Fluorescence microscopy is a mainstay for microscopy in biology. There was a rapid development of techniques, probes, and equipment like detectors and cameras in the last decades. The result is a big variety of chemically dyes like ATTO or FITC that are used for labeling. Furthermore, it is possible to add almost any variant of the GFP superfamily (sfGFP, dsRED, YFP, etc.) to the protein of interest for analysis of fused proteins in living environments (Han et al., 2013).

Confocal laser scanning microscopy (CLSM) is used to obtain high-resolution images of optical sections in different depths of a specimen. It is possible to reconstruct a 3D structure of a sample by adding all measured z-focal planes at one position. Originally patented by Marvin Minsky in 1957 (Minsky, 1957), Thomas and Christoph Cremer were able to introduce a laser scanning process in 1978 (Cremer and Cremer, 1978) that made CLSM the state of the art in biological microscopy techniques it is today.

The image formation begins with a laser beam that passes an aperture and is focused behind the aperture via an objective lens into the specimen with fluorescent dyes (Figure 1). The emitting fluorescent light and the scattered laser light pass the objective lens. A filter blocks the original excitation wavelength, so that only the fluorescence light is passed to the detector. A pinhole can be used to sharpen images and to record images of certain z-focus planes.

CLSM is a microscopy technique for direct noninvasive imaging that can be used on thick, living specimens like whole cells. Especially for biological samples the dye concentration is the major parameter for the quality of an image, due to the signal to noise ratio. For specimens with distinct concentration of dyes in thin sections (200 nm) another method is available: Total internal reflection fluorescence microscopy (TIRF) (Ambrose, 1956; Axelrod, 1981).



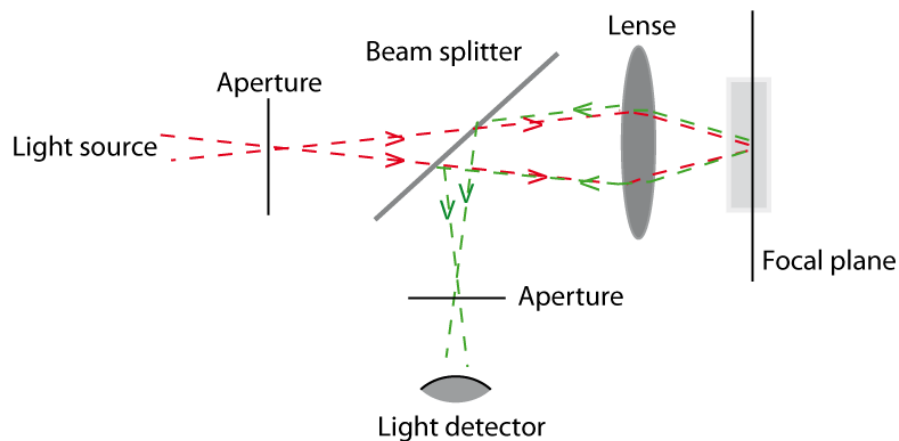


**Figure 1: Light path in a confocal light microscope, schematic overview.**

The light originates of a laser source. It is focused with a lens behind the aperture and sent through the specimen, where fluorescent light emits. The beam splitter the scattered light is focused with an aperture and sent to the light detector that records the image blocks the original excitation wavelength.

TIRF is used for examination of cell surfaces, e.g. cell adhesion molecules or membrane dynamics, when the overall expected signal to noise ratio is very poor due to a high number of non-fluorescent molecules in the surrounding (Ambrose, 1956). TIRF uses an evanescent wave that only occurs if the light is totally internally reflected. It excites exclusively fluorophore in a restricted region adjacent to the specimen-glass barrier. The result is the illumination of the plasma membrane and the cytoplasm with a maximal depth of 200 nm (Figure 2A).

As TIRF is a method to image exclusively thin sections near surfaces without actually slicing the specimen, there is another technique to do the opposite in terms of sample thickness. For imaging of living tissue with very high depth - about several millimeters - two-photon microscopy has been established by Winfried Denk in the 1990 (Denk et al., 1990). This technique uses red excitation light in the IR range that can excite the typical fluorescence organic dyes (Figure 2B). The difference to fluorescence microscopy is that two photons of IR light need to be absorbed for excitation. An advantage of the IR light in the thick specimen is that the scattering over the whole specimen is minimized. Furthermore, the background signal is suppressed and the penetration depth maximized while photo toxicity is low comparable to other FM techniques.

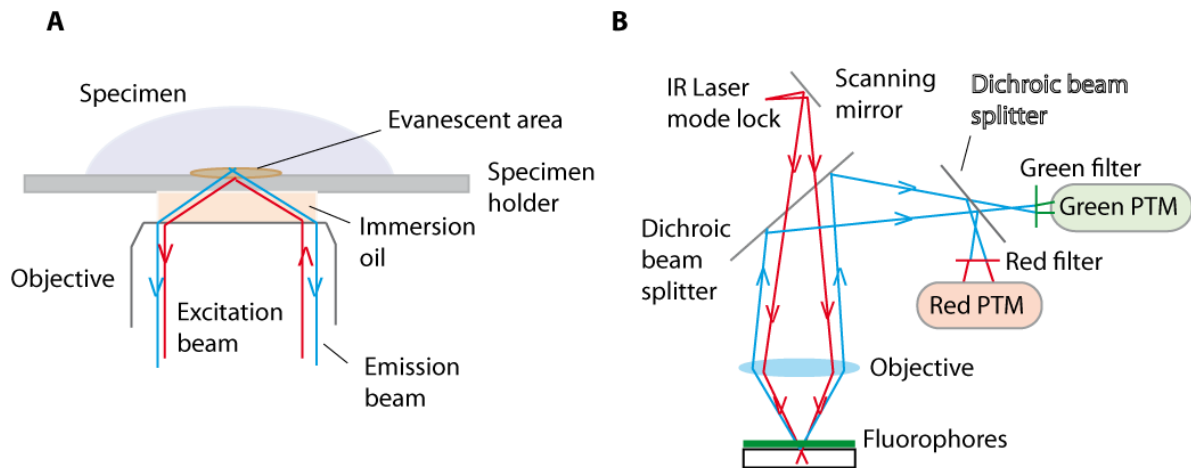


**Figure 2: Light pathways for TIRF and two-photon microscopy.**

The images are adapted from Diao et al. (Diao et al., 2012) and Denk et al. (Denk et al., 1990). (A) For TIRF microscopy an emission beam is sent through the specimen. Only if total internal reflectance occurs an excitation beam is emitted and collected. (B) Two-photon microscopy uses a long range IR laser pulse that activates the fluorophore in the sample. The emitted light is sent over scanning mirrors and beam splitter to the detector unit (green PTM). The red IR light is filtered before image processing.

Although there have been many huge developments in microscopy, the resolution is limited to 200 nm due to Abbe's law. It says that a photon is a particle with a certain wavelength. Based on the wavelength of visible light with the lowest value of 400 nm, the maximum resolution can only be half of the wavelength and is thus limited to 200 nm.

However, in the last decade super-resolution light microscopy techniques have been established. These are mainly Stimulated Emission Depletion (STED) (Hell and Wichman, 1994) and Stochastic Optical Reconstruction Microscopy (STORM) (Rust et al., 2006). Both techniques use blinking probes that are switchable. Based on the concept that there is only a distinct number of fluorophore "on" at a distinct time point, it is possible to calculate the exact position in the sample using the point spread function. By using mathematic corrections it is so far possible to obtain a resolution down to 25 nm (Jones et al., 2011).

These new techniques are especially interesting to use in imaging transport processes for example in neurons (Willig et al., 2006; Westphal et al., 2008). This was a further step towards the explanation of many dynamic events within organisms and cells.

Although there have been made great achievements, a major disadvantage of fluorescence microscopy is still the low quantum yield (QY) as well as a low signal to noise ratio of the dyes and probes. Especially the signal to noise ratio is very challenging for super-resolution microscopy as the dyes have to be very bright and blinking for analysis via point spread function. Furthermore, it has not been possible to perform live cell imaging and dynamics with the super-resolution techniques, yet as this is limited by the irregular blinking of the dyes we know today

(Jones et al., 2011; Shao et al., 2011; Zanicchi et al., 2011). For structural analysis of static systems, super-resolution microscopy has been proven a very powerful tool.

To summarize, the ability to image thick living samples is a major advantage of light microscopy over electron microscopy. Disadvantages are low signal to noise ratios and sample preparation especially for super-resolution light microscopy. Live cell imaging is until now only possible with conventional CLSM techniques that cannot yet overcome the limitation of 200 nm resolution. To break these boundaries, new stable blinking and bright probes would be needed as well as further development of the super-resolution technologies.

### 1.1.2 Electron Microscopy

Electron microscopy is a rather old technique. The first operating machine was built by Ernst Ruska 1931, published 1932 (Knoll and Ruska, 1932) and awarded with a Nobel prize in 1987. Because it uses electrons instead of photons, it can resolve structures at the atomic range beyond 20 nm. The de Broglie wave-particle duality provides the basis with electrons moving through specimens like waves and thus being almost unlimited in resolution. This is a huge advantage compared to fluorescence microscopy. Instead of photons/light, the electrons travel to a detector and give rise to the image. The electron beam is focused by a set of electromagnetic lenses, analogue to the lens systems in light microscopes.

The typical electron microscope is a transmission electron microscope (TEM). The newest and most powerful model, built by Hitachi, can emit electrons with an energy of 1 MeV (Hitachi, 2015). The transmitted electrons are collected by an image recording system. To create a stable electron beam within the column, the machine operates in a vacuum mode. Because of the high proportion of water in biological sample, these normally need to be dehydrated, which makes *in situ* imaging under native conditions almost impossible up to now.

Nonetheless, TEM is not only used for material sciences but also for biological specimens to attain atomic resolution. However, besides the water and vacuum challenge, biological samples need special treatment due to their low internal contrast resulting from the low-atomic-number elements CHNOP composition and their radiation damage sensitivity. To circumvent these challenges biological specimens are prepared by embedding in matrices, cutting in thin slices, and staining with heavy metal salts.

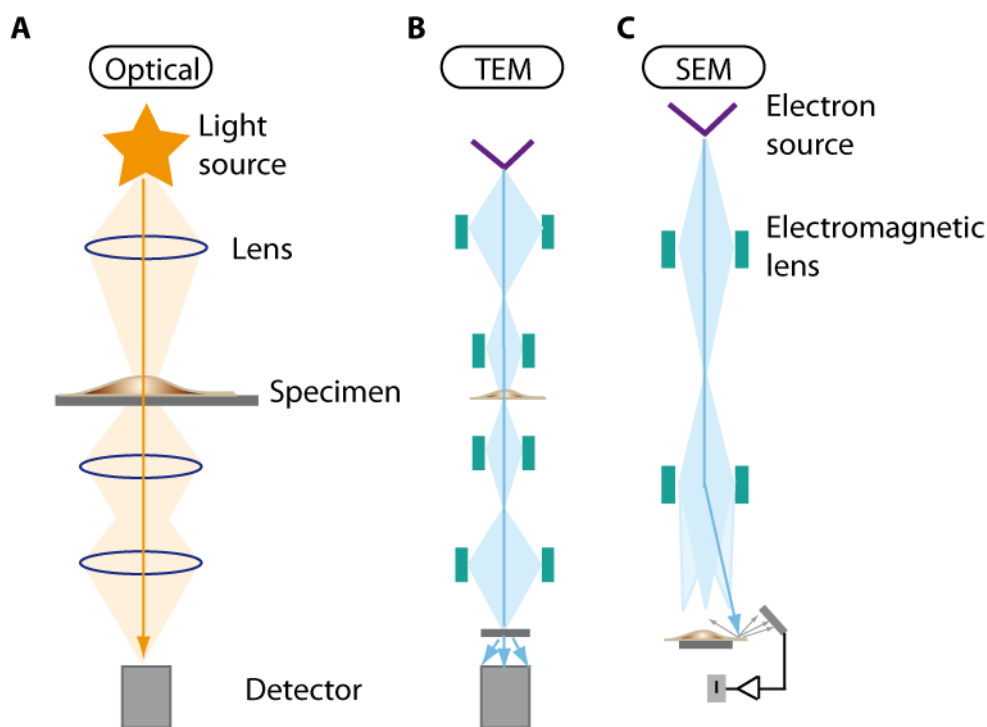


**Figure 3:** Scheme of available electron microscopy techniques.

The image is adapted from Aseyev *et al.* (Aseyev, 2013). (A) Light path in optical microscopy (B) electron path in transmission electron microscopy and (C) electron path of scanning electron microscopy with a detector unit. In all three microscopy methods, the photons or electrons are focused via optical/electromagnetic lenses. The image is composed of the signals collected by the detector.

The invention of cryo-EM helped to visualize biological samples near their native, hydrated state. Cryo-EM is a technique that images samples in a cryogenic state (McDowall *et al.*, 1983). The samples are frozen in liquid nitrogen and helium. This preparation reduces the radiation damage occurring to the sample and makes it possible to image at a quasi-hydrated state. Although this is a great advantage, this method still requires thin slices to obtain good contrast of thicker specimens like viruses (Adrian *et al.*, 1984) and bacteria or cells (Dubochet *et al.*, 1985).

Best results of cryo-EM could be obtained for large biological molecules like proteins. Today protein structures can be solved out of cryo-EM datasets (Liao *et al.*, 2013; Zhang *et al.*, 2013; Bartesaghi *et al.*, 2015; Wang *et al.*, 2015). In comparison to X-ray crystallography, it collects data of a sample in a native state, while the sample, conformation can change during crystal formation. X-ray crystallography on the other hand can only show a static view of a protein. The resolution of cryo-EM solved structures is nowadays about 2 Å (Bartesaghi *et al.*, 2015).

Another EM technique is scanning electron microscopy (SEM) available (von Ardenne, 1938). Using SEM, typically the surface of a specimen is coated with thin metal layer, like gold (Suzuki, 2002). The coated surface of the specimen is scanned with a focused electron beam to create a picture. The main information obtained is the topography of the sample. The resolution of SEM

analysis is about 1 nm. The electrons detected are secondary and back-scattered electrons of the sample.

Typically for EM, biological specimens are treated with glutaraldehyde for fixation, stained with osmium salts and dehydrated for any type of EM imaging (Massover, 2008; Nakakoshi et al., 2011).

An interesting fact of SEM is that it can be used for environmental scanning (ESEM) in liquid vapor of unstained biological specimens. Instead of the metal coating used in SEM as a conductivity layer for the back-scattered electrons, the gaseous phase in the detector unit is used to create the image (Stokes, 2003; Stokes et al., 2003; Muscariello et al., 2005; Kirk et al., 2009; Yang et al., 2012; Hao et al., 2013). The resolution is limited to a few nanometers comparable to SEM. A major advantage of ESEM over SEM is that biological specimens do not require intensive sample preparation. However, there are limitations due to the gaseous detector unit. To create images, a certain distance between detector and specimen has to be installed so that the gaseous phase covers the whole sample. This has to be taken into account when e.g. thick mammalian cells shall be investigated. Furthermore, the radiation damage of the sample is higher compared to SEM because the water molecules in the gas phase can form radicals that undergo chemically reactions with the specimen.

### **1.1.2.1 In-liquid TEM**

The previously mentioned conventional EM techniques have their limitations whenever biological samples shall be investigated. Mostly it is the aqueous sample, its surrounding, and its low contrast ability because of the low atomic weight composition. In order to be able to do live cell imaging the cells should be intact and not dissected, which had been done before to obtain images of cell compartments and intracellular structures. One solution to solve the vacuum/water challenge was to create a sealed chamber so that the water could remain in and around the sample only. Creating an aqueous environment around a biological sample allows imaging in a more native state compared to the EM methods used until then. The group of Niels de Jonge invented a sample chamber made out of silicon nitride that can occupy biological material without dehydration and other sample preparations (de Jonge et al., 2009). Another sample chamber made of graphene was used for similar experiments (Park et al., 2015). Both materials, Silicon nitride and graphene, are electron transparent. This means that the electrons travel through the material with almost no interactions so that an image of the actual sample within the chamber can be created. These windows replace the analogue glass function in light microscopy.

Having a suitable material for imaging at hand was the first step towards imaging of biological samples in aqueous environment; the next step was to create a sample holder that could be used for imaging using the new sample chambers, as the conventional holder could only carry 2D metal grids. The new sample chambers were thicker than the metal grids so that the holder had to be modified. The group of Prof. R.J. Dwayne Miller (MPI Hamburg, Germany and University of Toronto, Toronto, Canada) developed a silicon nitride nanofluidic cell and a customized sample holder that can be used in conventional JEOL TEMs (Mueller et al., 2013). The liquid static cell is nanofabricated and has a thickness of 150-400 nm after assembly. The variation of the thickness occurs due to the used spacer and bulging during measurements. The bulging can be explained due to the pressure correction of the liquid inside the chamber and the vacuum in the microscope column. A schematic overview of the sample chamber is shown in Figure 4.

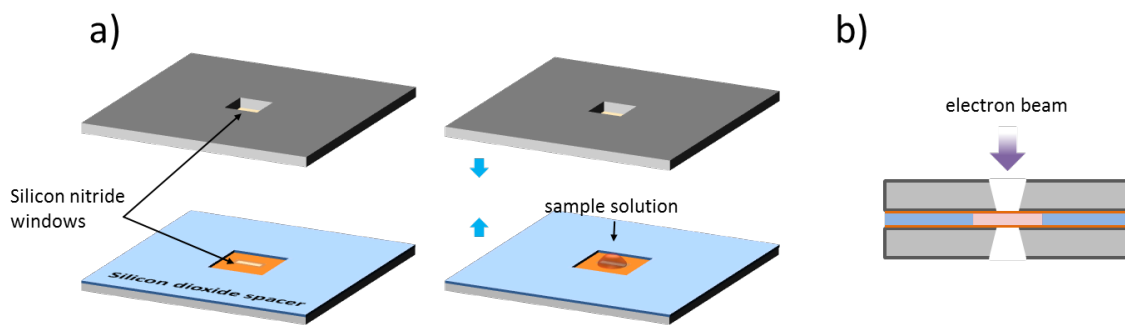


**Figure 4: Schematic overview of a silicon nitride chamber for in-liquid TEM not drawn to scale. The nanofluidic chambers are composed of an outer area of silicon dioxide as spacer (blue). The inner area is made out of silicon nitride (orange). The liquid sample is added to the inner area and the nanofluidic chamber sealed for imaging (reprinted with permission from Keskin et al.).**

The sample can be directly loaded to the viewing area before the nanofluidic cell is closed by a second window and mounted to the sample arm that is customized as well. This construction enables imaging of liquid samples like nanoparticle solutions (Mueller et al., 2013), viruses (Cameron Varano et al., 2015), or even mammalian cells (de Jonge et al., 2009) without any slicing or extensive preparation and staining procedures, typical for EM.

The image is created comparable to conventional copper grids covered with carbon films. The resolution depends on the thickness of the liquid layer. A thick layer increases the travel distance of scattered electrons so that more energy can be lost in the meanwhile. This lowers the resolution. However, resolutions beyond 200 nm down to 10 nm could already be obtained (Mueller et al., 2013; Keskin et al., 2015).

It was further possible to image mammalian cells grown on the silicon nitride windows using SEM (de Jonge et al., 2009). Although these nanofluidic cells allow to image biological samples in liquid environment, imaging was performed in SEM mode to reduce possible radiation damage to the samples.

## 1.2 Probes for Microscopy

Light and electron microscopy can give an overview of a specimen. However, to investigate a specific area or even class of molecules, single proteins, or oligonucleotides, they need to be tagged specifically.

Fluorescent light and electron microscopy operate with probes to illuminate the area or protein of interest.

Although there are huge differences to create a signal in fluorescence or in electron microscopy, they have two things in common:

- (i) The probe should be as small as possible, so that it does not interfere with the sample and
- (ii) The probe should be genetically encoded.

The first point addresses the challenges that appear when the probes are bigger than the molecules of interest, because it might change their activity or pathway within the cell. The second point addresses that probes attached after biosynthesis cannot be used to visualize e.g. movements or dynamic events starting at time point zero. They need to be introduced to the sample first, which requires sample preparation and possibly alteration during this process. A clonable tag is already at the right position because it is fused to the molecules of interest. Although fused proteins allow visualizing from time point zero, controls are required to verify that the tag did not alter the process itself.

Latest microscopy devices combine fluorescence and electron microscopy. This development opens the field for bimodal probes that are suitable for fluorescence and electron microscopy, which again increases the need to develop new probes. Furthermore, it is challenging to find a probe that allows live cell imaging with both fluorescent light and electron microscopy.

### 1.2.1 Fluorescent Probes

The basic physical property for fluorescent light microscopy is that the probe emits light. Mostly light emission can be obtained after excitation, typically by absorption of a shorter wavelength light pulse of the probe. The difference between the absorption and emission maxima is a key parameter and named “Stokes-Shift” (Figure 5) (Coling and Kachar, 2001; Valeur, 2002).

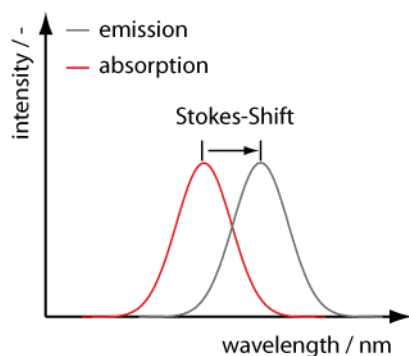


Figure 5: Stokes shift.

The difference between the maxima of the absorption and emission shows the electronic transition of a fluorophore.

The physical description of light emission is an energy transfer. This energy transfer occurs in the outer electron orbitals of a probe (Lakowicz, 2006). The outer electron orbitals determine the wavelength of absorption and emission next to the efficiency of the probe, which results in brightness and duration of the emitted light. The probe absorbs photons in the ground state ( $S_0$ ), which leads to alterations in the rotational, vibrational and electronic state of its electrons and to their excitation to a higher energy level ( $S_2$ ) (Valeur, 2002; Lichtman and Conchello, 2005). A systematical scheme of the energy transfer steps is depicted in the Jablonski energy diagram (Figure 6).

Fluorescent dyes mainly use conjugated double bonds with aromatic  $\pi$ -bonds. The electrons of the  $\pi$ -bonds move easily to outer orbital electrons because of the low energy differences between ground and excited state. As a rule of thumb, the more conjugated bonds the lower is the excitation energy that the electrons need for excitation (Zhang et al., 2002; Lichtman and Conchello, 2005; Tsien et al., 2006).

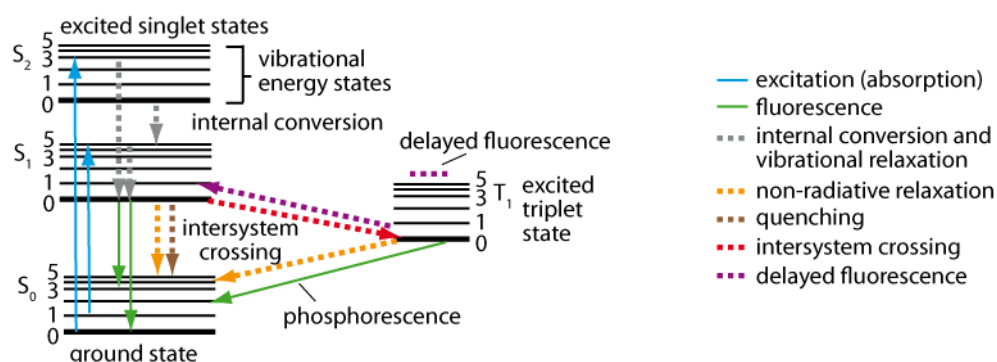


Figure 6: Jablonski energy diagram.

The energy transitions of electrons in fluorophores are depicted using the Jablonski energy diagram (adapted from Lichtman *et al.* (Lichtman and Conchello, 2005)). It describes the different stages of electrons during excitation (blue) over internal conversion (dashed grey), non-radiative relaxation (orange), intersystem crossing (red) between the excited triplet state and fluorescence (green).



The excitation needs to give enough energy in form of photons to induce the change of the vibrational and rotational state to convert into the higher energy state. The transition can originate from one single photon, but for complete excitation of the dye, many transitions are needed. A size for the probability of a fluorophore to absorb a photon is the molar extinction coefficient  $\epsilon$ . Small organic fluorophores have a typically  $\epsilon$  of 25,000-200,000  $\text{M}^{-1} \text{cm}^{-1}$ , while the most common clonable probe enhanced green fluorescence protein (EGFP) has a  $\epsilon$  value of 60,000 (Lichtman and Conchello, 2005; Resch-Genger et al., 2008).

As depicted in the Jablonski energy diagram (Figure 6), the emission spectrum is based on the variety of different pathways to lose absorbed energy. The emission spectrum is characteristic and cannot be shifted to another wavelength by additional excitation. It solely relies on the drop back to a lower ground state. However, the energy is less compared to the absorbed photons and is released via vibrational relaxation in the ps range (Lichtman and Conchello, 2005).

The energy loss from excited to ground state is also known as “forbidden transition” into a triplet state. In the triplet state the vibrational energy levels overlap with the lowest S1 levels and undergoes the reversion to ground state ( $\mu\text{s}$ ) resulting in phosphorescence (Lichtman and Conchello, 2005).

Another key parameter next to the excitation and emission difference of the probe is its quantum yield (QY). The quantum yield is determined as the total light emission over the entire fluorescence spectral range taking into account the ratio of fluorescence emission to non-radiative energy losses. Typically increasing the number of  $\pi$ -bonds increases the QY. Bright probes showing high QY are favorable as they reduce doubts about the signal with a strong signal to noise ratio and are easier to track (Lichtman and Conchello, 2005; Tsien et al., 2006; Resch-Genger et al., 2008).

Based on the mentioned physical properties required for dyes used in fluorescence light microscopy, there are two classes of fluorescent probes based on organic composition:

- (i) Organic dyes, e.g. ATTO, Cy, FITC, Alexa, etc.
- (ii) Fluorescent proteins of the GFP superfamily.

Both classes and prominent examples will be explained according in the following chapters.

A third growing class is based on fluorescent nanoparticles, for example quantum dots (Reed et al., 1988). These quantum dots are semiconductors with a nanometer scale. A typical core consist e.g. of Cd/Se (Zhao et al., 2004). The fluorescence occurs due to light absorption followed by

electron excitation from the valence to the conduction band over the band gap (optoelectronic properties) (Alivisatos, 1996). A hole is left behind in the valence band. This hole can bind with the electron and form an exciton. During the transition to ground state the energy is emitted as light, which is the observed fluorescence. The band gap can be tuned by the particle diameter resulting in different colors (Wu et al., 1987).

### 1.2.1.1 Organic Dyes

Organic dyes are small in sizes and have a good quantum yield, low photobleaching, low photo toxicity and switchable fluorescence (Tsien et al., 2006). Nevertheless, it is not possible to integrate them directly into the genetic information for the protein of interest. They are mostly attached to antibodies for immunostaining (Giepmans et al., 2006) or by orthogonal chemistry (Schulz et al., 2013; Holstein et al., 2014) to the molecule of interest. Some of the dyes specifically bind to specific biomolecules, for example the dye DAPI or Hoechst. These only bind to nucleic acids. Organic dyes are derivatives of e.g. xanthene (fluorescein (FITC), rhodamine, Texas Red), coumarine, oxazine (Nile red).

**Table 1: Common used organic fluorescent dyes and some parameters (Abcam, 2014).**

Fluorescent dye	Excitation $\lambda/\text{nm}$	Emission $\lambda/\text{nm}$	QY	Specificity
LysoTracker Blue	373	421	n/a	Lysosomes
Hoechst 33258	352	455	0.83	DNA
Fura-2 High $\text{Ca}^{2+}$	336	504	n/a	$\text{Ca}^{2+}$ Flux
FITC	495	517	n/a	n/a
Alexa488	493	520	0.92	n/a
SYBR Green I	498	522	n/a	n/a
Cy3	550	570	0.15	n/a
Ethidium Bromide	524	605	n/a	DNA/RNA
ReAsH	597	608	n/a	CCXXCC
Cy5	650	670	0.28	n/a

The new super-resolution microscopy techniques STED and STORM require switchable, blinking organic dyes. Commonly Atto 532, Alexa Fluor 647, Cy 5 and 7 or Rhodamine B are used (Fernandez-Suarez et al., 2008). There is an additional class of fluorophores for super-resolution imaging: photo caged fluorophores. These have to be activated with an activating

wavelength so that the protective group releases the actual fluorophore. The advantage for fluorescence and super-resolution fluorescence microscopy is that the signal can be switched on when it is needed and thus signal to noise is reduced. Furthermore, there is only a finite number of transversions of a dye possible so that the lifetime can be controlled (Rust et al., 2006; Fernandez-Suarez et al., 2008). Especially for live-cell imaging a tunable probe can be important because the event of interest can occur over several minutes or at some specific time points during cell division.

### 1.2.1.2 Genetically Encoded Fluorescent Proteins

Fluorescent proteins can be directly fused to the protein of interest. The most famous clonable fluorescent probe is the green fluorescence protein (GFP). It was discovered 1962 by Shimomura (Shimomura et al., 1962a), who was awarded with a Nobel prize lately. The green fluorescent protein forms a  $\beta$ -sheet barrel (Yang et al., 1996). The barrel itself has no fluorescent characteristics. It consists of 11 antiparallel  $\beta$ -sheets (Ormö et al., 1996). The fluorescent chromophore is built internally of the amino acid residues 65 (Ser), 66 (Tyr), 67 (Gly) (Heim et al., 1994). The excitation wavelength for GFP is 488 nm, while the emission wavelength is 510 nm (Shimomura et al., 1962b).

The main challenging point about all fluorescence proteins is the low signal to noise ratio due to high background fluorescence. It is not possible to directly switch fluorescence proteins on in a certain area of the sample. Nowadays, there are many GFP variants available that are optimized according to their signal to noise ratio. Additional new variants have been developed to create a broader color spectrum (Heim et al., 1994). The best variant upon quantum yield is the so-called enhanced GFP (EGFP) (Cormack et al., 1996). Other attempts to gain a higher signal to noise ratio use multiple copies of GFP attached to the protein or area of interest as shown in Querido *et al.* for the MS2coat strategy (Querido and Chartrand, 2008). A major issue of the constructs using multiple copies is always the high molecular weight that is added to the molecule of interest. Generally spoken the protein or area of interest should be altered as less as possible. By attaching many copies of dyes or fluorescent proteins, the sample can have a size that is multiple times of the original. Thus, the dynamics and the behavior might be altered.

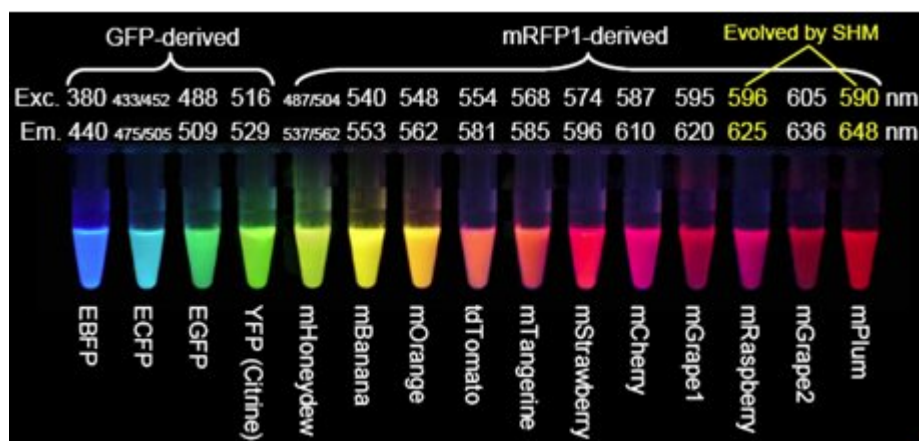


Figure 7: Variety of GFP proteins reproduced of R. Tsien's Nobel Prize lecture 2008.

The different fluorescent proteins derived of GFP, called GFP superfamily, are depicted (image is courtesy of Tsien, 2008).

In terms of switchable light emission and thus better signal to noise ratio, split GFP was developed (Cabantous and Waldo, 2006). Based on the ability of re-conformation of the single  $\beta$ -sheets into the protein,  $\beta$ -sheet 11 was extracted from the GFP DNA and produced separately. Fluorescence could only be imaged, if  $\beta$ -sheet 11 was added to the sample containing the GFP barrel 1-10. This approach shows an effect similar to a switchable probe.

### 1.2.2 Aequorin as a Potential Bimodal Probe

Aequorin (AQ) was discovered, together with GFP, 1962 by Shimomura *et al.* (Shimomura et al., 1962a). It has been widely used for calcium signaling experiments during the last decades (Blinks et al., 1982; Shimomura et al., 1988; Rizzuto et al., 1992; Brini et al., 1993, 1994; Robert et al., 2000; Torrecilla et al., 2000; Missiaen et al., 2004; de la Fuente et al., 2012; Webb and Miller, 2012).

The enzyme belongs to the family of luciferases (Shimomura et al., 1962a). It emits blue light with a wavelength of 467 nm upon binding of up to three  $\text{Ca}^{2+}$  ions within the highly conserved EF-hand motifs (Shimomura and Johnson, 1970). Sequence analysis of AQ revealed that out of four EF-hand motifs three can bind calcium (I aa 24-35, II aa 117-128 and III aa 153-164) (Charbonneau et al., 1985; Inouye et al., 1985). The results of the latest studies showed that binding of only one  $\text{Ca}^{2+}$  is sufficient to trigger the light emission (Toma et al., 2005; Tricoire et al., 2006).

Aequorin in its apoform has a molecular weight of 21.5 kDa and a length of 189 amino acids. Several isoforms are known today (Hastings et al., 1969; Charbonneau et al., 1985).

The first amino acid sequence of AQ was published by Charbonneau in 1985 (Charbonneau et al., 1985). Cyanogen bromide cleavage of the protein was used to reveal a minimum of three isotypes with substitutions at 16 positions. The work of Charbonneau assigned three internally EF-hand motifs homolog to calmodulin and troponin C, which explained the high  $\text{Ca}^{2+}$  affinity of AQ.

Within the same year, Inouye *et al.* were able to publish the first cDNA sequence of AQ and demonstrated that it was possible to clone the DNA into bacterial vector systems (Inouye et al., 1985).

The natural role of AQ is the activation of GFP in the jellyfish (Shimomura et al., 1962a; Prendergast and Mann, 1978). A major difference to GFP is that the chromophore, coelenterazine (CTZ, first mentioned in Shimomura *et al.* (Shimomura and Johnson, 1975)), cannot assemble from amino residues of the enzyme itself, instead it has to be taken up (Shimomura et al., 1974; Shimomura and Johnson, 1975; Toma et al., 2005). The chromophore was first named as AF350 based on the UV absorption maximum at 350 nm (Shimomura and Johnson, 1969). CTZ is bound in the active center of the enzyme by the residues His 169, Tyr 173 and Tyr 184 (Head et al., 2000).

The structure was solved 2000 by Head and coworkers (Head et al., 2000). It shows a globular protein with a hydrophobic core cavity and two pairs of EF-hand motifs that are arranged back to back. It consists mostly of  $\alpha$ -helices that interplay during binding (Head et al., 2000).

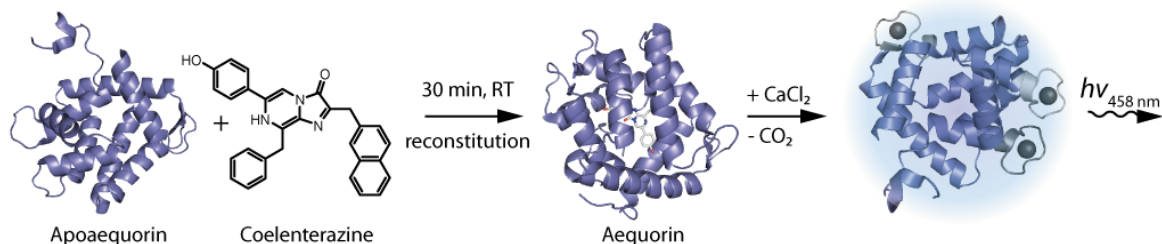


**Figure 8: Reconstitution of Apoaequorin to Aequorin**

Apoaequorin has to undergo reconstitution for luminescence activity. It is incubated with CTZ to form aequorin. The luminescence is triggered by the addition of  $\text{Ca}^{2+}$  ions and blue light with a wavelength of 458 nm is emitted. The figure is created based on the pdb file 1SL8.

Binding of  $\text{Ca}^{2+}$  or  $\text{Sr}^{2+}$  ions induces a conformational change of the  $\alpha$ -helices, which leads to the decarboxylation of coelenterazine to coelenteramide and the final light emission (Shimomura and Johnson, 1970, 1978; Shimomura et al., 1974; Allen et al., 1977).

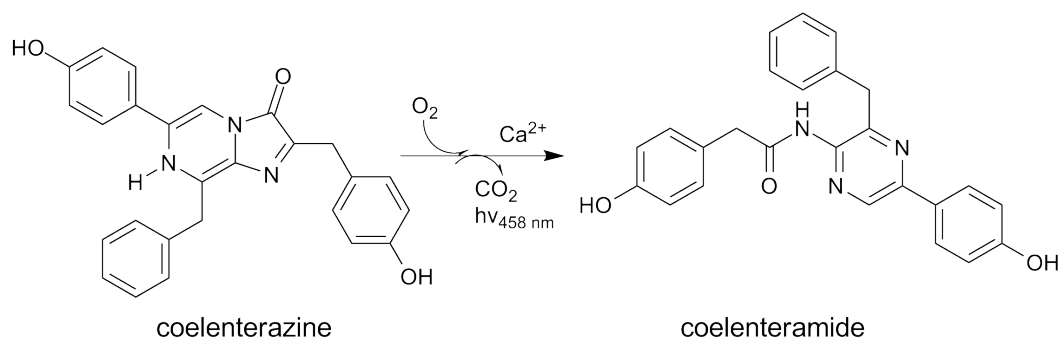


**Figure 9: Reaction of coelenterazine to coelenteramide**

The light emission occurs during the relaxation of the first singlet excited state of the oxyluciferin (Charbonneau et al., 1985).

It is known that energy of more than 60 kcal/mol at the maximum is released by the intramolecular reaction, which results in the blue light and heat (Shimomura and Johnson, 1970; Charbonneau et al., 1985). This is equivalent to a quantum yield of 0.23 photons per mol protein at 25 °C and 0.29 at 5 °C in aqueous solutions and 0.37 in alcohol, respectively. The dissociation constant for CTZ could be calculated to 0.5 mM for the protein. Reconstitution for 25-30 min leads to 50% photo protein, after 3h 90 %. Regeneration after the first light emission could be achieved by ion exchange chromatography using a DEAE column. It was found that CTZ addition to reconstituted protein led to weak and continuous luminescence parallel to the regeneration, while the normal observed light emission was very fast (ms). Addition of reducing agents like  $\beta$ -mercaptoethanol and an excess of CTZ resulted in light emission for several hours and a total photon emission five times higher compared to the fast emission (Shimomura and Johnson, 1975).

Apoaequorin was often found in a dimeric state, which could be decreased by the addition of reducing agents (Prendergast and Mann, 1978). Next to reducing agents, like  $\beta$ -mercaptoethanol or dithiothreitol (DTT), monovalent ions were found to be helpful for stable light emission as tested in Shimomura *et al.* (Shimomura and Shimomura, 1984). Addition of 150 mM KCl was helpful to achieve stable luminescence values as it stimulates intracellular ion conditions. If buffers with low ionic strength were used, huge error bars could be obtained from the data (Shimomura and Shimomura, 1984). It was known that  $\text{Ca}^{2+}$  could trigger the luminescence; however, the interplay of the  $\text{Ca}^{2+}$  concentration and the brightness of the induced luminescence have not been explained yet. The work of Allen *et al.* answered the question whether the luminescence rate of AQ is proportional to the concentration of  $\text{Ca}^{2+}$  in a range of 10 nM to 0.01 M (Allen et al., 1977). They found that at low concentrations the light emission seems to be  $\text{Ca}^{2+}$  independent and does not necessarily show the before observed luminescence peak. Higher

concentrations need to be in proportional ground settings to show the typical luminescence behavior. According to their findings, the differences occur due to the oxygen levels that are required for light emission.

In 1985 Ray *et al.* published that the oxidation of the chromophor happened upon metal ion binding (Ray *et al.*, 1985). They also found that spontaneous emission could occur, but only with a rate smaller than  $10^{-6}$  of  $\text{Ca}^{2+}$  induced emission.

Because of the bimodal structure of the active protein, consistent of the chromophor and the apoprotein, semi synthetic aequorin variants were produced. Synthetic concentrates of CTZ analogs were synthesized. One of these was published by Shimomura in 1988 (Shimomura *et al.*, 1988). Here, the CTZ was modified with a hydroxyl-group that resulted in a fast luminescence rise time. The quantum yield could be increased. The chromophor is a imidazolopyrazinone in its oxidized form (Kemple *et al.*, 1990; Shimomura *et al.*, 1990).

Further, variants of the apoaequorin for low  $\text{Ca}^{2+}$  concentrations, bright luminescence, improved stability, or slow decay were introduced in the following 10 years. Nomura *et al.* postulated that the C-terminal proline is required for bioluminescence and stability of the enzyme (Nomura *et al.*, 1991). Kendall *et al.* were able to find a variant with 20x lower activity with  $\text{Ca}^{2+}$  (Kendall *et al.*, 1992). The substitution D119A in EF-hand motif 2 leads to a decreased  $\text{Ca}^{2+}$  affinity ( $K_d(\text{Ca}^{2+})$  13  $\mu\text{M}$  AQ and 0.26 mM D119A), which made it possible to measure  $\text{Ca}^{2+}$  inside organelles with higher  $\text{Ca}^{2+}$  concentrations compared to the cytosolic  $\text{Ca}^{2+}$  concentration, like mitochondria.

All developments for new apoaequorin variants were based on the knowledge of EF-hand motifs and the positions within these motifs that are necessary for ion binding. Furthermore, they were able to target specific organelles, e.g. mitochondriae (Rizzuto *et al.*, 1992) or nucleus (Brini *et al.*, 1993), by adding an N-terminal KDEL sequence.

Based on other enzymes containing EF-hand motifs, like obelin or calmodulin, many substitutions have been tested before (Snyder *et al.*, 1990; Permyakov *et al.*, 2000; Pardoux *et al.*, 2012). Today there are several slow decay, bright, thermostabilized or low affinity variants known<sup>72,84</sup>. Furthermore, synthetic CTZ analogues were tested to obtain higher half-life times or wavelength shifts of the emitted light. All of these have already been used for imaging<sup>88-93</sup>.

Promiscuous metal binding activity of AQ could be shown by Kemple *et al.* (Kemple *et al.*, 1990). They tried Mn(II) and trivalent lanthanides to trigger luminescence. While  $\text{Mn}^{2+}$  showed inhibitory effects and only one tight binding, calcium and lanthanides competed with 1.92 and 1.38  $\mu\text{M}$  association constants.

Aequorin has the possibility to bind metal ions and emit light, which makes it a high potential candidate as a bimodal probe for light and electron microscopy.

### 1.2.2.1 EF-hand Motifs

Aequorin has a naturally high affinity for calcium due to the EF-hand motifs (Head et al., 2000). The so-called EF-hand motifs are highly conserved motifs. They can bind metal ions with very high affinity in the nanomolar range (Cates et al., 1999). The motif is a helix-loop-helix motif that mainly binds calcium ions. Typically, the  $\text{Ca}^{2+}$  ion is bound in the 12 amino acid residues long loop (Gifford et al., 2007).

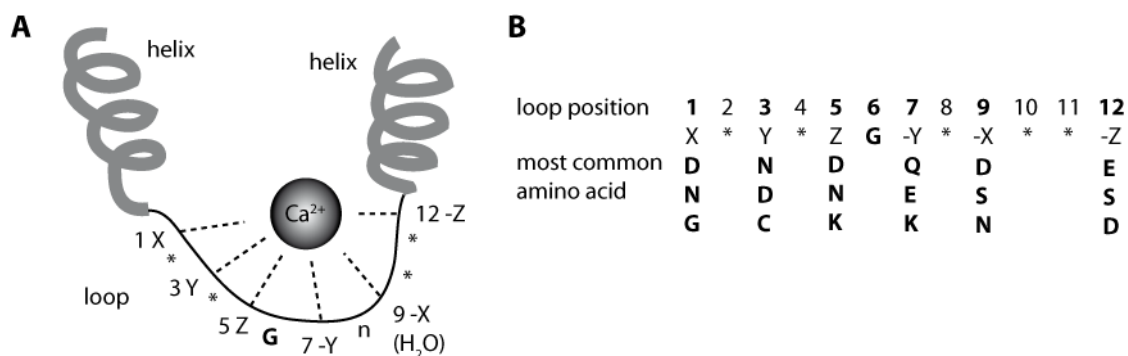


**Figure 10: Schematic drawing of an EF-hand motif.**

**(A) Helix-loop-helix motif of the EF-hand.** The loop consists of 12 amino acids. Positions 1, 3, 5, 7, 9, and 12 coordinate the metal ion binding. Position 6 is a highly conserved glycine. Position 9 coordinates the metal ion via a water molecule. **(B) Overview of the most common amino acids at the 6 coordinating positions so far.** The figure is adapted from Gifford *et al.* (Gifford et al., 2007)

The  $\text{Ca}^{2+}$  ion is coordinated in a pentagonal bipyramidal manner. The ion is stabilized via amino acid residues 1, 3, 5, 7, 9 and 12 of the loop (Strynadka and James, 1989). While positions 1, 3, 5, and 12 coordinate the metal with their carboxylate oxygens, position 7 uses the backbone carbonyl oxygen together with a water molecule. Position 9, also known as gateway position, binds via a water molecule the  $\text{Ca}^{2+}$  ion. Although these positions are mainly involved in binding, the remaining 6 positions in the loop stabilize metal ion coordination as well (Strynadka and James, 1989; Snyder et al., 1990; Gifford et al., 2007; Jafarian et al., 2011). Next to these important positions, position 6 of the loop is important. Substitution of the conserved glycine at this position led to complete loss of function.

Other important positions for binding are position 1, 3, and 12. If position 1 is substituted, there can be complete loss of binding. Position 3 and 12 show less impact, but nonetheless substitutions at this position lead to low  $\text{Ca}^{2+}$  affinity variants (D119A, E128G).

It is known that EF-Hand motifs can also bind lanthanide ions (Hogue et al., 1992; Drake et al., 1996). Drake *et al.* were able to reduce the  $\text{Ca}^{2+}$  affinity by substituting at the gateway position 9 towards acidic side chains (Glu or Asp). The ionic charge selectivity of this EF-hand motif variants was  $10^3$  fold higher for trivalent cations, and a partial loss of size selectivity could be measured (Drake et al., 1996). Another high potential spot for substitution towards trivalent and



bigger ions is position 7. Nitz and coworkers wrote that substitution to W or F resulted in higher affinity for lanthanides (Nitz et al., 2003), which would be more suitable for electron microscopy due to the higher number of electrons in lanthanides.

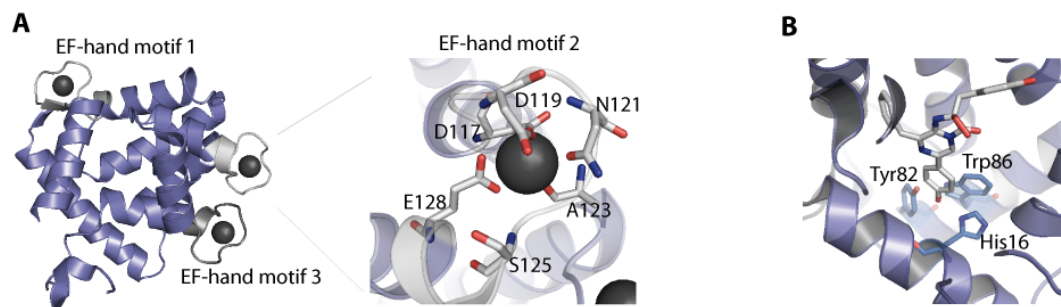


**Figure 11: Protein structure of AQ according to PDB 1SL8.**

(A) EF-hand motifs colored in grey, alpha helices in purple. EF-hand motif 2 zoomed out and positions 1, 3, 5, 7, 9, and 12 depicted in sticks. (B) Catalytic triade consisting of the three residues His16, Tyr82 and Trp86 (blue) that bind to CTZ (depicted in grey sticks).

Furthermore, so-called Lanthanide-binding-tags (LBT) have been established by Barbara Imperiali's group as contrast agents for magnetic resonance imaging (MRI). These tags are short peptides containing the 12 amino acids for loop formation to bind metal ions (Franz et al., 2003; Nitz et al., 2003; Daughtry et al., 2012). The 12 amino acids originate from an EF-Hand motif. The results after screening of libraries showed also tryptophan on position 7 and glutamic acid at position 9 as the best substitutions for lanthanide binding. It is also necessary for MRI to enhance the amount of heavy atoms in order to increase the contrast of a picture. Atoms with higher electron numbers have more electrons that align due to their magnetic spin. This is the reason for a good contrasted image.

### 1.2.2.2 CTZ Binding

Aequorin has two functions: one is the binding of metal ions that can be used for contrast in EM and the other is the luminescence activity upon binding of the metal ions that can be used for fluorescence microscopy. As already mentioned, there were CTZ analogues synthesized that induce different luminescence properties.

Native CTZ binds via hydrogen bonds by amino acids His16, Tyr82, and Trp86 as catalytic triad. The active site is located in the center of the globular AQ and surrounded by  $\alpha$ -helices. These helices form a cavity with  $600 \text{ \AA}^3$  that exclude access for solvents (Head et al., 2000).

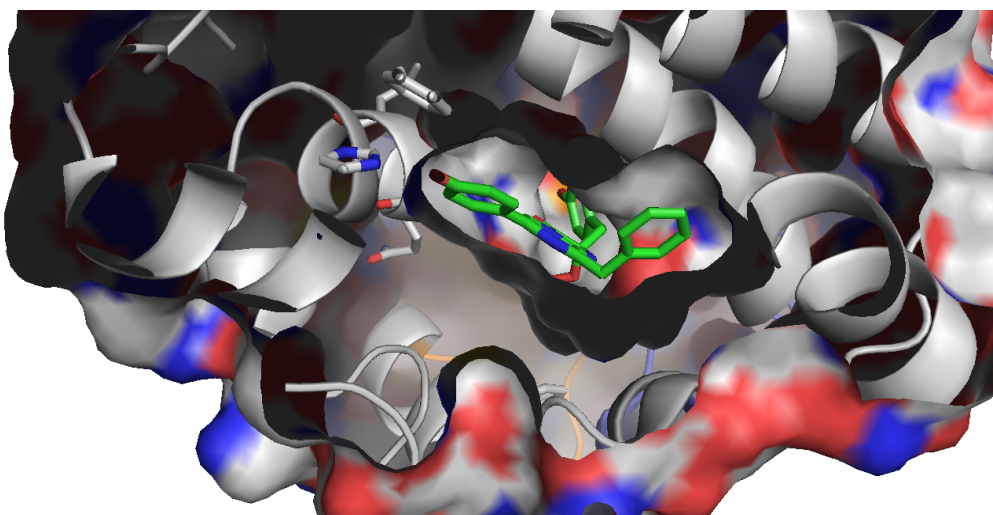


Figure 12: CTZ cavity of Aequorin.

Coelenterazine (green) is located in the center of AQ in a cavity that excludes access for solvents. The enzyme is shown with hydrophobic (red areas) and hydrophilic areas (blue areas).

It was found that a substitution of Tyr82 to Phe leads to a 37 nm shift in the emitted wavelength. The additional hydroxyl group is essential for the stabilization of the CTZ within the active site, which explains the enormous wavelength shift (Head et al., 2000; Dikici et al., 2009).

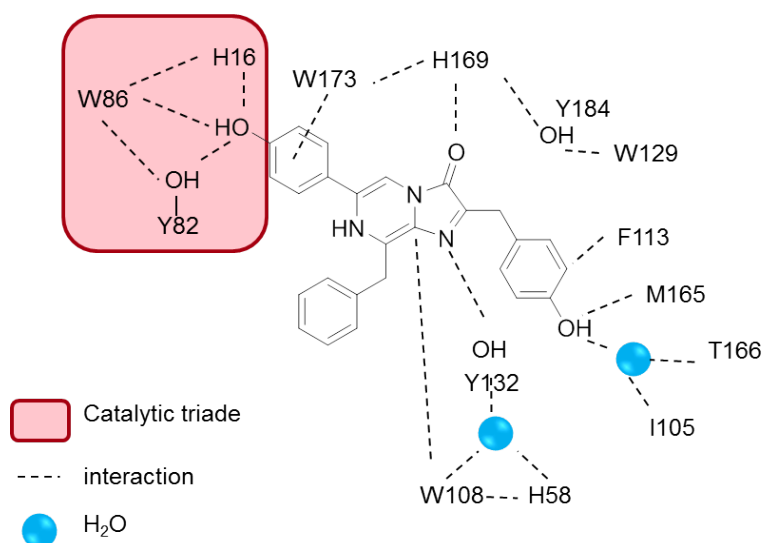


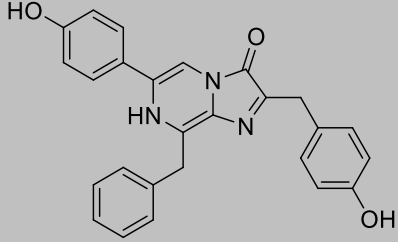
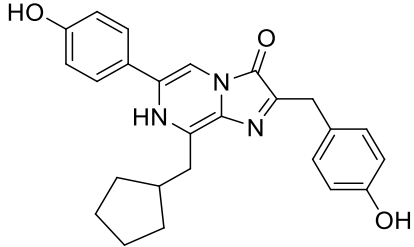
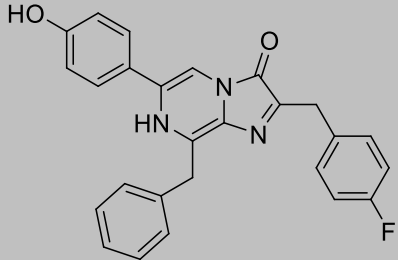
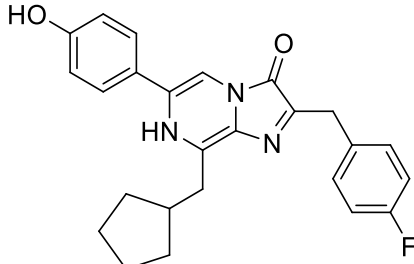
Figure 13: Interaction of the amino acid residues of AQ with CTZ.

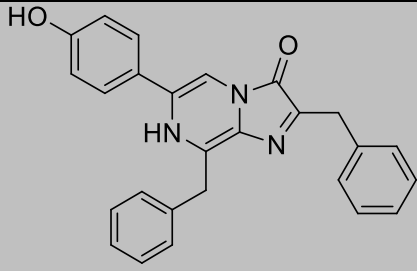
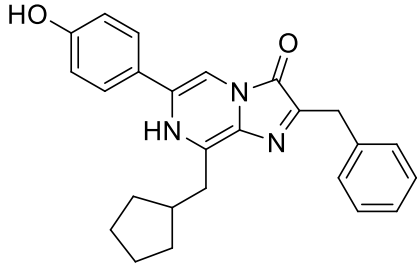
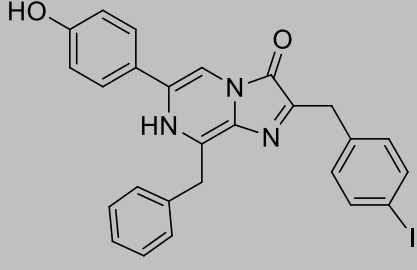
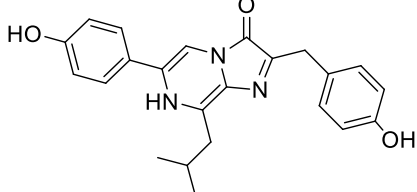
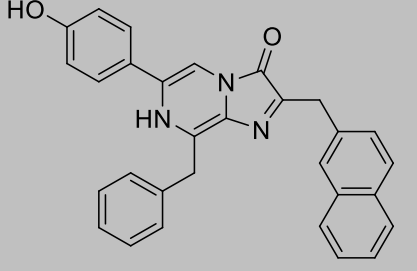
The catalytic triad is marked red. Water molecules for interaction are shown as blue dots (adapted of (Head et al., 2000)).

Other important amino acids are Trp129, Phe149 and Glu164 - Gln168. Phenylalanine 149 and Gln168 participate in stabilization of the CTZ peroxide during light emission (Head et al., 2000; Dikici et al., 2009). Binding of Ca<sup>2+</sup> disrupts the coordination of CTZ by Glu164-Gln168, Phe149, and Trp129. The displacement of the helices flanking the C-terminus relocates Tyr184. Furthermore, the hydrogen bonds to His169 are disrupted, which leads to peroxidation of the CTZ and light emission (Head et al., 2000).

In general, tighter binding of CTZ to AQ results in brighter luminescence. The binding affinity of CTZ analogues can be stronger compared to native CTZ, so that these analogues can also be used for different experimental designs regarding higher luminescence values or longer life-times (Shimomura et al., 1988, 1993). Commercially available are CTZ native, cp, f, fcp, h, hcp, i, ip, and n (Table 2).

**Table 2: Overview of CTZ analogs according to Shimomura et al. (Shimomura et al., 1988, 1993; Shimomura, 1991)**

Structure	Name	$\lambda_{Em}$ (nm)	Relative intensity	Half-rise time (s)
	native	465	1	0.4-0.8
	cp	442	15	0.15-0.3
	f	473	18	0.4-0.8
	fcp	452	135	0.4-0.8

	h	475	10	0.4-0.8
	hcp	444	190	0.15-0.3
	i	476	0.03	8
	ip	441	47	1
	n	467	0.01	5

### 1.2.3 Scattering Probes

The contrast of transmission electron micrographs is created in a different way compared to fluorescence microscopy. Here, the nature/quality of the sample matters. As biological specimens mainly consist of light atoms like carbon, nitrogen, oxygen, phosphorus, and hydrogen, they will not give highly contrasted pictures. Instead of light emission for detection in fluorescence microscopy, electron microscopy requires heavy atoms that have dense electron shells and are able to scatter electrons (Egerton, 2005) (Figure 14).

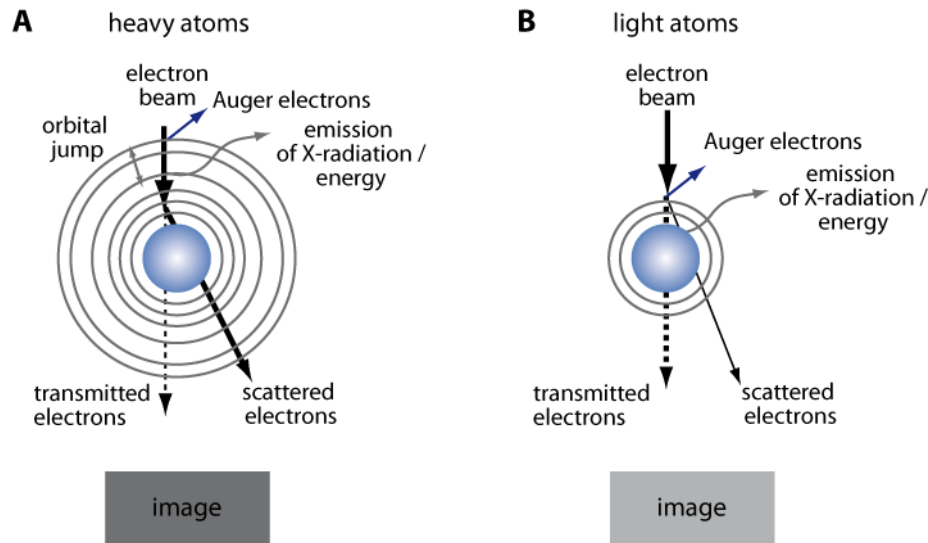


Figure 14: Beam path and principle of contrast in electron microscopy.

(A) Interaction of the electron beam with the electrons of a heavy atom, e. g. metal ions. Multiple electrons surround the core. Various interactions, such as Auger electrons, scattered electrons, transmitted electrons can occur. Moreover, energy emission (X-radiation) and orbital jumps can occur. (B) Interaction of the electron beam with light atoms such as carbon, oxygen. The figure is adapted from the Electron Microscopy Tutorial of the University of Utah (The University of Utah)

In TEM measurements, bright field and dark-field mode as well as diffraction can be used to investigate a sample. The typical imaging technique in TEM is bright field mode. Here, the contrast is formed by absorption of the electron by the samples. Heavy atoms with more electrons appear darker compared to light atoms with less electrons (Egerton, 2005). There are only few probes and stainings for the application of electron microscopy on biological specimens available.

#### 1.2.3.1 Classical Negative Staining

Biological samples are treated with heavy metal salts like uranium chloride or osmium salts for negative staining. These staining salts are highly toxic. Furthermore, the samples are embedded in epoxy resin and cutted at a microtome (Egerton, 2005; Nakakoshi et al., 2011).

Another state of the art approach is the use of immunogold (see chapter 1.2.3.3). Here, antibodies against the protein of interest are immobilized on gold nanoparticles. The antibody determines the specificity whereas the nanoparticles give contrast (Suzuki, 2002).

### 1.2.3.2 Genetically Encoded Probes

In other attempts, clonable probes for electron microscopy were established analogue to the concept of GFP for FLM. The most common are metallothioneins (Braun et al., 2002; Fukunaga et al., 2007; Zhou et al., 2012), ferritins (Wang et al., 2011), ReAsH (Griffin et al., 1998) and MiniSOG (Shu et al., 2011).

Metallothioneins can bind up to 30 gold atoms, which gives the necessary contrast. While the bound heavy atoms, mostly gold or iron, give rise to a contrasted picture, the molecular weight of the protein is changed by a huge factor due to the binding of these atoms (Braun et al., 2002; Fukunaga et al., 2007; Zhou et al., 2012).

The applications of ReAsH and MiniSOG have been established in the last decade. Both are bimodal for fluorescence and electron microscopy. ReAsH uses arsene for contrasting. Due to the fact that arsene is toxic, ReAsH cannot be applied in live-cell imaging (Braun et al., 2002; Fukunaga et al., 2007; Zhou et al., 2012). MiniSOG oxidizes diaminobenzidine, which precipitates and is then stainable with osmium salts, which is also toxic. For that reason, MiniSOG is also not a suitable probe for live cell imaging. Furthermore, the samples undergo fixation during the electron microscopy and there is again no live cell imaging possible (Shu et al., 2011).

All staining/contrasting methods available so far can contrast only thin, fixed samples and are not suitable for live cell imaging in electron microscopy.

### 1.2.3.3 Gold Nanoparticles as Probes for Imaging

Gold nanoparticles (AuNPs) have a 150 years long history (Faraday, 1857). The synthesis of AuNPs with high yields, various sizes, and shapes was expanded during the last 60 years. By the use of citrate stabilization it became possible to synthesize biocompatible AuNPs (Turkevich et al., 1951; Frens, 1973), which are multifunctional and show low toxicity in cell culture experiments (Connor et al., 2005; Vijayakumar and Ganesan, 2012).

The Turkevich method is a synthesis strategy for citrate stabilized AuNPs in water (Turkevich et al., 1951). This method is still used today to produce water soluble AuNPs mainly for life science applications.

The Turkevich-method uses gold chloride and sodium citrate for the reduction to colloidal gold particles with a diameter ranging from 20 nm to 150 nm with good size distribution within a few nanometer. The first step is the nucleation to seeds, which do not provide perfect colloidal shape. The shape then changes during the reduction process to the final colloidal shape (Turkevich et al., 1951).

The AuNPs are prepared in aqueous solution and thus phase extraction from organic phase is not necessary. As a result, there are no laborious cleaning steps needed before coupling with biomolecules.

Manipulation of AuNPs upon electron energy input was examined in several studies using conventional TEM and in-liquid TEM (Bakshi et al., 2007; Wang et al., 2009; Evans et al., 2011; Zheng et al., 2012). For example Bakshi *et al.* and Wang *et al.* examined possible 1D pearl-necklace like structures to 2D structures that can form during TEM imaging (Bakshi et al., 2007; Wang et al., 2009). Furthermore, Evans *et al.* investigated the growth of nanoparticles using in-liquid TEM (Evans et al., 2011).

Gold nanoparticles can be easily coated with biomolecules like sugars (de la Fuente and Penadés, 2006), peptides (Lévy et al., 2004), nucleic acids (Farokhzad et al., 2004) or antibodies (El-Sayed et al., 2005). The coupling occurs via thiol-gold bonds on the nanoparticle's surface (Mirkin et al., 1996).

Mirkin *et al.* published a coupling method via a tight thiol-gold bonding (Mirkin et al., 1996). They used 5'-thiol modified ssDNA and added these to an AuNP solution. The bonding between thiol-groups and gold is nearly as strong as gold-gold bonds (Häkkinen, 2012). The modified ssDNA replace the citrate on the AuNP surface.

Antibody-AuNP-hybrids represent the oldest class of AuNPs adaption for imaging and are used for immunogold staining in electron microscopy (Faulk and Taylor, 1971). After fixation and permeabilization, the antibody targets the structure of interest and the AuNP gives the needed contrast for imaging in electron microscopy.

Chad Mirkin established coupling of thiol-modified DNA or RNA strands to AuNPs. They have developed the golden standard of coupling by reducing the thiol group of the oligonucleotide and stabilization (maturation) of the oligonucleotide-AuNP with sodium chloride and a sodium phosphate buffer (Mirkin et al., 1996).

These functionalized AuNPs have been widely used to show specific endocytosis. One example is the endocytosis of the prostate specific membrane antigen (PSMA) (See chapter 1.5).

Gold nanoparticles have been used to target PSMA by functionalizing the surface with an RNA aptamer selected against PSMA (Farokhzad et al., 2004). An aptamer is an oligonucleotide that has been selected against a molecule of interest by the so-called Systematic Evolution of Ligands by EXponential Enrichment (SELEX) procedure (Cox and Ellington, 2001).

For PSMA, Lupold *et al.* selected a 2'-fluoro modified aptamer, A9 (Lupold et al., 2002). The ability to target PSMA with this anti-PSMA-A9-AuNPs has been shown by several groups (Farokhzad et al., 2006; Javier et al., 2008; Kim et al., 2010). Furthermore, it was possible to use the AuNPs for contrast in CT and to load them with the drug doxorubicin (Kim et al., 2010). This was the first time that the AuNPs directly were used for imaging.

In this work, anti-PSMA-A9-AuNPs were applied to contrast PSMA positive LNCaP prostate cancer cells in electron microscopy.



### 1.3 Mutagenesis Techniques for Protein Engineering

Protein Engineering describes a process that develops or optimizes activities of proteins. It is based on the naturally given promiscuity. This means that although the enzymes and proteins we know today are highly specific, they might be able to use other substrates with lower probability compared to the natural substrate. Normally this promiscuity is a small fraction of the activity to the natural substrate.

In general, there are two strategies for protein engineering: rational design and directed evolution. Rational design ideally starts with a structure of the protein of interest. Based on the structural and functional information, the activity can be optimized towards the natural or a new substrate. However, the structural information is often the bottleneck of this approach. Until today, there are still a lot protein structures unknown, so that the base for rational design is not given for every case. Furthermore, substitutions and their effects are difficult to predict. One substitution can cause severe differences in folding and stability of the protein inactive variants can occur. While the required structural and functional information are the drawback of rational design and extensive computational research is to introduce the mutations are well developed. Typically, site-directed mutagenesis methods e.g. QuikChange® (Stratagene, 2007), Cassette PCR (Urban et al., 1997) or Megawhop (Miyazaki, 2011) are used.

Directed evolution uses random mutagenesis resulting in libraries of mutants instead of site-directed mutagenesis, which produces only a single mutant. In order to find candidates with improved activity, a screening method searching for the desired activities has to be applied to the new variants. Once the first candidates are found, several rounds of further mutagenesis are carried out to find the best new variant. Technically, the mutations are introduced via NNK-libraries (1.3.3), error prone PCR (1.3.4). These rounds can be also named as generations and mimic the natural evolution process, so that the procedure was named directed evolution. In the best possible outcome, the protein variants lose specificity for the original substrate (completely) and shows high activity for the new substrate. Limitations for directed evolution are the amount of possible variants that can be screened. While there are pipetting robots available that can be programmed, the parameters and read out conditions of the screening have to be set carefully. Sometimes there is actually no screening method available for the desired activity. Frances H. Arnold, the most prominent researcher in this field, postulated “You get what you screen for” (Schmidt-Dannert and Arnold, 1999). Positive candidates after screening need verification according to structure and activity. Typically, bacteria are used for gene expression. The created library, containing the mutated genes, is inserted into vectors and bacteria transformed with the vectors. Other screening systems are for example yeast display, ribosome display, or phage display.

In this work, rational design and NNK libraries were used to engineer an aequorin variant with higher affinity to  $\text{Sm}^{3+}$  ions.

### 1.3.1 QuikChange®

The QuikChange® method was commercialized by Stratagene and is an *in vitro* site-directed mutagenesis technique.

It is designed to introduce point mutations using oligonucleotide primers carrying the mutation. The oligonucleotide primers are each complementary to the opposite strands of the used vector and are extended during PCR with a *Pfu* polymerase. The *Pfu* polymerase is used because of its low error rate and high fidelity. Both strands of the vector are synthesized so that a new vector with a nick is produced. The parent vector is typically dam-methylated and can be digested using DpnI. After transformation of *E. coli* cells with the new mutation-containing vector, the *E. coli* cells can repair the nick automatically.

### 1.3.2 Megaprimer Whole Plasmid PCR

Megaprimer Whole Plasmid (MEGAWHOP) PCR is an alternative to conventional ligation of inserts into vectors. It circumvents the calculations of insert to vector ratio, multiple copies of inserts and offers good results. It is a modified QuikChange® method that creates so-called mega primers with a typical length of 100 or more nucleotides. As described for the QuikChange® method, the mutations are inserted into the oligonucleotide primers that replace the homologous region in the template vector. These megaprimers are used for amplification of a whole plasmid. The dam-methylated parental vector is digested as well and the new vector used for transformation of *E. coli* cells. MEGAWHOP can be used for the synthesis of random mutagenesis libraries (Miyazaki and Takenouchi, 2002; Miyazaki, 2011).

### 1.3.3 NNK Libraries

It is possible to screen all amino acids at one certain position in a protein by introducing an NNK triplet on the genomic level. The introduction of an NNK triplet means that in the corresponding codon of the amino acid, on position 1 and 2 of the codon all four bases G, T, A and C can be present, while on position 3 only G or T are used. This triplet covers codons for all 23 proteinogenic amino acids. The advantage over NNN libraries is the reduced number of clones that need to be screened to get 95 % coverage of all possible amino acids at one position. A screening of 94 colonies covers all 20 amino acids (Reetz et al., 2008). Typically, this is done in

96-well plates in combination with a high-throughput screening (HTS). The easiest readout is a photometric read out with multiwell plate reader.

The NNK triplet is introduced into the gene by PCR with NNK oligonucleotides. The PCR reaction is a standard PCR. The PCR product can be cloned into the vector of choice and bacteria cells transformed with the new vector.

If two or more positions are altered at the same time for one activity center, the procedure is named combinatorial active site saturation tests (CASTing (Reetz et al., 2006)) (1.4).

### 1.3.4 Error Prone PCR

Error prone PCR is a technique that is often used to generate libraries. The reaction itself is a PCR with *Taq* polymerase. *Taq* polymerase is preferred compared to *Pfu* or other polymerases because it has no 3'-5' exonuclease proof reading function. Above the missing proof reading, *Taq* polymerase has a higher error rate ( $8 \cdot 10^{-6}$ ) compared to *Pfu* ( $1.3 \cdot 10^{-6}$ ) (Cline et al., 1996) or Phusion ( $4.4 \cdot 10^{-7}$ ) (New England Biolabs Inc.).

The error rate is a key factor for the creation of error prone libraries. The error rate itself can be enhanced by higher  $Mg^{2+}$  concentrations, addition of  $MnCl_2$  and different concentrations and ratios of dNTPs compared to standard PCR reactions. All three possibilities result in random mistakes in the PCR product that lead to protein variants after protein production (Fromant et al., 1995; Wilson and Keefe, 2001; Cirino et al., 2003).

The PCR product needs to be inserted into a suitable vector and bacteria for protein production and testing. The readout would be a HTS as mentioned above. The number of clones tested after error prone PCR can be calculated according to the length of the gene, and the parameters chosen for the PCR. It creates 15-30 mutations per gene (Drummond et al., 2005). Typically, only six to eight amino acid substitutions are possible with error prone PCR. The error rate and the resulting mutations and substitutions can be adjusted by addition of  $MnCl_2$  instead of  $MgCl_2$  to the reaction and different concentrations of pyrimidines or purines. To cover all possible variants of an error prone PCR normally between  $10^4$  to  $10^6$  clones need to be screened. Nonetheless, it is a good method if no structural information is available of the active center.

## 1.4 Iterative Saturation Mutagenesis – Combinatorial Active Site Saturation Test

The iterative saturation mutagenesis is a procedure that was first described by Reetz *et al.* to find variants that have improved activity for example enantioselectivity, thermostability or substrate acceptance, or binding to a new target (Reetz and Carballeira, 2007). Based on its promiscuity for

other substrates, the parent is iteratively mutated on genomic level. The positions for the saturation mutagenesis can be chosen based on the structural data. If the structure is known, the saturation mutagenesis can be performed at positions that are known to have an influence for the functionality. The example of Reetz and Carballeira is given below Figure 15. Four sites were randomized using saturation mutagenesis. The libraries are subsequently screened and the best hit of each library is identified. For iterative saturation mutagenesis, this best hit of the first generation is the template for the saturation mutagenesis at the respective other sites. This can be continued for multiple rounds. The occurring redundancy in some cases is expected as depicted in Figure 15.

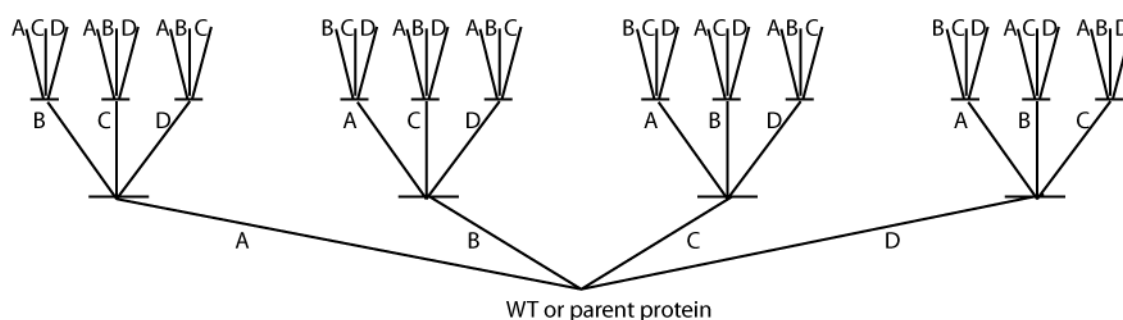


**Figure 15: Scheme of iterative saturation mutagenesis with four randomization sites.**

Based on the wildtype four different mutagenesis sites are randomized. As seen in the upper level redundancies can occur and is expected (modified of Reetz et al. 2007 (Reetz and Carballeira, 2007))

A specialized method is the combinatorial active site saturation test (CASTing) (Reetz et al., 2006). CASTing required structural information of the protein and focuses on active sites and binding pockets. The catalytically active center is used as starting point (Figure 16). Based on this starting points the Cartesian space within a radius of 10 Å is divided into regions with defined binding. These regions are randomized with saturation mutagenesis for an improved functionality (Dröge et al., 2006). For example, two or more amino acids facing the substrate from opposite directions are substituted via NNK libraries. The variants are screened for activity on the desired substrate and further randomized to enhance the activity. After several rounds, there should be some variants with increased activity.

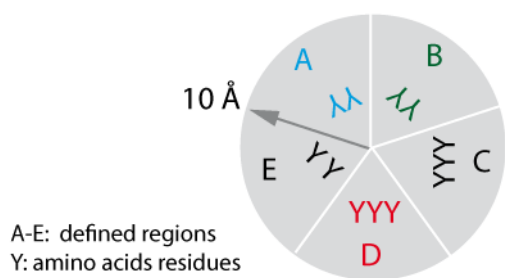


Figure 16: Scheme of defined regions (A-E) within a distance of 10 Å from the active site for CASTing. The amino acids (Y) within a radius of 10 Å were selected and divided into five defined regions (A-E). Some regions have two (A, B, E) and some three (C, D) amino acids that are within the radius. In this example three sites were selected for saturation mutagenesis (A, B, D) (adapted from (Reetz and Carballeira, 2007)).

## 1.5 Endocytosis and the Prostate Specific Membrane Antigen

The internalization of compounds required for cell survival, signaling etc. is called endocytosis. It describes many types of cellular uptake events. Mostly large polar molecules are absorbed via endocytosis. Today there are three main pathways known: (A) phagocytosis (B) pinocytosis and (C) receptor-mediated endocytosis like clathrin-mediated endocytosis (CME). The mechanism and detailed information about endocytosis are summarized in Doherty and McMahon (Doherty and McMahon, 2009).

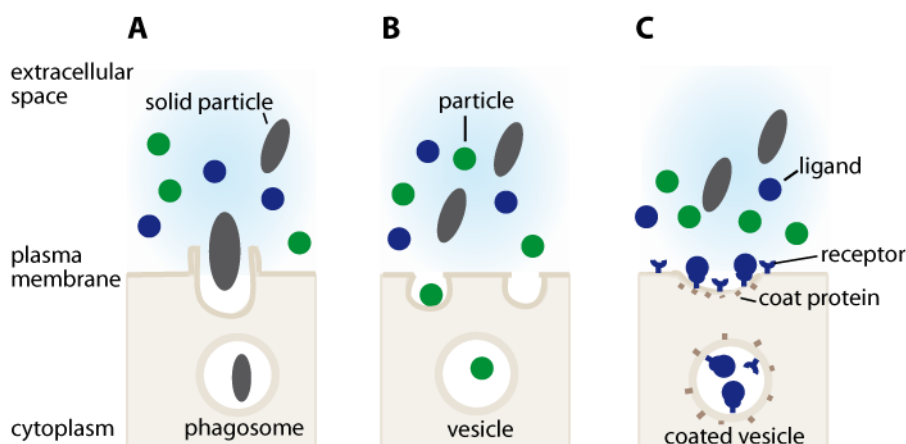


Figure 17: Schematic overview of the three main endocytosis pathways. (A) Phagocytosis is the internalization of big solid particles (ca. 0.75 μm) of the extracellular space. (B) Pinocytosis internalizes smaller particles (ca. 0.5 μm). A pocket is formed of the plasma membrane. It internalizes mostly fluids. (C) Receptor-mediated endocytosis is the most common endocytosis. Receptors are internalized using coat proteins like caveolae or clathrin for recycling. (adapted from Campbell's Biology text book (Campbell, N.A., & Reece, 2008))

Phagocytosis describes the uptake of large matter – around 0.75  $\mu\text{m}$  of size – out of the surrounding area. Mainly cell debris, microorganisms and apoptotic cells are internalized via phagocytosis (Doherty and McMahon, 2009). The plasma membrane uses pseudopodia to incorporate solid particles.

Macropinocytosis occurs in areas of ruffled plasma membrane. It typically forms a pocket of the plasma membrane that has a diameter of 0.5-5  $\mu\text{m}$ . Macropinocytosis invaginates mostly large volumes of extracellular fluids including molecules in a non-specific manner. The internalized vesicle fuses with endosomes and processes to lysosomes (Doherty and McMahon, 2009).

Caveolae-mediated endocytosis is, beyond clathrin-mediated endocytosis, the main receptor-mediated internalization type. Here, the plasma membrane forms pockets together containing caveolin and an enriched bilayer of cholesterol and glycolipids. In contrast to clathrin-coated vesicles (CCVs), they have a diameter of only 50 nm, while CCVs have a typical diameter of 100 nm. Furthermore, they differ in shape. CCVs typically show a soccer ball structure. Caveolae vesicles have flask like structures in the membrane. This form of endocytosis is common in pneumocytes, fibroblasts, adipocytes and endothelial cells (Doherty and McMahon, 2009).

One of the best-examined internalization systems is clathrin-mediated endocytosis. The vesicles form a characteristic polygon soccer ball shape with the help of clathrin. The protein coordinates a structure of hexagonal or pentagonal subunits composed to bigger vesicles capable to transfer substantial amounts of membrane within cells. Furthermore, the question was addressed whether CCVs might have different functions in different cells. One aspect all cell types had in common was that the CCVs appear to be involved in the secretory pathways, because of findings of resorbed plasma membrane and extracellular proteins.

Today we know that there is a variety of transmembrane receptors and their ligands, which are recycled via CME (Rappoport and Simon, 2003). The cargo is assigned by accessory proteins and can be limited to 20 different cargos. The accessory protein (AP) 2 is known to be quite universal, although there are others known to be very specialized. Some accessory proteins can modulate actin polymerization as an add-on to the coordination of clathrin nucleation at the plasma membrane (Rappoport, 2008; Doherty and McMahon, 2009). The composition of CCPs can vary about a huge range depending on many factors like concentration of each cargo type, mobility of the cargo in the plasma membrane, affinity of adaptor protein binding to the cargo and concentration of the AP (Doherty and McMahon, 2009).

The internalization is a multi-step and highly dynamic process. The AP coordinates the clathrin nucleation at the plasma membrane, which leads to polymerization of clathrin. This results in curved lattices that stabilize the deformation of the attached membrane. For membrane scission,

dynamin is required. It forms helical polymers around a constricted neck. The budding requires GTP for the membrane fission and ends in the irreversible release of the CCV into the cell. The clathrin basket is released later from the vesicle by auxilin and Hsc70 and undergoes trafficking and delivery to the final destination and fusion to lysosomes (Doherty and McMahon, 2009; Humphries and Way, 2013).

The recycling processes of the receptors are crucial for cell survival. A disordered CME can result in diseases. Mild phenotypes, where accessory proteins are mutated, can cause hypercholesterolemia. There are also severe diseases known resulting in neurodegeneration (Alzheimer, Huntington), cancer, etc. (Doherty and McMahon, 2009).

It is of high importance to investigate the processes of internalization as good as possible to find new strategies to move a step towards to cure these diseases.

A prominent and well-studied example for clathrin-mediated endocytosis is the prostate specific membrane antigen (PSMA). It is an epithelial cell membrane antigen overexpressed in some prostate cancer cells. It is also known as glutamate carboxypeptidase II (GCPII), *N*-acetyl-L-aspartyl-L-glutamate peptidase I (NAALADase I), or NAAG peptidase. Although the name biased that the antigen is exclusively presented in prostate cancer cells, it can also be found in kidney, small intestine and the central and peripheral nervous system (Barinka et al., 2004; Chang, 2004).

It is known that PSMA has similarities with the transferrin receptor and undergoes clathrin mediated endocytosis (Rajasekaran et al., 2005; Goodman Jr. et al., 2007).

Because prostate cancer is a common cancer type, it was and is in focus for novel therapeutics like aptamers. As mentioned above (1.2.3.3) Lupold *et al.* selected an aptamer against PSMA (Lupold et al., 2002). The aptamer has a tight binding to PSMA (nanomolar range) and the ability to transfer the chemotherapeutic agent doxorubicin into the cells. This specific cell addressing was visualized by the combination of the aptamer and gold nanoparticles in computer tomography and TEM (Javier et al., 2008);

In this thesis, the construct of anti-PSMA aptamer A9 and AuNPs was used to visualize the endocytosis process with the new in-liquid TEM technology.

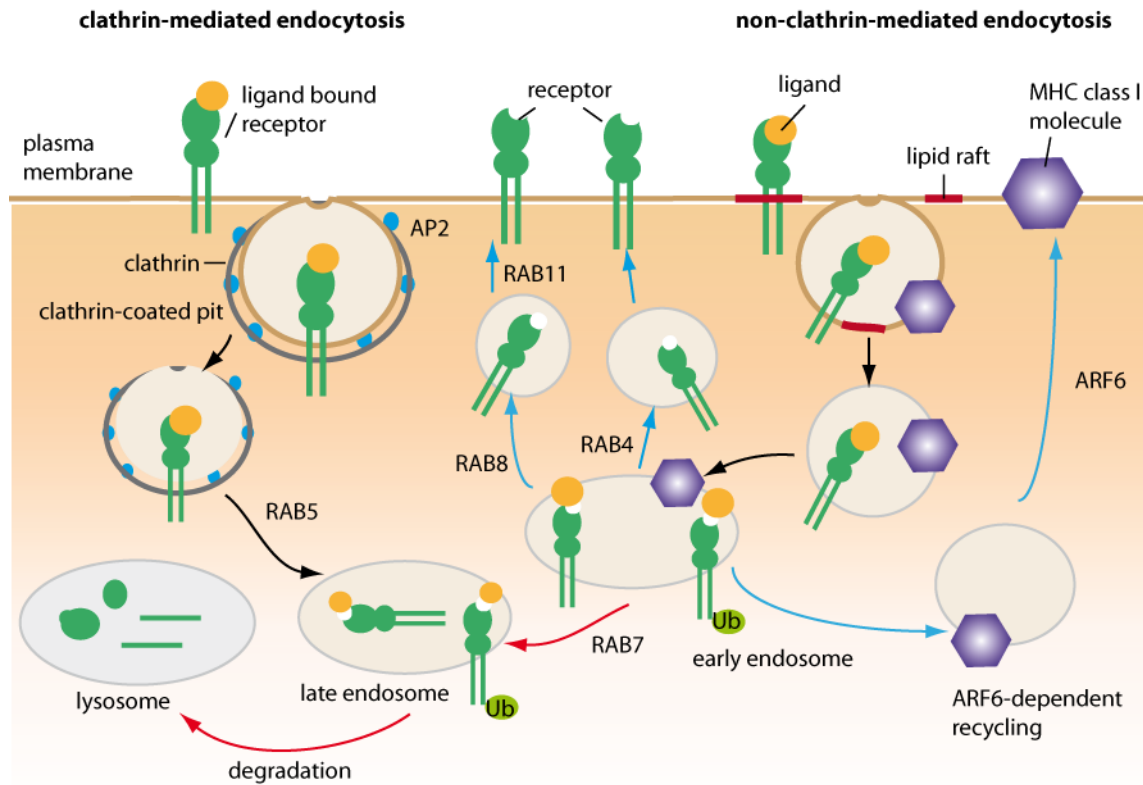


**Figure 18: Scheme of clathrin-mediated and non-clathrin mediated endocytosis of a receptor.** The image depicts the clathrin-mediated endocytosis of a ligand bound receptor (left side) and its associated proteins such as AP2 and RAB5. In the middle receptor recycling is shown as well as degradation into lysosomes. The right side shows non-clathrin-mediated endocytosis and ARF6-dependent recycling. (adapted from Scita and Di Fiore 2010 (Scita and Di Fiore, 2010))

## 1.6 Morphological Changes During Mammalian Cell Adhesion

The adhesion process is well-known today (Muller and Dufrene, 2011; Chi et al., 2014). To contact the surface the cells have adhesion molecules like cadherins or integrins that interact with the cytoskeleton. Adhesion occurs filopodia and lamellipodia at the membrane edges (Gumbiner, 1993, 1996; Cramer, 1997). During adhesion the endothelial cells change their shape towards their characteristic stretched structures that have been imaged with conventional light microscopy. The adhesion process has many parallels to the process of cell division. Gauthier *et al.* showed the different shapes of membranes during mitosis via SEM (Gauthier et al., 2012). The cell membrane occurs in various different shapes as different molecules such as actin, glycoproteins, phospholipids, etc. are present at the membrane regarding to the phase of settlement or division.

During cell adhesion the transport systems are activated and allow rapid accumulation of adhesion molecules (Gumbiner, 1996; Shafaq-Zadah et al., 2016). For the transport of the



molecules and receptors different types of vesicles like transport and secretory vesicles or clathrin-coated pits (CCP), vesicles after micropinocytosis and stress vesicles are present.

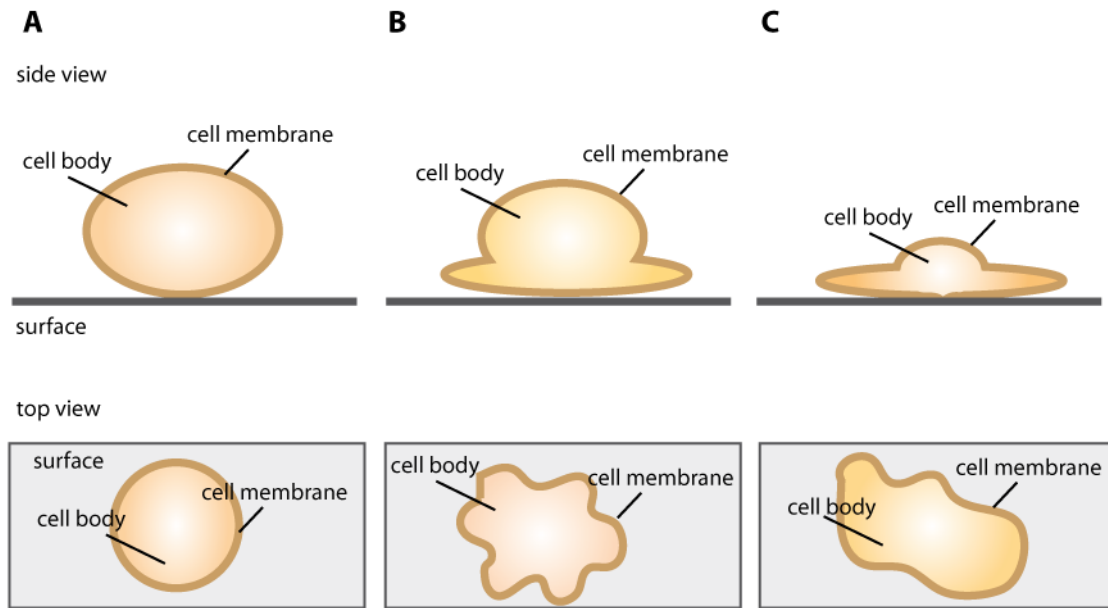


**Figure 19: Morphological changes of a cell during adhesion to a surface.**

(A) First, the cell is round and floating above the surface that can be e.g. glass, plastic, or silicon nitride. (B) According to the cell, flattening of the cell can be observed and first adhesion points are built. This happens within one to 6 hours after seeding. (C) The full adhesion leads to a stretched cell with the characteristic shape. (adapted from Gauthier et al. (Gauthier et al., 2012)).

## 2 Aim of This Work

In terms of this thesis, the usability of metal ions as contrast agents for in-liquid TEM imaging of mammalian cells should be analyzed. The metal ions were components of the probe that should be developed in this thesis.

In-liquid TEM of mammalian cells was established in collaboration with Prof. R.J. Dwayne Miller's group of the Max-Planck-Institute for Dynamic and Structure of Matter (Hamburg, Germany). This new technique was used to investigate biological specimens without the sample preparation normally required for TEM, such as embedding, dehydration, and staining. For the establishing of in-liquid TEM, experiments with gold nanoparticles as probes were performed analogue to the reported experiments of others (Grogan and Bau, 2010; Mueller et al., 2013). Further, the influence of the electron radiation during in-liquid TEM measurements for the stability and behavior of DNA as one class of biomolecules should be tested. To track the DNA, gold nanoparticles were functionalized with DNA. The DNA on the AuNPs was designed so that DNA-multimers could be formed *in vitro*. The stability of these clusters should also be investigated under the electron beam (Strategy 1).

In-liquid TEM was also used to image mammalian cells and to analyze their stability and behavior during electron exposition in terms of cell morphology and for TEM images of whole cells with temporal resolution.

Secondly, aequorin, a light-emitting enzyme should be engineered via saturation mutagenesis and rational design to bind  $\text{Sm}^{3+}$  ions instead its natural substrate  $\text{Ca}^{2+}$ . The  $\text{Sm}^{3+}$  ions should be used instead of the  $\text{Ca}^{2+}$  ions to create contrast in electron microscopy. The aim during this thesis was the combination of light emission and contrasting due to the metal ion for electron microscopy and as a result a first step towards a clonable, bimodal probe based on aequorin (Strategy 2).

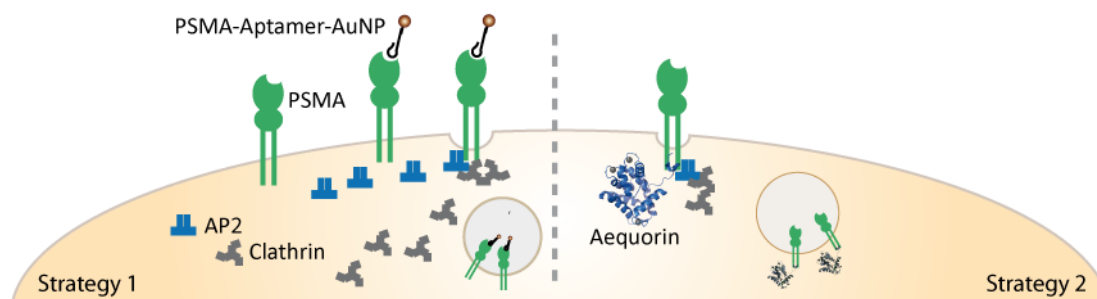


**Figure 20:** Schematic overview of the two strategies to image clathrin mediated endocytosis in real time. Strategy 1 uses anti-PSMA functionalized AuNPs for imaging. Strategy 2 uses AQ fused to PSMA and  $\text{Sm}^{3+}$  as probe for imaging.

### 3 Results

In the framework of this thesis, in-liquid transmission electron microscopy was established in collaboration with Prof. R.J. Dwayne Miller's group of the Max-Planck-Institute for Dynamic and Structure of Matter (Hamburg, Germany). In-liquid TEM was used to investigate biological specimens in a conventional TEM under vacuum. The metal ion based probes developed in this thesis were used for in-liquid TEM to enhance the contrast of biological specimens in in-liquid TEM. For the establishment of the new technique the stability and behavior of DNA-functionalized AuNPs upon electron radiation influence was tested. Experiments of AuNPs and in-liquid TEM were already performed and reported (Grogan and Bau, 2010; Mueller et al., 2013). The DNA was designed so that AuNP clusters consisting of multiple single DNA-functionalized AuNPs were able to form *in vitro*. The clusters' stability was then analyzed via in-liquid TEM. Furthermore, in-liquid TEM was used to image mammalian prostate cancer cells PC3 and LNCaP without any further sample preparation grown on nanofluidic silicon nitride sample cells with the scope to image cellular dynamics. The PSMA positive LNCaP cells were targeted with functionalized anti-PSMA-aptamer AuNPs.

Secondly, the light emitting enzyme aequorin was engineered to bind  $\text{Sm}^{3+}$  ions instead its natural substrate  $\text{Ca}^{2+}$  with consistent luminescence abilities. The binding of the relatively heavier  $\text{Sm}^{3+}$  ion is needed for the aimed bimodality use of aequorin as a probe for fluorescence light and electron microscopy based on the light emission of aequorin due to  $\text{Sm}^{3+}$  binding and contrast ability of  $\text{Sm}^{3+}$  in EM.

#### 3.1 In-liquid TEM Experiments

##### 3.1.1 Gold Nanoparticles for In-Liquid-TEM Imaging

Gold nanoparticles show good contrast in conventional TEM measurements. Furthermore, they have been widely used for immunogold staining of biological specimens in TEM measurements before (Faulk and Taylor, 1971; Suzuki, 2002; Sperling et al., 2008) . Because of their good contrast abilities AuNPs were also used to test the new in-liquid TEM devices (Evans and Browning, 2013) and it was possible to show their Brownian motion in liquid (Mueller et al., 2013). Based on the convincing reported results of AuNPs in combination with TEM even with biological material and their high (Faulk and Taylor, 1971; Liu et al., 2007; Javier et al., 2008; Chuang et al., 2009; Kim et al., 2010; Ryou et al., 2010; Shi et al., 2011), AuNPs were used in this thesis to test the nanofluidic sample cells for in-liquid TEM. All experiments using in-liquid TEM were performed in collaboration with Prof. R.J. Dwayne Miller's group of the Max-Planck-

Institute for Dynamic and Structure of Matter (Hamburg, Germany). Parts of the results were published in Keskin S., Besztejan S. *et al.*

It is a huge goal to watch DNA synthesis in real time on a molecular level. A first step towards this goal is imaging of DNA hybridization with molecular resolution. One part of this thesis was to achieve this step using in-liquid TEM to monitor DNA coated AuNP multimerization in aqueous environment. To do so, two DNA coated AuNPs with different diameters that were able to form multimers via simultaneous hybridization to a third, free ssDNA containing complementary sections for each DNA-AuNP class, were used (Figure 21).

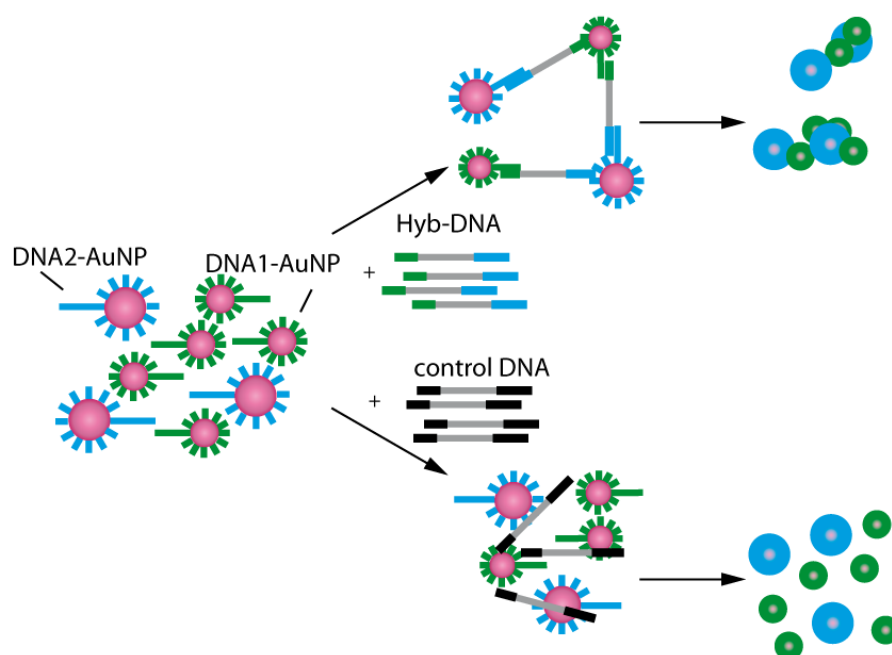


**Figure 21:** Schematic overview of multimerization for DNA1-AuNP and DNA2-AuNP with Hyb-DNA and the control DNA.

DNA1-AuNPs have an AuNP core of 17.5 nm and a 3'-thiol modified single stranded DNA (green) attached to the surface. DNA2-AuNPs consist of a 61.2 nm AuNP core and a 5'-thiol modified single stranded DNA (blue), length of DNA strands not drawn to scale. (Reprinted from Keskin *et al.* 2015)

Two different sizes of AuNPs in diameter (17.5 and 60 nm) were chosen in order to be able to distinguish between the two classes and visualize hybridization of the ssDNA strands easier. If hybridization occurred multimers consisting of big and small DNA-AuNPs were formed. Both, 20 nm (DNA1) and 60 nm (DNA2) AuNP cores were completely coated with thiol-modified DNA1 or DNA2.

Coupling was performed using a protocol modified from Mirkin *et al.* (Mirkin *et al.*, 1996) and was analyzed using DLS and UV-Vis spectroscopy (Figure 22A, B). The number of DNA molecules on DNA1- and DNA2-AuNPs was calculated to cover the whole surface of the AuNPs after coupling. DLS measurements showed increased diameters for both particles after

coupling procedure, which indicates successful DNA coupling/binding (Figure 23A). The 20 nm DNA1-AuNPs showed a diameter of  $84 \pm 10$  nm after coupling (light green), which is an increase of 60 nm. The 60 nm based DNA2-AuNPs (blue) showed increased diameter after coupling (light blue) as well (before coupling  $67 \pm 3$  nm vs. after coupling  $113 \pm 7$ ). UV-Vis analysis of the SPR showed a shift towards higher wavelengths. This is typical for particles with a bigger hydrodynamic shell, which is due to the DNA extensions on the surfaces (light green and light blue curve in Figure 23B).

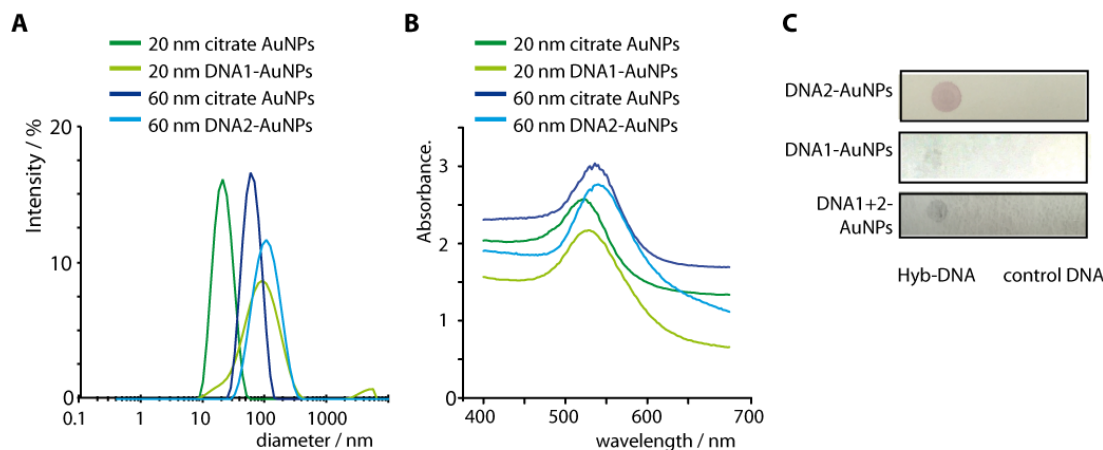


**Figure 22: Characterization of functionalized DNA coated AuNPs.**

**(A)** DLS analysis of AuNPs before (citrate stabilized) and after coupling with thiol-modified DNA, **(B)** UV-Vis spectra of AuNPs before and after coupling. **(E)** Hybridization functionality test of DNA1- and DNA2-AuNPs to Hyb-DNA and a control DNA on nylon membrane. (Reprinted from Keskin *et al.*)

In order to check the accessibility of DNA1 and DNA2 for hybridization, binding to a third ssDNA with complementary regions for DNA1 and DNA2 was analyzed. The ssDNA was spotted on a nylon membrane, which was subsequently incubated with the functionalized AuNPs. Due to accumulation of AuNPs, the hybridization of the DNA-AuNPs to the immobilized ssDNA can be observed as pink spot. Using this method hybridization of the 60 nm DNA2-AuNPs to the complementary ssDNA could be observed (Figure 22C, upper panel, left side). In contrast, no spot was visible where a control DNA without complementary regions was used (right side). Hybridization could also be observed using DNA1-AuNPs (middle panel) and a mixture of both DNA1- and DNA2-AuNPs (lower panel). A control with plain citrate stabilized AuNPs showed already aggregation resulting in a color change from pink to blue in the hybridization solution due to lower stability.

Hybridization of ssDNA and DNA AuNPs was also analyzed using UV Vis spectroscopy. DNA1- and DNA2-AuNPs were mixed with either a single stranded hybridization DNA (Hyb-DNA) that has complementary units for both DNA1 and DNA2 or with a control DNA lacking complementary parts for hybridization.

In order to promote hybridization, DNA-AuNPs and Hyb-DNA were incubated with a temperature gradient from 80 to 20 °C and a gradient of 1 °C/min. After separation from unbound DNA by centrifugation, the hybridized DNA-AuNPs were analyzed via UV-vis spectrometry of the SPR (Figure 23A, B). Decreased absorption (Figure 23A) indicates successful hybridization to Hyb-DNA and could be underlined by reduced peak areas (Figure 23B).

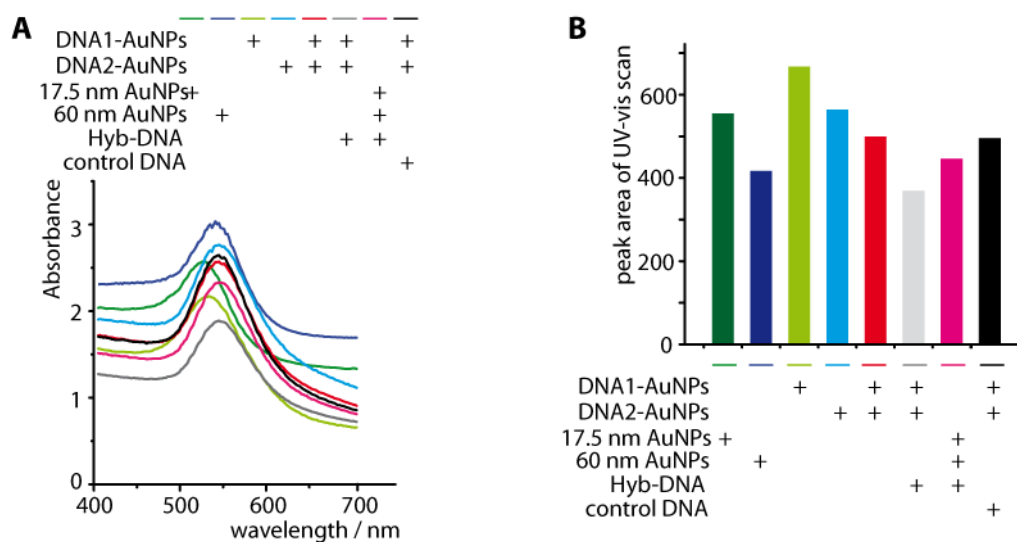


**Figure 23: Monitoring the hybridization of DNA1-AuNP and DNA2-AuNP with Hyb-DNA and controls *in vitro* via UV-vis spectroscopy.**

**(A) UV-Vis spectra of AuNPs after hybridization with Hyb-DNA and control DNA, (B) calculated peak area of the data in (A). (Reprinted from Keskin *et al.*)**

The particles were washed two times before in-liquid TEM measurements to remove unbound DNA from the samples. The resulting samples were named No.1 (plain citrate stabilized AuNPs), No.2 (DNA1-AuNP mixed with DNA2-AuNPs), No.3 (control DNA mixed with DNA1-AuNP and DNA2-AuNP) and No.4 (DNA1-AuNP and DNA2-AuNP with Hyb-DNA) (Figure 24).

For in-liquid TEM measurements, 1  $\mu$ L of each sample was added to the silicon nitride viewing window on the nanofluidic plates. The window was closed in a sandwich-like manner by a second silicon nitride nanofluidic cell creating a static cell (approximate total height: 200 nm). Still frames and videos were taken of the whole viewing area. Multimers of DNA1- and DNA2-AuNPs were only visible in samples containing both DNA-AuNPs as well as Hyb-DNA (Figure 24, No.4). In samples lacking one component or containing control DNA instead of Hyb-DNA, respectively, no multimers could be observed (No.1,2,3),

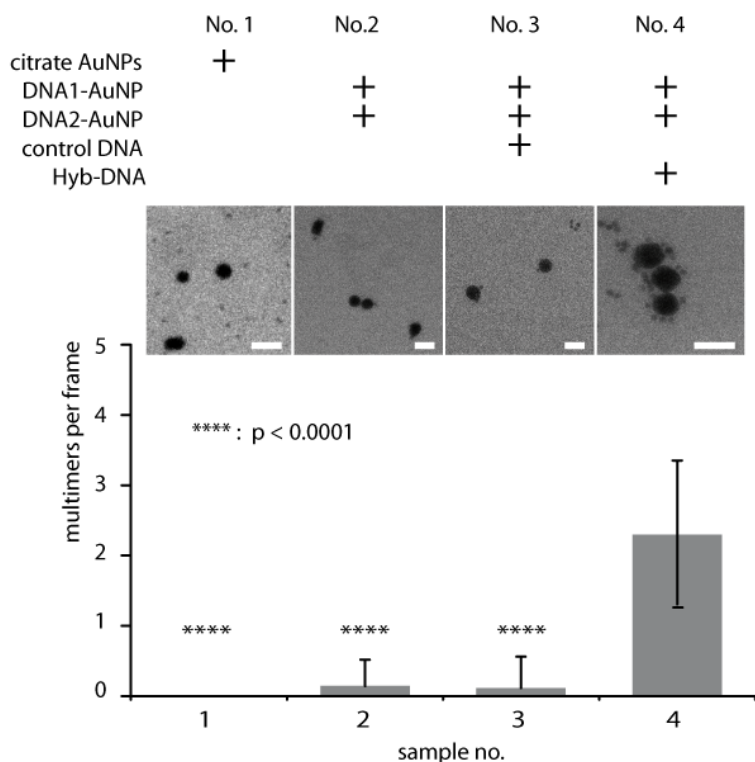


**Figure 24: Multimerization of DNA-AuNPs upon hybridization of ssDNA.**

In-liquid TEM images of different samples. Images were taken at an electron energy of 200 kV, an electron dose of  $15 \text{ e}^- \text{ nm}^{-2}$ , and an exposure time of 2s. The scale bars for each TEM image represent 100 nm; and the histogram shows the average number of multimers observed per TEM frame and the results of the t-test. For each sample, at least three independent measurements of different hybridization batches and different nanofluidic cells were used in order to increase the statistical reliability and test reproducibility. For the calculation of the t-test and p-values, at least 30 TEM frames per measurement within the  $100 \times 15 \mu\text{m}$  viewing range of the nanocell were analyzed. The error bars represent standard deviation (frame-to-frame variability). (Reprinted from Keskin *et al.*)

Figure 24 shows TEM images obtained for each of the samples. Negatively charged citrate stabilized AuNPs (sample No.1) locate in the solution separately. Due to the repulsive electrostatic forces between the particles, no multimerization was observed. For DNA-AuNPs without Hyb-DNA strand (No.2) or with control DNA (No. 3) some multimers could be found.

The highest number of multimers containing both types of functionalized AuNPs was expected in sample No.4 (DNA1-AuNP and DNA2-AuNP mixed with Hyb-DNA). As plotted in Figure 24B, a 2.7 multimers per frame could be observed in this sample. Significance was analyzed using t-test. The p-values are given for each control sample.

The next step towards observing DNA hybridization on a molecular level was the analysis of the dynamics of the single and multimer DNA-AuNPs in solution via TEM.

The main advantage of in-liquid TEM is the possibility to image motion in real time with high resolution. This means it is possible to observe changes that occur in a sample during the

measurement. Thus, one can visualize the spatial and temporal aspects of moving particles. The analysis of the spatial and temporal aspects was done in cooperation with Prof. Miller's group.

Interactive motion of single DNA-AuNP structures could be imaged. These were coming into close vicinity leading to assembly into one-dimensional structures once the electron beam intensity exceeded  $110 \text{ e}^- \text{ nm}^{-2} \text{ s}^{-1}$ . This value was considered as threshold value for the observed dynamics in sample No.4. Dynamics of DNA-AuNP cluster formations could be observed for more than 3 minutes with nanometer spatial resolution.

The total length of a dimer composed of both DNA1- and DNA2-AuNP and bridged by Hyb-DNA is approximately 120 nm (Figure 25). After hybridization, single stranded regions of 39 nucleotides (nt) as spacer between the hybridized regions of two DNA-AuNPs are flanked by the two 21 nt long double stranded areas and spacer regions for AuNP attachment. Considering a length of 340 pm per base pair and a total DNA length of 116 nt between both AuNP cores, the distance can be roughly calculated to 39 nm keeping in mind that single stranded regions in general are shorter compared to ds regions. Thus the distance between small and large AuNP is expected to show a variation within  $\sim 40$  nm based on the flexibility of ssDNA in liquid.

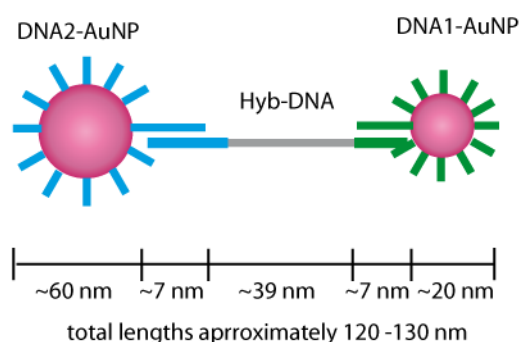


**Figure 25: Schematic drawing of a DNA1- and DNA2-AuNP dimer (not drawn to scale). The approximately distances of the components in a dimer of DNA1- and DNA2-AuNP bridged via Hyb-DNA are depicted.**

Figure 26A shows the trajectory of a small particle in a multimer (in-liquid TEM image as inset), (B) the measured interparticle distance between the large and small particle and (C) the displacement of the small particle relative to the position in the previous TEM frame over 30s.

The edge-to-edge linear distance of the small AuNP to the two bigger AuNPs was measured at each time step. The distance between the small and large AuNP fluctuates within 30 nm, which is within the calculated range of 39 nm, as mentioned above. Furthermore, the resolution of the small particle changed in consecutive TEM frames, due to the movements in liquid and thus variations in the z-position (displacement plot in Figure 26C) (Peckys and de Jonge, 2014).



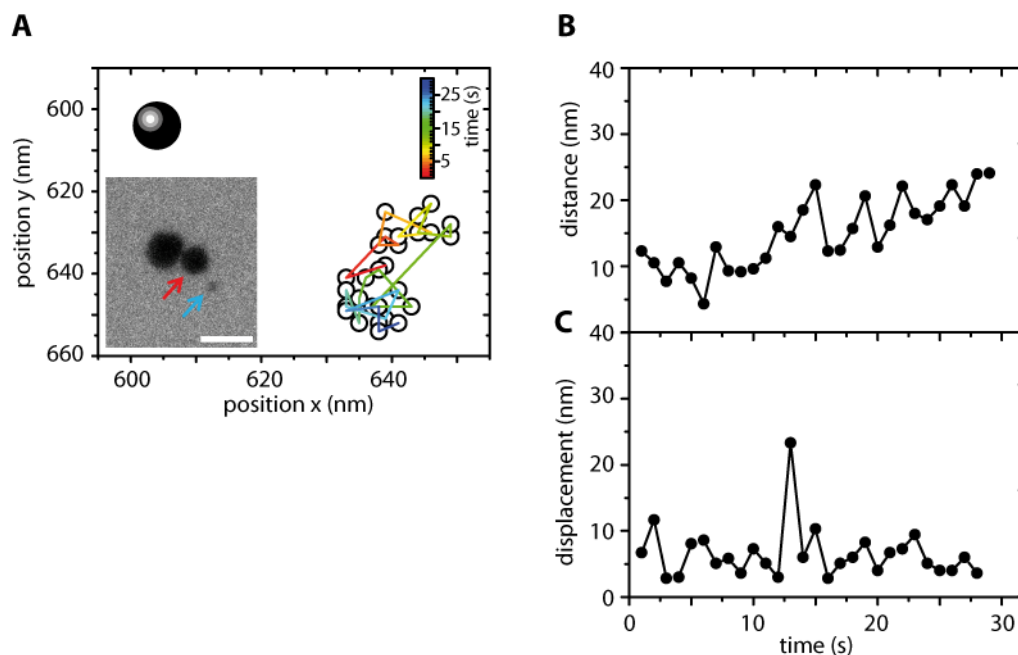


Figure 26: 2D analysis of a multimer's motion.

(A) Trajectory of a small DNA1-AuNP (18 nm) bridged to a large DNA2-AuNP (55 nm, shown as black sphere) for 30 s with the color index showing the time traces of the motion; the in-liquid TEM image of the system is given as an inset picture (red and blue arrows are pointing to the large and small particle, respectively) with a scale bar of 100 nm; (B) the interparticle distance and (C) the displacement of the small particle for 30 s. Voltage and electron dose rate are 200 kV and  $15 \text{ e}^- \text{ nm}^{-2} \text{ s}^{-1}$ , respectively. (Reprinted from Keskin *et al.*)

The motion of individual DNA-AuNP conjugates without multimer formation of the controls without Hyb-DNA was investigated for comparison. An average displacement of 10 nm in 1 s steps could be calculated for DNA1-AuNP conjugates, with  $\sim 290$  nm displacement after 30 s. The small particle of the multimer (Figure 26A) shows a displacement of 7.6 nm on average for 1 s time steps, while its distance to the large particle fluctuates within 40 nm. The displacement of the small AuNP suggests that the single stranded DNA does not affect the velocity of the displacement of the particle. The DNA hybridization of the two sections is strong enough to keep the small particle attached to the large particle. The large particle in the multimer did not show any significant motion, which can be explained by its larger mass.

Larger displacements and interactive motion were observed within multimers of small and large DNA-AuNPs at higher electron beam intensities. Figure 27A shows the trajectories of three individual multimers of sample No.4 that assemble to one big cluster.

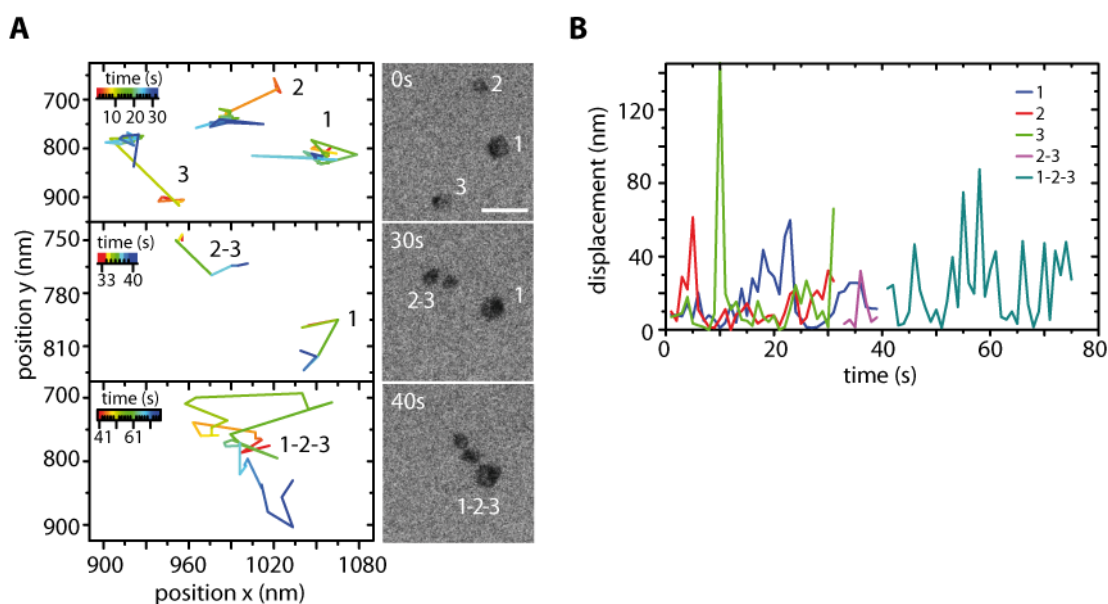


Figure 27: Time sequential formation of DNA-AuNP clusters at higher electron doses.

(A) Trajectories of DNA-AuNPs (No.4) with corresponding TEM images in liquid and (B) the displacement of each labeled nanoparticle system with time steps of 1s. Scale bar is 100 nm for all TEM images. Voltage and electron dose rate are 200 kV and  $110 \text{ e}^- \cdot \text{nm}^{-2} \cdot \text{s}^{-1}$ , respectively. The center points of the clusters or multimers of at least three AuNPs (mixed sizes) are selected while calculating the trajectories in time. (Reprinted from Keskin *et al.*)

The displacement that led to assembly with an electron dose rate of  $110 \text{ e}^- \cdot \text{nm}^{-2} \cdot \text{s}^{-1}$  was random and varied between 5 and 70 nm at intervals of 1 s for both particles (Figure 27B). The AuNPs of sample No.1 (citrate stabilized) did not exhibit such interactive motions nor could assembly be observed at the same or even higher electron dose rates. The particles of No.1 had very slow dynamics and small displacements compared to the sample with DNA1- and DNA2-AuNPs with Hyb-DNA, so that the viewing time was several minutes to detect movements. The significant difference in the behavior of the particles once DNA is attached to the surfaces and an electron beam stronger than  $110 \text{ e}^- \cdot \text{nm}^{-2} \cdot \text{s}^{-1}$  is used needs to be discussed.

The assembly of higher order multimers upon energy input by the beam, it could be observed that the particles tend to form pairs, then trimers and finally 2D structures at  $110 \text{ e}^- \cdot \text{nm}^{-2} \cdot \text{s}^{-1}$ . Figure 28 shows the in-liquid TEM images of (A/B) sample No.4 and (C/D) sample No.1 at different time points. In sample No.4, single DNA-AuNPs form mostly trimers after 110 s beam exposure, while the citrate, stabilized AuNPs (No.1) did not show any significant multimers after the same time of beam exposure.

However, the clusters composed of more than three DNA-AuNPs showed a different ordering. They form into even more random structures than 1D pearl-necklace type and 2D aggregates of AuNPs reported in the literature previously (Bakshi *et al.*, 2007; Wang *et al.*, 2009). Figure 29 shows in-liquid TEM images of two clusters before and after merging (A) followed by their 3D configurations after forming a bigger cluster at 3 s (B). The in-liquid TEM images show that

small particles cannot be resolved clearly since they can locate in the interface or on the surface of the big particles. Many small particles were visible within the sample. They appeared as fast moving particles in different z-layers moving in and out of the focus plane.

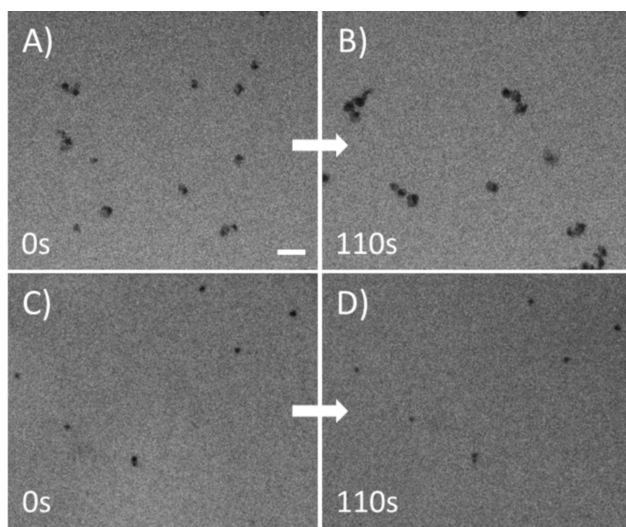


Figure 28: AuNP clusters in motion.

(A) and (B) Liquid-TEM images of DNA-AuNP-multimers (No.4) and (C) and (D) citrate-AuNPs (No.1) at different time points. Electron dose rates are 110 and 140  $e^-/nm^2s$  for sample No.4 and No.1, respectively. Voltage is 200kV. Scale bar represents 100nm. (Reprinted from Keskin *et al.*)

The lower part of the new cluster tilts while it assembles with the upper part as seen in the 3D model. The interaction of the DNA strands during hybridization for assembly might induce the tilting effect. It could be observed that once two clusters merge the overall structure starts to rotate in 3D fashion. The overall height of the final cluster ( $\sim 90$  nm) depicted in Figure 29B is smaller than the total spacer thickness (150-200 nm) of the liquid cell. The 3D analysis was done by the group of Prof. Miller. The free space in the liquid cell can affect and limit the configuration of the structures formed as well as the DNA.

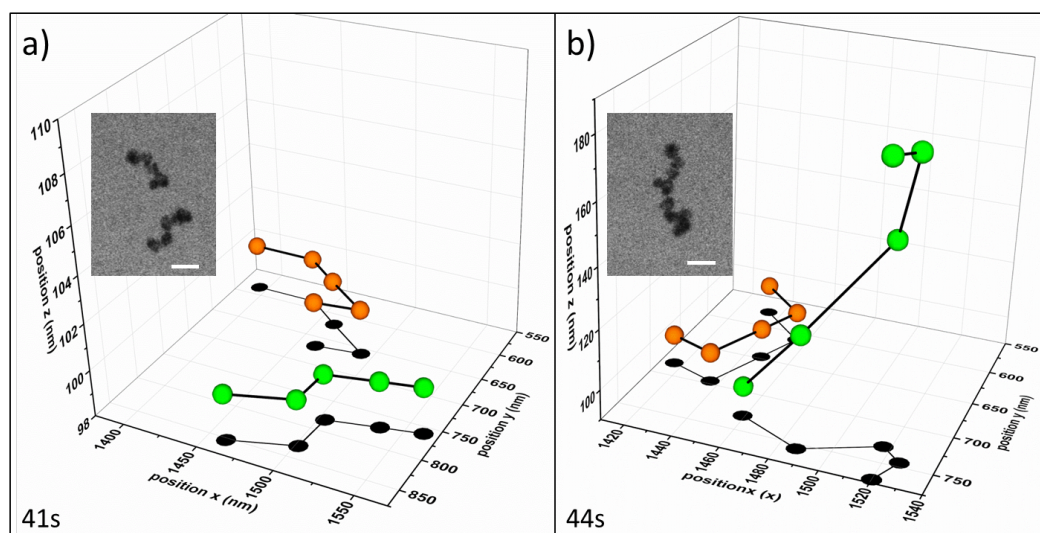


Figure 29: 3D configurations of two clusters along with the projections on x-y axes.

(A) Before and after they assemble (B) and their liquid-TEM images at 0s and 19s (inset) in solution. The resolved large particles in Cluster-1 and Cluster-2 were shown as orange and green spheres, respectively. The scale bars are 100nm. Voltage is 200kV and electron dose rate is  $108 \text{ e}^-/\text{nm}^2\text{s}$  (reprinted from Keskin *et al.*).

In-liquid TEM was successfully used to show the hybridization of ssDNA immobilized on AuNPs to a hybridizing ssDNA strand (Hyb-DNA) (Figure 28). Furthermore, it was possible to induce interactions of the DNA using the electron beam and create bigger multimers over several minutes. The additional multimerization only observed in sample No.4 indicates that the DNA was stable under the beam conditions of these experiments. It shows the robustness of the molecule for further applications with similar energy entries as for the enhancement of radiation therapy.

### 3.1.2 Mammalian Cells in In-Liquid TEM

Based on the good results of DNA stability during in-liquid TEM imaging mammalian cells were imaged using in-liquid TEM. This is the next step towards live cell imaging with a resolution down to a few nm. It has already been shown by Park *et al.* (Park et al., 2012) and de Jonge *et al.* (de Jonge et al., 2009) that cells can be imaged using graphene or silicon nitride windows (1.1.2 above). However, the resolution was still limited to 50 nm due to the thickness of the cells and the water layers in the viewing area (de Jonge et al., 2009; Park et al., 2012).

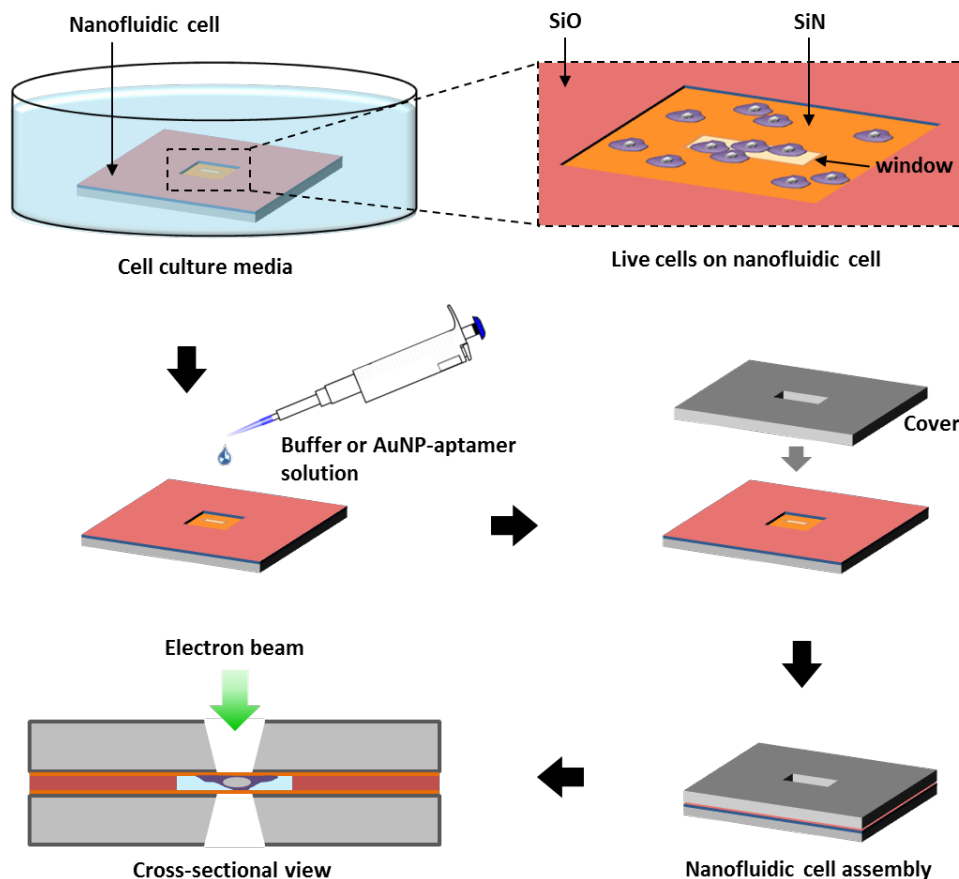


Figure 30: Schematic overview of sample preparation for in-liquid TEM measurements

The nanofluidic cell was inserted into a well containing cell culture media and mammalian cells are seeded directly on the electron transparent silicon nitride of the nanofluidic cells (not drawn to scale). The viewing area was  $200 \times 100 \mu\text{m}$ . The spacer of the nanofluidic cell was made out of silicon oxide (SiO). The mammalian cells were cultivated for 3-24 hours according to specifications for the following experiments. In this period, additional assay components such as DNA-AuNPs can be added to the cells. The cells on the nanofluidic cell were washed with PBS to reduce background from media or buffer additives such as protein and sugars or high salt concentrations. The nanocell is closed with an identical cover and sealed for imaging in the customized holder.

A schematic overview of the nanocell for fixed and non-fixed cells is depicted in Figure 30. The nanocells contain electron transparent silicon nitride windows, that are deposited on the silicon oxide with low pressure chemical vapor deposition (LPCVD) and have a material thickness of 50 nm with an elastic modulus of  $\sim 230$  GPa that allows bulging of the nanocell (Vlassak and Nix, 1992; Kraft and Volkert, 2001). This allows deformation of the nanocell according to the sample.

Considering that a live cell's thickness can be higher than the total spacer thickness of the nanocell (400-800 nm), the bulging of the nanocell allows thicker mammalian cells within the nanofluidic cells. Moreover, the mammalian cells are hermetically sealed within the nanofluidic cell and touch both windows due to their height. The live cells can expand not only in height (y-axis), but also in width (x-axis) and z-axis. This means that the volume of the nanofluidic cell can be fully occupied in all three axes. The mammalian cells or other samples can be attributed to be inside the silicon nitride area and not below or above the imaging plane of the nanofluidic cells (Park et al., 2012). Further, variable spacers can be used by adding multiple layers of silicon oxide as spacer. The spacers for mammalian in-liquid TEM were at least 8-times thicker compared to the DNA-AuNP in-liquid TEM experiments (800 nm vs. 100 nm). However, they were chosen to be as thin as possible for a good contrast of the mammalian cells without squeezing these. Thin spacers are preferred because they reduce the amount of liquid around the cell. This increases the spatial resolution especially at low electron doses, since thick layers of liquid around the specimen lead to multiple scattering of electrons. The spacers for the mammalian cells needed to be thicker due to the mentioned height of the cells. Furthermore, low electron doses lead to less radiation damage on the cells and an increased total imaging time before any visible damage occurs. Based on the published studies on DNA-gold nanoparticles, it was known that DNA can tolerate an electron dose of 15-20  $e^-/\text{nm}^2\text{s}$  without showing any structural damage for hours. This was a higher dose compared to the one used for cell in-liquid TEM (7  $e^-/\text{nm}^2\text{s}$ ).

With a setup consisting of 200 x 50  $\mu\text{m}$  silicon nitride viewing areas and a spacer thickness of 800 nm human PC3 cancer cells were imaged using in-liquid TEM. The prostate cancer cells were directly seeded on the Silicon nitride windows. The cells were allowed to attach to the window by cellular adhesion molecules, which took approximately 3-6 h. The cells were grown over night for complete attachment and fixed with 4% paraformaldehyde (PFA) solution. Fixation stops cell division and preserves the adhesion on the surface. The fixed cells were washed with PBS and sealed with 1  $\mu\text{L}$  of ddH<sub>2</sub>O to avoid drying of the sample during the imaging.

The fixed PC3 cells on the nanocell were first imaged using conventional light microscopy (Figure 31A). These images were used as a map for the subsequent electron microscopy images. Figure 31B-F show the in-liquid TEM images of fixed PC3 cells. The cells were imaged at low dose (7  $e^-/\text{nm}^2\text{s}$ ). It was possible to resolve cellular structures without staining and with high contrast even at electron doses  $<7 e^-/\text{nm}^2\text{s}$ . The cells were stable for 90-120 min after the first exposure continued for up to 120 min and first indications for structural damage, floating membrane parts, were observed 90-120 min after the first exposure. The highest contrast of structures characteristic for PC3 cells suggested that membrane and nucleus were imaged.

Furthermore, nucleoli could be seen (Figure 31D). Nucleus structures were verified using fluorescence labeling with Hoechst 33258 and FLM (overlay of the FLM image with bright field in Figure 31G). The contrast can be attributed to enhanced electron scattering from relatively heavy atoms present in certain areas of the unstained cells (z-contrast). One of the building blocks of biomolecules is phosphorus, apart from the few metal ions. Despite of these, mammalian cells consist mainly of light atoms (CHNOP). Phosphorus is mainly found within DNA and RNA as well as phospholipids in the membranes. This fact explains the relatively high contrast of these regions in unstained cells compared to other cellular structures in the TEM images. The lipid bilayers of the membranes in cells are thus natural accumulation areas. These natural enrichments were enough to obtain contrasted images that allow identification of subcellular structures.

In-liquid TEM measurements could be used to identify cells without any additional staining. It was even possible to visualize a PC3 cell during mitosis as depicted in Figure 31B. The imaged cell showed the separation into two nuclei (Figure 31A). In-liquid TEM of this area verified the two forming nuclei and the curvature of the cell membrane that is typical for the state before cell division (Lodish et al., 2000).

One cell showed holes in the membrane 90 min after the first electron exposure (Figure 31G). The damage was visible as a detached part of the nucleus membrane. It was possible to image the movements within the window and drift in the surrounding. The movements proved that there was still liquid within the nanofluidic cell and thus the sample fully hydrated.

All of the other tested fixed cells did not exhibit any visible damage over 90 min of imaging at a low electron dose mode ( $7 \text{ e}^-/\text{nm}^2\text{s}$ ).

This approach shows that it is possible to image whole cells without additive staining or sample preparation in their liquid environment using in-liquid TEM. The experiments state that subcellular organelles like nuclei and nucleoli can be visualized as well as membranes. This was a further step towards live cell imaging with in-liquid TEM aiming *in situ* imaging of DNA within the mammalian cell.

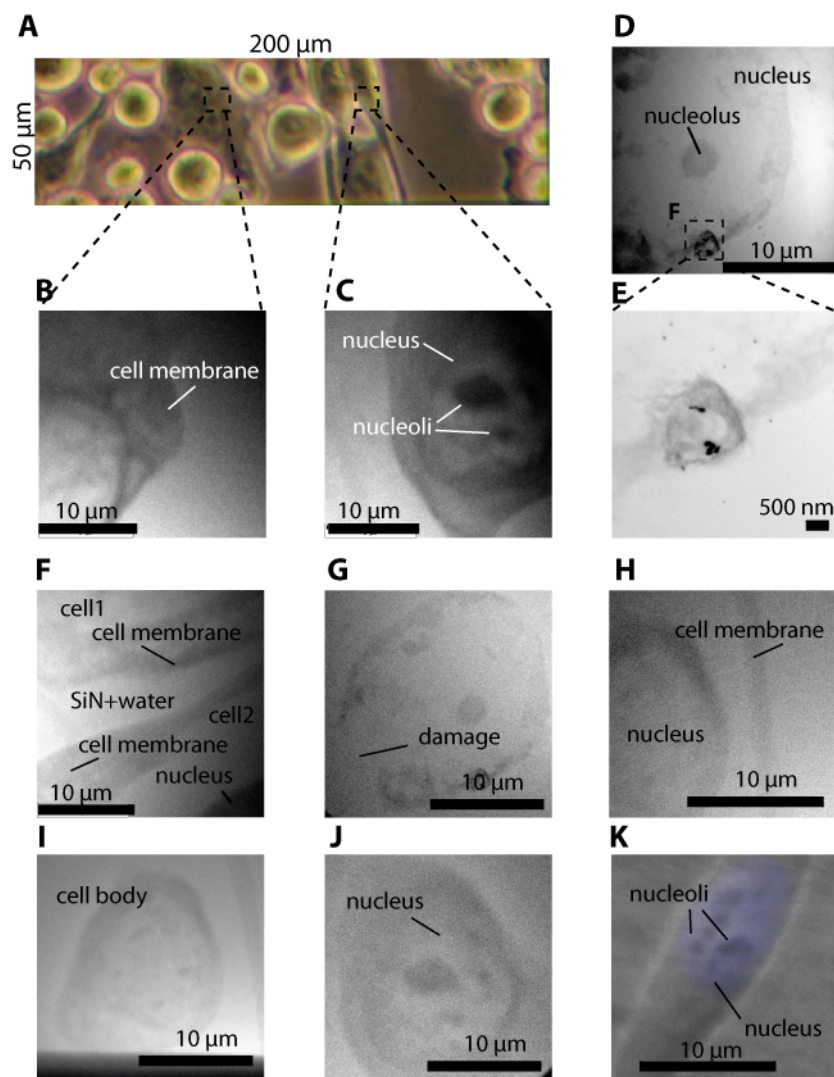


Figure 31: In-liquid TEM micrographs of unstained human PC3 cells.

Paraformaldehyde (PFA) fixed PC3 cells were grown on 200x50  $\mu\text{m}$  silicon nitride windows. Scale bars represent 10  $\mu\text{m}$  in all images. The cells were incubated for 5 h on the Silicon nitride and fixed with 4 % PFA solution in PBS for 30 min at room temperature. (A) Light microscopy image of the viewing area. Areas analyzed with in-liquid TEM are marked with dashed lines. The samples were stored at 4°C until TEM imaging. (B)-(J) TEM imaging; the overall imaging time varied between 90-120 min at an electron dose rate of maximum 7  $e^-/\text{nm}^2\text{s}$ . Cells were not stained for in-liquid TEM imaging. (B) PC3 cell captured during mitosis. Two different cytoplasms (light grey) surrounded by cell membrane structures can be seen (darker structures). (C) Cell body of a PC3 cell. The image shows an overview of the cell with cytoplasm and nucleus structure. (D) High resolution image of another nucleus of a PC3 cell (different measurement). Nucleolus and nucleus membrane are visible with good contrast. (E) High resolution image of the marked area in (D) showing substructures within the nucleus membrane. Scale bar is 500 nm in this image. From this image, the achieved resolution could be estimated to be 40 nm for cell imaging using in-liquid TEM (F) Image of two cell borders showing cell membranes and an area of Silicon nitride without any cellular material in between. (G) Same cell as shown in (D) after 90 min exposure. Parts of the boundary is missing and marked as damage. (H-J) In-liquid TEM images of other fixed PC3 cells. (K) Confocal light microscopy overlay of a PC3 cell imaged in TEM and optical fluorescence mode (Hoechst 33258) to visualize the DNA staining (blue). The image shows long stretched PC3 cell with the nucleus and nucleoli structures as seen in (C) and (J).



### 3.1.3 Imaging of Cellular Dynamics in PC3 Cells

The fixation of the PC3 cells preserves the shape and allows imaging periods of at least two hours. In contrast, DNA synthesis and cellular dynamics have to be imaged in non-fixed cells, as the fixation stops cellular processes. Based on the experiences gained with fixed cells two aspects were:

- (i) Natural contrast allows identification of cellular components and
- (ii) PC3 cells on silicon nitride nanocells can be imaged for at least 2 hours without embedding in any resins.

Both, natural contrast and imaging times of 2 hours, allow the imaging of mammalian cells without additional sample preparation in order to visualize cellular dynamics or morphological changes of the cell for example during cell division or adhesion.

An interesting time point for imaging is the settlement phase, where adhesion to the surface and morphological and structural changes of the cells occur.

In order to establish in-liquid TEM imaging conditions for non-fixed cells, the PC3 cells were seeded on the Silicon nitride window and allowed to settle down on the material for 4 h at 37°C and 5% CO<sub>2</sub> in a cell culture incubator. The adhesion was monitored using conventional light microscopy (Figure 32). After 1 h, (Figure 32 upper panel) most of the cells were still round and floating above the window. After 4 h, (Figure 32 middle panel) some cells already contacted the silicon nitride but still appeared in round shapes. After 24 h, (Figure 32 lower panel) the cells showed the typical long stretched neuron like shape.

The PC3 cells were seeded on the silicon nitride window. After 4 h incubation the cells were already loosely settled and the nanofluidic cell closed as described in (9.6.5 below). The PC3 cells were still in the settlement phase; hence, they did not show the typical long stretched shape.

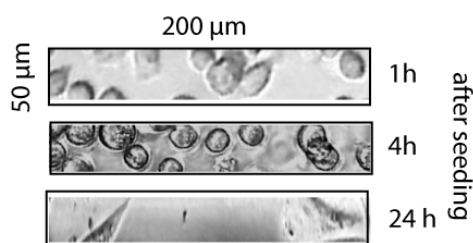


**Figure 32:** Light microscopy images of the silicon nitride viewing areas of nanofluidic cells seeded with PC3 cells.

PC3 cells were directly seeded on the silicon nitride material for attachment. Light microscopy images were taken 1 h, 4 h, and 24 h after seeding. Images were taken before closing the nanofluidic cell and in-liquid TEM measurements.

An entire cell was imaged in four individual TEM frames to compile the whole cell (Figure 33A). It was technically not possible to reduce to a lower magnification capturing the whole cell, as the TEM mode would have changed. A major difference to the fixed cells could be recognized within the putative cell membrane. The cell membrane was not as dense and distinct as the ones seen in the fixed cells (Figure 31B and F). It was moreover comparable to a mesh network like structure. This could be explained by the fact that this cell was in the adhesion phase and not fully settled as the fixed ones. This means that various contacts of the cell membrane need to be established so that the cell can settle down on the silicon nitride surface.

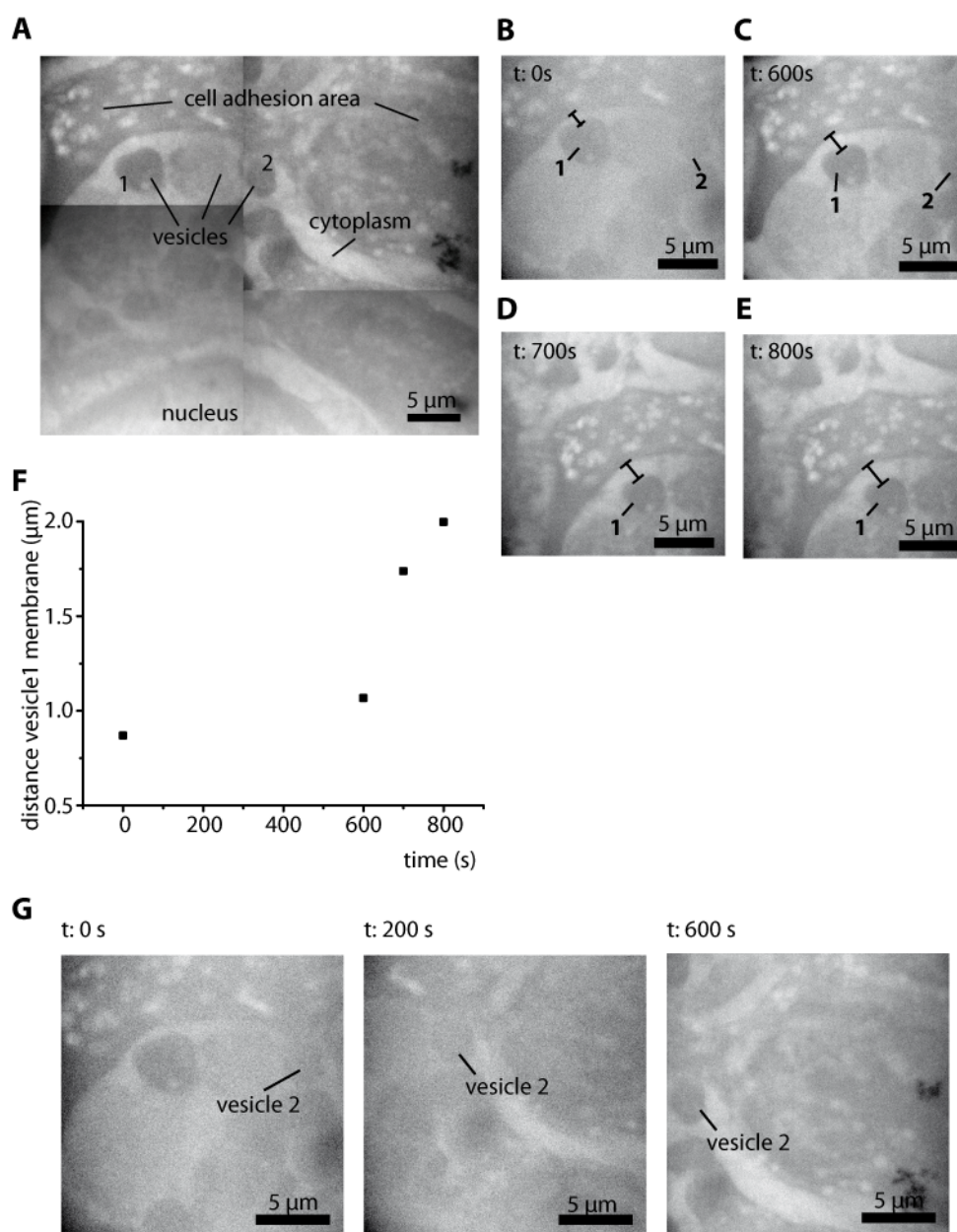


**Figure 33:** In-liquid TEM imaging of living PC3 cells without any contrasting agents. Cells were directly seeded on Silicon nitride windows, allowed to settle down for 4h and prepared for imaging. Scale bar represents 5  $\mu\text{m}$  (A) Compiled image of a PC3 cell with four single images, showing a displacement in some parts of the cell. (B-E) show images of vesicle 1 at different time points of (B) 0 s, (C) 600 s, (D) 700 s and (E) 800 s. (F) Plot showing the edge-to-edge distance between vesicle 1 and the cell membrane at different time points. (G) Displacement of vesicle 2 over time (different imaging views).

Single frames of the cell were obtained every 100 s to visualize changes within the membrane. Two structures close to the cell membrane showed a displacement over time (Figure 33B-E). The displacement indicates a possible motion in the cell during the imaging (marked vesicle 1 and 2 in Figure 3B-E). The vesicles had a comparable contrast to the membrane. Their close proximity to the membrane, shape and movement to the inner cell area suggest that these might be vesicles. The second vesicle (vesicle 2) could be found to be even closer to the membrane (Figure 33B and C). It was observed that the vesicles moved towards the center of the cell over time, as reported in the literature for example for CCPs (Rappoport and Simon, 2003). However, the diameter of the imaged vesicles with 3  $\mu\text{m}$  is different from the diameter that is known for CCPs with 100 nm (Saffarian et al., 2009). The distance between vesicle 1 and the cell membrane at different time points was measured and plotted (Figure 33F). Vesicle 1 had an area of approximately 13  $\mu\text{m}^2$  and moved about 1  $\mu\text{m}$  towards the cell center within 13 min. There was no further motion detectable for vesicle 1 and 2 after 13 min.

The live cells in this measurement were imaged continuously for 2h at a low dose rate of 10  $\text{e}^-/\text{nm}^2\text{s}$  without showing any recognizable damage. Imaging non-fixed live cells for such a long time with continuous electron exposure has not been reported, yet.

### **3.1.4 Visualization of Anti-PSMA-Aptamer Functionalized Gold Nanoparticles in LNCaP Cells Using In-Liquid TEM**

It was possible to image fixed and non-fixed mammalian cells using in-liquid TEM. However, the calculation of the achieved resolution is challenging as cellular, fully hydrated material is highly flexible and has no distinct or most favorable crystalline point or edge as constant for calculation. Resolutions can only be low valuable approximations at certain time points considering dynamics of cellular substructures.

In order to overcome these limitations AuNPs as solid crystalline high scattering and contrasting probes (see paragraph 1.2.3) within living cells were used. In order to direct the AuNPs towards and within specific cells, 2'-fluoropyrimidine stabilized RNA aptamers were used for biofunctionalization of the AuNPs. The aptamer targets a specific antigen on the surface of the cells.

For this experiment LNCaP, cells were used, which are human prostate cancer cells like PC3 with the difference, that they present the prostate specific membrane antigen (PSMA) on their surface.

This antigen and its endocytosis and thus dynamics are well-known (Anilkumar et al., 2003; Goodman Jr. et al., 2007). Furthermore PSMA was already proven to be a suitable target for anti-PSMA-aptamer functionalized gold nanoparticles (Javier et al., 2008; Kim et al., 2010). The anti-PSMA RNA aptamer used for these experiments was selected by Lupold *et al.* (Lupold et al., 2002).

The anti-PSMA-AuNPs were prepared following a protocol described in Kim et al. According to this protocol, a 5'-thiol-modified capture DNA oligonucleotide was immobilized on the surface of the AuNPs with a core size of 20 nm (scheme given in Figure 34A). The capture oligonucleotide had a complementary region for hybridization with the anti-PSMA RNA aptamer. It functioned as spacer between the AuNP and the aptamer and ensured the correct folding of the aptamer, which is required for binding to PSMA. Introduction of 2'-fluoropyrimidines resulted in a higher stability of the aptamer. Higher stability of the RNA aptamer was also important regarding damage due to the electron radiation.

The gold nanoparticles were coupled with the capture oligonucleotide so that statistically 176 DNA molecules would cover the entire surface of the AuNP. The procedure for coupling was modified by Mirkin et al. (Mirkin et al., 1996). After coupling, unbound DNA was removed by washing and centrifugation. Analysis was performed using DLS and UV-Vis spectroscopy of the SPRs (mean diameters are plotted in Figure 34B). The 2'-fluoro-stabilized anti-PSMA RNA aptamers and scrambled control RNAs were hybridized to the coupled AuNP cores for final functionalization. Both, anti-PSMA-AuNPs and control PSMA-AuNPs showed increasing diameters upon coupling and after hybridization of the aptamer or a scrambled control RNA.

**Table 3: Diameter of AuNPs during functionalization measured via DLS.**

Sample	Diameter (nm)
20 nm AuNPs	28±2
Coupled AuNPs	46±5
Anti-PSMA AuNPs	135±23
Control PSMA AuNPs	730±293

The DLS data for the scrambled control RNA shows wider diameter for the particles, which can be explained due to the non-existing 3D shape of the RNA molecule, which results in higher flexibility and bigger hydrodynamic shells. The aptamer itself folds up to a dense 3D structure, which leads to a smaller diameter in DLS.

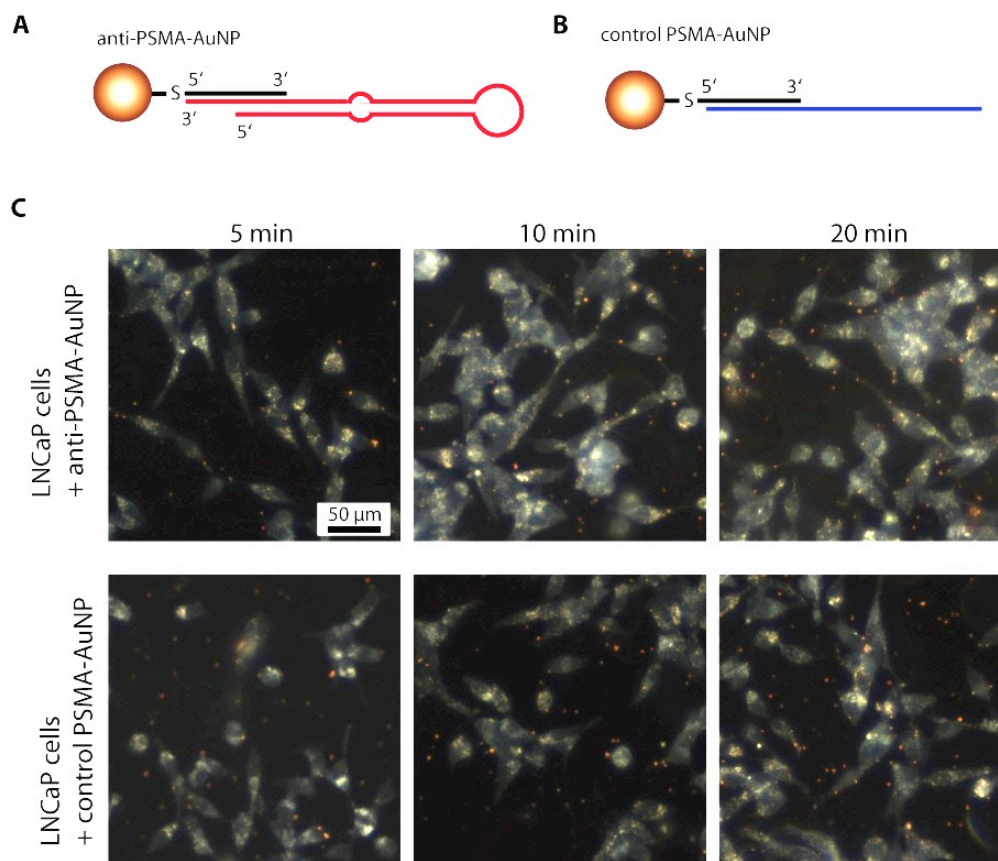


**Figure 34:** Characterization of anti-PSMA-AuNPs and analysis of their internalization into LNCaP cells. (A) Schematic drawing for functionalized anti-PSMA AuNPs (not drawn to scale) and (B) control PSMA AuNPs. (C) Dark field microscopy images of LNCaP cells treated with either anti-PSMA-AuNPs or control-AuNPs for 5, 10 and 20 min. Scale bar represents 50  $\mu\text{m}$  and is the same for all the images.

The internalization of these functionalized AuNPs into LNCaP cells was tested before in-liquid-TEM measurements. Therefore, LNCaP cells were seeded on glass coverslides and incubated with a media solution containing 1 nM anti-PSMA-AuNPs or control-AuNPs, respectively. The gold nanoparticle solutions were removed from the cells after 5, 10, or 20 min. The cells were washed and analyzed using dark field microscopy (Figure 34C). Dark-field imaging detects the scattered light instead of the phase contrast image. The cells themselves scatter light, causing a slight background signal that can be used similar as an overlay image to see the cells. The scattering of AuNPs is stronger than the autoscattering of the cells and appears as characteristic orange spots. It was possible to find these orange spots within the cells only in the samples treated with the PSMA-AuNPs after 20 min incubation (Figure 34C). Although there were also orange spots detectable in the samples treated with the control PSMA AuNPs after 5, 10, and 20 min, these were mainly randomly distributed over the whole viewing area. There was no concentration of the signals detectable within the LNCaP cells as in the sample with anti-PSMA AuNPs.

After dark field microscopy results showed the internalization of the anti-PSMA-AuNPs, in-liquid TEM measurements of LNCaP cells targeted with anti-PSMA AuNPs were performed. LNCaP cells were directly seeded on the silicon nitride nanocells and cultured in medium. The nanocell was closed as described (3.1.2 above). It was possible to obtain images of non-fixed LNCaP cells like the PC3 cells, showing the reproducibility of the nanocell in-liquid TEM approach even on other cell lines. Figure 35 shows an in-liquid TEM image of LNCaP cells targeted with anti-PSMA-AuNPs. The cells were imaged first with conventional light microscopy (Figure 35A) and prepared for in-liquid TEM imaging. The in-liquid TEM image was captured three hours after the light microscopy image. The AuNPs were detectable in the sample and appeared as small black spots that were either stuck on fixed points (green circles, Figure 35) or fast moving particles getting into and out of the focus plane. Many non-moving black spots could be seen in the area of the LNCaP cells. Many other AuNPs appeared as fast moving AuNPs that could not be tracked easily. The differences of these subgroups suggested that the one on the LNCaP cells were bound to surface presented PSMA, due to the attached anti-PSMA aptamers.

In general, LNCaP cells had a major disadvantage compared to the PC3 cells. LNCaP cells showed damages already after 30 minutes with an electron beam rate of  $20 \text{ e}^-/\text{nm}^2\text{s}$ . The obtained contrast of the LNCaP cells was rather low compared to the PC3 cells, so that a higher electron rate was needed to achieve the necessary contrast. The low contrast of the LNCaP cells also occurred due to the strong scattering of the AuNPs that led to “overexposure” of the weaker autocontrast of the LNCaP cell. As a result, a part of the cell membrane detached and drifted in the surrounding with a lot of cell debris. This leads to the suggestion that LNCaP cells are less tolerant to electron radiation compared to PC3 cells even though the dose rate was higher.

In collaboration with the group of Prof. R.J. Dwayne Miller, we were able to calculate a resolution using an algorithm to detect the AuNPs and overlay these. The integrated intensity of the AuNPs was plotted and fitted with a Gaussian fit. From the Gaussian fit the calculated resolution was approximately 10 nm.

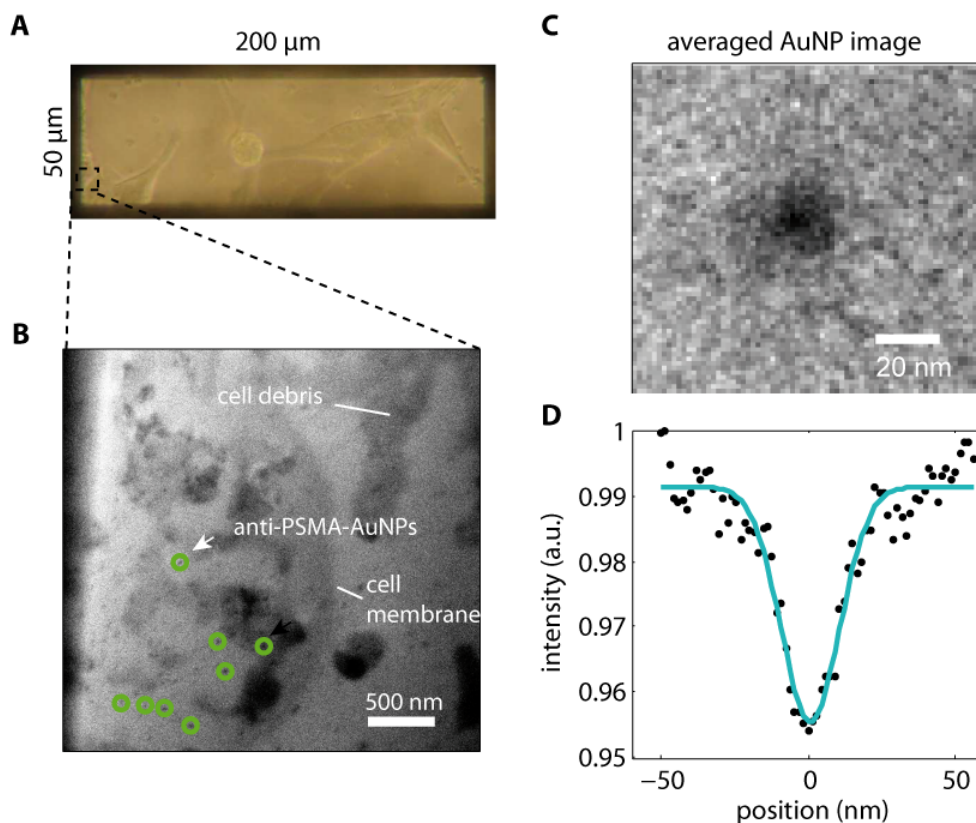


**Figure 35: In-liquid TEM image of LNCaP cells targeted with anti-PSMA-AuNPs.** Upper panel (A) shows the light microscopy image of the nanocell viewing area with LNCaP cells directly grown on the window imaged 3 hours before in-liquid TEM measurements. The area used for in-liquid TEM is marked with dashed lines. (B) In-liquid TEM image of the marked area showing the membrane of the cell and single or cluster forms of anti-PSMA-AuNPs in the liquid (small black spots highlighted with green circles) and different parts of the cell, as well as cell debris. (C) Averaged image of the highlighted particles analyzed with an algorithm written by Dr. Stephanie Manz (MPI, Hamburg). (D) Gaussian fit of the integrated profile of the averaged particles that were depicted in (C).

Overall, LNCaP cells were not as stable as PC3 cells under the electron beam. This was in accordance with observations from cell culture experiments. Here, LNCaP cells were less tolerant to temperature, or shearing forces compared to the more robust PC3 cells. The added anti-PSMA-AuNPs, black dots (some highlighted green Figure 35), could not be used to image the internalization via CME because the cell was not stable enough for long-time imaging. Nonetheless, it was possible to image attached anti-PSMA AuNPs on the LNCaPs and use their crystalline cores for the calculation on the resolution, which was given with 10 nm.





### 3.2 Engineering of Aequorin Variants with Improved $\text{Sm}^{3+}$ Binding Affinity as Potential Bimodal Probe for Light and Electron Microscopy

Aequorin has the ability to bind metal ions, which triggers light emission (Shimomura and Johnson, 1970). Both features, metal ion binding and light emission, are combined in one enzyme which paves the way for a potential bimodal probe for electron as well as fluorescence microscopy. The metal ions can function as contrasting agents in EM, although a heavier atom than the naturally preferred  $\text{Ca}^{2+}$  is needed to enhance the contrast. Another advantage is that the light emission upon metal ion binding is proportional to the concentration of the metal ions (Allen et al., 1977), which enables triggering of the luminescence for light microscopy.

The metal ions are bound by the highly conserved EF-hand motifs (1.2.2.1). Aequorin has four EF-hand motifs of which three are active for canonical high affinity  $\text{Ca}^{2+}$  binding (Charbonneau et al., 1985; Inouye et al., 1985; Head et al., 2000). Best contrast abilities in TEM measurements require high electron numbers (Figure 14 - 1.2.3 above). As calcium is a light element compared to other metals, the affinity of AQ's EF-hand motifs had to be changed to a higher affinity for a metal ion that is heavier than  $\text{Ca}^{2+}$  to create more contrast in TEM.

Due to the desired application of AQ as a bimodal probe in mammalian cells, there were further requirements for the metal ion:

- low toxicity,
- a low level in cells to preserve the trigger for light emission,
- transport ability via ion channels into the cells,
- ion diameter comparable to  $\text{Ca}^{2+}$ ,
- the ability to induce luminescence in AQ.

As mentioned in 1.2.2.1 it is known that EF-hand motifs can bind lanthanide ions like  $\text{Sm}^{3+}$  (Hogue et al., 1992; Drake et al., 1996). The  $\text{Sm}^{3+}$  ions are 3.75 times heavier compared to  $\text{Ca}^{2+}$  ions, while the ionic radius is in the same range (140 pm). It was already possible to create so-called Lanthanide-binding-tags (LBT) that have been established for MRI imaging as contrast agents. These tags are short peptides containing the 12 amino acids building the binding loop for metal ions (Franz et al., 2003; Daughtry et al., 2012).

While the ion conformation of  $\text{Ca}^{2+}$  within the EF-hand motif is known to be in a pentagonal bipyramidal geometry (Flaherty et al., 1993; Drake et al., 1996; Cates et al., 1999; Ohashi et al., 2005),  $\text{Sm}^{3+}$  ions normally can be found in a spherical hexagonal symmetry geometry (Snyder et al., 1990). Based on these findings, it should be possible to optimize the binding ability of aequorin according to bind  $\text{Sm}^{3+}$  ions with higher affinity than  $\text{Ca}^{2+}$ .

In order to find a suitable metal ion wild type AQ was tested for promiscuous metal ion binding and luminescence ability upon binding using a luminescence assay (9.7.6 below). Next to  $\text{Ca}^{2+}$  as positive control,  $\text{Co}^{2+}$  and  $\text{Sn}^{2+}$  as divalent and trivalent  $\text{Sm}^{3+}$  were tested (Figure 36).

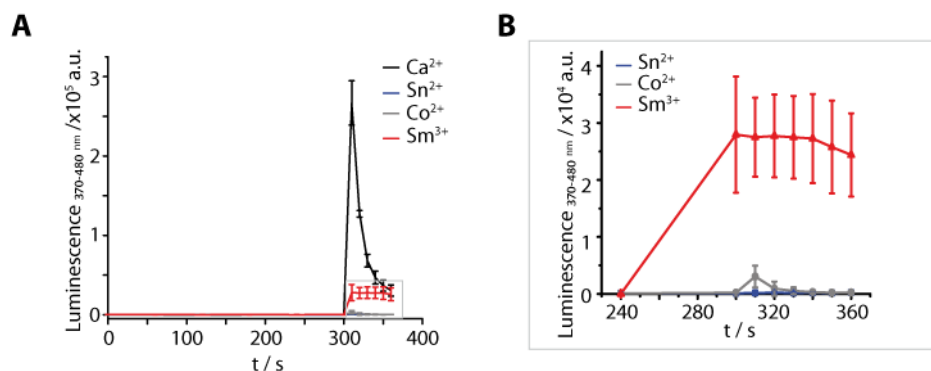


**Figure 36: Promiscuous luminescence triggering of AQ wt**

(A) Luminescence after reconstitution of enzyme (2.5  $\mu\text{M}$ ) and CTZ (5  $\mu\text{M}$ ) for 20 min at RT. During reconstitution luminescence was measured every 2 min with a multiplate reader in luminescence mode (370-480 nm). AQ wt (2.5  $\mu\text{M}$ ) luminescence was triggered by addition of 100  $\mu\text{M}$   $\text{CaCl}_2$  (black),  $\text{SnCl}_2$  (blue),  $\text{CoCl}_2$  (grey) or  $\text{SmCl}_3$  (red) to the solution. Triggered luminescence was measured in triplicates in 1 min intervals. Mean values were plotted against time, error bars represent SDs. (B) Inset of the luminescence triggered with  $\text{Sn}^{2+}$ ,  $\text{Co}^{2+}$  and  $\text{Sm}^{3+}$ .

While the highest luminescence signal was recorded for  $\text{Ca}^{2+}$  ions ( $2.7 \cdot 10^5$  a.u. black curve),  $\text{Sm}^{3+}$  had the second highest luminescence ( $2.8 \cdot 10^5$  a.u. red curve A and B) for AQ wt.

It is reported that EF-hand motif 2 has the highest affinity to  $\text{Ca}^{2+}$  (Tricoire et al., 2006) (1.2.2 above). As a result, further mutagenesis was focused on EF-hand motif 2 (amino acid residues 117-128). All mutations and resulting substitutions were inserted via MEGAWHOP PCR (9.1.1.1 below). *E.coli* BL21(DE3)pLysS cells were used for protein production (9.7.4). Proteins were purified in a two-step protocol using IMAC via N-terminal His-tag followed by anion exchange chromatography (DEAE) to remove  $\text{Ca}^{2+}$  traces and produce an active apoaequorin (9.7.5 below).

Substitutions can easily lead to unstable proteins so that a good starting point for protein engineering had to be assigned. Thermostabilized proteins are beneficial due to higher protein stability (Tsuzuki et al., 2005). The thermostabilized aequorin variant (AQ TS) Q168R/L170I was already reported (Tsuzuki et al., 2005) and therefore also tested as starting point for protein engineering. Furthermore, already published low  $\text{Ca}^{2+}$  affinity variants D119A or E128G were possible starting points as well, as they offer reduced binding affinity to  $\text{Ca}^{2+}$  (Plieth, 2006; Tricoire et al., 2006). To combine thermostability and the two low  $\text{Ca}^{2+}$  affinities the substitutions D119A and E128G were introduced to AQ TS. The resulting two variants were named TS D119A, TS E128G and tested as possible starting points compared to the low  $\text{Ca}^{2+}$  affinity

isoform LAAQ, AQ TS and AQ wt for their  $\text{Sm}^{3+}$  induced luminescence for further engineering (Figure 37).

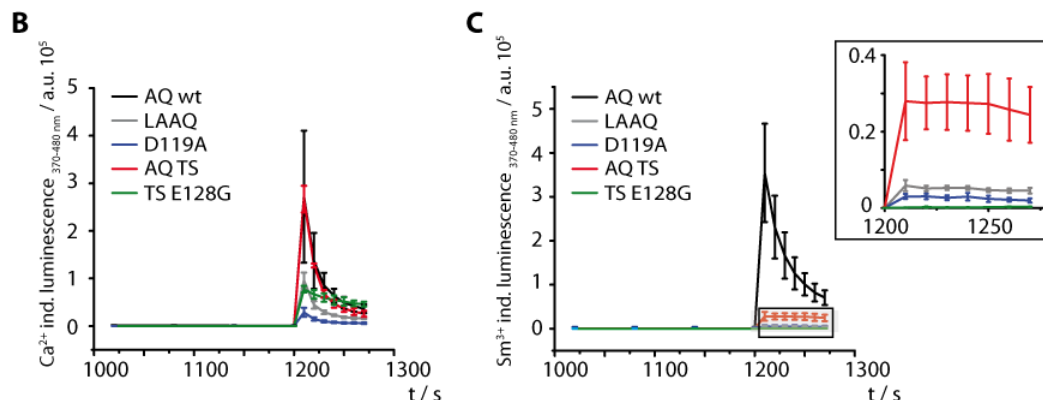


**Figure 37:** Luminescence activity of known low  $\text{Ca}^{2+}$  affinity AQ variants triggered with  $\text{Ca}^{2+}$  and  $\text{Sm}^{3+}$ . (A)  $\text{Ca}^{2+}$ -triggered luminescence curves and (B)  $\text{Sm}^{3+}$ -triggered luminescence curves. After reconstitution of enzyme ( $2.5 \mu\text{M}$ ) and CTZ ( $5 \mu\text{M}$ ) for 20 min at RT, the luminescence of the enzymes was triggered by addition of  $100 \mu\text{M}$   $\text{CaCl}_2$  or  $\text{SmCl}_3$  to the solution. During reconstitution luminescence was measured every 2 min with a multiplate reader in luminescence mode (370-480 nm), while after addition of the salt solutions luminescence was measured in 1 min intervals. Measurements were performed in triplicates. Mean values were plotted against time, error bars represent SDs. Aequorin wt is shown as black curve, AQ TS in red, TS D119A in grey, LAAQ (low  $\text{Ca}^{2+}$  affinity isoform) in dark blue and TS E128G in green.

As expected the known low  $\text{Ca}^{2+}$  affinity variant LAAQ (blue) and the new variants TS D119A (grey), TS E128G (green) had low  $\text{Ca}^{2+}$  induced luminescence compared to AQ wt (black) and AQ TS (red), which are overlaid in co-incidentally Figure 37A. The  $\text{Sm}^{3+}$  induced luminescence for TS D119A, TS E128G, and LAAQ were the lowest detected from this set of variants so that they were not used as starting points for protein engineering (Figure 37B). Aequorin wild type showed the highest  $\text{Sm}^{3+}$  induced luminescence. The thermostabilized variant AQ TS  $\text{Sm}^{3+}$ -induced luminescence was only 10 % of the AQ wt  $\text{Sm}^{3+}$ -triggered luminescence, but it had the advantage that the light emission remained at a stable level and showed slow decay, so that AQ TS was chosen as starting point for further engineering.

Not only affinity was a major aspect for new variants but also the luminescence intensities are parameters that were analyzed and optimized. The luminescence intensity is related to the binding of CTZ (Allen et al., 1977) and the concentration of metal ions. Due to the stabilization of CTZ by different amino acid residues of different subunits of the enzyme, variants have been established with higher luminescence and stabilized CTZ binding (Brini et al., 1999; Tsuzuki et al., 2005; Tricoire et al., 2006).

Two strategies were used to find a new variant with improved affinity for  $\text{Sm}^{3+}$  and  $\text{Sm}^{3+}$ -triggered luminescence: saturation mutagenesis and rational design. Because EF-hand motif 2 has the highest affinity for  $\text{Ca}^{2+}$ , this EF-hand motif was chosen for the first substitutions. All substitutions were based on AQ TS, which showed  $\text{Sm}^{3+}$  luminescence activity and is a

thermostabilized variant. AQ TS was engineered using NNK libraries for saturation mutagenesis (1.3.3) at all 6 ion coordinating positions. In parallel, rational site-directed mutagenesis (1.3.2) of the key positions 7 and 9 was performed based on published data for lanthanide binding tags (LBTs) (Drake et al., 1996; Franz et al., 2003; Nitz et al., 2003; Daughtry et al., 2012). A schematic overview is given in Figure 34. The results of both strategies are described in the following chapters.

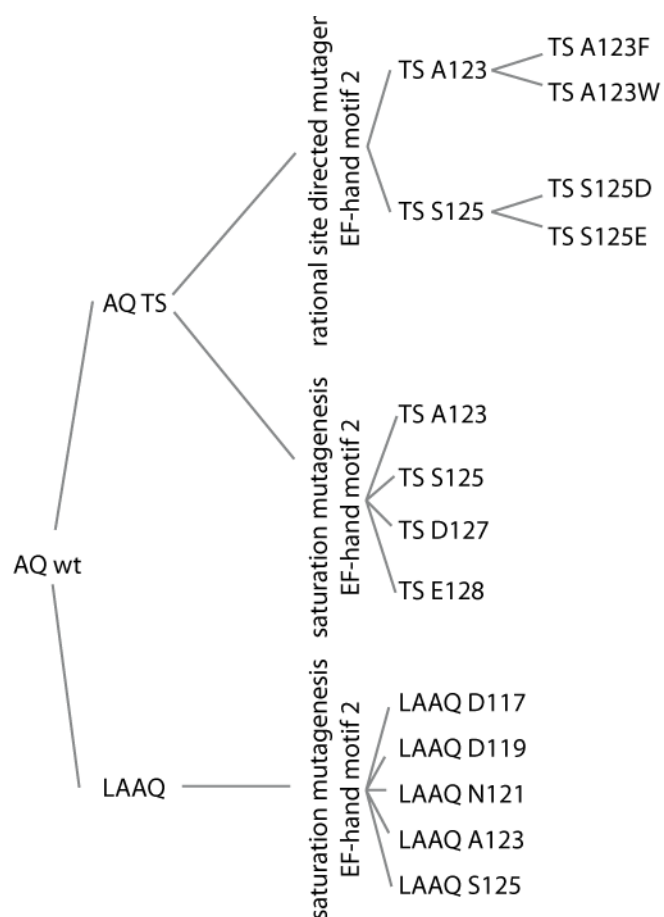
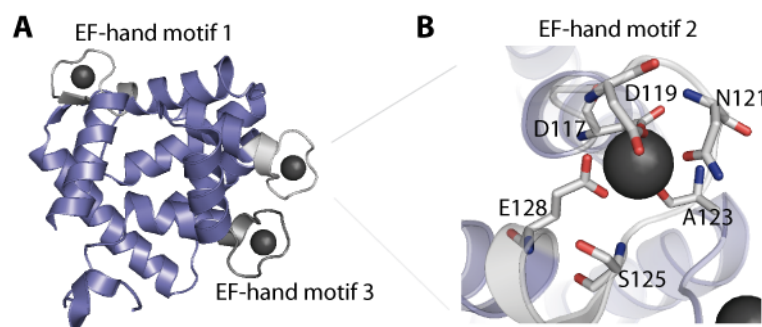


Figure 38: Schematic overview of the site-directed and saturation mutagenesis performed on EF-hand motif 2 in AQ TS.

Engineering started from AQ TS with saturation and site-directed mutagenesis in parallel. The upper tree shows the rational site-directed mutagenesis of position 7 TS A123 to TS A123F and TS A123W and position 9 TS S125 to TS S125D and TS S125E. The lower part shows the 7 positions tested in saturation mutagenesis using NNK libraries on the DNA level. Positions 12 (TS E128) and 11 (TS D127) were tested first to open the loop for the bigger  $\text{Sm}^{3+}$  ions. The other positions were tested based on the low affinity isoform LAAQ that had a lower coefficient of variance compared to the AQ TS based libraries and thus a smaller number of false positives.

### 3.2.1 Saturation Mutagenesis for an Improved Aequorin

AQ TS EF-hand motif 2 were tested for the desired  $\text{Sm}^{3+}$  binding and enhanced  $\text{Sm}^{3+}$  luminescence using saturation mutagenesis. The positions 1, 3, 5, 7, 9 and 12 of an 12 amino acid long EF-hand motif coordinate the ion binding within the loop (Cates et al., 1999). The positions are shown in Figure 39A.



**Figure 39: Protein structure of AQ with bound  $\text{Ca}^{2+}$  (pdb dataset 1SL8).**

**(A)** Protein structure of AQ (purple) with bound  $\text{Ca}^{2+}$  (black dots) within the three active EF-hand motifs (grey). The inset shows a detailed view of the amino acids (sticks) coordinating the ion binding of EF-hand motif 2.

To analyze their impact for binding of the heavier, bigger, and trivalent  $\text{Sm}^{3+}$  ion, variants of all of these six positions and one additional not directly coordinating amino acid (position 11) were screened for improved  $\text{Sm}^{3+}$  luminescence. For saturation mutagenesis, NNK codons on DNA level at the corresponding amino acid position were introduced into the gene. The NNK codon allows all four bases at position 1 and 2 of the codon and only G and T at position 3. As a result, it is possible to cover all of the 20 possible amino acids at this position. In order to screen 95 % of all possibilities 94 colonies need to be analyzed (for more details see chapter 1.3.3 above).

As  $\text{Sm}^{3+}$  is slightly bigger in diameter (122 pm) compared to  $\text{Ca}^{2+}$  (114 pm) the first attempt focused on widening the loop. To do so, the closing position 12 (E128) was analyzed first. Furthermore, the influence of the non-coordinating position 11 (D127) was tested for improved variants as well, based on the assumption that widening the loop requires more stability by the neighboring amino acids of the loop. For these two libraries at position 11 and 12, AQ TS was used as parent, while for positions 1-9 the isoform variant LAAQ with a better  $\text{Sm}^{3+}/\text{Ca}^{2+}$  luminescence ratio of 0.88 vs. 0.1 AQ TS was used due to lower coefficient of variation (CV) in the high-throughput screening (HTS).

**Table 4: Overview of the CV values for AQ TS and LAAQ in the HTS**

	CV
AQ TS OD <sub>600</sub> 0.8	0.43±0.14
AQ TS OD <sub>600</sub> 1.8	0.42±0.10
LAAQ OD <sub>600</sub> 1.8	0.39±0.07

Moreover, for positions 7 and 9 a second library was tested based on AQ TS, as these positions were important for the rational design.

The following results are described in the order of analysis as descending position numbers.

### 3.2.1.1 EF-hand motif 2 - Position 12

Position 12 is the closing position of the loop and interacts directly with the ion in the loop (Gifford et al., 2007). The amino acid glutamine ranges into the loop region and undergoes stacking with the  $\text{Ca}^{2+}$  in the pentagonal bipyramidal shape (Head et al., 2000).

The overall luminescence induced with  $\text{Ca}^{2+}$  detected in the crude cell lysate (9.7.2) was in the threshold range with a luminescence value  $\leq 200$  for mostly every well. There were three wells B7, C8, and C10 with high  $\text{Sm}^{3+}$  induced luminescence (red -  $3 \cdot 10^4$ ) (Figure 40A). The calculated  $\text{Sm}^{3+}/\text{Ca}^{2+}$  luminescence values are shown as a heat map in Figure 40B.

These three wells (B7, C8, and C10) and wells A1, A5, A8, B5, C11, C12, and D8 were tested in fivefold measurements for rescreening and verification of the  $\text{Sm}^{3+}/\text{Ca}^{2+}$  luminescence ratio in the first single well screening (Figure 40C). The luminescence values were plotted as mean values normalized to AQ TS for each ion.  $\text{Sm}^{3+}$ -triggered luminescence is shown as black bars and  $\text{Ca}^{2+}$  triggered luminescence is depicted as grey bars in an overlay. The resulting normalized  $\text{Sm}^{3+}/\text{Ca}^{2+}$  luminescence value is shown in the third y-axis (blue). None of the tested clones could overcome the threshold set to 12.5-fold higher  $\text{Sm}^{3+}/\text{Ca}^{2+}$  luminescence ratio compared to the parent because of the high CV values above 40 %. However, the sequences of the clones with the best  $\text{Sm}^{3+}/\text{Ca}^{2+}$  luminescence ratio C10, C11 and C12 were analyzed, resulting in the variant TS E128G. The screening assay confirmed an already known low affinity  $\text{Ca}^{2+}$  variant ( $\text{Ca}^{2+}$ -triggered luminescence  $3 \cdot 10^3$  a.u. purified enzyme vs.  $2.7 \cdot 10^5$  AQ TS).

A detailed characterization of purified TS E128G showed that this variant had a wide emission wavelength shift towards shorter wavelengths (from 450 nm (AQ TS) to 410 nm), when induced with  $\text{Sm}^{3+}$ . It could thus be used if two different parameters need to be detected e.g. in a multi-color assay. The induced intramolecular changes of AQ upon ion binding leads to CTZ decarboxylation and determines the emission wavelength of AQ.

The effective concentrations for 50 % of luminescence ( $\text{EC}_{50}$ ) as an indirect measure of ion affinity (Allen et al., 1977; Tricoire et al., 2006) for both ions were in the same range as parent AQ TS ( $\text{EC}_{50}$  ( $\text{Ca}^{2+}$ ): 133  $\mu\text{M}$  vs. 82 mM and  $\text{EC}_{50}$  ( $\text{Sm}^{3+}$ ): 249  $\mu\text{M}$  vs. 265  $\mu\text{M}$ ). Thus, TS E128G did not show improved  $\text{Sm}^{3+}$  luminescence.

The library of position 12 - E128 - resulted in one improved low  $\text{Ca}^{2+}$  affinity, slow decay variant: TS E128G. This variant was already published by Tricoire *et al.* (Tricoire et al., 2006) and was already mentioned above. The characterization of TS E128G can be found in the appendix (11.4 below).

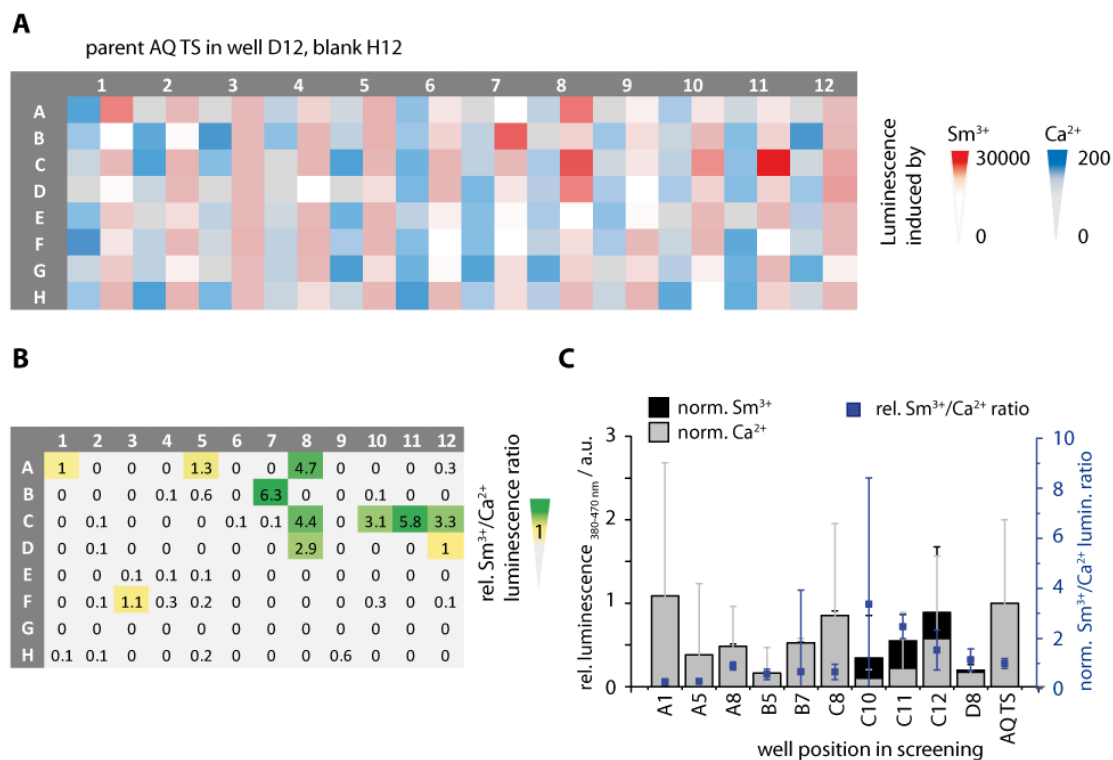


**Figure 40: Results of saturation mutagenesis at position 12 of EF hand motif 2 in AQ TS.** (A) Heat map of  $\text{Sm}^{3+}$ - (red) and  $\text{Ca}^{2+}$ -triggered (blue) luminescence for each well of a 96-well plate. (B) Calculated  $\text{Sm}^{3+}/\text{Ca}^{2+}$  luminescence ratio of each well. Ratios above 1 are shown in green, near to 1 in yellow, and below 1 in grey. (C) Relative luminescence triggered with either  $\text{Ca}^{2+}$  or  $\text{Sm}^{3+}$  was normalized to the corresponding triggered luminescence of AQ TS. Normalized  $\text{Sm}^{3+}$  induced luminescence is represented with black bars, while normalized  $\text{Ca}^{2+}$ -triggered luminescence is shown in grey bars with corresponding SD as error bars. The resulting  $\text{Sm}^{3+}/\text{Ca}^{2+}$  luminescence ratio of the normalized values is shown as blue squares with SD as error bars.

### 3.2.1.2 EF-hand motif 2 - Position 11

Position 11 of EF-hand motif 2 in AQ TS (D127) was the next analyzed position using saturation mutagenesis. Although this position is not directly involved in ion coordination, the assumption was made that loop widening for the bigger  $\text{Sm}^{3+}$  ion needs additional stabilization of neighboring amino acids apart from the 6 canonical amino acids.

The results of the screening showed overall good luminescence values induced by  $\text{Sm}^{3+}$  ions ( $1.5 \cdot 10^5$  marked red in the heat map Figure 41A). The  $\text{Ca}^{2+}$ -triggered luminescence in the crude cell lysate was lower compared to  $\text{Sm}^{3+}$ -triggered luminescence ( $0.5 \cdot 10^5$  marked blue in the heat map) (Figure 41A). Thus, there were some high potential candidates, which had high  $\text{Sm}^{3+}/\text{Ca}^{2+}$

luminescence ratios as shown in heat map Figure 41B with calculated  $\text{Sm}^{3+}/\text{Ca}^{2+}$  luminescence values.

In the rescreening 20 wells were fivefold tested (Figure 41C). The luminescence values were plotted as mean values normalized to AQ TS for each ion.  $\text{Sm}^{3+}$ -triggered luminescence is shown as black bars and  $\text{Ca}^{2+}$  triggered luminescence is depicted as grey bars in an overlay. The resulting normalized  $\text{Sm}^{3+}/\text{Ca}^{2+}$  luminescence value is shown in the third y-axis (blue). The candidates with an  $\text{Sm}^{3+}/\text{Ca}^{2+}$  luminescence ratio above 12.5 % (C11, D11, E10 and F4) were chosen for sequencing. It turned out that two out of four substituted variants could be obtained from this library: TS D127G (D11) and TS D127R (F4), while the two other were false positives AQ TS and had no substitution.

These two variants TS D127G and TS D127R were purified and further characterized according to their *in vitro* luminescence behavior,  $\text{EC}_{50}$  values, emission half-lives ( $t_{1/2}$ ) and melting temperature ( $T_M$ ) (Figure 41D). The data showed that the luminescence ratio was only increased for the variant TS D127R in comparison to AQ TS (0.3 vs. 0.1 parent). Although the ratio was improved, the  $\text{EC}_{50}$  values for  $\text{Sm}^{3+}$ -triggered luminescence was in the same order of magnitude as parent (150  $\mu\text{M}$  vs. 130  $\mu\text{M}$ ). The  $\text{EC}_{50}$  values for  $\text{Ca}^{2+}$  ions were slightly altered. TS D127R had an increased  $\text{EC}_{50}$  ( $\text{Ca}^{2+}$ ) value with 30  $\mu\text{M}$  compared to parent (50  $\mu\text{M}$ ), which is the opposite of the desired parameters.

The variant TS D127G had no improved luminescence ratio and a decreased  $\text{EC}_{50}$  ( $\text{Ca}^{2+}$ ) value with 74  $\mu\text{M}$ , which is in general beneficial for the aim of less  $\text{Ca}^{2+}$  affinity and higher affinity for  $\text{Sm}^{3+}$ . However, it was not as good as TS D127R in terms of the  $\text{Sm}^{3+}/\text{Ca}^{2+}$  luminescence ratio.

The substitution to arginine seems to result in tighter binding to the metal ions compared to the substitution to glutamic acid, although the polarity is the opposite one. This could be due to repellent forces that push the ion deeper into the loop of the twelve amino acids. Tighter binding can lead to a more completed intramolecular transversion. This should be observable as brighter luminescence signal. While TS D127R is a bright variant (luminescence  $> 3 \cdot 10^5$  a.u.), TS D127G is a low luminescence, glowing variant (luminescence  $< 1 \cdot 10^5$  a.u.). The glowing character is underlined by the long luminescence half-lives. The half-life of TS D127G induced with  $\text{Sm}^{3+}$  is 20 times longer than AQ TS induced with  $\text{Sm}^{3+}$  and 60 times longer than  $\text{Ca}^{2+}$ -induced luminescence of TS D127G. Long and stable luminescence can be favorable for application of the new variant in cell culture as the signal to noise ratio is crucial for a significant signal for imaging with FLM and there must be enough time to find the area of interest.



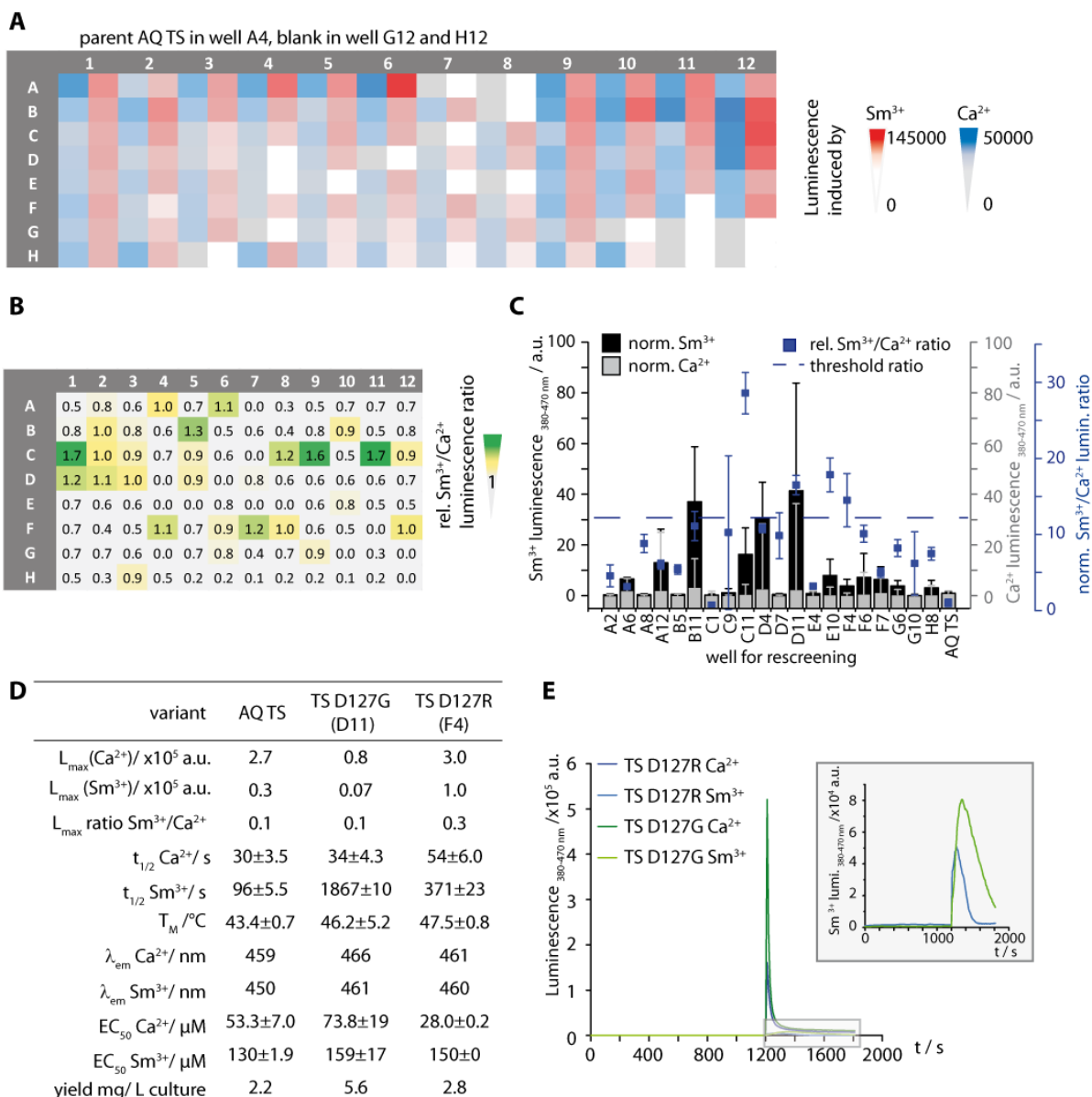


**Figure 41: Results of saturation mutagenesis at position 11 of EF hand motif 2 in AQ TS.**

(A) Heat map of  $\text{Sm}^{3+}$ - (red) and  $\text{Ca}^{2+}$ -triggered (blue) luminescence for each well of a 96-well plate. (B) Calculated  $\text{Sm}^{3+}/\text{Ca}^{2+}$  luminescence ratio of each well. Ratios above 1 are shown in green, around 1 in yellow, and below 1 in grey. (C) Results of rescreening plotted by luminescence calculated as normalized values to  $\text{Ca}^{2+}$  or  $\text{Sm}^{3+}$  induced AQ TS luminescence. Normalized  $\text{Sm}^{3+}$  induced luminescence is represented with black bars, while normalized  $\text{Ca}^{2+}$ -triggered luminescence is shown in grey bars with corresponding SD as error bars. The resulting  $\text{Sm}^{3+}/\text{Ca}^{2+}$  luminescence ratio of the normalized values is shown as blue squares with SD as error bars. The dashed blue line shows the defined threshold of 12.5-times the luminescence of AQ TS induced with  $\text{Ca}^{2+}$ . (D) Table of characterized parameters of the new variants found in the screening. (E) Luminescence curves of TS D127R with  $\text{Ca}^{2+}$  (dark blue) and  $\text{Sm}^{3+}$  (light blue) and TS D127G with  $\text{Ca}^{2+}$  (dark green) and  $\text{Sm}^{3+}$  (light green). The inset shows a magnification of the  $\text{Sm}^{3+}$  induced luminescences.

The melting temperatures ( $T_M$ ) analyzed by CD spectroscopy were in the same order of magnitude for both new variants and the parent and underline good stability of the new variants.

Mutagenesis of position 11 resulted in one improved variant TS D127R with a three-fold higher  $\text{Sm}^{3+}/\text{Ca}^{2+}$  luminescence ratio over AQ TS. TS D127G had the same  $\text{Sm}^{3+}/\text{Ca}^{2+}$  luminescence

ratio as parent and was not further used. TS D127R was used for further combinations of promising positions out of the rational design (3.2.2.3 below).

### 3.2.1.3 EF-hand motif 2 - Position 9

Position 9 has a special role for metal ion coordination as it is typically not directly involved in binding but uses a water molecule over dipole interactions with the amino acid side chain for coordination in the planar dimension (Gifford et al., 2007).

In derogation from the libraries for position 12 and 11 the libraries starting from position 9 to 1 were created using the low  $\text{Ca}^{2+}$  affinity isoform LAAQ due to lower CVs compared to the AQ TS based libraries. This decision was made to reduce the false positive clones that do not have improved  $\text{Sm}^{3+}/\text{Ca}^{2+}$  luminescence ratio.

Transformation of *E. coli* BL21(DE3)pLysS with the vector containing the NNK library for position 9 resulted in only 20 colonies on one plate of the LAAQ based library, which was not enough to cover the minimum number of 90 clones for 95% coverage of the 20 possible amino acids at one position. The AQ TS based library was cloned as well, as position 9 is important for the binding of bigger and trivalent ions (Drake et al., 1996). The library of this position yielded also only in 20 colonies maximum per plate. Transformation was repeated several times to obtain at least 94 colonies for the screening. The challenges remained for the 96-deep-well plate cultivation in media as only 22 colonies grew. Nonetheless, these 22 were screened like the other libraries. The resulting  $\text{Sm}^{3+}/\text{Ca}^{2+}$  luminescence ratios were almost zero for all of them, so that rescreening was not performed for this position.

This position was also examined in the rational design (3.2.2.2 below) because of the described impact of this position on the ion stabilization (Drake et al., 1996). It is the closing position of the planar loop and coordinates size selectivity (Drake et al., 1996) (1.2.2.1 above). The results are shown in chapter 3.2.2.2 below.

### 3.2.1.4 EF-hand motif 2 - Position 7

Previous publications on Lanthanide-binding-tags showed that position 7 is very important for the binding of bigger and trivalent ions (Franz et al., 2003; Nitz et al., 2003; Daughtry et al., 2012). The position is located in the middle of the loop (Gifford et al., 2007).

The NNK based library for A123 was cloned into the vector containing LAAQ and expressed as described in (9.7.1 below). The variants were screened for their  $\text{Sm}^{3+}$ - (red) and  $\text{Ca}^{2+}$ -triggered (blue) luminescence activity (Figure 42A). The screening showed 11 candidates with improved

Sm<sup>3+</sup>/Ca<sup>2+</sup> luminescence ratios (Figure 42B). The luminescence values for both ion-induced luminescences were very low (1000 a.u.) compared to other LAAQ libraries tested (luminescence value up to 10,000 a.u.) (3.2.1.5 below).

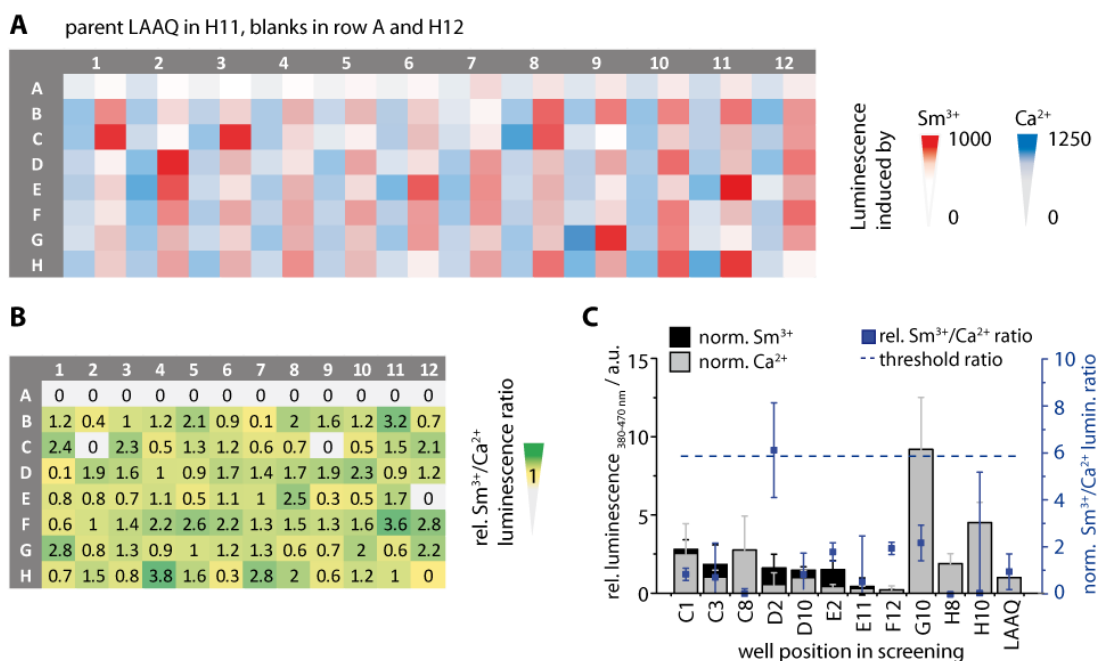


**Figure 42 Results of saturation mutagenesis at position 7 (A123) of EF hand motif 2 in LAAQ**  
**(A)** Heat map of Sm<sup>3+</sup>- (red) and Ca<sup>2+</sup>-triggered (blue) luminescence for each well of a 96-well plate. **(B)** Calculated Sm<sup>3+</sup>/Ca<sup>2+</sup> luminescence ratio of each well. Ratios above 1 are shown in green, around 1 in yellow, and below 1 in grey. **(C)** Results of rescreening plotted by luminescence calculated as normalized values to Ca<sup>2+</sup> or Sm<sup>3+</sup> induced AQ TS luminescence. Normalized Sm<sup>3+</sup> induced luminescence is represented with black bars, while normalized Ca<sup>2+</sup>-triggered luminescence is shown in grey bars with corresponding SD as error bars. The resulting Sm<sup>3+</sup>/Ca<sup>2+</sup> luminescence ratio of the normalized values is shown as blue squares with SD as error bars. The dashed blue line shows the defined threshold.

The best eleven clones (C1, C3, C8, D2, D10, E2, E11, F12, G10, H8 and H10) were tested in a rescreening round with fivefold measurements of each clone. These clones showed Sm<sup>3+</sup> and Ca<sup>2+</sup> luminescence in the screening, which is depicted in red (Sm<sup>3+</sup>) and blue (Ca<sup>2+</sup>) signals in Figure 42A. Although a luminescence ratio above 1 could be also obtained from other wells, for example such as G1 (2.8) or H7 (2.8), these had only poor luminescence values (below 500 a.u.). Only samples that showed luminescence values above 500 a.u. were possible candidates for rescreening. The candidate D2 showed an improved Sm<sup>3+</sup>/Ca<sup>2+</sup> luminescence ratio that was six times higher compared to LAAQ. For the libraries based on LAAQ the normalized threshold was defined as 6-fold higher luminescence for significance. The best variants D2, F12, and G10 were analyzed via sequencing. Two (D12 and G10) out of these three variants had the substitution A123W the third one (F12) was not substituted.

The results are in accordance with the work of the group of Barbara Imperiali, who showed that a substitution from alanine to tryptophan or phenylalanine at this position on an EF-hand motif was preferred for lanthanide binding (Nitz et al., 2003, 2004; Daughtry et al., 2012).

Because substitutions towards tryptophan and phenylalanine at position 7 is already reported in the literature, A123W and A123F were chosen for parallel rational design using site-directed mutagenesis. Detailed characterization is given in chapter 3.2.2 below.

### 3.2.1.5 EF-hand motif 2 - Position 5

Position 5 (N121) of EF-hand motif 2 holds the amino acid arginine in the parental enzyme. This position stabilizes the planar orientation of the ion within the loop (Snyder et al., 1990; Gifford et al., 2007). It is known that substitutions to S, D and K can also occur naturally in this position (Gifford et al., 2007).

The NNK library was cloned based on LAAQ and screening for  $\text{Ca}^{2+}$ - (blue) and  $\text{Sm}^{3+}$ -triggered (red) luminescence performed as described in (9.7.2 below). The luminescence obtained of this library were 10-times higher than for the library of A123 (3.2.1.4 above) and is shown in the heat map in Figure 43A. The calculated  $\text{Sm}^{3+}/\text{Ca}^{2+}$  luminescence ratio of the library led to 16 candidates for rescreening (Figure 43B). Overall low luminescence  $< 500$  was an exclusion criterion for the rescreening, although their ratio was bigger than 1. This was the case for B1, B4, C1, C10, D4, D11, E6, F8-10, G1, G5, G7-G10, H1-H3, H6, H8, and H9.

The rescreening of the best 16 clones showed some very bright variants (B5, C6, E3, E11, F4)) compared to LAAQ (Figure 43C) The clone tested of well E3 had a 250-times brighter  $\text{Ca}^{2+}$  induced luminescence. Because a higher  $\text{Sm}^{3+}$ -triggered luminescence was desired instead of a higher  $\text{Ca}^{2+}$ -triggered luminescence, this clone was not further examined and was not analyzed via sequencing. However, there was no significantly higher  $\text{Sm}^{3+}$  induced luminescence value detectable in rescreening. This means that there was no variant with improved  $\text{Sm}^{3+}/\text{Ca}^{2+}$  luminescence ratio.

The clone H10 had an  $\text{Sm}^{3+}/\text{Ca}^{2+}$  luminescence ratio comparable to LAAQ and was thus sequence analyzed. The sequence analysis showed that the tested variant is substituted N121V LAAQ. Although it showed no  $\text{Sm}^{3+}/\text{Ca}^{2+}$  luminescence ratio improvements in the crude cell lysate, the variant was produced and purified from *E. coli* BL21(DE3)pLysS for further characterization and comparison to AQ TS. The purified variant had a significantly lower  $\text{Sm}^{3+}/\text{Ca}^{2+}$  luminescence ratio with 0.05 compared to the screening directly in the cell lysate and medium (3.2 in Figure 43B). AQ TS has a ratio of 0.1 so that only variants with an  $\text{Sm}^{3+}/\text{Ca}^{2+}$  luminescence ratio  $> 0.1$  were defined as improved variant.

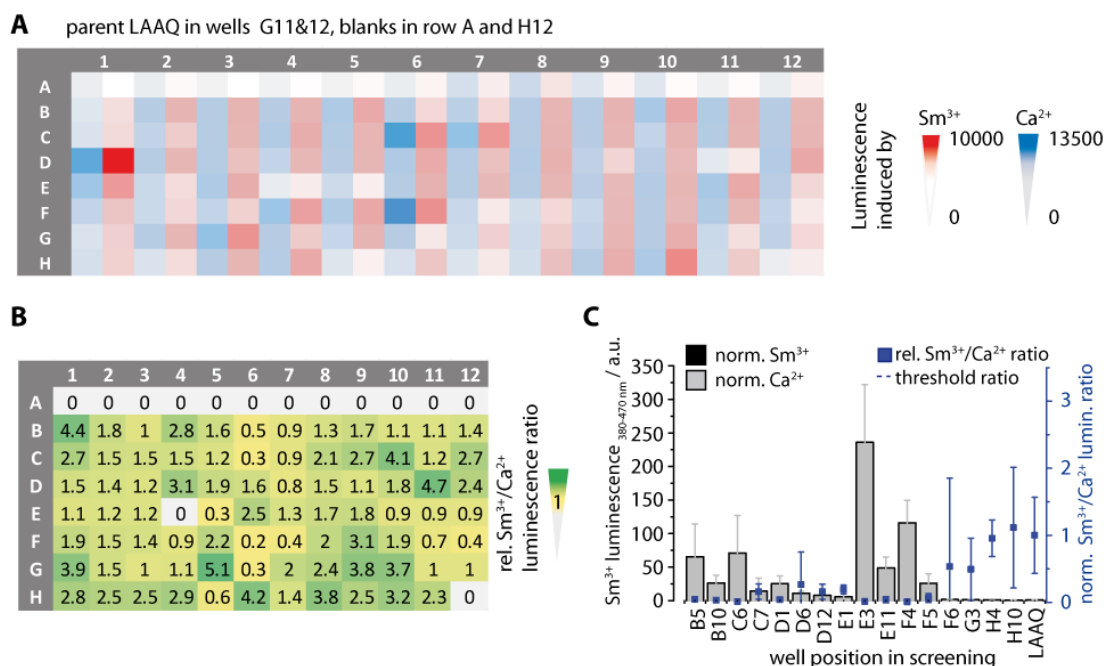


**Figure 43: Results of saturation mutagenesis at position 5 of EF hand motif 2**

**(A)** Heat map of  $\text{Sm}^{3+}$ - (red) and  $\text{Ca}^{2+}$ -triggered (blue) luminescence for each well of a 96-well plate. **(B)** Calculated  $\text{Sm}^{3+}/\text{Ca}^{2+}$  luminescence ratio of each well. Ratios above 1 are shown in green, around 1 in yellow, and below 1 in grey. **(C)** Results of rescreening plotted by luminescence calculated as normalized values to  $\text{Ca}^{2+}$  or  $\text{Sm}^{3+}$  induced AQ TS luminescence. Normalized  $\text{Sm}^{3+}$  induced luminescence is represented with black bars, while normalized  $\text{Ca}^{2+}$ -triggered luminescence is shown in grey bars with corresponding SD as error bars. The resulting  $\text{Sm}^{3+}/\text{Ca}^{2+}$  luminescence ratio of the normalized values is shown as blue squares with SD as error bars. The dashed blue line shows the defined threshold.

The  $\text{EC}_{50}$  ( $\text{Sm}^{3+}$ ) of N121V LAAQ was decreased to  $190 \mu\text{M}$  compared to AQ TS  $270 \mu\text{M}$  (factor 1.4). This means that the variant N121V LAAQ is able to reach 50% of the maximal luminescence with a concentration 1.4 times lower compared to AQ TS. This would be beneficial but the  $\text{EC}_{50}$  value for  $\text{Ca}^{2+}$  ions was slightly decreased to  $60 \mu\text{M}$  as well while AQ TS could be assigned to  $80 \mu\text{M}$ .

This substitution had no further improvement for the  $\text{Sm}^{3+}$ -triggered luminescence, instead it showed better luminescence with  $\text{Ca}^{2+}$  ions compared to AQ TS and was therefore not further used.

### 3.2.1.6 EF-hand motif 2 - Position 3

Position 3 is known to be a key position for decreased  $\text{Ca}^{2+}$  affinity of the enzyme (see D119A) (Kendall et al., 1992; Plieth, 2006; Gifford et al., 2007). The low  $\text{Ca}^{2+}$  affinity variant D119A is widely used to image high concentration  $\text{Ca}^{2+}$  flux in mitochondriae (de la Fuente et al., 2012).

The library for this position was cloned via MEGAWHOP PCR using LAAQ as parent. *E. coli* BL21DE3 pLysS cells were transformed with the resulting vector. The number of clones after transformation was low so that only 50 clones could be tested for luminescence. The cells were cultivated in 96-deep-well plates and luminescence induced with either 100  $\mu\text{M}$   $\text{Sm}^{3+}$  or  $\text{Ca}^{2+}$  as described in (9.7.2 below).

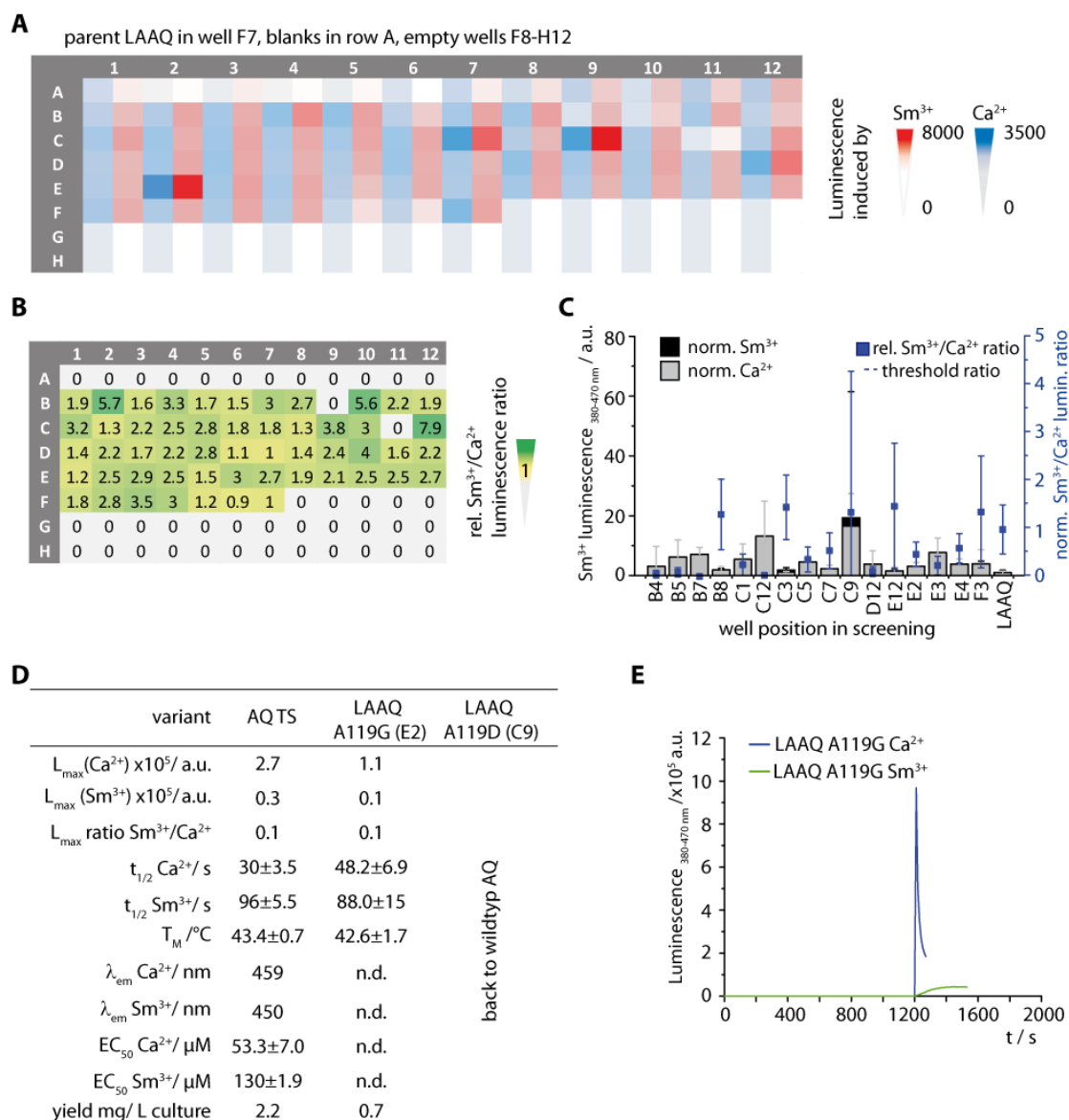


Figure 44: Results of saturation mutagenesis at position 3 of EF hand motif 2

(A) Heat map of  $\text{Sm}^{3+}$ - (red) and  $\text{Ca}^{2+}$ -triggered (blue) luminescence for each well of a 96-well plate. (B) Calculated  $\text{Sm}^{3+}/\text{Ca}^{2+}$  luminescence ratio of each well. Ratios above 1 are shown in green, around 1 in yellow, and below 1 in grey. (C) Results of rescreening plotted by luminescence calculated as normalized values to  $\text{Ca}^{2+}$  or  $\text{Sm}^{3+}$  induced AQ TS luminescence. Normalized  $\text{Sm}^{3+}$  induced luminescence is represented with black bars, while normalized  $\text{Ca}^{2+}$ -triggered luminescence is shown in grey bars with corresponding SD as error bars. The resulting  $\text{Sm}^{3+}/\text{Ca}^{2+}$  luminescence ratio of the normalized values is shown as blue squares with SD as error bars. The dashed blue line shows the defined threshold.

The obtained luminescence was lower compared to the library of position 5 (3.2.1.5 above). The overall  $\text{Ca}^{2+}$  induced luminescence was low with only 3000 a.u. (blue - Figure 44A). Because the

low  $\text{Ca}^{2+}$  affinity variant LAAQ was used as base for the library the low luminescence values can be explained. The  $\text{Sm}^{3+}$  induced luminescence was comparable with 8000 a.u. to the library tested before.

Based on the  $\text{Sm}^{3+}/\text{Ca}^{2+}$  luminescence ratio levels shown as heat map in Figure 44B there were not many candidates for rescreening. The best 16 candidates were tested in five-fold in the rescreening (Figure 44C). No variant could exceed the threshold defined as 6-fold norm. luminescence ratio. The clones B8, C3, C9, E12, and F3 were slightly above 1, so that these were further analyzed. The CV values were slightly better compared to the AQ TS based libraries (25%) but this still means that false positives occur in at least one out of four clones. Sequence analysis was performed for C3, C9, and E2 of which two substitutions could be found. The clone E2 could be assigned as LAAQ A119G, which was further characterized. A119G LAAQ had no further improvements regarding  $\text{Sm}^{3+}$ -triggered luminescence. Another variant, which could be found, was A119D LAAQ, which is the back conversion to the originating amino acid of the wild type AQ.

The characterization of A119G showed that the luminescence values for  $\text{Ca}^{2+}$  and  $\text{Sm}^{3+}$  were rather low  $1.1 \cdot 10^5 / 0.1 \cdot 10^5$  a.u. The  $\text{Sm}^{3+}/\text{Ca}^{2+}$  luminescence ratio was calculated to 0.1, which is in the same range as AQ TS (0.1). In summary, no improved variant was found at this position.

### 3.2.1.7 EF-hand motif 2 - Position 1

Position 1 is an essential position as it opens the ion coordination loop. Substitutions at this position can lead to the removal of the  $\text{Ca}^{2+}$ -binding ability of the EF-hand motif (Tricoire et al., 2006). It mainly coordinates the binding of metal ions. An example is described in Tricoire *et al.*: D117G. This variant is a  $\text{Ca}^{2+}$  low affinity, glowing variant. Thus, alterations at this position have a great impact on the overall behavior of the enzyme.

Analysis of the library of position 1 (D117) had poor colony number (15 colonies). Sequencing of four colonies revealed only a few silent mutations. It is known that substitution at position 1 mostly leads to inactive variants (Tricoire et al., 2006). The obtained luminescence of clones were low ( $\text{Sm}^{3+}$  200 a.u. red,  $\text{Ca}^{2+}$  600 a.u. blue) and depicted in Figure 45A

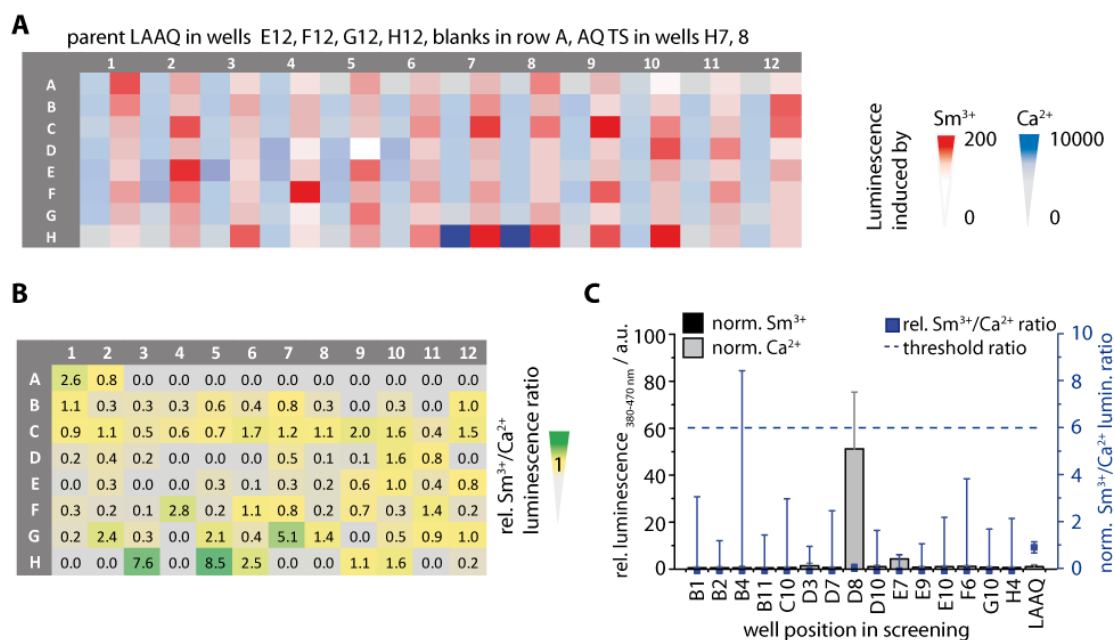


**Figure 45: Results of saturation mutagenesis at position 1 of EF hand motif 2**

(A) Heat map of  $\text{Sm}^{3+}$ - (red) and  $\text{Ca}^{2+}$ -triggered (blue) luminescence for each well of a 96-well plate. (B) Calculated  $\text{Sm}^{3+}/\text{Ca}^{2+}$  luminescence ratio of each well. Ratios above 1 are shown in green, around 1 in yellow, and below 1 in grey. (C) Results of rescreening plotted by luminescence calculated as normalized values to  $\text{Ca}^{2+}$  or  $\text{Sm}^{3+}$  induced AQ TS luminescence. Normalized  $\text{Sm}^{3+}$  induced luminescence is represented with black bars, while normalized  $\text{Ca}^{2+}$ -triggered luminescence is shown in grey bars with corresponding SD as error bars. The resulting  $\text{Sm}^{3+}/\text{Ca}^{2+}$  luminescence ratio of the normalized values is shown as blue squares with SD as error bars. The dashed blue line shows the defined threshold.

During screening of the library, there was no variant detectable with a higher  $\text{Sm}^{3+}/\text{Ca}^{2+}$  luminescence ratio compared to the parent (Figure 45B). Although in Figure 45B G7, H3 and H5 had higher luminescence ratios, the single  $\text{Sm}^{3+}$  luminescence values (depicted in Figure 45A) was low ( $< 200$  a.u.) and thus they were excluded.

Nonetheless, the 15 best clones were selected for rescreening in fivefold. The rescreening shown in Figure 45C confirmed that there was no variant with improved  $\text{Sm}^{3+}/\text{Ca}^{2+}$  luminescence ratio from this library. No clone had a normalized  $\text{Sm}^{3+}/\text{Ca}^{2+}$  luminescence ratio over the threshold of 6 (blue dashed line) illustrated in Figure 45C.

### 3.2.1.8 Summary of the Saturation Mutagenesis Approach

The six essential positions for ion binding D117 (1), D119 (3), N121 (5), A123 (7), S125 (9), and E128 (12) as well as the stabilizing position 11 D127 were tested for improved  $\text{Sm}^{3+}$ -triggered luminescence using NNK libraries.

The libraries for D117 (position 1), N121 (position 5) and S125 (position 9) showed no improvement for the  $\text{Sm}^{3+}/\text{Ca}^{2+}$  luminescence ratio. For these positions only low numbers of



colonies could be obtained so that screening required multiple attempts of plating in order to achieve more than 50 colonies. The low colony number might be explained due to lack of the resistance gene for the selection antibiotic ampicillin, which was in the pRSET vector containing the gene for AQ.

Position 3 resulted in the two variants A119G and A119D. The variant A119D LAAQ is the back conversion of the low affinity variant to the wild type and was thus not further analyzed.

The results of position 7 showed the improved variant A123W LAAQ. Because this substitution is known to be preferred for lanthanide binding tags by the work of Barbara Imperiali's group it was chosen for rational design as well and tested for  $\text{Sm}^{3+}$  induced luminescence separately.

Screening of the library at position 11 TS D127 lead to two variants TS D127G and TS D127R. While TS D127G had no improvements for the  $\text{Sm}^{3+}/\text{Ca}^{2+}$  luminescence ratio, the variant TS D127R had improved  $\text{Sm}^{3+}/\text{Ca}^{2+}$  luminescence ratio by factor 3 and a lower  $\text{EC}_{50}$  value for  $\text{Sm}^{3+}$  with 150  $\mu\text{M}$ . This variant was used to combine the results of rational design and saturation mutagenesis screening (3.2.2.5 below).

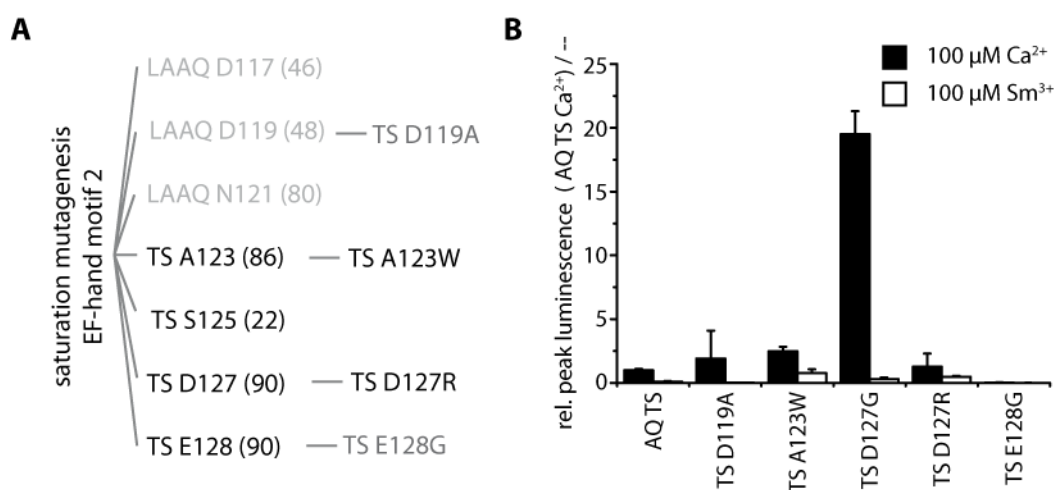


Figure 46: Results of the saturation mutagenesis.

(A) Organigram of the screened positions for saturation mutagenesis. The number of clones is given in brackets. New obtained variants with improved  $\text{Sm}^{3+}/\text{Ca}^{2+}$  luminescence ratios are given in black, already known variants in grey. (B) Overview of the relative peak luminescence triggered with  $\text{Ca}^{2+}$  (black bars) or  $\text{Sm}^{3+}$  (white bars) calculated to AQ TS triggered with  $\text{Ca}^{2+}$ .

The library TS E128 resulted in TS E128G, which was already known as a low  $\text{Ca}^{2+}$  affinity variant. It was also further used for the combination of the best substitutions from rational design to obtain the best  $\text{Sm}^{3+}$  binding aequorin variant (3.2.2.5 below).

### 3.2.2 Engineering of Aequorin using Rational Design

It is reported that lanthanide ions like  $\text{Sm}^{3+}$  can induce luminescence upon binding to AQ (Rao et al., 1980; Kemple et al., 1990; Robert et al., 2000). Rational design was performed in parallel to the saturation mutagenesis libraries with the aim to enhance the  $\text{Sm}^{3+}$  binding of AQ. Based on the research of Nitz *et al.* on troponin C EF-hand motifs as lanthanide binding tag (Franz et al., 2003), substitutions at position 7 (alanine) of EF-hand motif 2 in AQ TS towards phenyl alanine (TS A123F) and tryptophan (TS A123W) were introduced. These substitutions should coordinate trivalent ions better due to their bigger side chain and the polar benzyl ring as stabilization of the ion.

Because  $\text{Sm}^{3+}$  is not only trivalent but also bigger as  $\text{Ca}^{2+}$  the substitutions at position 9 (serine), also known as gateway position (Drake et al., 1996), to aspartic acid or glutamic acid were introduced to EF-hand motif 2 for further improvements due to more space.

Combinations of position 7 and 9 (EF-hand motif 2) were tested and the best variant was further combined with the best variants of the saturation mutagenesis (3.2.1 above).

On the basis that the  $\text{Ca}^{2+}$  affinity of the three EF-hand motifs, decreasing from EF-hand motif 2, to EF-hand motif 3, and EF-hand motif 1, the best substitutions were inserted successively into the two other EF-hand motifs.

#### 3.2.2.1 EF-hand Motif 2 - Position 7 – Allowing Binding of Different Valencies

Position 7 of a 12 amino acid long EF-hand motif is important for the planar coordination of the ion and thus allows binding of ions with a different valency (Cates et al., 1999). The reported LBT for MRI imaging were developed based on EF-hand motifs. These had substitutions at position 7 to tryptophan or phenylalanine (Nitz et al., 2003). These insertions offer a bigger area for interaction due to stabilization of the ion by the amino acid's side chain (Figure 47A).

Mutations were inserted by MEGAWHOP PCR (9.1.1.1), and variants were produced and purified (9.7.5). The variants AQ TS A123W and TS A123F showed high maximum luminescence values when induced with 100  $\mu\text{M}$   $\text{Ca}^{2+}$  or  $\text{Sm}^{3+}$ . The substitutions led to so-called bright variants with threefold higher luminescence induced with  $\text{Ca}^{2+}$  (black bars) and 7-times higher luminescence induced with  $\text{Sm}^{3+}$  (white bars) compared to parent AQ TS (Figure 47B). Overall, the  $\text{Sm}^{3+}/\text{Ca}^{2+}$  luminescence ratio induced with 100  $\mu\text{M}$  of each metal ion could be increased by factor 3 for both variants (Figure 47B). This was a step forward to a variant with improved  $\text{Sm}^{3+}$ -triggered luminescence.

Furthermore, the light emission wavelength changed for both new variants. TS A123F induced with  $\text{Ca}^{2+}$  had a shift of 12 nm (459 nm to 471 nm) (dark green) and  $\text{Sm}^{3+}$  11 nm (grey) towards higher wavelengths (450 nm to 461 nm), while TS A123W emission shifted only 7 nm with  $\text{Ca}^{2+}$  (red) and 5 nm with  $\text{Sm}^{3+}$  (orange) (Figure 47C).

The  $\text{EC}_{50}$  values as an indirect measure of ion affinity were tested as well. The variant TS A123F was more or less in the same order of magnitude as parent regarding  $\text{EC}_{50}(\text{Ca}^{2+})$  and  $\text{EC}_{50}(\text{Sm}^{3+})$  (Figure 47D). However, TS A123W was the first variant obtained so far with a three-time higher  $\text{EC}_{50}(\text{Ca}^{2+})$  of 130  $\mu\text{M}$  compared to AQ TS 53.3  $\mu\text{M}$ , which means that a higher concentration of  $\text{Ca}^{2+}$  is needed to yield 50 % of the maximum luminescence. This was the first time that a higher concentration was needed for 50 % of the maximal luminescence and indicates less  $\text{Ca}^{2+}$  affinity. The  $\text{EC}_{50}(\text{Sm}^{3+})$  was comparable to parent (Figure 47D).

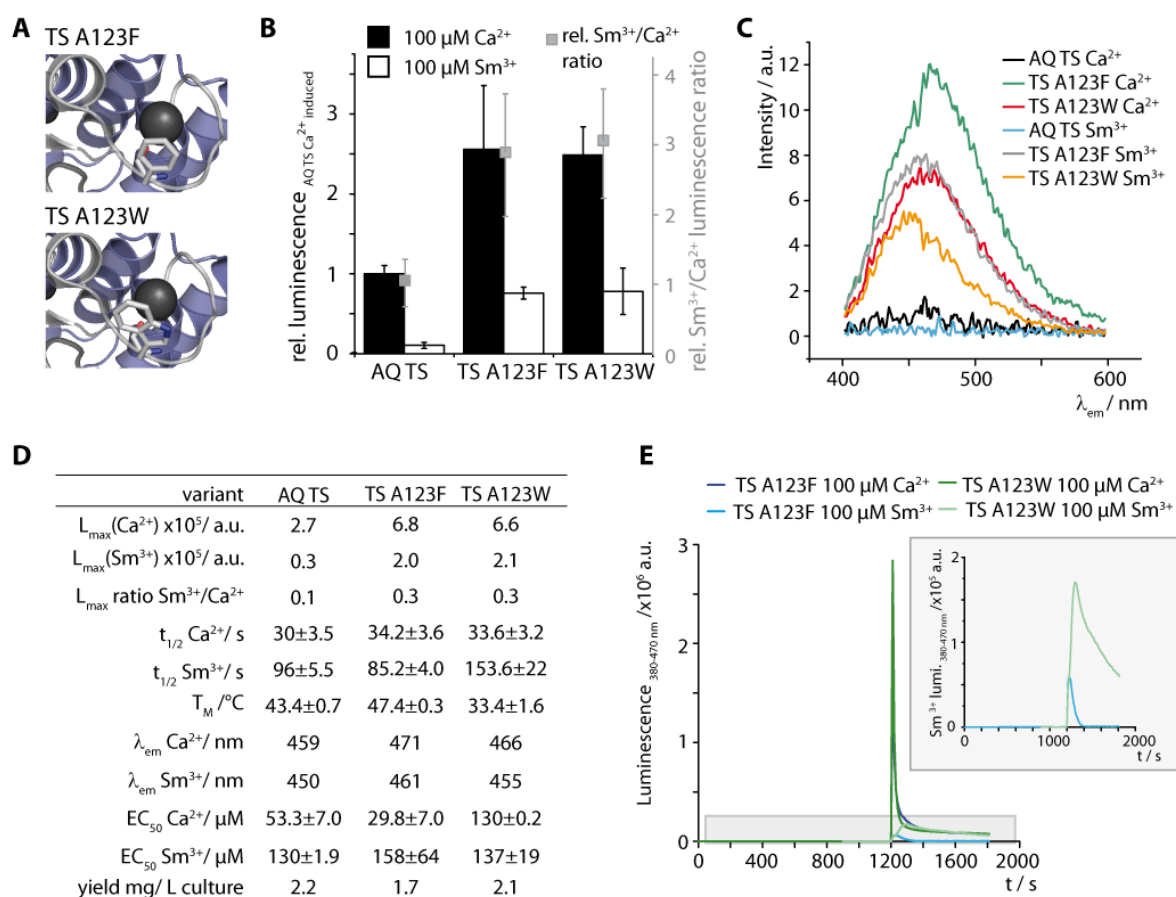


**Figure 47: Characterization of variants at position 7 EF-hand motif 2 after site-directed mutagenesis**  
**(A)** Modified crystal structure with substitutions according to PDB 1SL8. **(B)** Maximum relative luminescence of TS A123F and TS A123W compared to parent AQ TS 100  $\mu\text{M}$   $\text{Ca}^{2+}$ . Black bars induced with  $\text{Ca}^{2+}$ , white  $\text{Sm}^{3+}$  (100  $\mu\text{M}$ ) induced. **(C)** Relative  $\text{Sm}^{3+}/\text{Ca}^{2+}$  luminescence ratios of maximum luminescence values calculated to AQ TS. **(D)** Table of characterization parameters of variants TS A123F and TS A123W. **(E)** Luminescence curves are plotted for TS A123F with  $\text{Ca}^{2+}$  (dark blue) and  $\text{Sm}^{3+}$  (light blue) and TS A123W with  $\text{Ca}^{2+}$  (dark green) and with  $\text{Sm}^{3+}$  (light green) against time.

Next to the luminescence intensity the half-life is also important for a bimodal probe due to the flash-like light emission of AQ. Triggered luminescence was recorded for both ions (Figure 47E) and the half-lives calculated. The half-lives for  $\text{Ca}^{2+}$ -triggered luminescence were in the same dimension as parent for both variants (around 30 s) (Figure 47D and E). An exception was the half-life of  $\text{Sm}^{3+}$  induced luminescence of TS A123W, which was 1.5-fold, compared to parent (150 vs. 90 s) (Figure 47D). Longer luminescence is favorable for light microscopy in order to locate the area of interest.

In summary, substitution at this position improved the  $\text{Sm}^{3+}/\text{Ca}^{2+}$  luminescence ratio by factor 3 for both variants TS A123F and TS A123W. The higher  $\text{EC}_{50}(\text{Ca}^{2+})$  value indicates reduced  $\text{Ca}^{2+}$  affinity, but was only detectable for TS A123W. Furthermore, emission wavelengths shifts could be obtained, which might allow detection of two different components when a mixture of AQ TS and TS A123F is used.

### 3.2.2.2 EF-hand Motif 2 - Position 9 – Widening the Ion Diameter Restriction

Position 9 of an EF-hand motif is known to be the “gateway” position because of the end position in the loop (Drake et al., 1996). Substitutions of serine to either aspartic acid or glutamic acid will reduce the ion size selectivity according to Drake *et al.* (Drake et al., 1996). This is beneficial for the suggested  $\text{Sm}^{3+}$  binding with its bigger ion size (122 pm) compared to  $\text{Ca}^{2+}$  (114 pm). A structure is given in Figure 48A. The NNK library of the respective position yielded almost no clones so that there was no complete screening possible (3.2.1.3).

After cloning, the variants of AQ TS were produced, purified, and tested on luminescence activity with  $\text{Ca}^{2+}$  and  $\text{Sm}^{3+}$ . Interestingly, TS S125D production had a good yield of 2.1 mg/L culture. TS S125E underlined the difficulties seen in the saturation mutagenesis as the yield was only 0.1 mg/L culture.

However, both ions induced luminescence (Figure 48B). Substitution at position S125 to D resulted in a bright variant. The  $\text{Ca}^{2+}$ -triggered luminescence (black bars) was 10-times higher compared to parent. The  $\text{Sm}^{3+}$  induced luminescence (white bars) was 5.6 times higher compared to AQ TS. The  $\text{Sm}^{3+}/\text{Ca}^{2+}$  luminescence ratio was 0.5 times higher compared to parent (Figure 48B, grey data points).

The emission wavelengths were almost comparable to AQ TS. One exception is a shift to higher wavelength of 8 nm for  $\text{Ca}^{2+}$  in combination with TS S125D (dark green curve). (Figure 48C).

The substitution S125D/E should decrease the ion size selectivity and affinity. Decreased ion affinity can be indirectly measured by the luminescence value triggered with each ion. For neither

substitution, a decreased  $EC_{50}$  could be observed. The  $EC_{50}(Ca^{2+})$  for TS S125D and TS S125E were even two-fold increased (ca. 20  $\mu M$ ) (Figure 48D). This was the opposite change and thus not towards a variant with less  $Ca^{2+}$  luminescence activity.

Noticeable is the very high  $T_M$  value of  $56 \pm 0.7$  °C for TS S125D indicating high stability of the enzyme.

The luminescence half-lives were calculated for both ions. The typical luminescence curves are shown in Figure 48E. While TS S125D triggered with  $Ca^{2+}$  showed the already mentioned high luminescence intensity (blue),  $Sm^{3+}$ -triggered luminescence of TS S125D was very stable (light blue) with calculated 1200 s (Figure 48D).

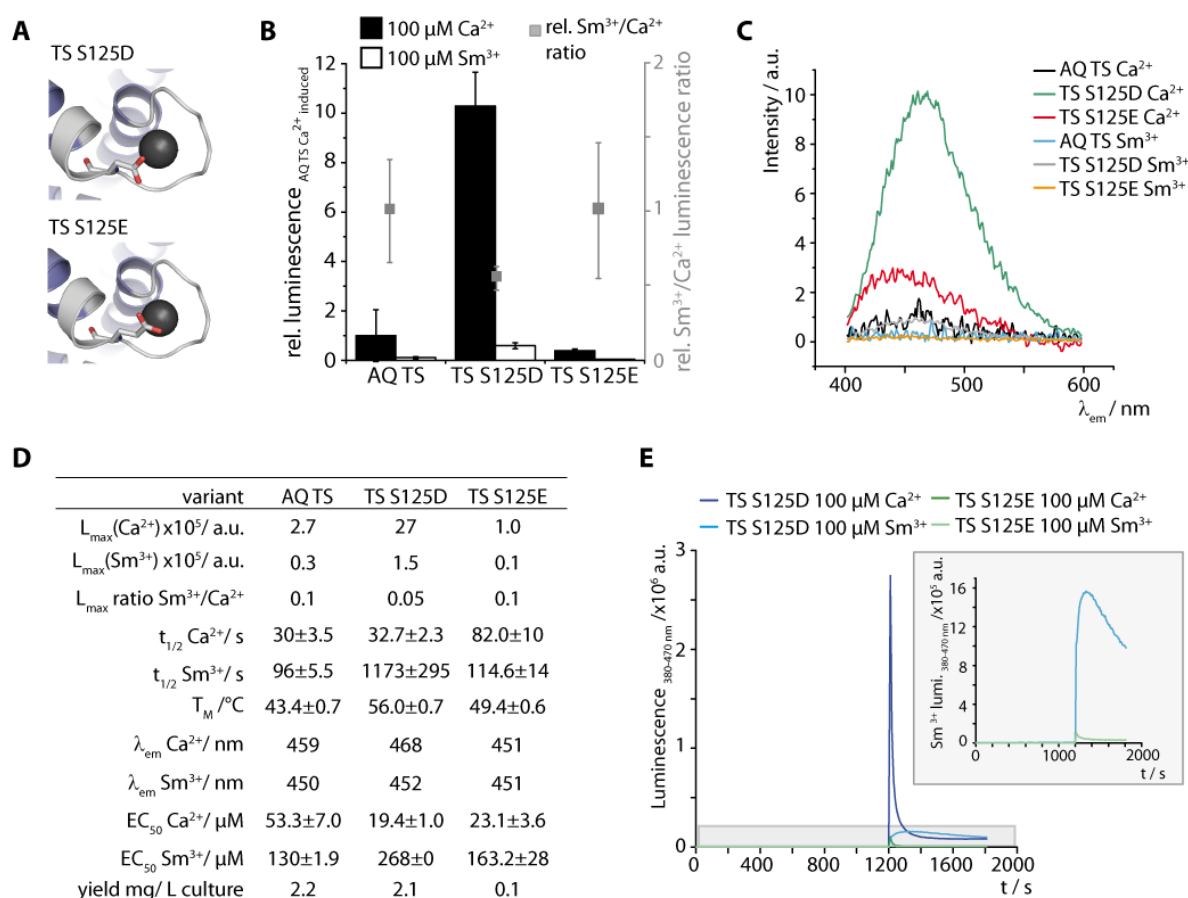


**Figure 48: Characterization of variants TS S125D and TS S125E.**

(A) Modified crystal structure with substitutions according to PDB 1SL8. (B) Maximum relative luminescence of TS S125D and TS S125E compared to parent AQ TS 100  $\mu M$   $Ca^{2+}$ . Black bars induced with  $Ca^{2+}$ , white  $Sm^{3+}$  (100  $\mu M$ ) induced. (C) Relative  $Sm/Ca$  luminescence ratios of maximum luminescence values calculated to AQ TS. (D) Table of characterization parameters of variants TS S125D and TS S125E. (E) Luminescence curves are plotted for TS S125D with  $Ca^{2+}$  (dark blue) and  $Sm^{3+}$  (light blue) and TS S125E with  $Ca^{2+}$  (dark green) and with  $Sm^{3+}$  (light green) against time.

Additional substitutions at this position to Gly and Arg were tested upon their influence (data obtained together with Franziska Böwer and described in her bachelor thesis 2014). The variant TS S125G could be purified but was not active. Circular dichroism (CD) measurements revealed

that the folding was not correct, as there were no characteristic minima at 210 and 220 nm for the AQ's  $\alpha$ -helices. The substitution TS S125R should create opposite charge and thus reduce binding of either ion. While there was still moderate  $\text{Ca}^{2+}$  luminescence detectable,  $\text{Sm}^{3+}$  induced luminescence was low (data is given in the appendix). This fact supports the preferred substitution with negatively charged amino acids like Glu and Asp to enhance binding of positively charged ions.

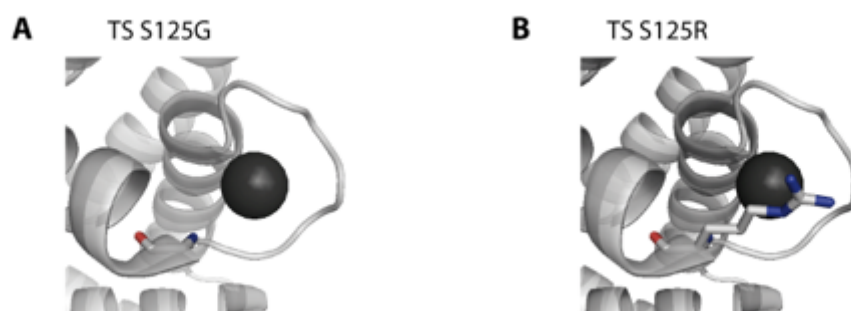


**Figure 49: Modeled structure of TS S125G and TS S125R.**

In summary, the analyzed variants TS S125D, TS S125E, TS S125G, and TS S125R had no directly noticeable benefit for the desired higher affinity to  $\text{Sm}^{3+}$  instead of  $\text{Ca}^{2+}$ . However, TS S125D showed a long luminescence half-life when induced with  $\text{Sm}^{3+}$ . This is also important for the final goal of stable light  $\text{Sm}^{3+}$  emission of AQ in cells for bimodal imaging.

### 3.2.2.3 EF-hand motif 2 - Double substitutions based on position 7 and 9

As mentioned before,  $\text{Sm}^{3+}$  has a bigger diameter compared to  $\text{Ca}^{2+}$  ions and is trivalent, which needs different coordination compared to  $\text{Ca}^{2+}$ . The analysis of position 7 and 9 variants showed first improvements for TS A123W regarding a higher affinity for  $\text{Sm}^{3+}$  ions and stable  $\text{Sm}^{3+}$ -triggered luminescence for TS S125D. Variants that did not show the best improvements in terms of luminescence in the first instance, such as TS A123F and TS S125E, can still enhance the luminescence in combination with other variants, so that all four substitutions were mixed and tested.

All four variants (TS A123F S125D, TS A123F S125E, TS A123W S125D and TS A123W S125E) were cloned, produced, and purified (9.7.4 below). The structures are given as models based on a published structure of AQ TS (pdb file 1SL8) in Figure 50A. The variants were tested for luminescence activity (9.7.6 below) with  $\text{Ca}^{2+}$  (black bars) and  $\text{Sm}^{3+}$  (white bars) (Figure 50B). TS A123F S125E induced with 100  $\mu\text{M}$   $\text{CaCl}_2$  was the brightest variant in this set compared to parent with an almost 40-fold luminescence. The  $\text{Sm}^{3+}$ -induced luminescence was higher than that of the parent for all variants except TS A123W S125D. The single substitutions TS A123W

and TS S125D had improvements compared to AQ TS. The combination of both did not show any further or even additive effects regarding the goal of improved  $\text{Sm}^{3+}$ -triggered luminescence. The highest achieved  $\text{Sm}^{3+}/\text{Ca}^{2+}$  luminescence ratio for the variants was detected for TS A123W S125E and is 8-fold higher compared to parent (grey data points, Figure 50B).

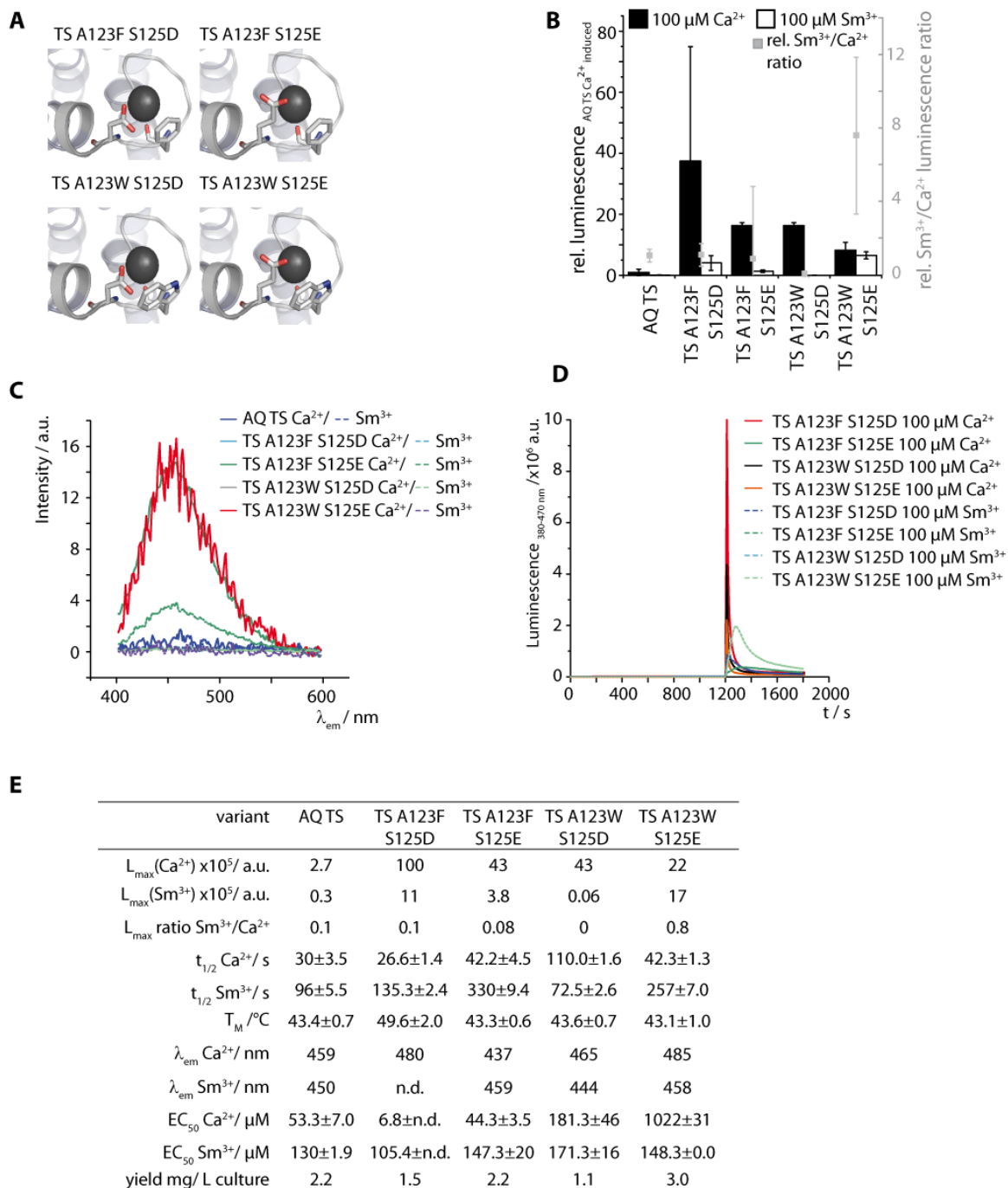


**Figure 50: Characterization of AQ TS variants with double substitutions at position 7 and 9 of EF-hand motif 2.**

(A) Modified crystal structure of AQ TS with substitutions based on PDB 1SL8. (B) Maximum relative luminescence of double substitutions compared to parent AQ TS (2.5  $\mu\text{M}$ ), black bars induced with  $\text{Ca}^{2+}$ , white bars induced with  $\text{Sm}^{3+}$  (100  $\mu\text{M}$ ). (C) Relative  $\text{Sm}^{3+}/\text{Ca}^{2+}$  luminescence ratios of maximum luminescence values. (D) Table of characterization parameters of the variants with double substitutions.

The variants showed a variety of different emission wavelength shifts to the shorter and longer wavelengths (Figure 50C). TS A123F S125D (light blue) had an emission wavelength shift of 21 nm towards longer wavelengths for  $\text{Ca}^{2+}$ , while the  $\text{Sm}^{3+}$ -triggered emission wavelength was not detectable due to the short luminescence half-life (70 s) and low luminescence value of 5000 a.u.

TS A123F S125E, triggered with  $\text{Ca}^{2+}$ , had a shorter emission wavelength (437 nm) compared to AQ TS (Figure 50C). The  $\text{Sm}^{3+}$ -triggered wavelength was shifted 9 nm towards longer wavelengths. TS A123W S125D wavelength triggered with  $\text{Ca}^{2+}$  was only slightly shifted from 459 to 465 nm and  $\text{Sm}^{3+}$  induced light emission shifted 6 nm towards shorter wavelength (444 nm). The variant TS A123W S125E showed the widest shift, when induced with  $\text{Ca}^{2+}$ , to 485 nm (26 nm) and an 8 nm shift towards longer wavelengths (458 nm) with  $\text{Sm}^{3+}$ . The typical luminescence curves are shown in Figure 50D.

All new variants induced with  $\text{Ca}^{2+}$  were brighter than AQ TS. The  $\text{Sm}^{3+}$ -triggered luminescence values were lower than the  $\text{Ca}^{2+}$ -triggered values of AQ TS, except for TS A123W S125D and TS A123W S125E that were higher than AQ TS  $\text{Ca}^{2+}$  luminescence. This is the first time that the  $\text{Sm}^{3+}$ -triggered luminescence of variants (TS A123F S125D  $11 \cdot 10^5$  a.u.; TS A123F S125E  $3.8 \cdot 10^5$  a.u.; TS A123W S125E  $17 \cdot 10^5$  a.u.) was higher compared to AQ TS  $\text{Ca}^{2+}$  luminescence (TS  $2.7 \cdot 10^5$  a.u.) as shown in Figure 50B and E.

The  $\text{EC}_{50}$  is a first important hint for the ion affinity as luminescence intensity correlates to ion concentration. Variant TS A123F S125D had a 7-times improved  $\text{EC}_{50}(\text{Ca}^{2+})$  value of only 7  $\mu\text{M}$  compared to the parental 50  $\mu\text{M}$ . The double variant TS A123F S125E appeared to be almost like parent according to the  $\text{EC}_{50}$  values (Figure 50E). The variants based on TS A123W were not as bright as those based on TS A123F but the  $\text{EC}_{50}$  values were reduced. TS A123W S125D had an almost 4-times reduced  $\text{EC}_{50}(\text{Ca}^{2+})$ . TS A123W S125E showed a reduced  $\text{EC}_{50}(\text{Ca}^{2+})$  by factor 20. This was the highest reduction obtained from all tested variants and a major step towards a new variant with improved  $\text{Sm}^{3+}$  affinity and less  $\text{Ca}^{2+}$  affinity as well as improved  $\text{Sm}^{3+}/\text{Ca}^{2+}$  luminescence ratio. The  $\text{EC}_{50}(\text{Sm}^{3+})$  observed for TS A123W S125E was in the same order of magnitude as AQ TS.

The variant TS A123W S125E showed the best improvement regarding  $\text{Sm}^{3+}/\text{Ca}^{2+}$  luminescence ratio and  $\text{EC}_{50}$  values. As the measured  $\text{EC}_{50}$  values only allow to estimate the affinity, more values that are precise should be measured. In order to obtain a  $K_d$  value for the promising variant TS A123W S125E isothermal titration calorimetry (ITC) was used. This method uses the enthalpy that can be measured during binding of two molecules to calculate the  $K_d$ , which is the reciprocal difference of the enthalpy ( $\Delta H$ ). The ions were titrated stepwise to the enzyme and the



enthalpy changes recorded. The  $K_d$  values were measured of AQ TS and TS A123W S125E with  $\text{Ca}^{2+}$  and  $\text{Sm}^{3+}$  of different protein production and purification charges. Figure 51 depicts an ITC curve for AQ TS and the variant TS A123W S125E titrated with  $\text{CaCl}_2$  (Figure 51 A and B) and  $\text{SmCl}_3$  (Figure 51 C and D). The curves showed differences between TS AQ and TS A123W S125E during titration with  $\text{CaCl}_2$  or  $\text{SmCl}_3$ . This can be explained by the differences of the binding of the enzymes to each metal ion and the differences between the enzymes themselves. The saturation phase was reached earlier for the titration of AQ TS with  $\text{CaCl}_2$  compared to TS A123W S125E with  $\text{CaCl}_2$  keeping in mind that AQ TS was titrated with 0.1 mM  $\text{CaCl}_2$  while TS A123W S125E was titrated with 0.5 mM  $\text{CaCl}_2$ . AQ TS was almost directly saturated, which can be seen by the lack of the first half of the sigmoidal curve. The molar ratio has to be extrapolated. The reaction with  $\text{CaCl}_2$  was exotherm for both enzymes, which can be seen by the negative  $\mu\text{cal}/\text{sec}$ . The molar ratio for the titration of TS A123W S125E with  $\text{CaCl}_2$  has the turning point around 1, which means that one  $\text{Ca}^{2+}$  bound to TS A123W S125E. Both enzymes titrated with  $\text{CaCl}_2$  had molar ratios around 1 according to the ITC measurements. This is in good agreement with the literature that only one  $\text{Ca}^{2+}$  is sufficient to induce the needed intramolecular rotation for the light emission (1.2.2 above) (Toma et al., 2005; Tricoire et al., 2006).

The titration with  $\text{SmCl}_3$  did not only show different curves, it also shows a different stoichiometry and a different type of binding. In contrast to  $\text{Ca}^{2+}$  binding  $\text{Sm}^{3+}$  binding is endothermal, which can be seen by the positive  $\mu\text{cal}/\text{sec}$  values. The molar ratio for both, AQ TS and TS A123W S125E, is 1:3. Here, three  $\text{Sm}^{3+}$  ions are needed for saturation.

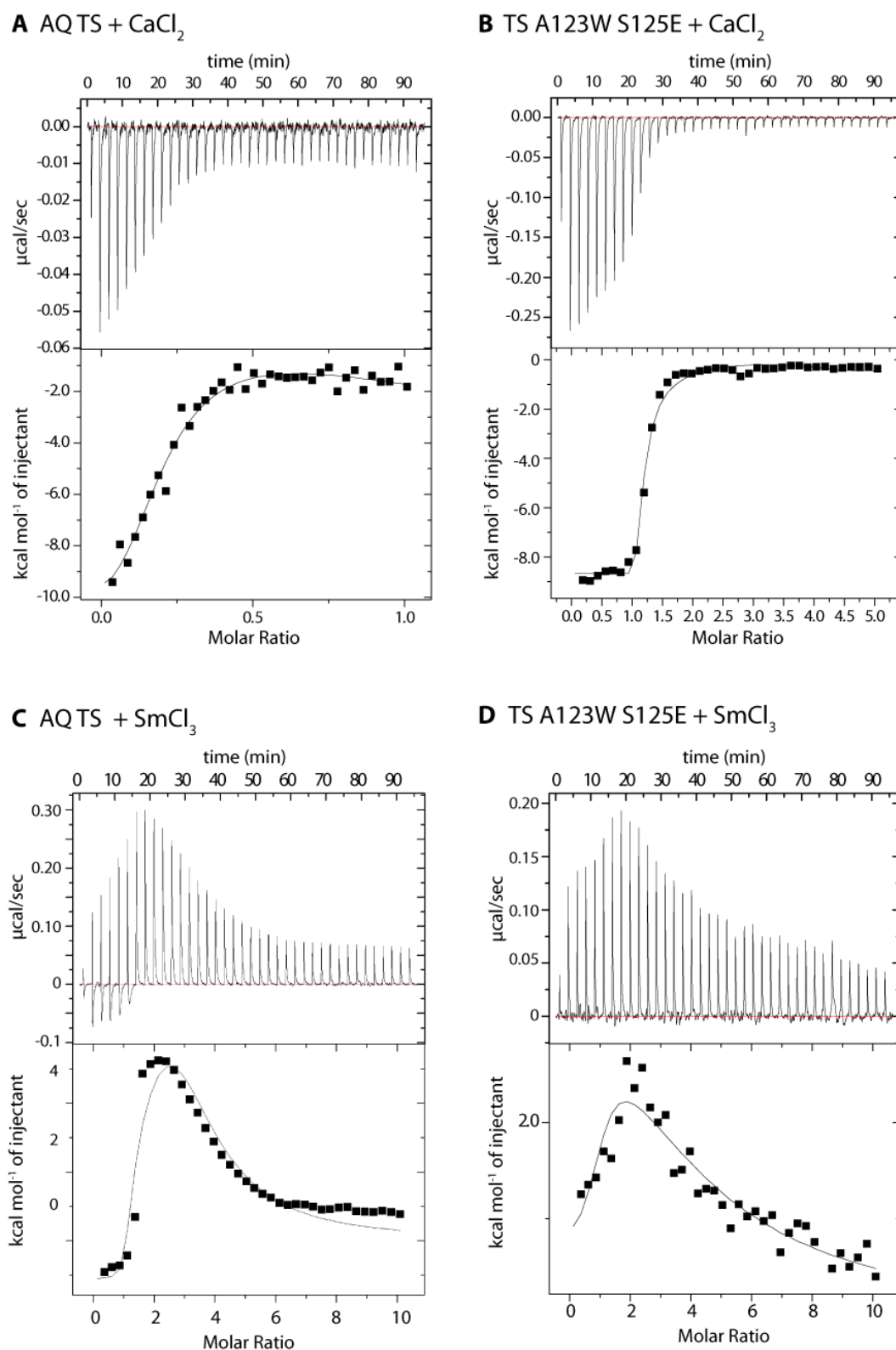


Figure 51: ITC measurements of AQ TS and TS A123W S125E with  $\text{CaCl}_2$  and  $\text{SmCl}_3$ .

(A) AQ TS (20  $\mu\text{M}$ ) titrated with 1  $\mu\text{L}$  steps of 0.1 mM  $\text{CaCl}_2$ . Enthalpies over time are shown in the upper panel. The lower panel shows the integrated areas of the peaks plotted against the molar ratio of ion to enzyme. The saturation phase is already achieved after 30 min. (B) TS A123W S125E (20  $\mu\text{M}$ ) with 1  $\mu\text{L}$  steps of 0.5 mM  $\text{CaCl}_2$  is depicted analogue to (A). The saturation phase for TS A123W S125E was achieved after 30 min of titration with the higher concentration (0.5 mM). (C) AQ TS titrated against  $\text{SmCl}_3$ . The enzyme solution had a concentration of 20  $\mu\text{M}$  while the titrant  $\text{SmCl}_3$  had a concentration of 0.1 mM. (D) Titration of TS A123W S125E (20  $\mu\text{M}$ ) with 0.1 mM  $\text{SmCl}_3$ .

The  $K_d$  values were calculated using Origin and the sequential binding model with 4 steps, one step for each EF-hand motif in AQ. The measurements could verify the improvements previously indicated by the  $EC_{50}$  values. TS A123W S125E had an approximately 30-fold reduced affinity to  $Ca^{2+}$  and a 40-times improved affinity for  $Sm^{3+}$  (Table 5). This verified the  $EC_{50}$  values and states TS A123W S125E as the first improved variant for improved  $Sm^{3+}$  affinity and  $Sm^{3+}$ -triggered luminescence.

**Table 5:  $K_d$  values calculated from ITC measurements of AQ TS and TS A123W S125E. Mean values were calculated of two independent measurements of two different protein purification charges.**

	$K_d/\mu M$	
	AQ TS	TS A123W S125E
$Ca^{2+}$	$0.1 \pm 0.05$	$2.8 \pm 1.1$
$Sm^{3+}$	$4.1 \pm 0.5$	$0.1 \pm 0.01$

#### 3.2.2.4 Detailed characterization of TS A123W S125E

Since luminescence is not only dependent on the ion binding but also of the type and binding of CTZ (1.2.2.2 above), CTZ analogues were tested. The most common eight CTZ analogues (cp, f, fcp, h, hcp, i, ip, and n) were used in this test for further improvements regarding  $Sm^{3+}$ -triggered luminescence intensity and stability (Figure 52).

Binding of CTZ is a parameter that is important for the brightness of the enzyme. Furthermore, exchange of native CTZ to an analogue can already shift the emission wavelength, or enhance the response time and half-life of the new apoaequorin. For cell culture experiments the analogue CTZ hcp is preferred because it shows a 190 times higher luminescence intensity and has faster response time compared to native CTZ (Shimomura et al., 1988, 1993; Shimomura, 1991).

The luminescence was tested of AQ TS A123W S125E with  $Ca^{2+}$  and  $Sm^{3+}$  ions and the eight CTZ analogues (Figure 45). The  $Sm^{3+}$ -triggered luminescence (blue curves) was in the same range or even higher (Figure 52E and F) than  $Ca^{2+}$ -triggered luminescence (black curves) for some combinations. Furthermore, the luminescence decay was slower, which is depicted by the slope.

The CTZ scan was also performed for AQ TS as the substitutions of TS A123W S125E can affect differences in CTZ binding (Figure 53). The use of different CTZ analogues addresses the binding affinity of aequorin to CTZ and the intramolecular conformational change upon ion binding.

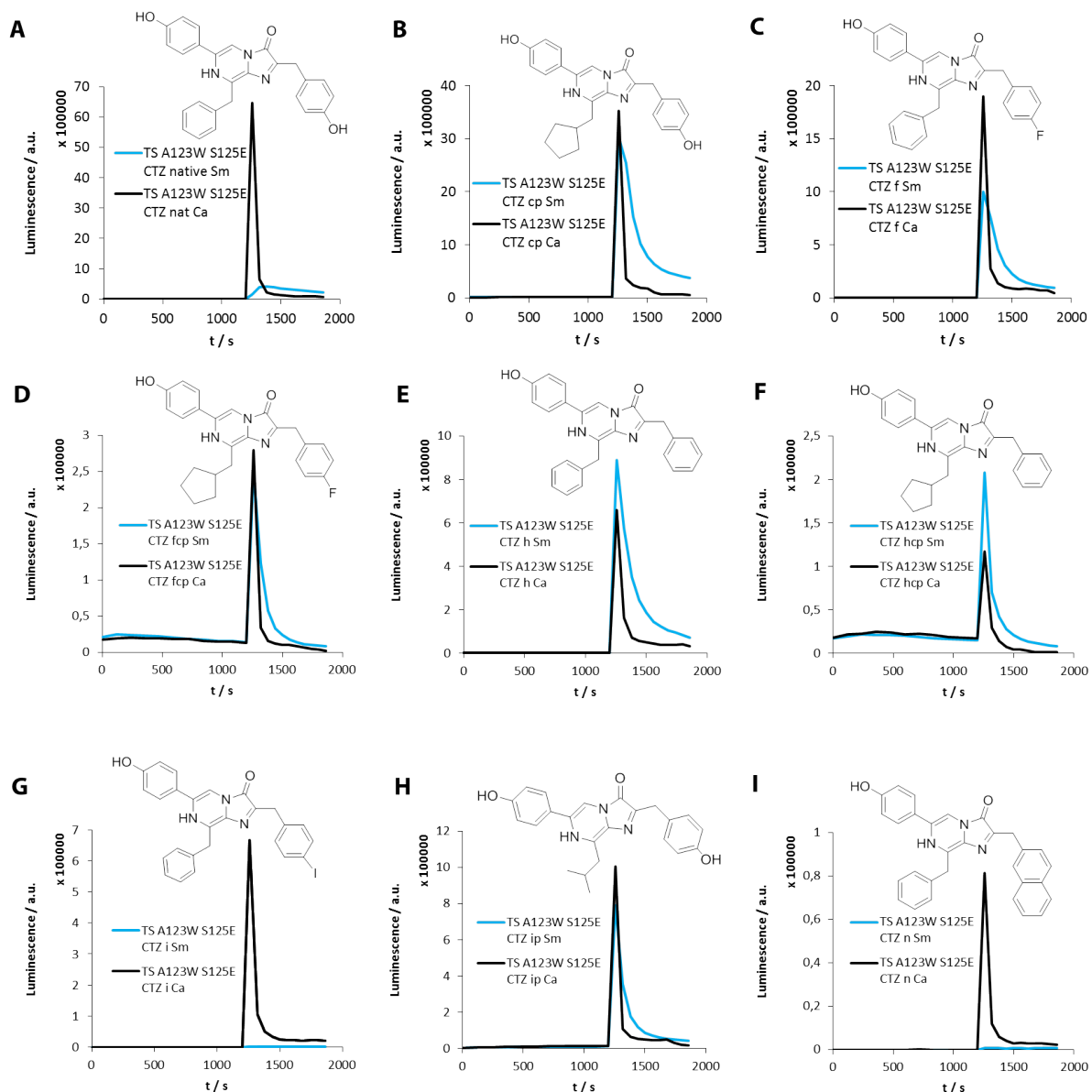


**Figure 52:** Luminescence curves of TS A123W S125E tested with 8 CTZ analogues in combination with  $\text{Sm}^{3+}$  and  $\text{Ca}^{2+}$ .

Luminescence triggered with  $\text{Sm}^{3+}$  is depicted in blue, while  $\text{Ca}^{2+}$  induced luminescence is black. Native CTZ was used in (A), apoenzymes were loaded with (B) CTZ cp, (C) CTZ f, (D) CTZ fcp, (E) CTZ h, (F) CTZ hcp, (G) CTZ i, (H) CTZ ip and (I) CTZ n. Maximum luminescence differs with the analogues.

The results of both CTZ scans with TS A123W S125E and AQ TS were calculated relative to the  $\text{Sm}^{3+}/\text{Ca}^{2+}$  luminescence ratio of AQ TS with native CTZ (Figure 53). The  $\text{Sm}^{3+}/\text{Ca}^{2+}$  luminescence ratios of AQ TS (black bars) were mostly below the values of TS A123W S125E (white bars) for all CTZ analogues. It was possible to enhance the ratio of AQ TS with CTZ cp, f, fcp, h, hcp, and ip compared to native CTZ. TS A123W S125E showed higher luminescence ratio with nearly all CTZ analogues, despite CTZ i and n. The best result could be obtained for TS A123W S125E with CTZ hcp, as expected. This combination had a 370-times higher luminescence ratio value compared to AQ TS native CTZ and 100-times higher compared to TS A123W S125E with native CTZ. The explanation can be found in the high total luminescence

triggered by  $\text{Sm}^{3+}$  (Figure 52). The tested variant TS A123W S125E belongs to the group of bright variants. The reconstitution with CTZ hcp could improve the  $\text{Sm}^{3+}/\text{Ca}^{2+}$  luminescence ratio even further.

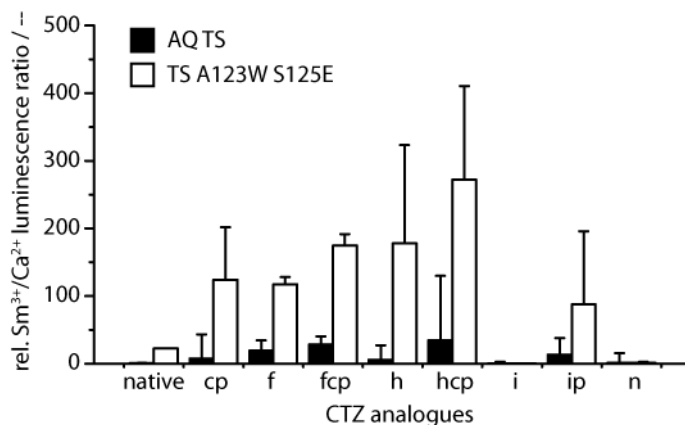


**Figure 53: Normalized  $\text{Sm}^{3+}/\text{Ca}^{2+}$  luminescence ratios of TS A123W S125E and CTZ analogues in relation to AQ TS with CTZ native.**

Data were obtained of two independent measurements in triplicates of AQ TS (black bars) and TS A123W S125E (white bars) in combination with CTZ native and the analogues cp, f, fcp, h, hcp, i, ip and n. The luminescence ratios of  $\text{Sm}^{3+}$ - and  $\text{Ca}^{2+}$ -triggered luminescence were calculated in relation to the ratio of AQ TS with native CTZ.

The positions 7 and 9 in EF-hand motif 2 are the position 123 and 125 in protein context. Both positions are not directly involved in CTZ binding, but they are within a 4 Å distance from the active site, which can contribute to binding via secondary van-der-Waals interactions. Especially the substitutions from A to W and S to E can have an impact on the CTZ binding because both residues occupy more room compared to the original ones (Figure 50A). The substituted amino acids stabilize  $\text{Sm}^{3+}$  in a different way compared to the parent AQ TS. Thus, structural changes of the enzyme could be possible as well.

To test the structural changes, CD measurements of both AQ TS and TS A123W S125E were performed. Due to the prominent  $\alpha$ -helical units in AQ, minima around 210 and 220 nm were expected.

It was possible to see differences between AQ TS and TS A123W S125E directly in CD spectroscopy (Figure 54). The curve for the new variant TS A123W S125E has lower minima at 210 and 220 nm (Figure 54B, green line) compared to AQ TS (Figure 54A, black line). This indicates that the structure might be slightly different compared to parent.

Upon ion binding the  $\alpha$ -helices move towards each other, which causes differences in AQ's shape. These can be detected in CD measurements. Data was recorded for both enzymes treated with  $\text{CaCl}_2$  and  $\text{SmCl}_3$  (Figure 54). AQ TS triggered with  $\text{Ca}^{2+}$  led to more prominent minima at

210 and 220 nm, indicating more stability of the  $\alpha$ -helices (Figure 54A, red curve). Binding of  $\text{Sm}^{3+}$  had no influences on the molar ellipticity (blue curve Figure 54A).

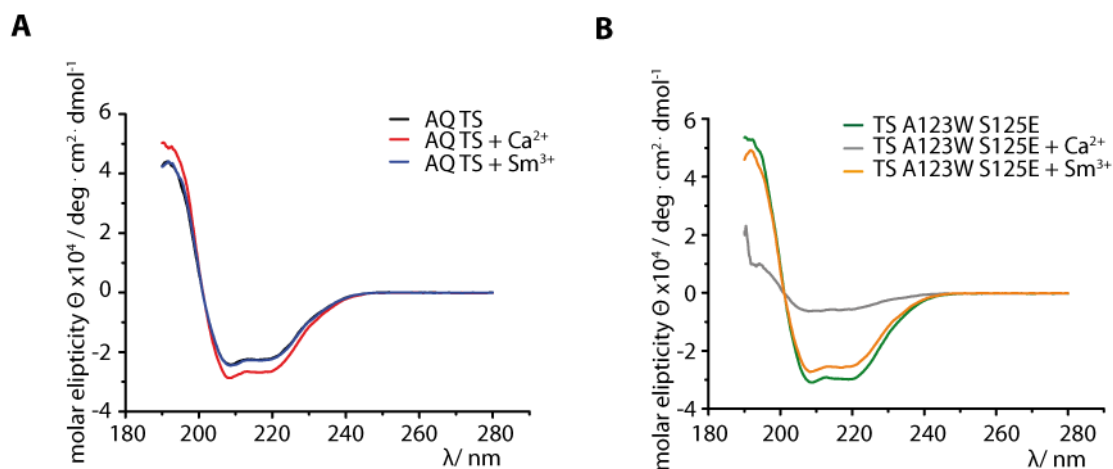


**Figure 54: Molar ellipticity measured by CD spectroscopy of AQ TS and TS A123W S125E.**

(A) Ellipticity of AQ TS (5  $\mu\text{M}$ ) was measured without ions (black), with  $\text{Ca}^{2+}$  (red) or  $\text{Sm}^{3+}$  (blue) starting from 280 to 190 nm. (B) Ellipticity of TS A123W S125E was measured alone (green), with  $\text{Ca}^{2+}$  (grey) and with  $\text{Sm}^{3+}$  (yellow) starting from 280 to 190 nm. Molar ellipticity was calculated and plotted against wavelength.

The molar ellipticity of TS A123W S125E showed similar minima as AQ TS (Figure 54B), which indicates that the globular folding is also comparable to AQ TS in terms of the  $\alpha$ -helices. The detected minima of TS A123W S125E alone (Figure 54B, green curve) and triggered with  $\text{Sm}^{3+}$  (Figure 54B, yellow curve) showed the expected minima at 210 and 220 nm, as well. The shift towards lower molar ellipticity triggered with  $\text{Sm}^{3+}$  indicates a stronger rotation of the  $\alpha$ -helices so that the characteristic minima are less prominent. The signals obtained of TS A123W S125E with  $\text{Ca}^{2+}$  (Figure 54B, grey) showed a significant change. Minima were also detected at 210 and 220 nm, but the absolute molar ellipticity values were higher compared to TS A123W S125E and TS A123W S125E  $\text{Sm}^{3+}$ . This indicates that the intramolecular rotation of the  $\alpha$ -helices, induced upon  $\text{Ca}^{2+}$  binding, destabilizes TS A123W S125E. This could be a reason for the detected less affinity for  $\text{Ca}^{2+}$  by ITC measurements. However, it clearly demonstrates that the rotation upon  $\text{Ca}^{2+}$  binding changes the structure of TS A123W S125E.

In summary, it was possible to improve the enhancement detected for the  $\text{Sm}^{3+}/\text{Ca}^{2+}$  luminescence ratio by reconstitution with CTZ analogs such as hcp, fcp, ip, and cp. All of these CTZ analogs had a cyclopentenyl group that can interact with AQ. The interaction seems to be beneficial and improves the luminescence.

Furthermore, it was possible to detect structural changes based on CD spectrometry of AQ TS compared to TS A123W S125E after  $\text{Ca}^{2+}$  binding. This structural change could be a reason for the loss of  $\text{Ca}^{2+}$  activity of TS A123W S125E.

### 3.2.2.5 EF-hand Motif 2 – Combination of Variants of Saturation Mutagenesis and Rational Design

The best variant of the rational design, TS A123W S125E, was combined with the known and verified low affinity variant D119A (position 3) and the best hit of the seven libraries tested in HTS - TS D127R, position 11 (3.2.1.2 above). The new variants TS D119A A123W S125E, TS A123W S125E D127R, and TS D119A A123W S125E D127R were cloned, purified, and tested for luminescence with  $\text{Ca}^{2+}$  and  $\text{Sm}^{3+}$ .

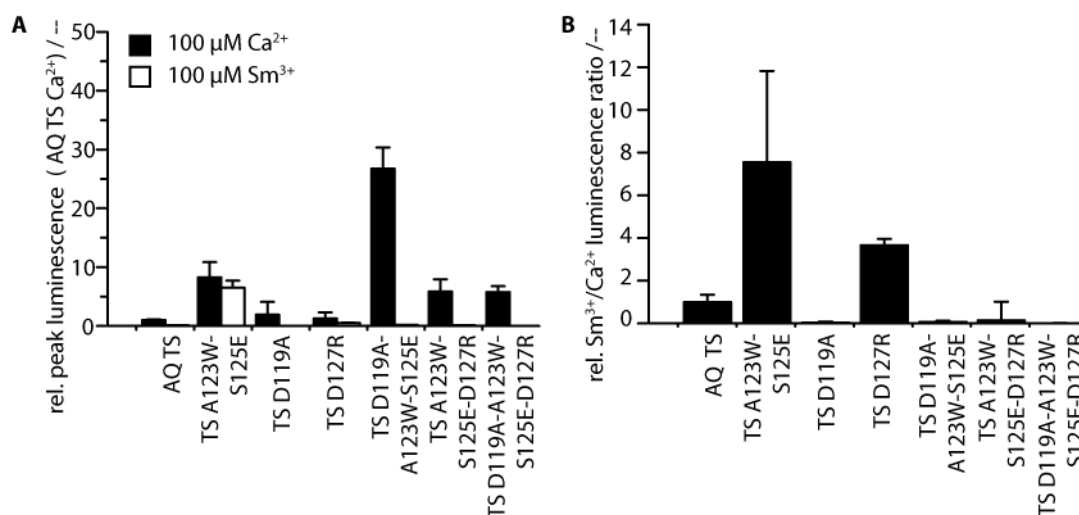


Figure 55: Characterization of AQ variants with combined substitutions of rational design and saturation mutagenesis.

(A) Relative peak luminescence calculated to AQ TS with  $\text{Ca}^{2+}$ .  $\text{Ca}^{2+}$  triggered luminescence is shown in black,  $\text{Sm}^{3+}$  triggered luminescence in white. For luminescence values 6 to 12 measurements of different protein purifications were measured to calculate mean values and standard deviations. Luminescence was collected between 380-470 nm. For luminescence 2.5  $\mu\text{M}$  enzyme were mixed with buffer containing 1 mM DTT and 5  $\mu\text{M}$  CTZ. The enzyme was allowed to reconstitute to apoaequorin for 20 min at room temperature and luminescence triggered with 100  $\mu\text{M}$   $\text{CaCl}_2$  or  $\text{SmCl}_3$ . Data points were collected in duplicates of two different protein purifications. Values are plotted as mean values with standard deviations. (B) Relative  $\text{Sm}^{3+}/\text{Ca}^{2+}$  luminescence ratios of variants created with rational design and combination with iterative saturation mutagenesis hits.

Although the improvements of substitutions to TS A123W S125E showed tremendous effects resulting in weaker  $\text{EC}_{50}(\text{Ca}^{2+})$  values, 40-fold improved  $K_d$  for  $\text{Sm}^{3+}$  and 8-fold higher  $\text{Sm}^{3+}/\text{Ca}^{2+}$  luminescence, introduction of low affinity substitution D119A led to loss of all of these improvements. The luminescence value triggered with  $\text{Ca}^{2+}$  was extremely high considering that D119A is known to be a low  $\text{Ca}^{2+}$  affinity variant (3.2). The combination of these substitutions had no beneficial effect to  $\text{Sm}^{3+}$  induced luminescence and the  $\text{Sm}^{3+}$  affinity measured by  $\text{EC}_{50}$ . Instead, the opposite effect was the case with an  $\text{EC}_{50}$  value for  $\text{Sm}^{3+}$  ions that was 4-times weaker than the parental one (504  $\mu\text{M}$  vs. 130  $\mu\text{M}$ ). Based on the detected differences of the  $\text{EC}_{50}$  values it seems that position three of the loop is even more important for  $\text{Sm}^{3+}$  binding than for  $\text{Ca}^{2+}$  binding. An substitution to alanine might change the coordination of the ion.



**Table 6: Characterization of TS D119A A123W S125E, TS A123W S125E D127R, and TS D119A A123W S125E D127R.**

Tested parameters are peak luminescence ( $L_{\max}$ ),  $\text{Sm}^{3+}/\text{Ca}^{2+}$  luminescence ratio ( $L_{\max}$  ratio  $\text{Sm}^{3+}/\text{Ca}^{2+}$ ), half-lives with each ion ( $t_{1/2}$ ), melting temperature ( $T_M$ ), emission wavelength ( $\lambda_{\text{em}}$ ), effective concentration 50 % ( $\text{EC}_{50}$ ) and yield in mg per L culture.

variant	AQ TS	TS A123W S125E	TS D119A A123W S125E	TS A123W S125E D127R	TS D119A A123W S125E D127R
$L_{\max}(\text{Ca}^{2+}) \times 10^5 / \text{a.u.}$	2.7	22	71	16	15
$L_{\max}(\text{Sm}^{3+}) \times 10^5 / \text{a.u.}$	0.3	17	0.5	0.6	0.03
$L_{\max}$ ratio $\text{Sm}^{3+}/\text{Ca}^{2+}$	0.1	0.8	0.0	0.0	0.0
$t_{1/2} \text{Ca}^{2+} / \text{s}$	30±3.5	42.3±1.3	24±0.8	19±1.3	38±2.4
$t_{1/2} \text{Sm}^{3+} / \text{s}$	96±5.5	257±7.0	plateau	296±34	plateau
$T_M / ^\circ\text{C}$	43.4±0.7	43.1±1.0	36.5±1.7	n.d.	n.d.
$\lambda_{\text{em}} \text{Ca}^{2+} / \text{nm}$	459	485	463	450	443
$\lambda_{\text{em}} \text{Sm}^{3+} / \text{nm}$	450	458	462	450	n.d.
$\text{EC}_{50} \text{Ca}^{2+} / \mu\text{M}$	53.3±7.0	1022±31	71.7±n.d.	25.4±0.1	62.5±0
$\text{EC}_{50} \text{Sm}^{3+} / \mu\text{M}$	130±1.9	148.3±0.0	504±n.d.	139.5±0	126.8±0
yield mg/ L culture	2.2	3.0	1.3	3.6	0.7

No cumulative effects of TS A123W S125E D127R regarding the  $\text{Sm}^{3+}/\text{Ca}^{2+}$  luminescence ratio were detectable (ratio 0.03) (Table 6).

The combination of both D119A and D127R with the best variant TS A123W S125E so far resulted in TS D119A A123W S125E D127R. This variant had also no enhanced  $\text{Sm}^{3+}/\text{Ca}^{2+}$  triggered luminescence (ratio 0.0) (Table 6). But the  $\text{EC}_{50}$  ( $\text{Sm}^{3+}$ ) value could be improved compared to TS D119A A123W S125E and was restored to the range of parent (127  $\mu\text{M}$  vs. 504  $\mu\text{M}$  for TS D119A A123W S125E). It seems that the substitution D127R is at least balancing the loss of coordination of  $\text{Sm}^{3+}$  that was observed for D119A.

Although the positions alone were promising, there were no cumulative effects detectable within the tested variants. All findings could be substantiated by  $\text{EC}_{50}$  values that were at least in the range of parental  $\text{EC}_{50}$  for  $\text{Ca}^{2+}$ . A reason could be that

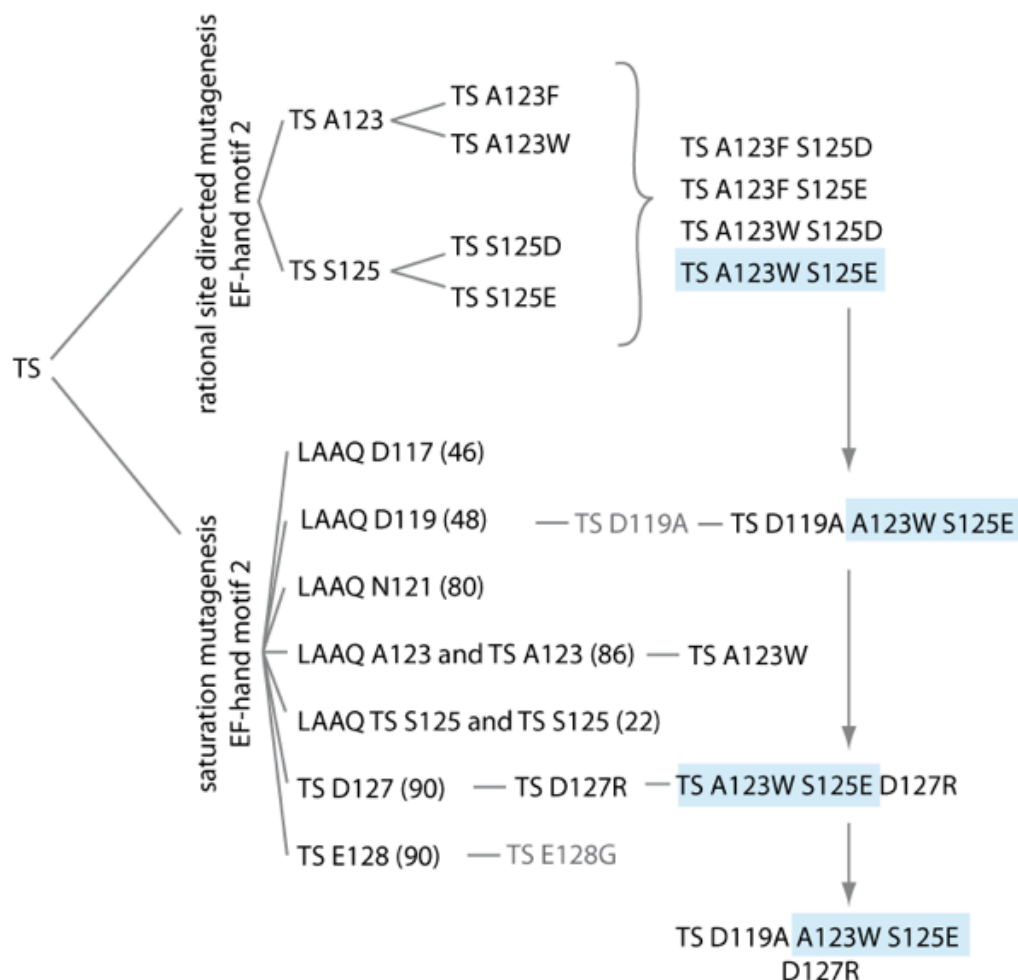


Figure 56: Schematic overview of the tested variants. The best substitutions (TS A123W S125E) in different variants are highlighted blue. Already known substitutions in literature are depicted in grey (D119A and E128G). The number of tested colonies is given in brackets.

### 3.2.2.6 Analogue Substitutions at Position 7 and 9 in EF-hand Motif 3

Based on the findings of the best substitutions at position 7 and 9 in EF-Hand motif 2 towards tryptophan and glutamic acid these substitutions were inserted to the next EF-hand motif 3. Tricoire *et al.* explained that the EF-hand motifs of AQ have different  $\text{Ca}^{2+}$  affinity. Ion binding occurs successively starting with EF-hand motif 2, followed by motif 3 and last motif 1 (Tricoire *et al.*, 2006).

Substitutions in EF-hand motif 3 also inherit slow luminescence decay and bright variants (Tsuzuki *et al.*, 2005). The thermostabilizing substitutions Q168R L170I are located directly after EF-hand motif 3 within a  $\alpha$ -helix that also contains the residues Met165, Thr166, His169, and Trp 173. These amino acids contribute in CTZ binding (1.2.2.2 above, Figure 13). This is the reason why it affects more likely the luminescence intensity instead of ion affinity (Tricoire *et al.*, 2006).

Based on TS A123W S125E the substitutions at position 7 and 9 were additionally introduced to EF-hand motif 3 resulting in the variant named TS A123W S125E Q159W D161E. Furthermore, a variant with substitutions in position 7 and 9 of EF-hand motif 3 only, TS Q159W D161E, was cloned. The enzymes were produced, purified, and tested for activity with  $\text{Sm}^{3+}$  and  $\text{Ca}^{2+}$ .

The new variant with substitutions only in EF-hand motif 3, TS Q159W D161E, showed low luminescence activity compared to AQ TS induced with  $\text{Ca}^{2+}$  or  $\text{Sm}^{3+}$  (Figure 57A and B). The combinatorial variant TS A123W S125E Q159W D161E triggered with  $\text{Ca}^{2+}$  (Figure 57A, black bars) had a 15-fold improved luminescence compared to AQ TS and TS A123W S125E. The  $\text{Sm}^{3+}$ -triggered luminescence was almost doubled (Figure 57A, white bars) calculated to AQ TS and 3-times lower compared to TS A123W S125E. Due to the high  $\text{Ca}^{2+}$ -triggered luminescence, the  $\text{Sm}^{3+}/\text{Ca}^{2+}$  luminescence ratio was not improved towards  $\text{Sm}^{3+}$  (Figure 57A, grey data points). TS Q159W D161E had a 2-fold higher  $\text{Sm}^{3+}/\text{Ca}^{2+}$  luminescence ratio, but the overall luminescence was lower (Figure 57B, inset).

The  $\text{EC}_{50}$  values are predictors for the ion affinity that correlate with the light intensity. However, the bright variant TS A123W S125E Q159W D161E had higher  $\text{EC}_{50}$  values for both ions (120  $\mu\text{M}$   $\text{Ca}^{2+}$  / 230  $\mu\text{M}$   $\text{Sm}^{3+}$ ) compared to AQ TS (50  $\mu\text{M}$ /130  $\mu\text{M}$ ) and AQ TS (1022  $\mu\text{M}$ /150  $\mu\text{M}$ ). Bright luminescence normally occurs of variants with high  $\text{Ca}^{2+}$  affinity. The substitutions only in EF-hand motif 3 resulted in a low luminescence variant with lower  $\text{EC}_{50}$  values. Both results are contradictive to the theory and are discussed in details in chapter 4.2 below. There is a lot known about the affinity of AQ's EF-hand motifs but it is still not answered yet how many EF-hand motifs need to be occupied for luminescence.

Substitution of EF-hand motif 3 alone and in combination with EF-hand motif 2 had no further improvements regarding the  $\text{Sm}^{3+}/\text{Ca}^{2+}$  luminescence ratio or a more significant change in  $\text{EC}_{50}$  values.

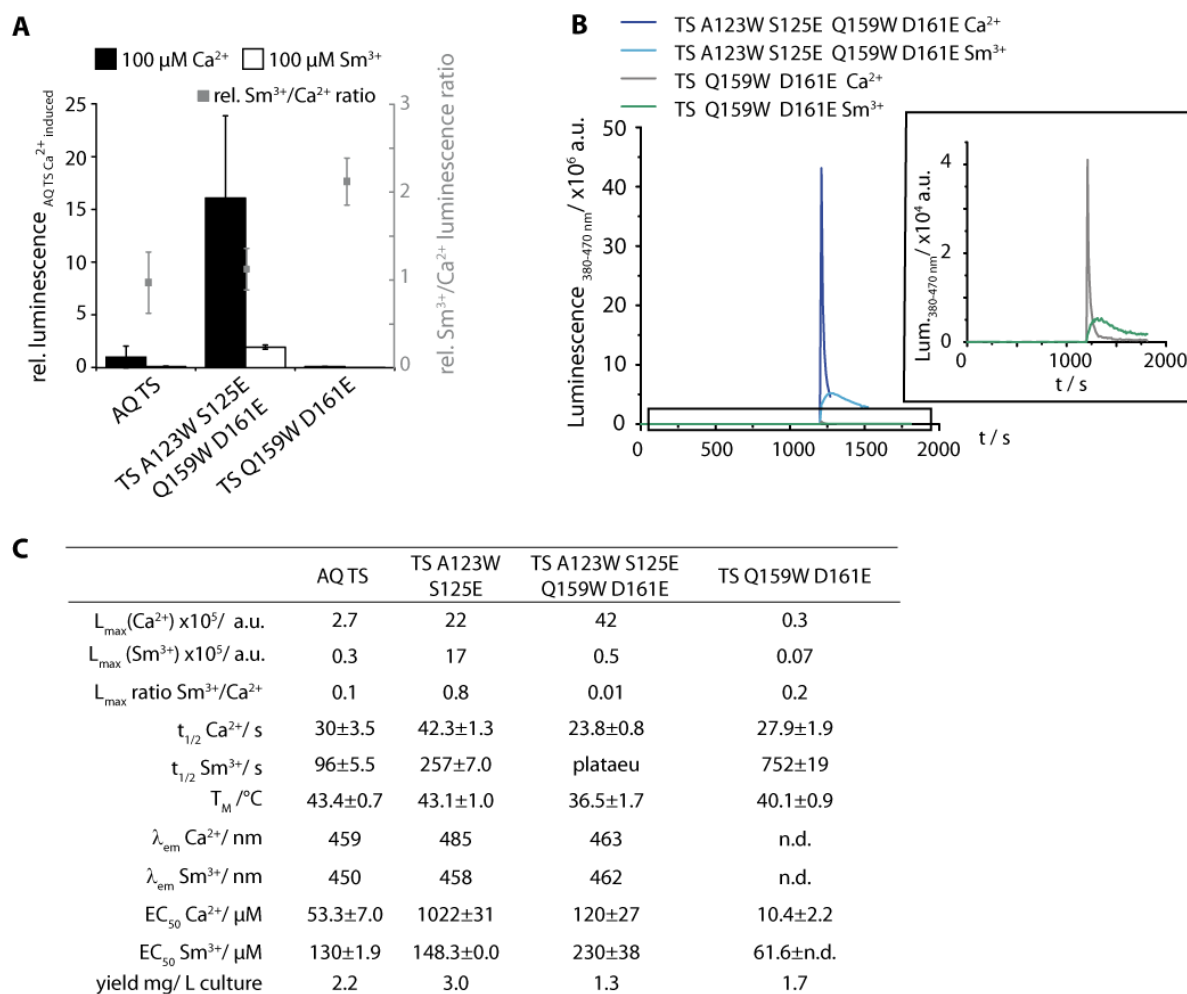


Figure 57: Characterization of AQ variants with substitutions at position 7 and 9 in EF-hand motif 3 and in combination with EF-hand motif 2.

(A) Relative peak luminescence calculated to AQ TS with  $\text{Ca}^{2+}$ .  $\text{Ca}^{2+}$  triggered luminescence is shown in black,  $\text{Sm}^{3+}$  triggered luminescence in white. For luminescence, values 6 to 12 measurements of different protein purifications were measured to calculate mean values and standard deviations. Luminescence was collected between 380-470 nm. For luminescence  $2.5 \mu\text{M}$  enzyme were mixed with buffer containing 1 mM DTT and 5  $\mu\text{M}$  CTZ. The enzyme was allowed to reconstitute to apoaequorin for 20 min at room temperature and luminescence triggered with 100  $\mu\text{M}$   $\text{CaCl}_2$  or  $\text{SmCl}_3$ . Data points were collected in duplicates of two different protein purifications. Values are plotted as mean values with standard deviations. Relative  $\text{Sm}^{3+}/\text{Ca}^{2+}$  luminescence ratios were calculated and plotted as grey data points. (B) Luminescence curves of TS A123W S125E Q159W D161E with  $\text{Ca}^{2+}$  (dark blue) and  $\text{Sm}^{3+}$  (light blue) and TS Q159W D161E with  $\text{Ca}^{2+}$  (grey) and  $\text{Sm}^{3+}$  (green). The inset shows a magnified plot of TS Q159W D161E luminescence. (C) Table of characterization parameters for both variants compared to AQ TS.

### 3.2.2.7 Analogue Substitutions at Position 7 and 9 in EF-hand Motif 1

The third active EF-hand motif to substitute for enhanced  $\text{Sm}^{3+}/\text{Ca}^{2+}$  luminescence ratio and  $\text{Sm}^{3+}$  affinity was EF hand motif 1. This EF-hand has the lowest  $\text{Ca}^{2+}$  affinity and is reported to be the last occupied one (Tricoire et al., 2006). This EF-hand motif is at the N-terminal side of the enzyme and is located near to coelenterazine just as EF-hand motif 3 (1.2.2.2 above, Figure 13). The catalytic triad is in the neighboring beta sheets. Substitutions in this EF-hand motif can induce massive changes in the protein's luminescence character, although it is known to be the EF-hand motif in aequorin with the lowest activity (Tsuizuki et al., 2005; Tricoire et al., 2006).

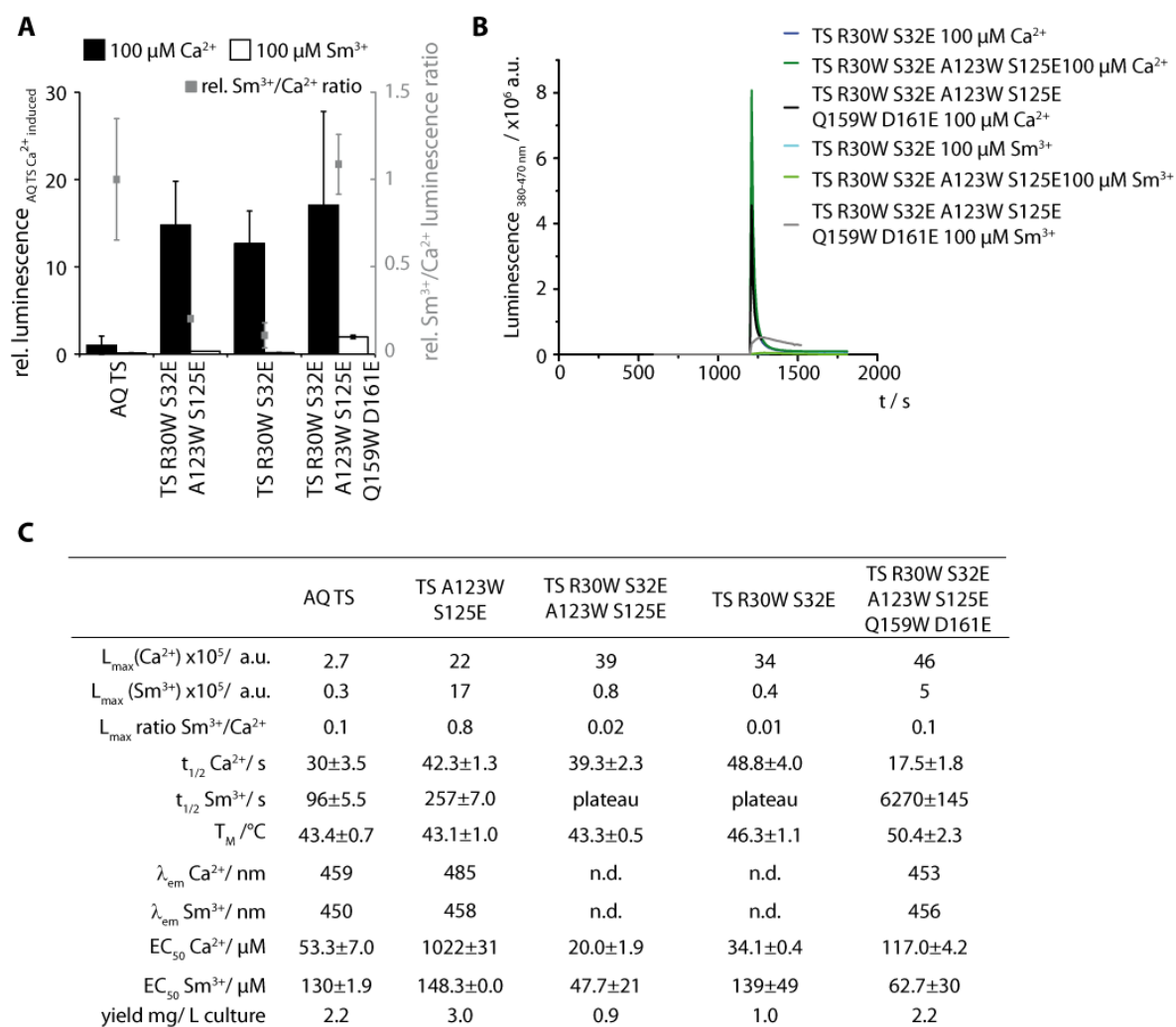


Figure 58: Characterization of EF-hand motif 1 variants.

(A) Relative peak luminescence calculated to AQ TS with  $\text{Ca}^{2+}$ .  $\text{Ca}^{2+}$  triggered luminescence is shown in black,  $\text{Sm}^{3+}$  triggered luminescence in white. For luminescence values 6 to 12 measurements of different protein purifications were measured to calculate mean values and standard deviations. Luminescence was measured between 380-470 nm. For luminescence 2.5  $\mu\text{M}$  enzyme were mixed with buffer containing 1 mM DTT and 5  $\mu\text{M}$  CTZ. The enzyme was allowed to reconstitute to apoaequorin for 20 min at room temperature and luminescence triggered with 100  $\mu\text{M}$   $\text{CaCl}_2$  or  $\text{SmCl}_3$ . Data points were collected in duplicates of two different protein purifications. Values are plotted as mean values with standard deviations. Relative  $\text{Sm}^{3+}/\text{Ca}^{2+}$  luminescence ratios were calculated and plotted as grey data points. (B) Luminescence curves of TS R30W S32E (dark blue), TS R30W S125E A123W S125E (dark green), and TS R30W S32E A123W S125E Q159W D161E with  $\text{Ca}^{2+}$  (black) and  $\text{Sm}^{3+}$  (light blue) and TS Q159W D161E with  $\text{Ca}^{2+}$  (light green) and  $\text{Sm}^{3+}$  (grey). (C) Table of characterization parameters for both variants compared to AQ TS.

Consecutively the positions 7 and 9 of EF-hand motif 1 were substituted (R30W, S32E). Next to the single EF-hand substitution, the combinatorial variants with EF-hand motif 2 and 3 were also produced. After purification, the variants TS R30W S32E, TS R30W S32E A123W S125E, and TS R30W S32E A123W S125E Q159W D161E were tested upon their luminescence behavior.

All of the new variants had higher luminescence values when triggered with  $\text{Ca}^{2+}$  compared to parent AQ TS. Luminescence with  $\text{Sm}^{3+}$  was low and thus the  $\text{Sm}^{3+}/\text{Ca}^{2+}$  luminescence ratios not improved (Figure 58A).

Remarkably, the luminescence duration of the variants TS R30W S32E and TS R30W S32E A123W S125E Q159W D161E triggered with  $\text{Sm}^{3+}$  showed a plateau. This states that although the luminescence is not bright, it is at least stable for a long period. The luminescence half-life was even longer compared to the best variant TS A123W S125E (257 s). Stability of the signal is also important for a microscopy probe in order to find the area of interest. Due to the long-lasting low luminescence induced with  $\text{Sm}^{3+}$  and the higher luminescence triggered with  $\text{Ca}^{2+}$ , the  $\text{Sm}^{3+}/\text{Ca}^{2+}$  luminescence ratio was not improved compared to AQ TS (Figure 58A).

The  $\text{EC}_{50}$  values for TS R30W S32E and the variant with substitutions in all three EF-hand motifs TS R30W S32E A123W S125E Q159W D161E were twice as good for  $\text{Sm}^{3+}$  and two times lower for  $\text{Ca}^{2+}$  (Figure 58C). Although this is beneficial, it is not comparable to the 20-time decreased  $\text{EC}_{50}$  value for TS A123W S125E and  $\text{Ca}^{2+}$  (3.2.2.3 above).

The substitutions at position 7 and 9 to tryptophane and glutamic acid in EF-hand motif 1 alone or in combination with EF-hand motif 2 or in all three EF-hand motifs did not result in a further improved variant in terms of  $\text{Sm}^{3+}$  affinity and  $\text{Sm}^{3+}/\text{Ca}^{2+}$  luminescence ratio. Thus, all of the variants with substitution in EF-hand motif 1 at position 7 and 9 had long  $\text{Sm}^{3+}$ -triggered luminescence half-lives or a plateau luminescence, respectively.

Based on the changes of the  $\text{EC}_{50}$  values, luminescence enhancement with CTZ analogues were tested for the best variant (luminescence ratio 0.1) out of this set, TS R30W S32E A123W S125E Q159W D161E. The results are plotted in Figure 59.

The best  $\text{Sm}^{3+}/\text{Ca}^{2+}$  luminescence ratios were obtained of the semi-synthetic aequorin variants (1.2.2 above) reconstituted with CTZ analogs fcp, hcp, and ip. The ratio was 17-times higher with hcp and ip compared to native CTZ and parent AQ TS.

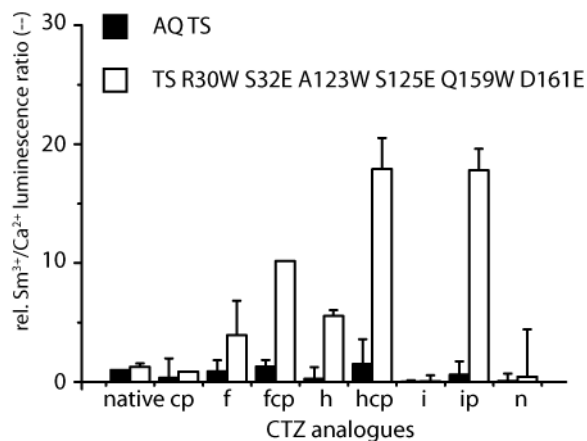


Figure 59: Variants including substitutions at position 7 and 9 in EF-hand motif 1, 2 and 3 and CTZ analogues.

AQ TS is shown in black bars, TS R30W S32E A123W S125E Q159W D161E in white bars. Data was obtained of two independent purifications in duplicates. Luminescence values were calculated as ratios and mean values and standard deviation. The plotted data are shown as relative values based on the ratio of AQ TS with native CTZ.

Still the highest luminescence ratio was measured with TS A123W S125E and CTZ hcp with 375-times improved luminescence compared to parent AQ TS with native CTZ and 20-times higher luminescence compared to AQ TS with CTZ hcp (3.2.2.3 above).

Overall, the new variants TS R30W S32E and TS R30W S32E A123W S125E Q159W D161E could show stabilized  $\text{Sm}^{3+}$  luminescence and slightly increased  $\text{EC}_{50}$  values, but they were not comparable to the improvements of TS A123W S125E.

### 3.2.3 Aequorin in TEM

The best variant found after systematical testing of library approaches and rationally design was TS A123W S125E. It had 40-times higher  $\text{Sm}^{3+}$  affinity and 30-times lower  $\text{Ca}^{2+}$  affinity compared to AQ TS. Furthermore, the  $\text{Sm}^{3+}/\text{Ca}^{2+}$  luminescence ratio could be improved by factor 8, while the variant had higher overall luminescence compared to AQ TS. The luminescence ability with  $\text{Sm}^{3+}$  was mentioned above. To create the contrast in EM,  $\text{Sm}^{3+}$  is the important parameter for the probe. Samarium is a heavy metal with 150 u and should be able to give contrast to a sample consisting of light biological material.

The contrasting ability aequorin should be tested using conventional TEM measurements without liquid. Aequorin was immobilized onto gold nanoparticles using the N-terminal His<sub>6</sub>-tag. The gold nanoparticles with a diameter of 14 nm were previously coupled with an anti-His<sub>6</sub> antibody that provided the binding ability for the proteins and incubated with the protein and  $\text{SmCl}_3$ , or  $\text{CaCl}_2$ , respectively. His-tagged pumilio proteins, not able to bind  $\text{Sm}^{3+}$ , were immobilized via the His-tag as negative controls. The solutions were incubated for 4 h at room temperature. In order to check the functionality of the immobilized aequorin a luminescence activity assay was performed using the AQ-AuNPs mix (Figure 60).

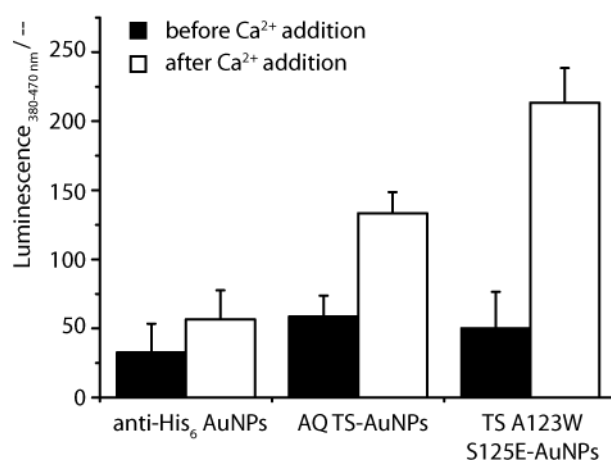


**Figure 60: Luminescence assay of immobilized AQ enzymes on anti-His<sub>6</sub> AuNPs.** Samples of anti-His<sub>6</sub> AuNPs, AQ TS-AuNPs, and TS A123W S125E-AuNPs are shown before (black bars) and after (white bars)  $\text{Ca}^{2+}$  addition during light emission.

The immobilized AQ TS and TS A123W S125E were still active, although it is known that AuNPs can quench luminescence and fluorescence. Considering the low concentration of the AuNPs after hybridization (10 nM) and quenching due to the AuNPs the obtained luminescence intensity of the immobilized enzymes is in agreement with the luminescence of purified enzymes (concentration of enzyme immobilized to purified approximately 1:25).

These samples were examined using conventional TEM. TS A123W S125E-AuNP had additional contrast close to the AuNP core (Figure 61A). TS A123W S125E-AuNP without addition of



$\text{SmCl}_3$  and  $\text{CaCl}_2$  salts did not raise any contrast around the AuNPs in TEM mode (Figure 61B). The sample of TS A123W S125E and  $\text{CaCl}_2$  (Figure 61C) had also no additional contrast. The control with immobilized non-  $\text{Sm}^{3+}$  binding Pumilio protein showed no contrast in TEM (Figure 61D).

Only incubation of the TS A123W S125E-AuNPs with  $\text{SmCl}_3$  led to the additional contrast in the area around the AuNP cores in TEM mode (dark grey area) as seen in Figure 61A. This area was localized only around the AuNP cores and not delocalized over the whole grid. It seemed that during the sample preparation for the conventional TEM imaging TS A123W S125E dried as a protein accumulation. It is known that AQ forms dimers (1.2.2 above) (Prendergast and Mann, 1978) due to the thiol groups so bigger multimers as they might be in Figure 61A can be explained.

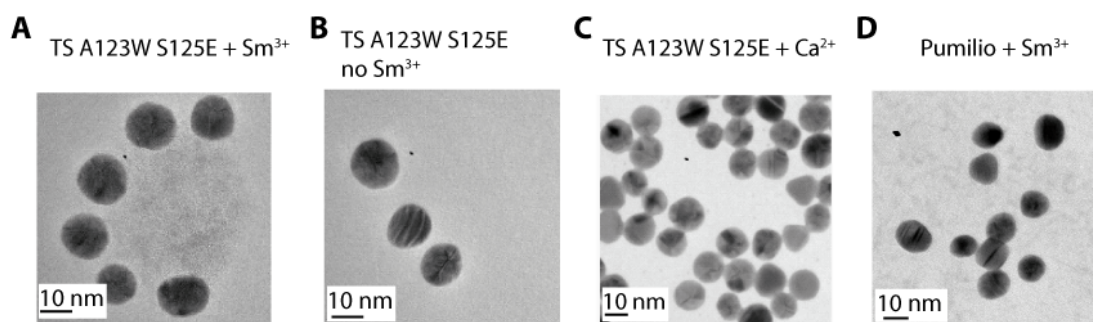


**Figure 61:** TEM images of aequorin immobilized on 14 nm anti-His<sub>6</sub> AuNPs. TEM images were taken of (A-C) TS A123W S125E AuNPs (A) with  $\text{Sm}^{3+}$ , (B) without  $\text{Sm}^{3+}$ , (C) with  $\text{Ca}^{2+}$  instead of  $\text{Sm}^{3+}$ , and (D) control Pumilio AuNPs.

To analyze the origin of the additional found contrast, Energy-dispersive X-ray spectroscopy (EDX) scans of these dark appearing areas were performed giving information on the elemental composition (Figure 62). These EDX scans showed that the darker appearing area is in good overlay with the Sm signals in this area, leading to the assumption that the signals derived of bound  $\text{Sm}^{3+}$ . Although the luminescence assay of immobilized TS A123W S125E on AuNPs showed that the enzyme is still functional (Figure 60), the overlay of the contrasted areas and the EDX Sm signal allowed the assumption of binding but did not prove that the Sm is bound to the protein. Due to the presence of several methionines and cysteines in AQ, EDX was also used to verify AQ's sulphur. The sulphur signal was very low compared to Sm, but the areas containing sulphur were in good overlay with the Sm areas.

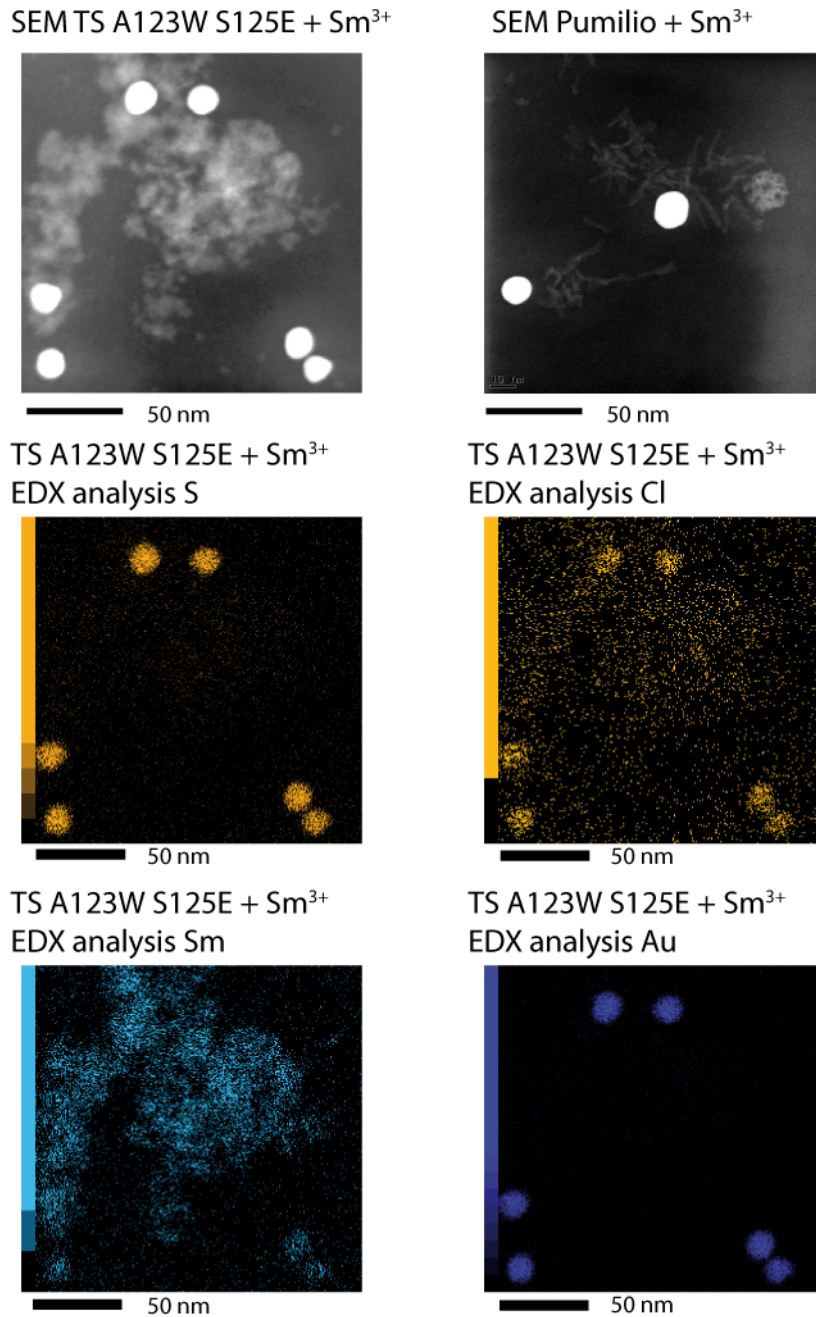


**Figure 62:** EDX analysis of TS A123W S125E (left) and Pumilio (right) immobilized on anti-His<sub>6</sub> AuNPs after incubation with SmCl<sub>3</sub>.

The sample was imaged using SEM (upper left panel) and scanned for the elements S, Cl, Sm and Au. Sulphur was scanned to visualize the protein distribution in the sample due to the cysteine and methionine residues. Chloride ions were used as counter ions and analyzed as well. Furthermore, Samarium was analyzed showing bright signals around the AuNPs (dark blue Au scan) and between the AuNPs. There is also a strong overlap of the area containing Sulphur and Samarium.

The results of TEM and EDX indicate that TS A123W S125E is a good candidate towards a probe for electron microscopy as it raises contrast due to the Sm<sup>3+</sup> binding.

### 3.2.4 Intracellular Application of TS A123W S125E in Mammalian Cell Culture

The final goal for AQ as a bimodal probe is the application in cell culture or even *in vivo* to track dynamics using the combination of fluorescence light and electron microscopy. The best variant found was TS A123W S125E with improved  $\text{Sm}^{3+}$  affinity and luminescence ratio (3.2.2.3 above) as well as contrasting ability in EM (3.2.3 above).

The next step was thus the production of TS A123W S125E in mammalian cells and triggered luminescence with  $\text{Sm}^{3+}$ .

First, the  $\text{Sm}^{3+}$  internalization ability of PC3 and LNCaP cells was tested. Samarium chloride ( $\text{SmCl}_3$ , final concentration 600 nM) was added to the cell culture media and after incubation for 0-90 min. The cells were prepared for element analysis using graphite furnace atomic absorption spectrometry (GF-AAS). Analysis of the samples showed internalization ability of  $\text{Sm}^{3+}$  in both cell lines (Figure 63). The maximal concentration of internalized  $\text{Sm}^{3+}$  was around 73 nM per cell. This is only a fraction of the average  $\text{Ca}^{2+}$  concentration of a cell, which can range from a few nanomolar to millimolar depending on the cell activity. An average concentration of ionized  $\text{Ca}^{2+}$  in the cytoplasm of mammalian cells is less than 0.2  $\mu\text{M}$  (Lodish et al., 2000). However, the experiments showed that  $\text{Sm}^{3+}$  was successfully internalized into both LNCaP and PC3 cells. The detected concentration per cell after 60 min incubation was 73 nM.

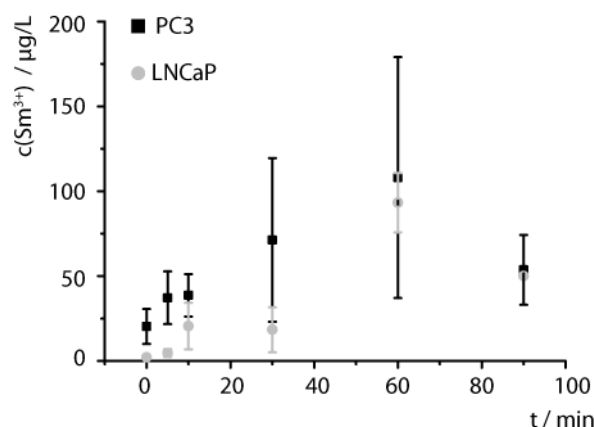


**Figure 63: Internalization of  $\text{Sm}^{3+}$  into PC3 and LNCaP cells analyzed via GF-AAS.**

The uptake of  $\text{SmCl}_3$  into PC3 cells (black rectangle) and LNCaP cells (grey dots) was analyzed after 5, 10, 30, 60, and 90 min after addition to the supernatant. The cells were washed before harvesting, counted, and  $10^5$  cells in 100  $\mu\text{L}$  analyzed via GF-AAS. Mean values and standard deviations of 6 independent measurements are plotted against time.

After successful internalization of  $\text{Sm}^{3+}$  by the cells, the next step was production of TS A123W S125E in PC3 or LNCaP cells. To achieve this, the cDNA for TS A123W S125E was cloned into the viral vaccine vector VR1012::AQ that was a kind gift of the Rizzuto lab (Padua, Italy). VR1012 inherits the sequence of the CMV promoter that is necessary for mammalian AQ

production. The previously used vector pRSET contains only a T7 promoter that is for bacterial expression only. The original vector VR1012::AQ carried the gene for wild type AQ. An N-terminal hemagglutinin (HA)-tag, which directs the protein into the cytoplasm, is attached to the AQ gene.

After successful cloning, PC3 cells and LNCaP cells should be transfected with the vector containing the gene for AQ wt as control and the new variant TS A123W S125E. Fugene HD™ and Lipofectamin 3000® were tested for transfection. Optimization had to be performed. The best results were obtained using PC3 cells transfected with Fugene HD™ (9.4.3 below). The cells were harvested 24 h after transfection. The protein production was analyzed via immunoblot (Figure 64).

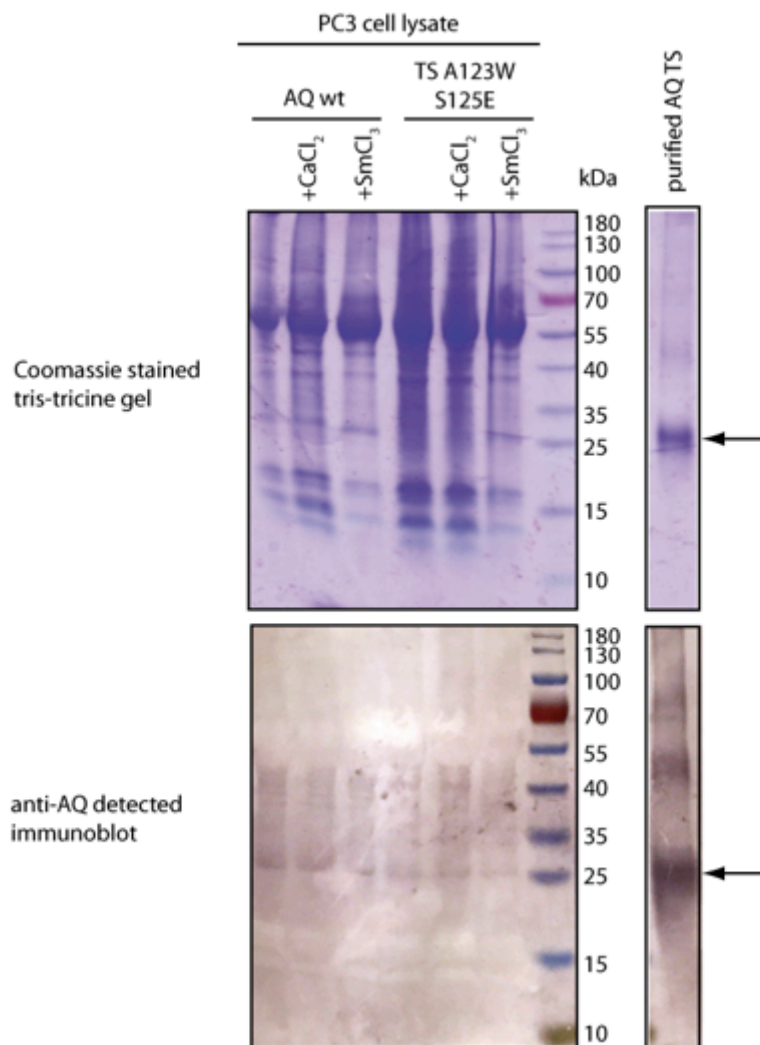


Figure 64: Analysis of AQ production in PC3 cell lysate after transfection.

10 % denat. tris tricine gel and immunoblot detected with anti-AQ IgG mouse. First three lanes show cell lysates of AQ wt transfected cells without any addition of salts (mock), followed by cell lysate of cells treated with CaCl<sub>2</sub> and SmCl<sub>3</sub>. Next three lanes show analog samples of cells transfected with VR1012::TS A123W S125E. Behind the marker lane purified AQ TS is shown for comparison. The upper panel shows the coomassie stained protein gel, while the lower panel shows the immunoblot detected with anti-AQ antibody.

It was possible to detect a signal at the same height (25 kDa) as purified AQ TS in the lanes containing AQ wt and TS A123W S125E in the coomassie stained gel and in the immunoblot detected with anti-AQ.

Next, the luminescence ability of the TS A123W S125E in PC3 cells was tested. The cells were fed after 6 h of transfection 30 mg/mL  $\text{Sm}^{3+}$  or  $\text{Ca}^{2+}$  by addition of  $\text{SmCl}_3$ ,  $\text{CaCl}_2$  to the media. The incubation with either  $\text{Sm}^{3+}$  or  $\text{Ca}^{2+}$  was ended 24 h after salt addition by washing the cells with PBS to remove free salt and kept in media afterwards.

Next, the luminescence of the transfected and fed cells was measured of 10,000 cells per well in triplicates. The results of the previously performed CTZ scan showed that the highest signals were obtained of any AQ variant reconstituted to semi-synthetic AQ with CTZ hcp (Figure 52). Either CTZ hcp or CTZ was added in a concentration of 50  $\mu\text{M}$  directly to the media and the cells incubated for 1 h in the dark at room temperature for reconstitution. CTZ and the analogues are cell membrane permeable and diffuse into the cell. Luminescence was measured over a period of 10 h. Maximum luminescence could be obtained directly in the beginning (Figure 65). Luminescence was higher for all samples treated with CTZ and  $\text{Ca}^{2+}$ . This can be explained by the additional intracellular  $\text{Ca}^{2+}$  concentration. The CTZ analogue hcp (black bars) showed higher luminescence compared to CTZ (white bars), which is reported in the literature (Shimomura et al., 1990, 1993; Shimomura, 1991) and was detected for purified enzymes as well (3.2.2.4). Although the luminescence was measured of mammalian cells instead of purified enzymes, there was still luminescence detectable.

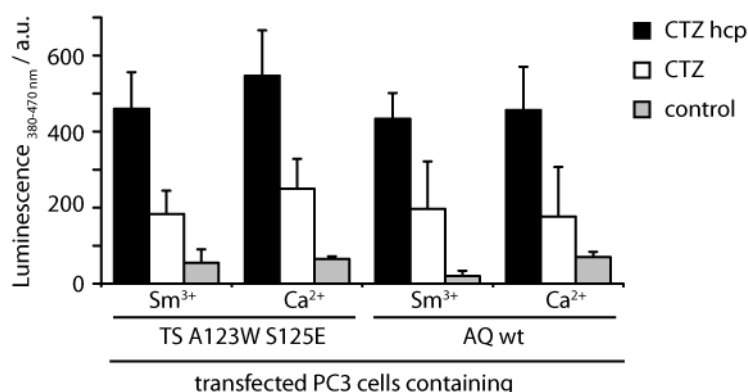


Figure 65: Luminescence assay of transfected PC3 cells with AQ wt and TS A123W S125E after 24 h transfection.

Luminescence of PC3 cells transfected with TS A123W S125E or AQ wt, grown with 30 mg/L  $\text{SmCl}_3$  or  $\text{CaCl}_2$ , respectively. For luminescence assays 10,000 cells were used per well in a 96 multi-well plate. Apoenzymes was constituted in cells with hcp (black bars), native CTZ (white) or not reconstituted (grey). Every sample was measured in triplicates. The cells were directly mixed with either CTZ or CTZ hcp and incubated for 1 hour in the dark at RT. Luminescence was detected using a multiplate reader.

The luminescence intensity was lower compared to the one of purified enzyme, and bacteria cell lysate, but significant as depicted in Figure 65. Transfected cells without CTZ or CTZ hcp addition were tested as control and for autoluminescence of the cells (grey bars). There was only weak background luminescence detected for cells containing TS A123W S125E and AQ wt, respectively.

In total, it was possible to introduce the new improved variant TS A123W S125E into mammalian prostate cancer cells PC3. The concentration of  $\text{Sm}^{3+}$  after 60 min incubation on the cells was determined via GF-AAS elemental analysis to a value of 73 nM/cell.

Intracellular protein production was verified via immunoblot of PC3 cells after 24 hours. It was further possible to detect luminescence of transfected cells with CTZ hcp and CTZ with either  $\text{Sm}^{3+}$  or  $\text{Ca}^{2+}$ . The semi-synthetic AQ enzymes reconstituted with hcp had a higher luminescence value, which is in line with the experiments of purified enzymes (shown in chapter 3.2.2.4 above). However, cells treated with  $\text{Ca}^{2+}$  had higher luminescence values, which can be assigned to the intracellular  $\text{Ca}^{2+}$  concentration. The results are discussed later.

### 3.3 Combination of In-liquid TEM and Aequorin as a TEM Probe

It was desired to merge strategy 1 and 2 of this thesis with the best variant TS A123W S125E as probe for in-liquid TEM in cells.

A first attempt was performed after the positive imaging results of unstained fixed and non-fixed cells using in-liquid TEM and the good contrasting results of TS A123W S125E in conventional TEM analysis.

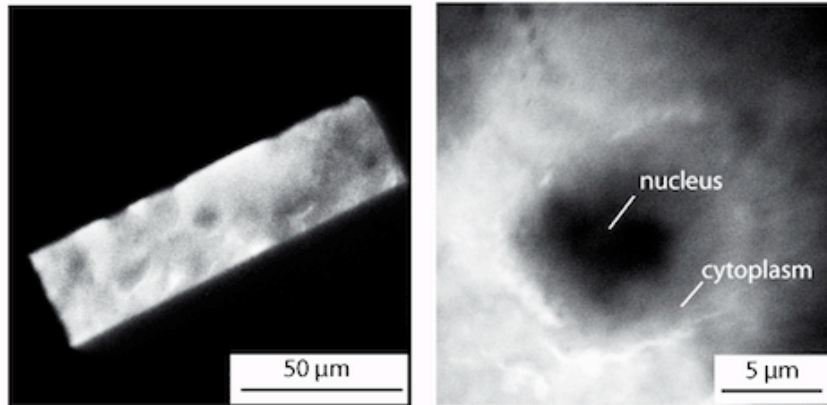
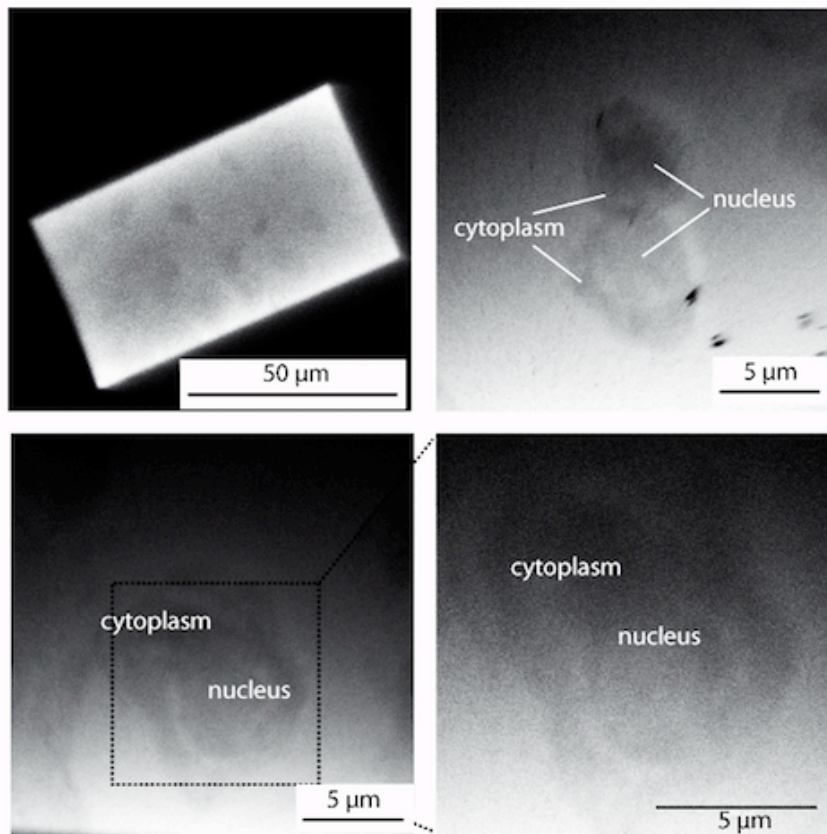
In order to broaden the range of tested cells for in-liquid TEM behavior and due to an easier transfection compared to PC3 cells, human embryonic kidney cells (HEK293T) were used for this experiment.

As this was a very first attempt, without any verification, at an early stage, it just gives an idea about the next straightforward steps of aequorin as a bimodal probe. However, it was possible to see a difference in the fixed cells treated with  $\text{SmCl}_3$  after transfection and those without (Figure 66).

The cells without  $\text{SmCl}_3$  were comparable to the PC3 cells showing dark areas for the nucleus and lighter areas for the cytoplasm (Figure 66A).

In Figure 66B the cells treated with  $\text{SmCl}_3$  are given. These do not show the dark areas for the nucleus. Instead, the cytoplasm has almost the same intensity as the nucleus. Furthermore, there is a lighter ring appearing as a border enclosing the nucleus area. It seems from these images that the cytoplasm gained contrast compared to the nucleus. At least for the lanthanide  $\text{Yb}^{3+}$  it is known that it has a cytoplasmatic localization (Foucault-Collet et al., 2013). However, verification and reproducibility of this experiment was not possible in time and need to be done as future follow-up experiment.

In summary, the advantages of TS A123W S125E over the existing tags are clear: (1) it can be fused to other proteins; (2) it emits light upon  $\text{Sm}^{3+}$  binding for light microscopy and (3) the  $\text{Sm}^{3+}$  raise contrast in TEM; (4) TS A123W S125E as tag for EM does not change the state (fix vs. non-fixed) of the cell as e.g. MiniSOG (Shu et al., 2011). Still there are also limitations. To mention some e.g. a suitable linker has to be found that allows both enzymes their functionality in terms of a fusion protein. The  $\text{Sm}^{3+}$ -triggered light needs to be stable over at least 5 minutes in order to find the area of interest during light microscopy and it needs to be switched on with very low concentration of  $\text{Sm}^{3+}$ , in the best case in the low nanomolar range, because mammalian cells seem to have limited internalization capability.

**A** HEK 293T TS A123W S125E**B** HEK 293T TS A123W S125E + SmCl<sub>3</sub>

**Figure 66:** In-liquid TEM of fixed HEK293T cells transfected with TS A123W S125E.

HEK293T cells were seeded on silicon nitride windows and transfected with VR1012::TS A123W S125E with Fugene HD according to the manufacturer's protocol. (A) Fixed HEK293T cells after transfection without additional SmCl<sub>3</sub>. Left panel shows an overview of the silicon nitride window in low magnification in TEM mode. The viewing area was 100x20 nm. Right panel shows a HEK293T cell with the characteristic black nucleus and the grey cytoplasm as marked in the image. (B) Fixed HEK293T cells after transfection and incubation with SmCl<sub>3</sub> for 1 hour. Left upper panel shows an overview of the viewing area that was 70x30 μm. Cells appear as dark grey areas. Other panels show HEK293T cells with higher magnification. Nucleus and cytoplasm are marked within the images.



## 4 Discussion

### 4.1 In-liquid TEM Experiments

In the following chapter, the results of the experiments with gold nanoparticles and in-liquid TEM are discussed.

#### 4.1.1 Visualization of Hybridized DNA-Gold Nanoparticles

Gold nanoparticles have been widely used as contrast agents in TEM for example in immunogold staining (Suzuki, 2002).

For the experiments shown in 3.1 above, AuNPs with a core diameter of 20 and 60 nm were successfully functionalized with 5'- and 3'-thiol modified DNA (DNA1 and DNA2). The thiol-modified DNAs were not complementary to each other. The AuNPs surfaces were fully covered with DNA. DNA1-AuNP and DNA2-AuNP could only form multimers by hybridization to the Hyb-DNA with complementary sections for DNA1 and DNA2. The hybridization reactions were performed before TEM analysis. It was possible to image multimers consisting of at least three AuNPs (DNA1- and DNA2-AuNPs) only of the actual sample (No.4). Control samples with the non-complementary control DNA (No.3) and a sample without any further DNA addition (No.2) and citrate stabilized AuNPs (No.1) did not have any mixed clusters imaged using in-liquid TEM.

The electron beam during imaging had an energy of  $110 \text{ e}^- \text{ nm}^{-2} \text{ s}^{-1}$ . This value was defined as threshold value for the observed dynamics in sample No.4, based on the theoretical study by Schneider *et al.* (Schneider et al., 2014) Their study shows the interactions between the electron beam and water. The electron beam can induce unintended chemical change in the sample. Moreover, they showed that these chemical changes led to growth of the citrate stabilized AuNPs under electron influence to big clusters. Plain citrate stabilized AuNPs fusion to big clusters upon beam energy was also reported by Liu *et al.* (Liu et al., 2013). The dose rate mentioned in Schneider *et al.* was given with  $7.5 \cdot 10^7 \text{ Gy/s}$ . The dose rate in the experiments explained in this work was below the value of Schneider *et al.* (Schneider et al., 2014) and thus did not cause any unintended chemical change in the samples.

However, energy dose rates above  $110 \text{ e}^- \text{ nm}^{-2} \text{ s}^{-1}$  were tested as well. Faster movements of the AuNPs could be observed when higher energy dose rates were used.

In contrast to citrate stabilized AuNPs, the DNA-AuNPs had slower displacements even at higher electron doses. A fusion to big multimers could not be observed either. An explanation might be that the DNA absorbed the energy and hybridized to other available DNA-AuNPs resulting in more complex multimers. Additionally, the DNA stabilized the AuNP core to a

higher degree than citrate or other ligands. The suggestion is underlined by the images after 110 s exposure. Surface passivation of AuNPs functionalized with ssDNA was reported before and observed in the performed experiments as well (Deka et al., 2015). Only the samples containing all components for hybridization formed multimers. This is in line with the reported passivation of the surface as all other samples did not show multimerization after beam exposure over several minutes. Upon energy input by the electron beam merging of smaller multimers of only 3 to 5 particles to bigger clusters was only observed in the actual sample (No.4). This might be due to hybridization of the attached ssDNA on the AuNPs and the Hyb-DNA in the mixture.

For *in vitro* hybridization of DNA, the mixture is typically heated (energy input) to build the hydrogen bonds between the nucleobases G/C and A/T. The electron beam has also the ability to heat the water in the chamber to a certain extent (ca. +10 to 20 °C). The temperature in the sample chamber is more or less around room temperature, although the TEM column is chilled with liquid nitrogen, so that the long beam and thus the increasing temperature explains the hybridization to bigger clusters. A precise measurement and temperature control is not possible yet but a modified sample arm capable of temperature control is in preparation.

Interaction of DNA-AuNPs in the samples without Hyb-DNA was significantly lower but was possible to a certain extent. This suggests that interactions between ssDNA and the gold surface are still possible, although the surface should be fully loaded with DNA. However, the flexibility of the DNA in liquid might allow weak interactions (Li and Rothberg, 2004). These interactions are rather unspecific and less pronounced for dsDNA due to the presentation of the negatively charged phosphate backbone of DNA to the surrounding (Watson, 1968; Bloomfield et al., 1999). The negatively charged phosphate backbone causes repulsive electrostatic interactions between dsDNA and negatively charged AuNPs.

It was possible to visualize the dynamics during bigger multimer formation. The lower part tilted while it assembled with the upper part. The interaction of the DNA strands during hybridization for assembly might induce the tilting effect. It was observed that once two smaller clusters merge, the overall structure starts to rotate in 3D fashion. The clustering and rotation is limited by the total height of the nanofluidic cell with a spacer thickness of 100-200 nm. This limits the configuration of the formed structures to a certain extent. However, increasing the spacer thickness causes multiple scattering events and results in a loss in the spatial resolution. (Peckys and de Jonge, 2014)

Another important point, next to the laborious sample preparation, that limits TEM studies of biological specimens in general is the electron radiation damage that occurs on the sample. The

damage can occur on all levels of biological molecules (DNA, RNA, lipids, proteins, etc.) (Watson, 1968; Bloomfield et al., 1999; Liao et al., 2003; Bakshi et al., 2007). To circumvent the damages cryo-EM or SEM were used before. The sample preparation, for both techniques, preserves the molecule's structure by cryogenic freezing or the added metal layer. In TEM imaging, there is no such preservation so that it was expected that the hybridization of the DNA could not be stable in the electron beam as it is multiple times higher (~3-5 Gy/s) than common radiation sources (1 Gy/s) (Schneider et al., 2014). According to the European radiation society the highest allowed radiation value (skin) is 0.5 Gy/s (European Nuclear Society, 2016). In contrast, the results showed that the hybridization was stable and could be even used for further multimerization. Although the multimerization can be a relict of electrostatic interactions, it was only observed in the sample containing DNA1-AuNPs and DNA2-AuNPs with Hyb-DNA. This suggests that the DNA has impact on the multimerization. Furthermore, the silicon nitride nanofluidic cell seems to preserve the integrity of the DNA during exposition to the electron beam compared to conventional TEM.

The obtained resolution of the DNA-AuNP in-liquid TEM experiments could be calculated to 10 nm. The achieved resolution was not high enough to visualize the hybridization of single DNA strands on the AuNPs, but a major step forward for this goal.

#### **4.1.2 In-liquid TEM of Mammalian Cells**

As already mentioned the bottleneck of biological specimens in TEM beside the high amount of water is the susceptibility towards electron radiation damage. State of the art sample preparation is to fix, dehydrate, stain, embed and slice or cryogenically freeze the cell before imaging.

Imaging of whole cells is possible using cryo electron tomography, but this method allows only resolutions to max. 5 nm and still requires cryogenic freezing (Hoenger and McIntosh, 2009). The nanofluidic cells made of graphene and silicon nitride allow encapsulation of biologic specimens without dehydration or freezing to preserve the sample (de Jonge et al., 2009; Park et al., 2015).

The results in chapter 3.1.2 above and 3.1.3 above showed contrasted images without additional sample preparation or staining of PC3 prostate cancer cells directly grown on the silicon nitride window. Independent experiments were performed of approximately 52 fixed cells PC3 cells of different passages and different days. We tested nanofluidic cells with different window sizes and spacers. The approximately 52 fixed PC3 cells were tested over 6 months on 13 different nanofluidic cells of the final set up (200x50  $\mu\text{m}$  size window with 800 nm spacer). The fixed PC3 cells resulted in reproducible contrasted images without any additional staining or sample

preparation. The contrasted areas could be assigned as nucleus, nucleoli and membranes due to their shape and structure that were compared with light microscopy images (Figure 31A and G) and images of conventional TEM for these cellular structures. For the assumption of the nucleus and nucleoli the DNA was stained with Hoechst dye for fluorescent imaging. Furthermore, the areas imaged with in-liquid TEM were matched with the light microscopy image taken before the in-liquid TEM measurement that was used as a "map".

To underline the presented findings state of the art probes could be used. For example, one could permeabilize the cells after fixation to perform immunostaining of the nucleus, the membrane or other cell compartments.

Contrast was different depending on the height of the mammalian and nanofluidic cells and the resulting thickness of the liquid layer. However, contrasted images were observed in all cases although no additional staining was used. Because of the visible subcellular structures, the obtained contrast is most likely z-contrast induced by the phosphorus as heaviest element in biological specimens. Phosphorus is a common building block for membranes as phospholipids and in DNA or RNA, which can be found in the nucleus. The black spots shown in a magnification of a nucleus membrane have diameters of 100-300 nm. The lower spot seems to consist of at least three independent spots that are smaller than 300 nm. By contrast and size distribution, it might be possible that these spots are RNPs. RNA and proteins are condensed in RNPs so that this could cause the good contrast. The RNPs in drosophila cells were reported with a diameter up to 200 nm (Speese et al., 2012). Human RNPs are mostly smaller and around 100 nm or even smaller as small ribonuclearproteins (ca. 10 nm) (Kastner et al., 1990; Köhler and Hurt, 2007). In the nucleus, hnRNPs are formed of the mRNA for the transport into the cytoplasm. Once in the cytoplasm the hnRNPs are matured to cytoplasmic RNPs that can be transported in the cell via the cytoskeleton (Wilhelm and Vale, 1993). Final verification has to be done using conventional well-approved light microscopy stainings as bimodal imaging to investigate the same cell in EM and FLM using MiniSOG staining or ReAsH. Moreover, immunolabeling with CdSe QD against RNPs might also be possible.

In terms of electron damages the structural integrity of fixed PC3 cells were maintained up to 2 h within the in-liquid TEM. As described for the DNA-AuNPs the silicon nitride windows seems to protect the cellular structures for longer imaging times.

Only one exception out of 52 cells was detected. One cell that was imaged with an electron dose rate above  $110 \text{ e}^- \text{ nm}^{-2} \text{ s}^{-1}$  had a visible damage 90 min after the first exposure. One part of the cell membrane detached and was floating in the surrounding liquid. This event was a single exception and can be assigned to the higher electron dose rate used. However, the floating proved that there was still liquid in the silicon nitride cell.

Derived from the good results of fixed cells, living PC3 cells were tested to visualize dynamics (3.1.3 above). Imaging of living cells was more challenging due to the time needed to close the nanofluidic cells, which takes up to 30 min. During this period, the cells are at room temperature without additional CO<sub>2</sub> supply, which is essential to maintain their pH-household. Temperature and missing pH-household are stress factors and increase cell death. The tested cells were seeded 4 h before imaging in order to visualize the adhesion on the silicon nitride material. The cellular shape at this time point was described above as round cell bodies that do not show the long stretched form as PC3 cells normally do. Single frames of the cells were captured in 100 s intervals of the attachment phase.

It seemed that the cell adhesion area was imaged. We were able to analyze possible dynamics or differences in shape due to the various types of contacts between the cell and the nanocell surface. The process and the molecules, cadherins and integrins, for adhesion are well-known today (Muller and Dufrene, 2011; Chi et al., 2014). The attachment is mainly mediated by glycoprotein interactions with the surface material and interaction with the cytoskeleton. The cell forms filopodia and lamellipodia as adhesive areas (Gumbiner, 1993, 1996; Cramer, 1997). Filopodia are punctual and slender extensions of the cell edges comparable to fingers. Lamellipodia occur as leading projections of cell edges and are often seen in cell migration. Actin filaments drive them. Endothelial cells need to flatten on the surface for attachment and form the characteristic stretched structures during this process. It is comparable with the shape changes during mitosis. The structural changes of the membranes were described by Gauthier *et al.* using SEM images (Gauthier et al., 2012). They could show that the cell membrane appears in various shapes according to the phase it is in, and different molecules including actin, glycoproteins, and phospholipids were present. The cell membrane can appear as distinct fine line or as mesh-like structure. This was in good agreement with the observed structures in in-liquid TEM.

Next to the membrane, changes of structures near to the membrane over time were observed. The assumption was made that these structures might be vesicles or bodies due to their comparable contrast and close proximity to the membrane. Shape and movement to the inner cell area underlined that these structures might be vesicles or bodies. One vesicle could be found to be even closer to the membrane. The displacement of the structure indicates a possible motion in the cell during the imaging. The observation clearly states that in-liquid TEM can be used to visualize dynamics of mammalian cells.

A famous class of vesicles are clathrin-coated pits (CCPs) (Pearse, 1976). The diameter of the imaged vesicles was 3 μm and thus 30 times bigger compared to the average size of CCPs with 100 nm (Saffarian et al., 2009). Vesicles of macropinocytosis (Mukherjee et al., 1997) or apoptotic bodies (Zhang et al., 1999) are typically between 1-5 μm in diameter. The movement of the

vesicles is retrograde and an indication towards macropinocytosis (Figure 33F). The stress during closing procedure of the nanofluidic cell and the beam might induce apoptotic bodies or stress vesicles. To precisely state the kind of vesicle, further analysis using co-staining or bimodal imaging with known specific fluorophores or immunogold labeling is needed. Possible targets could be RAB, Arf, or SNARE. Especially RAB proteins differ according to the type of endocytosis. The verification by size only as given above is not sufficient.

Nonetheless, it was possible to image dynamics of a living cell using in-liquid TEM without any additional sample preparation or staining.

Another aspect that is important for the comparison with other imaging techniques is the resolution. Nanofluidic cells are not well established, yet. It was possible to show good imaging results of DNA and cells using these nanofluidic cells and in-liquid TEM. The calculation of the obtained resolution is challenging, as the nanofluidic cells buldge within the vacuum of the TEM column. Soft materials such as biological specimens can undergo morphological changes within the silicon nitride windows. To calculate the resolution the energy profile is important. Crystalline structures as AuNP have a distinct energy profile in TEM. Soft biological material does not have this distinct profile.

This limitation was addressed in the experiment using LNCaP prostate cancer cells. These cells present the prostate specific membrane antigen (PSMA) on their surface, which is not presented on PC3 cells. This antigen can be specifically targeted using an anti-PSMA RNA based aptamer (Javier et al., 2008; Kim et al., 2010b). To include a crystalline structure anti-PSMA-AuNPs were used in the experiment.

A major disadvantage of LNCaP cells compared to PC3 cells was that the LNCaP cells were not as stable as PC3 cells under the electron beam. Damages in terms of detached membrane drifting in the surrounding and a lot of cell debris were detectable already after 30 minutes in the low dose beam mode ( $20 \text{ e}^-/\text{nm}^2\text{s}$ ). This leads to the suggestion that LNCaP cells are less tolerant to electron radiation compared to PC3 cells.

Another observation of the LNCaP cells and in-liquid TEM was that the contrast of the anti-PSMA AuNPs was not as high as the contrast in the experiments with unstained PC3 cells. The main reason for this is the height difference of the nanofluidic cell. The height difference of the nanofluidic cell used in the cell experiments compared to the height in the experiments with DNA-coated AuNPs is without consideration of the buldging is 800 nm vs. 100 nm. This means that the liquid layer is at least 8-times thicker resulting in more inelastic scattering and loss of transmitted electrons. Furthermore, the electron can also interact with the biological specimens. This yields to loss of resolution as recognized.

To identify AuNPs in an image, an algorithm was written by Dr. Stephanie Manz (Prof. Miller's group). The particles were averaged and the resolution calculated of the averaged AuNPs. The final resolution obtained via this procedure was 10 nm.

The experiments with living cells and in-liquid TEM showed robustness of the cells in the electron beam. It was possible to observe subcellular structures such as nucleus, nucleoli, and membranes. These could be verified with light microscopy. Furthermore, smaller structures were imaged that could be RNPs but need conventional bimodal staining for verification. Dynamics were observed of vesicles or bodies moving over a distance of 1  $\mu\text{m}$  towards the inner of the cell. A main challenge for in-liquid TEM of biological material in general is the calculation of the resolution. Because of the soft and weak scattering material, the calculation is challenging. We could calculate a resolution of 10 nm via added anti-PSMA-AuNPs to LNCaP prostate cancer cells.

The observed resolution was already a major step towards imaging of molecular dynamics e.g. DNA synthesis in its natural environment. To do so a resolution in the Angstrom regime is preferred. Electron microscopes with a more than 200 keV might already increase the resolution.

## 4.2 Engineering of Aequorin Variants with Improved $\text{Sm}^{3+}$ Binding Affinity Towards a Bimodal Probe for Light and Electron Microscopy

This chapter discusses the results of the saturation mutagenesis and rational design in order to engineer an AQ variant with improved binding affinity for  $\text{Sm}^{3+}$  as luminescence trigger. The  $\text{Sm}^{3+}$  ion should be used as contrasting agent for electron microscopy and the light emission upon ion binding for light microscopy. This was the first step towards the desired approach of a bimodal probe that can be fused to a protein of interest analogue to the GFP concept for light microscopy.

Aequorin was widely used for the visualization of  $\text{Ca}^{2+}$  in cells. A lot of research was dedicated to thermostabilized, low  $\text{Ca}^{2+}$  affinity variants, semi-synthetic variants with CTZ analogues to widen the color spectra and prolong the luminescence decay, slow decay and bright luminescent variants and is reported in the literature (Shimomura et al., 1988; Tsuzuki et al., 2005; Tricoire et al., 2006).

### 4.2.1 Saturation Mutagenesis for an Improved Aequorin Variant

Saturation mutagenesis was performed at all of the six ion coordinating positions of the 12 amino acid long loop. The advantage of saturation mutagenesis over conventional site-directed mutagenesis is that all possible 20 amino acids can be covered within 90 clones by introducing an NNK triplet on the DNA level at the desired position. Combining the amino acid good coverage with a high-throughput screening (HTS) it makes saturation mutagenesis a fast method to gain information of the necessary AQ substitutions for increased  $\text{Sm}^{3+}/\text{Ca}^{2+}$  luminescence ratio and  $\text{Sm}^{3+}$  affinity. Aequorin allows a photometrical HTS based on the luminescence upon ion binding.

A main challenge of high-throughput screening is a low coefficient of variation (CV). The CV is the quality criterion of the assay and thus should be as small as possible, at least below 20 %. This point will be discussed later.

The results of the saturation mutagenesis approach are summarized in the following as one chapter. General points are discussed in detail for the high-throughput screening for position 12 TS E128.

The first two libraries were produced for the 11<sup>th</sup> and 12<sup>th</sup> position at the end of the 12 amino acid long loop of EF-hand motif 2. The ion radius of  $\text{Sm}^{3+}$  is bigger (122 pm) compared to  $\text{Ca}^{2+}$  (114 pm), thus it needs more space in the loop. Based on this position 11 and 12 as closing position were chosen to widen the loop. Substitutions at position 1 of an EF-hand-motif are



often related to less or complete loss of function (Tricoire et al., 2006), so that position 12 was chosen for the first substitution. Position 12 only leads to variants with less activity.

Substitutions can reduce the protein stability, which can be mainly seen in destabilization of the structure, followed by less function. Along the theory that proteins fold in a funnel-like energy landscape (Luthey-Schulten and Wolynes, 1997) and the structure is composed by heat sensitive hydrogen bonds, van-der-Waals interactions, and disulphide bridges, it plausible to start from a thermostabilized variant, if available. Thermostabilized variants are in general more stable compared to non-thermostabilized variants and thus can cope substitutions better. For AQ the thermostabilized variant AQ TS was used as parent for the introduction of the NNK libraries at E128 and D127, position 12 and 11 of EF-hand motif 2.

The screening of the library TS E128 revealed only 10 variants with an  $\text{Sm}^{3+}/\text{Ca}^{2+}$  luminescence ratio  $\geq 1$ . The rescreening with five-times of each preselected clone showed the influence of the CV with a value  $\geq 25\%$ . The error bars were huge and a threshold had to be defined as 12-times the ratio of the parent AQ TS instead of a general threshold (sum of mean value and 3-times standard deviation) to reduce the number of false positives.

A reason for the high CV values might be that the *E. coli* cells used for the screening did not show uniform growth. The bacteria cells in row A of the 96-well plates grew faster compared to the cells in the other rows of the 96-well plates. To avoid these imbalances row A was filled with media only and not used for experiments. It was a blank row.

For the optimization of protein production cells of the *E. coli* strain BL21(DE3)pLysS were used for all libraries. These cells do not show basal expression of the protein due to the helper plasmid pLysS. In addition, different media were tested to uniform the growing of the cells and maximal yield of protein. The used media for the expression cultures was SOB/TB while the precultures were grown in 2YT media. Although 2YT media has more nutrients compared to normally used LB media, the richer SOB/TB media was used for optimal protein production. This medium has more salts and glucose added which increase the protein production.

Furthermore, the induction of protein production was not started at an  $\text{OD}_{600}$  of 0.6, in the log phase; instead, it was started at an  $\text{OD}_{600}$  of 1.3. This procedure enables evenly protein production in the stationary phase, but the proteins amounts varied still from well to well. Furthermore, the luminescence was tested in crude cell lysate, which might had an influence to the signal. Direct purification in the 96-well plate approach was too laborious and was not in line with a HTS, so that the threshold was set to 12.5-times the  $\text{Ca}^{2+}$ -triggered luminescence of AQ TS in order to exclude to many false positive results. As a rule of thumb the threshold is often given with 3-times the standard deviation. This value was just too low for the HTS.

Screening of AQ libraries was reported before (Tsuzuki et al., 2005; Tricoire et al., 2006). The reported approaches mostly used cell free expression to circumvent the variations. Another alternative was to include an Omp-tag for transport of the protein to the supernatant. Both alternatives were not available for this work.

While for position 12 the only variant with improved  $\text{Sm}^{3+}/\text{Ca}^{2+}$  luminescence ratio was the already known low  $\text{Ca}^{2+}$  affinity variant TS E128G, screening of position 11 led to a new improved variant, TS D127R. Although this position is not mainly involved in ion coordination of the bipyramidal pentagonal  $\text{Ca}^{2+}$ , it seemed that it had an impact on the coordination of  $\text{Sm}^{3+}$ . This indicates that the coordination of  $\text{Sm}^{3+}$  is indeed different to the coordination of  $\text{Ca}^{2+}$  and needs more than the usually available amino acid residues for tight coordination within the EF-hand loop.

Saturation mutagenesis had also some limitations, as it was not possible to produce enough clones at all tested positions either with LAAQ as parent or AQ TS. This was in particular the case for position 1 (D117), position 3 (D119) and position 9 (S125). The introduced substitutions at these positions seemed to limit the bacteria growth. Although transformation was repeated to cumulate at least 90 clones, these did not grow in the deep-well cultures. The suggestion was that because of the mutations for the substitution the vector, carrying the AQ and resistance gene for selection was ejected and the bacteria died.

However, position 1 and 3 are known to lead to less or loss of function (Drake et al., 1997), which was already reported by the low  $\text{Ca}^{2+}$  affinity variants D117G and D119A (Kendall et al., 1992; Tricoire et al., 2006).

In total, saturation mutagenesis yielded in the variants TS E128G, which was already reported, TS D127R, which showed improved  $\text{Sm}^{3+}/\text{Ca}^{2+}$  luminescence ratio by an increasement of factor 3 compared to parent AQ TS and last the verification of the important variant TS A123W. The variant TS A123W is discussed in more details in the rational design chapter of the discussion.

## 4.2.2 Engineering of Aequorin using Rational Design

Rational design at position 7 and 9 in AQ's EF-hand motif 2 was performed in parallel to the saturation mutagenesis based on the importance of these positions for lanthanide ion binding (Drake et al., 1996; Cates et al., 1999; Franz et al., 2003; Nitz et al., 2003; Gifford et al., 2007). Compared to saturation mutagenesis this method allows controlled mutagenesis at the desired position.

### 4.2.2.1 EF-hand Motif 2 - Position 7 – Allowing Different Valencies

Position 7 of EF-hand motif 2 was substituted to tryptophan or phenylalanine to allow binding of ions with a different valency (Cates et al., 1999; Nitz et al., 2003). The substitution leads to bigger amino acid side chains that can interact with the ion for higher stabilization and thus higher luminescence. This was detected for both TS A123F and TS A123W.

Higher absolute and relative luminescence for the variants TS A123F and TS A123W could be detected induced with both ions. Due to the 10-fold improved  $\text{Sm}^{3+}$ -triggered luminescence the overall  $\text{Sm}^{3+}/\text{Ca}^{2+}$  luminescence ratio was 3-times higher compared to parent for both variants.

Not only brightness but also wavelength shifts can be advantageous for future application to distinguish between often used  $\text{Ca}^{2+}$  detection using AQ or specifically turned on luminescence via  $\text{Sm}^{3+}$  ions. TS A123F induced with  $\text{Ca}^{2+}$  and  $\text{Sm}^{3+}$  shifted 12 nm and 11 nm towards higher wavelengths (~470 nm), while TS A123W emission shifted only 7 nm and 5 nm, respectively. The wavelengths shift can be related to the bigger side chains due to substitution. They cannot only coordinate the ion, which leads to intramolecular rotation and light emission, but they can also interact with the CTZ itself. The stacking of the CTZ in the active center is important for the emitted wavelengths.

The impact on intramolecular rotation of the  $\alpha$ -helices can also be analyzed indirectly by the titrated  $\text{EC}_{50}$  values. These are also a measure of ion affinity. TS A123W was the first variant obtained with a three-time decreased  $\text{EC}_{50}(\text{Ca}^{2+})$  of 130  $\mu\text{M}$  compared to AQ TS 50  $\mu\text{M}$ . This was a major step forward to a variant with desired higher  $\text{Sm}^{3+}$  affinity and lower  $\text{Ca}^{2+}$  affinity.

Overall, the substitution at this position to tryptophan and phenylalanine yielded in a variant with improved  $\text{Sm}^{3+}$ -triggered luminescence and luminescence ratio. Furthermore TS A123W had a decreased  $\text{EC}_{50}(\text{Ca}^{2+})$  value, which indicates reduced  $\text{Ca}^{2+}$  affinity. It can be stated, that the substitutions at position 7 were successful regarding a higher  $\text{Sm}^{3+}/\text{Ca}^{2+}$  luminescence ratio and  $\text{Sm}^{3+}$  affinity. Still, final improvements should be at least 10-times to the original values to claim a significant new variant towards the goal. Especially keeping in mind the final application as probe in mammalian cells that have a natural  $\text{Ca}^{2+}$  concentration around 0.2  $\mu\text{M}$ , the  $\text{Sm}^{3+}$  affinity needed to be higher than AQ TS while the  $\text{Ca}^{2+}$  affinity should be decreased as much as possible.

#### 4.2.2.2 EF-hand Motif 2 - Position 9 – Widening the Ion Diameter Restriction

Position 9 as “gateway” position was also reported to be important for trivalent ions. Because  $\text{Sm}^{3+}$  has a bigger ion diameter as  $\text{Ca}^{2+}$  the substitutions of serine to either aspartic acid or glutamic acid was important for improved binding according to Drake *et al.* (Drake et al., 1996). In saturation mutagenesis most of the clones of this position could not be used for screening. It seemed that variants with substitutions were either toxic or led to loss of the resistance gene for the selection of *E. coli* cells (3.2.1.3).

The rationally designed substitution at position S125 to D resulted in a bright variant with a 10-times higher  $\text{Ca}^{2+}$ -triggered luminescence compared to parent. Although the  $\text{Sm}^{3+}$  induced luminescence was 5.6 times higher compared to AQ TS, the luminescence ratio  $\text{Sm}^{3+}/\text{Ca}^{2+}$  was only 1.7 times higher compared to parent. Compared to the previously tested variants of position 7 the ratio was not as much as improved as for position 7.

Normally, decreased ion size selectivity should be recognizable in higher  $\text{EC}_{50}(\text{Ca}^{2+})$  values. However the  $\text{EC}_{50}(\text{Ca}^{2+})$  for TS S125D and TS S125E were even two-fold increased (ca. 20  $\mu\text{M}$ ) compared to parent AQ TS (50  $\mu\text{M}$ ). It seemed that the variant TS S125D and TS S125E were highly stable, which was also underlined with a very high  $T_M$  value of 56 °C for TS S125D.

The low number of clones in saturation mutagenesis was further analyzed by introducing additional substitutions at this position towards glycine and arginine and tested on their influence. TS S125G yielded in inactive protein (confirmed with CD measurements) proving the low or even missing luminescence in the saturation mutagenesis. The substitution TS S125R should create opposite charge and thus repulsive forces that push the ion tighter into the loop comparable to the substitution TS D127R. However, the  $\text{Sm}^{3+}$ -triggered luminescence was not improved, which supports that substitutions with negatively charged amino acids like Glu and Asp enhance binding of positively charged ions (Drake et al., 1996).

In summary there was no improved variant obtained of this position regarding  $\text{Sm}^{3+}$ -triggered luminescence and luminescence ratio or  $\text{EC}_{50}$  values. Nonetheless and based on the reported substitutions of LBT at position 7 and 9 of an EF-hand motif (Nitz et al., 2003; Daughtry et al., 2012), combinatorial effects of TS S125D and TS S125E with TS A123F and TS A123W were tested next.

#### 4.2.2.3 EF-hand Motif 2 - Double Substitutions Based on Position 7 and 9

Combinatorial effects of the positions 7 and 9 were tested for improved  $\text{Sm}^{3+}/\text{Ca}^{2+}$  luminescence and  $\text{Sm}^{3+}$  affinity based on the reported LBT double substitutions (Daughtry et al., 2012).

Combination yielded in four variants TS A123F S125D, TS A123F S125E, TS A123W S125D, and TS A123W S125E. All were active in luminescence tests. TS A123F S125E was the brightest variant with an almost 40-fold  $\text{Ca}^{2+}$  luminescence compared to parent AQ TS. However, the highest achieved  $\text{Sm}^{3+}/\text{Ca}^{2+}$  luminescence ratio for the variants was detected for TS A123W S125E (8-fold higher compared to parent). Although the substitutions at position 7 led to shifts of emission wavelengths towards higher wavelengths, the combination did not follow this trend. Shifts to shorter and longer wavelengths were detected for the variants. One exception is that TS A123W S125E showed the widest shift induced with  $\text{Ca}^{2+}$  to 485 nm and an 8 nm shift towards longer wavelengths (458 nm) with  $\text{Sm}^{3+}$ . This already indicated that there might be structural changes that led to the shift due to different binding and triggered intramolecular rotations.

The improvements detected in luminescence ratios were underlined by the  $\text{EC}_{50}$  values. The brightest variant TS A123F S125D had a 7-times improved  $\text{EC}_{50}(\text{Ca}^{2+})$  value of only 7  $\mu\text{M}$  compared to the parental 50 mM. The best variant TS A123W S125E showed a reduced  $\text{EC}_{50}(\text{Ca}^{2+})$  by factor 20 (1000  $\mu\text{M}$  vs. 50  $\mu\text{M}$ ). No other variant tested had such a high reduction. The  $\text{EC}_{50}(\text{Sm}^{3+})$  for TS A123W S125E was not improved but in the same order of magnitude as AQ TS.

The  $\text{EC}_{50}$  value is only an approximation of the affinity, due to the relation of luminescence brightness and metal ion concentration. The  $\text{K}_d$  values of TS A123W S125E as the best variant, judged by  $\text{Sm}^{3+}$ -triggered luminescence, luminescence ratio, and  $\text{EC}_{50}$  values, were measured via ITC. These ITC measurements verified the already observed improvements with a  $\text{K}_d(\text{Sm}^{3+})$  of 0.1  $\mu\text{M}$  against 4.1  $\mu\text{M}$  for AQ TS and  $\text{Sm}^{3+}$ . The  $\text{K}_d(\text{Ca}^{2+})$  for TS A123W S125E was almost 30-times less (2.8  $\mu\text{M}$ ) versus 0.1  $\mu\text{M}$  for AQ TS. The results of TS A123W S125E show the improvement towards higher affinity for  $\text{Sm}^{3+}$ . A higher  $\text{Sm}^{3+}$  affinity could allow application of TS A123W S125E as a bimodal probe. The new variant TS A123W S125E is a good candidate for further rounds of protein engineering to completely loose the  $\text{Ca}^{2+}$  binding ability and for enhanced and stable  $\text{Sm}^{3+}$ -triggered luminescence.

The  $\text{K}_d$  value calculation of the ITC raw data used a fit including all four EF-hand motifs. One might argue that only three EF-hand motifs actively bind ions, known from crystal structures (Head et al., 2000; Deng et al., 2005). However, systematical analysis of EF-hand motifs of

various proteins showed that EF-hand motifs exist in pairs. The preferred constellation is a heterodimer of two EF-hand motifs. The dimerization of the motifs stabilizes the loops before and after ion binding and moreover the resulting transformational change. Even if one unit of the dimer is not active, it is essential for the stability, affinity and transformational change (Gifford et al., 2007).

TS A123W S125E was the best variant according to the goal of a new AQ variant with higher  $\text{Sm}^{3+}$  affinity and  $\text{Sm}^{3+}/\text{Ca}^{2+}$  luminescence ratio.

The achieved improvements were pushed further by reconstitutions of TS A123W S125E with CTZ analogues for semi-synthetic AQ. Improvements cannot only be achieved by substitution but also by using CTZ analogues. Binding of CTZ or CTZ analogues changes the brightness and half-life (Shimomura et al., 1993). It was possible to enhance TS A123W S125E luminescence ratio with CTZ hcp for additional 17-times compared to AQ TS reconstituted with hcp.

As explained before high luminescence intensities suggest tight binding of CTZ and a high affinity for the metal ions, which results in a wider rotation of the  $\alpha$ -helices as activating energy for the decarboxylation of CTZ. The differences in  $K_d$  can be a first hint towards structural changes. To analyze structural changes during the binding of either  $\text{Ca}^{2+}$  or  $\text{Sm}^{3+}$  CD measurements of both AQ TS and TS A123W S125E with  $\text{Ca}^{2+}$ ,  $\text{Sm}^{3+}$  and without any addition of ions was performed. The collected spectra showed differences between TS A123W S125E and AQ TS. The new improved variant had minima that are more prominent at 210 and 220 nm for the  $\alpha$ -helices. This underlines the observed emission shifts due to a different intramolecular conformation upon ion binding. The lower  $K_d$  of TS A123W S125E and  $\text{Ca}^{2+}$  could be verified by a less prominent curve observed in CD measurements. This indicates that binding of  $\text{Ca}^{2+}$  induced a destabilizing conformation of the enzyme and less luminescence. Overall, the new variant TS A123W S125E seems to have a slightly different structure compared to AQ TS.

TS A123W S125E exhibited the best  $\text{Sm}^{3+}/\text{Ca}^{2+}$  luminescence ratio (0.8) improved by factor 8 compared to AQ TS (0.1). It showed high  $\text{Sm}^{3+}$  luminescence reconstituted with CTZ ( $1.7 \cdot 10^6$  a.u.) and a prolonged luminescence half-life of 257 s compared to  $\text{Sm}^{3+}$ -triggered AQ TS (97 s). Moreover, the  $K_d(\text{Sm}^{3+})$  for TS A123W S125E was 40-times higher (0.1  $\mu\text{M}$ ) compared to AQ TS (4.1  $\mu\text{M}$ ) while  $K_d(\text{Ca}^{2+})$  for TS A123W S125E was almost 30-times less (2.8  $\mu\text{M}$ ) versus 0.1  $\mu\text{M}$  for AQ TS.

As these results are a major step towards an improved AQ variant, further optimization towards the goal of a bimodal probe for electron and light microscopy could focus on even less  $\text{Ca}^{2+}$  affinity that results in loss of  $\text{Ca}^{2+}$ -triggered luminescence. To do so, TS A123W S125E was

combined with the best variant of the saturation mutagenesis, TS D127R and known low  $\text{Ca}^{2+}$  affinity variant TS D119A.

#### **4.2.2.4 EF-hand Motif 2 – Combinatorial Effects of Saturation Mutagenesis and Rational Design**

The best variant of saturation mutagenesis TS D127R (luminescence ratio almost 4-times improved), the low  $\text{Ca}^{2+}$  affinity variant TS D119A and the best variant of the rational design TS A123W S125E (luminescence ratio improved 8-times,  $\text{Sm}^{3+}$  affinity 40-times improved and  $\text{Ca}^{2+}$  affinity 20-times reduced) were combined for combinatorial effects for an even further improved variant, in terms of the  $\text{Sm}^{3+}/\text{Ca}^{2+}$  luminescence ratio.

The tested combinations were TS D119A A123W S125E, TS A123W S125E D127R, and TS D119A A123W S125E D127R. Although TS A123W S125E showed the highest  $\text{Sm}^{3+}$ -triggered luminescence and TS D119A luminescence was more or less in the range of parental AQ TS triggered with both ions, the combined variant was a bright variant induced with  $\text{Ca}^{2+}$ . The  $\text{Ca}^{2+}$ -luminescence was 30-fold higher compared to AQ TS and the  $\text{Sm}^{3+}$ -triggered luminescence relapsed to the parental luminescence induced with  $\text{Sm}^{3+}$ . The beneficial stabilizing of the ion and induced rotational transformation for light emission with  $\text{Sm}^{3+}$  observed for TS A123W S125E and proven with the CD measurements (Figure 54) were diminished by the combination with D119A. The CD spectra of TS D119A A123W S125E had only shallow minima compared to AQ TS and TS A123W S125E (Appendix). It is known that position 3 in an EF-hand motif is crucial for a tight binding of the ion. Naturally, the position is mostly occupied by Asp (76%) or Asn, whereas substitution to Ala is not often found in nature (Gifford et al., 2007). With the idea in mind that  $\text{Sm}^{3+}$  needs more space within the EF-hand motif the substitution D119A was chosen. However, it was clearly seen from the combinatorial variant TS D119A A123W S125E that additional space is not the main concern. Widening the loop by D119A also led to no further improvements for  $\text{Sm}^{3+}$  ions, although TS A123W S125E had drastically improved parameters. Instead, the additional D119A reconstituted the high  $\text{Ca}^{2+}$  affinity observed by the bright  $\text{Ca}^{2+}$ -triggered luminescence and low  $\text{Sm}^{3+}$  luminescence, which was exactly the opposite of the desired effect. This variant shows that although ideal conditions of the independent variants with low  $\text{Ca}^{2+}$  affinity (TS D119A) and high  $\text{Sm}^{3+}$  affinity (TS A123W S125E) were given, a combination of these does not necessarily yield in additional benefit for the goal of a variant with improved  $\text{Sm}^{3+}$  affinity.

The same observations were made for TS A123W S125E D127R in combination with D119A. The  $\text{Sm}^{3+}$ -triggered luminescence was even lower ( $0.03 \cdot 10^6$  a.u.) and the luminescence ratio inclined towards zero. All tested further combinations with TS A123W S125E in EF-hand motif 2 diminished the improvements gained before. It seems as if TS A123W S125E leads to a very stable coordination and rotational state for  $\text{Sm}^{3+}$  binding. Even the possible repulsive forces of D127R to push the  $\text{Sm}^{3+}$  deeper into the loop did not show improved  $\text{Sm}^{3+}/\text{Ca}^{2+}$  luminescence ratios combined with TS A123W S125E or with TS D119A A123W S125E. For TS D119A A123W S125E D127R and TS A123W S125E D127R CD spectra were also not as characteristic as TS A123W S125E and measurements for the  $T_M$  value were not successful due to huge scattering of the obtained data that did not show the typical sigmoidal curve.

The best variants obtained even after combination with the best variant of saturation mutagenesis and a low  $\text{Ca}^{2+}$  affinity variant was still TS A123W S125E.

#### 4.2.2.5 Adaption of the Best Substitutions to EF-hand Motif 3

Aequorin has three active EF-hand motifs. These bind  $\text{Ca}^{2+}$  with different affinities. The affinity decreases from EF-hand motif 2, to EF-hand motif 3 and EF-hand motif 1 (Tricoire et al., 2006). As explained before, EF-hand motifs occur in pairs. EF-hand motif 3 forms a heterodimer with EF-hand motif 2, which was described and engineered in chapter 3.2.2.3 above.

Although EF-hand motif 2 can be seen as “lead” for luminescence, substitutions in EF-hand motif 3 change the luminescence behavior as well. This motif inherits slow luminescence decay variants, bright variants and can also lead to removal of an essential  $\text{Ca}^{2+}$  binding site by substitution of D153G (shortly before EF-hand motif 3) (Tsuzuki et al., 2005). Furthermore, within the neighboring  $\alpha$ -helices of this motif the thermostabilizing substitutions Q168R L170I are located. But EF-hand motif 3 is also important for the CTZ binding, as it contains the residues Met165, Thr166, His169 and Trp 173 that interact with CTZ (1.2.2.2 above, Figure 13). All of these positions show the possible impact of EF-hand motif 3 for AQ’s luminescence (Tricoire et al., 2006).

The best substitutions in EF-hand motif 2 led to TS A123W S125E with highly improved  $\text{Sm}^{3+}$  affinity and luminescence parameters. These substitutions were adapted to EF-hand motif 3 for combinatorial effects and the variants TS Q159W D161E and TS A123W S125E Q159W D161E tested.



The variant TS Q159W D161E with analog substitutions to EF-hand motif 2 had low luminescence activity compared to AQ TS and TS A123W S125E induced with  $\text{Ca}^{2+}$  or  $\text{Sm}^{3+}$ . The  $\text{Sm}^{3+}/\text{Ca}^{2+}$  luminescence ratio was 2-fold higher than AQ TS, although the overall luminescence was lower. This result is in good compliance with the weaker affinity of EF-hand motif 3 compared to EF-hand motif 2. Additionally, it proves that changes in other EF-hand motifs also contribute to overall luminescence, which states the importance of not only EF-hand motif 2 but also EF-hand motif 3 for luminescence.

Bright luminescence normally occurs of variants with high  $\text{Ca}^{2+}$  affinity. The substitutions in EF-hand motif 3 resulted in a low luminescence variant and an  $\text{EC}_{50}$  ( $\text{Ca}^{2+}$ ) value of only 10.4  $\mu\text{M}$ . On the first view, this seems to be contradictive to the theory. However, one has to keep in mind that EF-hand motif 3 has lower affinity for ions compared to EF-motif 2. More important, the absolute luminescence value is not only due to the conformation change upon binding but also based on the interaction of the enzyme with CTZ. The emitted light originates from CTZ and not from AQ itself. This is a main difference to most of the known fluorescent proteins such as GFP. The conformational change is necessary as initial energy for the chemical decarboxylation of CTZ and light emission.

The crystal structure of AQ (Head et al., 2000) revealed that the induced conformational changes of EF-hand motif 3 disrupt the Glu164 – Gln168 and Phe149 – Trp129 bonds. The disruption results in destabilization of Tyr184 and Trp129. Both are in interaction with the CTZ peroxide. A weaker interaction with CTZ results in lower luminescence. This explains why the luminescence of TS Q159W D161E with  $\text{Ca}^{2+}$  and  $\text{Sm}^{3+}$  was low although the  $\text{EC}_{50}$  values were lower for 50 % of the maximum luminescence.

In order to test the additional effects of EF-hand motif 2 and 3 for luminescence substitutions at position 7 and 9 were introduced in both motifs resulting in TS A123W S125E Q159W D161E. The two EF-hand motifs are linked via short antiparallel  $\beta$ -sheets between the  $\alpha$ -helices of the motifs. This linker brings the loops and the ions into close proximity (Gifford et al., 2007). Based on this proximity it has been suggested that the EF-hand motifs can interact via hydrogen bonds (Marchand and Roux, 1998). Based on the interaction between the EF-hand motif pairs it was expected that combinatorial effects according to higher  $\text{Sm}^{3+}$  affinity and luminescence would occur, once both motifs were substituted. Similar results were observed for the LBT where multiple copies of the binding loop were used for higher affinities (Daughtry et al., 2012).

The combinatorial variant TS A123W S125E Q159W D161E had 15-fold improved  $\text{Ca}^{2+}$ -triggered luminescence compared to AQ TS and was in the same range as TS A123W S125E.

This could not be observed for the  $\text{Sm}^{3+}$ -triggered luminescence. Although the value was almost doubled ( $0.5 \cdot 10^6$  a.u.) compared to AQ TS ( $0.3 \cdot 10^6$  a.u.), it was lower compared to TS A123W S125E ( $1.7 \cdot 10^6$  a.u.). In consequence, the  $\text{Sm}^{3+}/\text{Ca}^{2+}$  luminescence ratio was not improved towards  $\text{Sm}^{3+}$  either (TS A123W S125E Q159W D161E 0.01 vs. TS A123W S125E 0.8). There was no co-operative effect of the EF-hand motifs visible by luminescence, instead the luminescence was lower.

The  $\text{EC}_{50}$  values for the bright variant TS A123W S125E Q159W D161E did not show co-operative effects regarding higher affinity for both ions ( $120 \mu\text{M Ca}^{2+}/ 230 \mu\text{M Sm}^{3+}$ ) compared to AQ TS ( $50 \mu\text{M}/130 \mu\text{M}$ ). The  $\text{EC}_{50}(\text{Ca}^{2+})$  value was more than two-fold higher, hence TS A123W S125E Q159W D161E needed a higher concentration for 50 % of maximal luminescence. The same could be observed for  $\text{Sm}^{3+}$ -triggered luminescence. The improvements of the  $\text{EC}_{50}$  values for TS A123W S125E were diminished in this new variant.

In summary, the adaption of substitutions at position 7 and 9 of the EF-hand loop 3 did not result in any further improvements regarding higher  $\text{Sm}^{3+}$  affinity or enhanced luminescence activity.

#### 4.2.2.6 Adaption of the Best Substitutions to EF-hand Motif 1

The substitution at position 7 and 9 was also adapted on EF-hand motif 1, which has the lowest affinity for  $\text{Ca}^{2+}$ . EF-hand motif 1 pairs with an inactive EF-hand motif within AQ. (Tricoire et al., 2006) It is also located near to coelenterazine just as EF-hand motif 3 (1.2.2.2 above) and inherits the catalytic triad in the neighboring beta sheets. Substitutions in this EF-hand motif can induce massive changes in the protein's luminescence character but can also lead insolubility of the protein (Tsuzuki et al., 2005; Tricoire et al., 2006).

The variants TS R30W S32E, TS R30W S32E A123W S125E, and TS R30W S32E A123W S125E Q159W D161E were tested on higher  $\text{Sm}^{3+}$  affinity and improved luminescence. Interestingly, all variants showed high  $\text{Ca}^{2+}$ -triggered luminescence with at least 12-times higher luminescence compared to AQ TS. TS R30W S32E and TS R30W S32E A123W S125E had lower  $\text{Sm}^{3+}$  induced luminescence than TS A123W S125E. The variant with substitutions at position 7 and 9 in all three EF-hand motifs (TS R30W S32E A123W S125E Q159W D161E) had 3-times higher  $\text{Sm}^{3+}$  luminescence compared to TS A123W S125E. But due to the higher

Ca<sup>2+</sup>-triggered luminescence, the Sm<sup>3+</sup>/Ca<sup>2+</sup> luminescence ratio was not improved (ratio 0.1) either.

The EC<sub>50</sub> for TS R30W S32E A123W S125E Q159W D161E was twice as good for Sm<sup>3+</sup> (63 vs. 130 μM) and more than two-times lower for Ca<sup>2+</sup> (120 vs. 50 μM) compared to AQ TS. However, it is not comparable to the 20-time decreased EC<sub>50</sub> value for TS A123W S125E and Ca<sup>2+</sup> (3.2.2.3 above).

As previously described, CTZ analogues can further enhance the Sm<sup>3+</sup>/Ca<sup>2+</sup> luminescence ratio. Based on the slightly improved Sm<sup>3+</sup> luminescence of TS R30W S32E A123W S125E Q159W D161E enhancement of luminescence was tested with the CTZ analogues as well.

The increased Sm<sup>3+</sup>/Ca<sup>2+</sup> luminescence ratios observed for semi-synthetic AQ TS and TS A123W S125E with hcp, fcp, and ip were obtained of TS R30W S32E A123W S125E Q159W D161E. The CTZ analogue luminescence assay and EC<sub>50</sub> values confirmed that the improvements of TS A123W S125E were not surpassed with any other variant tested in this work.

Although the luminescence itself was not improved and the indirect affinity measured via EC<sub>50</sub> showed no further improvement compared to TS A123W S125E, the variants containing substitutions of position 7 and 9 in EF-hand motif 1 showed all remarkably long Sm<sup>3+</sup> luminescence half-lives that yielded in a plateau. A long lasting luminescence will be important for *in situ* imaging in cells to find the area of interest within the sample. The reason could be conformational and structural changes induced by the substitutions, similar to the one explained for EF-hand motif 3. The catalytic triade is located near to EF-hand motif 1. Any substitutions or changes in this area can affect the catalytic triade and thus explains the longer luminescence half-lives.

To conclude, adaption of EF-hand motif 1 to the substitutions TS A123W S125E did not show further improvements regarding Sm<sup>3+</sup> affinity or luminescence. Thus, it had improved luminescence half-live even compared to TS A123W S125E.

#### **4.2.3 Contrasting Ability of TS A123W S125E in TEM**

The best variant of saturation mutagenesis and rational design was TS A123W S125E. This variant was tested for the aim to raise contrast in TEM.

Because proteins have typically a diameter of only a few nm and do not consist of heavy atoms AQ TS A123W S125E was immobilized in anti-His<sub>6</sub>-AuNPs via the N-terminal His-tag. This had

the advantage that the enzyme was accumulated around the AuNPs and the AuNPs could be used as positive signal in TEM. A control protein (pumilio) not capable of ion binding was tested as control and prepared for the measurements just as TS A123W S125E (described in 9.7.13 below). To ensure activity the resulting TS A123W S125E-AuNPs were tested for luminescence. Luminescence was detectable of the immobilized enzyme, even though AuNPs are known to quench luminescence. This proves that the luminescence of AQ in general and of TS A123W S125E in particular was significant and the enzyme active after immobilization.

The protein samples were added in a 10-fold excess to the anti-His<sub>6</sub>-AuNPs (14 nm AuNP core) for immobilization for 2 hours at 300 rpm and 25 °C. After the immobilization, the batch was splitted into three. One subset was treated with Sm<sup>3+</sup>, one with Ca<sup>2+</sup>, and one was untreated as control for further 3 h at 300 rpm and 25 °C. Excess of the salt was removed via centrifugation and resuspension in water. The cleaning step was repeated 3 times.

Analysis of TEM images of immobilized TS A123W S125E with Ca<sup>2+</sup>, without any salt and the control protein pumilio treated with Sm<sup>3+</sup> did not show any contrasted areas around the AuNPs. Only the sample of TS A123W S125E and Sm<sup>3+</sup> had additional contrasted areas located near to the AuNPs (ca. 40 nm). This allows the assumption that Sm<sup>3+</sup> was bound to TS A123W S125E. The contrast indicated the probing ability of TS A123W S125E. To verify these findings, EDX scans were used for analysis. These measurements allow elemental analysis. It could be shown that the contrasted areas originated of samarium accumulations and were in good agreement with the contrasted areas in the TEM and SEM imaging.

Although it proved the existence of Sm<sup>3+</sup> in the sample, it did not prove that the Sm<sup>3+</sup> was bound to TS A123W S125E. A match of an overlay of the sulphur and samarium EDX signals were a strong indicator for TS A123W S125E bound to Sm<sup>3+</sup>.

It would have been useful to prove the binding by mass spectroscopy (MS). This was tried with different matrices using MALDI and ESI and HPLC-MS. It was not possible to detect the native enzyme with any of the standard MS techniques. The necessary ionization for MS could not be realized. Alternatives for a Sm<sup>3+</sup> binding analysis could be Saturation-Transfer Difference (STD) NMR (Mayer and Meyer, 1999; Venkitakrishnan et al., 2012), electron diffraction of TS A123W S125E crystals with Sm<sup>3+</sup> or radiographic detection of one of the many Sm isotopes.

Limitations for STD NMR and electron diffraction would be the relatively high amount of protein (5-50 mg) and purity. A protocol for AQ crystals was given in Head *et al.*, who solved the structure in 2000 (Head et al., 2000). Radiographic detection of Sm<sup>3+</sup> binding by using one of the radioactive isotopes of Sm and realized using a protein gel is possible. Nonetheless, special safety

requirements are needed focusing on work safety for the  $\beta$ -radiation and especially for the long half-life for most of the Sm isotopes.

TEM imaging of TS A123W S125E revealed that the desired contrasting ability of AQ could be achieved. Contrasted areas around the AuNPs were detected and could be assigned as samarium located in an area with TS A123W S125E. This was underlined due to the overlay of sulphur and samarium in EDX elemental analysis.

#### **4.2.4 Intracellular Application of TS A123W S125E as Probe in Mammalian Cells**

The experiments with mammalian cells and in-liquid TEM (3.1.2 above) and the contrasting ability of TS A123W S125E paved the way for the final aim of TS A123W S125E as genetically encoded probe in TEM.

The many established different subcellular variants of AQ are summarized in Bonora *et al.* (Bonora *et al.*, 2013). The range of AQ used for imaging in a cell starts in the nucleus (Brini *et al.*, 1993) and ends in the plasma membrane (Marsault *et al.*, 1997). All of these were established to measure  $\text{Ca}^{2+}$  flux that naturally occurred in the cell.

TS A123W S125E was engineered to bind  $\text{Sm}^{3+}$  with higher affinity than  $\text{Ca}^{2+}$ . Samarium was chosen due to the higher mass (150 to 40 u) and because it does not naturally occur in the cell, allowing to switch the luminescence on. Furthermore, it is not toxic as other heavy metal salts.

However, cells selectively transport ions through the plasma membrane into the cytoplasm with specific ion channels. Thus, the incorporation of  $\text{Sm}^{3+}$  into mammalian cells had to be tested before luminescence assay could be performed. The results showed that approximately 20% of the added  $\text{Sm}^{3+}$  were already internalized ( $\sim 70$  nM/cell) into PC3 and LNCaP cells after 60 min incubation. The natural  $\text{Ca}^{2+}$  concentration of a cell can range from a few nM to the mM range. High  $\text{Sm}^{3+}$  affinity is thus essential for the new variant.

The proportion of internalized  $\text{Sm}^{3+}$  was not increased by longer internalization for 24 hours. It could already been shown that after 90 min the concentration drops, which leads to the assumption that the cells transport the  $\text{Sm}^{3+}$  out of the cell after a while. In most of the protocols for imaging of AQ in mammalian cells a reconstitution time for AQ and CTZ of more than 4 hours is given. This focuses the experimental design, if  $\text{Sm}^{3+}$  shall be used for triggering the luminescence. The reconstitution with CTZ should be almost completed before  $\text{Sm}^{3+}$  is added.

Keeping this in mind PC3 cells were transfected with the vector VR1012::TS A123W S125E. The used construct added a HA-tag to the N-terminus of TS A123W S125E for cytoplasmic

localization within the cell. The transfected cells did show a signal in the immunoblot at the height of ~25 kDa and ~50 kDa detected with anti-AQ. This was in good accordance to purified AQ TS as control. The signal at the height of ~50 kDa can be explained by the dimerization of AQ due to the many cysteines and methionines of the enzyme (Ray et al., 1985; Gifford et al., 2007).

TS A123W S125E and AQ wt were confirmed via immunoblot detected with an anti-AQ. Luminescence of cells containing AQ wt and TS A123W S125E with  $\text{Ca}^{2+}$  and  $\text{Sm}^{3+}$  could be detected. Previously described characteristics of the luminescence were also observed for the mammalian cell luminescence assays. CTZ hcp induced higher luminescence with both ions compared to CTZ. The  $\text{Sm}^{3+}$ -triggered luminescence for TS A123W S125E was approximately in the same range as  $\text{Ca}^{2+}$ -triggered luminescence.

The explanation for this observation is the natural intracellular  $\text{Ca}^{2+}$  concentration (varying between nanomolar and millimolar range) that was not blocked in this assay. Mammalian cells have a naturally  $\text{Ca}^{2+}$  household that can interact with AQ and with TS A123W S125E. This means that the actual concentration of  $\text{Ca}^{2+}$  in the cell is higher compared to  $\text{Sm}^{3+}$ , although the same concentration was added to the media. Because of this, the total signal obtained of  $\text{Sm}^{3+}$  triggered cells is lower compared to the *in vitro* assays (3.2.2.3 above).

To circumvent this limitation,  $\text{Ca}^{2+}$  could be complexed by the chelator BAPTA (Collatz et al., 1997) or using oxalates (Lieske et al., 1992) to bind  $\text{Ca}^{2+}$  as salt within the cell. This would reduce the intracellular calcium concentration. Another possibility would be to transfect two different AQ variants. TS A123W S125E and a high  $\text{Ca}^{2+}$  affinity variant that enables binding of free  $\text{Ca}^{2+}$  and emits light before TS A123W S125E does. Here the difference in the emitting wavelength comes into play as the signals temporarily overlap and need differentiation. TS A123W S125E had a 26 nm shift of  $\text{Ca}^{2+}$  triggered luminescence towards 485 nm compared to AQ TS 459 nm. This shift together with a temporal shift can be used to distinguish the variants. Moreover,  $\text{Ca}^{2+}$  SERCA pump inhibitors (summarized in Michelangeli F and East JM) (Michelangeli and East, 2011), of which thapsigargin (Lytton et al., 1991) is the most prominent one, could be used to reduce strong  $\text{Ca}^{2+}$  fluxes. A fully inhibition of  $\text{Ca}^{2+}$  flux would have much greater effect than could be suspected because  $\text{Ca}^{2+}$  is essential for cell signalling (Collatz et al., 1997; Kass and Orrenius, 1999; Pinton et al., 2007).

In order to show the  $\text{Sm}^{3+}$  induced luminescence *in situ* PC3 cells were reconstituted after transfection and triggered with  $\text{Sm}^{3+}$  for Fluorescence-activated cell sorting (FACS) analysis. This method allows the collection of data from single cells. However, it was not possible to obtain luminescence data due to the measuring mode of the FACS that generally uses a laser beam to

induce fluorescence. This overlapped with the luminescence signal of AQ in the cells and could not be switched off.

In summary, the experiments with PC3 cells showed that  $\text{Sm}^{3+}$  was internalized and TS A123W S125E could be produced in the cells. It was also possible to detect luminescence induced by  $\text{Ca}^{2+}$  or  $\text{Sm}^{3+}$  and AQ in PC3 cells. Light microscopy of transfected cells was not possible, yet due to limitations of the microscope.

### 4.3 Combination of In-liquid TEM and Aequorin as a TEM Probe

The best AQ variant TS A123W S125E was used for in-liquid TEM analysis of HEK293T cells transfected with VR1012::TS A123W S125E for protein production.

Images of HEK293T cells without TS A123W S125E were comparable to the observed structures of both PC3 and LNCaP cells showing the nucleus as high contrasted region as well as cellular borders. This shows the general ability of in-liquid TEM also to other mammalian cells and not only to prostate cancer cells.

Human embryonic kidney cells producing TS A123W S125E and incubated with  $\text{SmCl}_3$  had a different imaging profile as their nuclei did not had the highest contrast. Moreover, the cytoplasm seemed to gained contrast, which would be in line with the localization of HA-tagged TS A123W S125E. The HA-tag drives the accumulation of the enzyme in the cytoplasm.

Less dense nuclei were also observed of the LNCaP cells when anti-PSMA-AuNPs were added. Whenever metal ions were present the contrast of the biological specimen declined. This might be due to the higher electron density of the metal ions compared to the low scattering biological specimen that could overexpose the contrast of the biological material. The obtained contrast depends strongly on the overall scattering in the specimen. This means that an internal standard or a fix background signal, which always gives the same contrast, is needed for imaging.

The shown results are only preliminary results that give a hint towards the possibilities of in-liquid TEM in general and TS A123W S125E as a bimodal probe. Further optimization of the nanofluidic cell, such as temperature control or bigger viewing areas would be helpful. The optimization of TS A123W S125E would clearly be a more prominent loss of  $\text{Ca}^{2+}$  binding in terms of use as a bimodal probe. Further, additional  $\text{Sm}^{3+}$  binding sites would be preferable to enhance the contrast. This could be engineered by addition of linkers based on the LTB-tags that were used for MRI imaging (Daughtry et al., 2012).



## 5 Outlook

### 5.1 Experiments using In-liquid TEM

The results of the in-liquid TEM experiments did not only show that biological material such as DNA, RNA, proteins and cells in general are highly stable during electron exposure up to 2 h. The results of the experiments also open the possibility to visualize DNA synthesis in real time.

With the current setting, it would be interesting to image the used DNA1- and DNA2-AuNPs under temperature control during TEM imaging. It could be seen that the DNA strands can further hybridize upon additional energy. Because this energy can also appear as heat and DNA hybridization *in vitro* is normally temperature driven, an upgrade to a holder, which allows temperature control could answer the question if the observed further hybridization was actually such an event. The temperature in the nanofluidic cell during measurements is currently around room temperature. The designed hybridizing units had annealing temperatures calculated to 60 °C.

Moreover, bigger and higher order hybridized structures based on DNA origami (Rothemund, 2006) would be possible by introduction of hybridization units with different annealing temperatures so that stepwise growth of the origami would be visible and different shapes could be created just by temperature control.

For real time analysis of DNA synthesis, very thin liquid layer of only a few nm in height would be necessary. Ideally, the AuNPs would not be needed as contrasting points in the solution, because the DNA contrast would be sufficient. In some cases, it had been possible to see a halo around the AuNPs. Analysis of these particles showed that the halos only occurred when DNA was immobilized on the AuNPs and the liquid layer was very thin. This was the case for the areas near to the edges of the silicon nitride windows, due to less bulging in these areas.

The limiting factor is still the electron dose. Higher dose would allow higher resolution down to the sub-Angstrom regime. To reach this resolution a more powerful electron gun would be needed. Indeed this new electron gun has been engineered in the group of Prof. Miller at the MPI in Hamburg. The gun is called REGAE (*r*elativistic *e*lectron *g*un for *a*tomic *e*xploration). This electron gun can produce electrons that travel almost at relativistic speed. The advantage for biological samples is that the electron-associated damage would quasi occur behind the sample due to the high penetration depth of the ultrafast electrons.

The experiments of the mammalian cells imaged via in-liquid TEM showed that it was possible to obtain well contrasted images without any additional staining or sample preparation such as embedding, dehydration or cryogenic freezing.

However, the clear verification of any cellular component is necessary for interpretation of the data. Thus, well-established staining methods for light microscopy should be combined for bimodal imaging e.g. using AQ to prove the assigned substructures on the same sample. Immunogold labeling would also be possible if the cells are fixed and can be permeabilized for imaging, because it allows dark field light microscopy and in-liquid TEM.

One of the fixed cells was captured during mitosis. The visualization of cell division with high resolution could help to understand the details in this mechanism even better, which is important e.g. to develop new drugs to inhibit accelerated cell division in cancer cells.

Not only cell division is an interesting point for further investigation. There are a lot of diseases caused by cellular dysfunction e.g. Huntington (Rubinsztein and Carmichael, 2003; Pal et al., 2008), Alzheimer (Querfurth and LaFerla, 2010; Ballard et al., 2011), cystic fibrosis (Derichs, 2013) or lysosomal storage disease (Platt et al., 2012). All of the underlying causes such as amyloid fibril accumulation (Kulic et al., 2012), protein degradation (Farinha and Amaral, 2005) or splicing (Garcia-Blanco et al., 2004; Tazi et al., 2009) would be interesting to visualize using in-liquid TEM with the same before mentioned goal.

Cellular transport would be another focus for further experiments. The high contrast of the nucleus is a good starting point for analysis of nuclear transport of RNPs or other cellular components. Especially the visualization of the cellular transport of RNA with molecular resolution in neurons is interesting due to the unique local translation in this type of cells. The discovery of local translation in neurons shed a new light on the function of RNA in cells (Wang et al., 2010; Holt and Schuman, 2013).

First experiments regarding visualization of endocytosis as a cellular transport and key function of cellular homeostasis were tested using the anti-PSMA-AuNPs and LNCaP cells. The mechanism of endocytosis is still a model because it was not possible to image it in real time due to the size range beyond 100 nm with light microscopy. In-liquid TEM could overcome these limitations as the obtained resolution was calculated to 10 nm with a conventional 200 keV electron gun. To achieve a higher resolution a more powerful electron gun would be needed.

Next to the cellular dynamics, virus or bacterial infections and their life cycles within the host cell could also be observed using in-liquid TEM. Viruses were already imaged for a long time using conventional TEM. All images until now are still images and needed the before mentioned sample preparation like all other biological samples. The imaging of viruses *in situ* during

infection without any additional staining could give new answers to their internalization and programming abilities of host cells.

As already described in this chapter a more powerful gun could allow a higher resolution in general on biological specimens while the electron damage would be reduced. This gun could simplify the imaging with in-liquid TEM in terms of resolution but also exposure time. The time during sample preparation and imaging was rather long with up to 30 min and stresses the cells even more. Short exposure with REGAE could achieve the same resolution while the cell would not be in the beam for such a long time. Survival of the imaging process could be an additional benefit, if the cells should be further cultivated for follow-up experiments. This is not possible, yet.

## 5.2 Aequorin as a Bimodal Probe for Electron and Light Microscopy

Aequorin was already widely used for cellular imaging. The new variant has the advantage over the already existing variants that it can be triggered on by an external  $\text{Sm}^{3+}$  signal instead of the intracellular  $\text{Ca}^{2+}$ .

The achieved improvements for TS A123W S125E should be pushed further towards a higher  $\text{Sm}^{3+}$  affinity. The combinatorial variants of either saturation mutagenesis or rational design had no additional impact on the aim. Here, libraries based on TS A123W S125E as parent could result in an even better variant with less  $\text{Ca}^{2+}$  luminescence and brighter  $\text{Sm}^{3+}$  luminescence. A wider emission shift could also be an outcome that is advantageous for imaging comparable to the GFP family with different emission wavelengths. CD spectroscopy showed a structural change of TS A123W S125E compared to AQ TS. Thus, a crystal structure of TS A123W S125E would help to identify the structural changes induced by the substitutions and moreover the coordination of  $\text{Sm}^{3+}$ .

The results showed that the co-operative effect of the EF-hand pairs also has to be taken into account for improved variants. The CASTing procedure could help to find improved variants starting protein design at two neighboring EF-hand motifs as CASTing pairs.

The only bottleneck for these experiments is the high CV that led to a lot of false positive clones. It would be necessary to establish a good HTS based on cell-free protein production to reduce the false positive clones.

As depicted in the aims of this thesis TS A123W S125E should be used to visualize PSMA internalization. PSMA is a well-known protein of which clathrin-mediated endocytosis even tagged with antibodies has been reported (Liu et al., 1998; Goodman Jr. et al., 2007). Hence, it is a good model to study using in-liquid TEM and AQ.

It was reported that AQ could be fused to tags (HA, NLS, His etc.) as long as they are located at the N-terminal side. The C-terminal end is not suitable for fusion because it tucks into the enzyme for stabilization (Head et al., 2000). The fusion of TS A123W S125E would be the next step forward to achieve the aim of a generalized fusion tag in analogy to the GFP-probe concept. Linker lengths need to be tested to obtain the best result. Furthermore, the activity of fused TS A123W S125E has to be verified as well. Although TS A123W S125E was still active after immobilization on quenching AuNPs (3.2.3 above), fusion to such a big protein as PSMA could change TS A123W S125E's activity. One has to keep in mind that the linker is also essential for the activity. The linker could also consist of EF-loops as seen for the MRI LBTs to enhance the number of bound  $\text{Sm}^{3+}$ . This would result in synergistic effects of fusing two proteins together and enhancing the contrast for TEM.

In general, TS A123W S125E could be used as a fusion protein for imaging just as GFP is used. The difference would be that the light emission would need a trigger with  $\text{Sm}^{3+}$ . The clear advantage would be that it could be used bimodal for light and electron microscopy in living cells. All available tags for electron microscopy need further sample preparation (Das et al., 2006; Mercogliano and DeRosier, 2006) or do not allow living cells due to toxic salt accumulation as in ReAsh-tags (Machleidt et al., 2007) or polymerization that leads to cell fixation as for MiniSOG (Shu et al., 2011). Next, the size of the tag can alter the natural function of a protein. Especially for the mentioned metallothioneins, this can be an essential limit as they accumulate some hundred metal ions. TS A123W S125E is a small protein with 25 kDa that binds up to three  $\text{Sm}^{3+}$ , which are suitable to contrast a TEM image to a certain extent. The binding of three  $\text{Sm}^{3+}$  means that the molecular weight of the protein of interest increases in total about 25.5 kDa (sum of AQ and three  $\text{Sm}^{3+}$ ). This is only a fraction compared to the increased weight of metallothioneins.

However, TS A123W S125E or follow-up variants with further improved  $\text{Sm}^{3+}$  binding or even heavier ions could allow bimodal imaging of living cells using in-liquid TEM. This is a major step forward for the understanding of many dynamic processes as transport, DNA synthesis, or even infection and their underlying causes.



## 6 Summary

The work described in this thesis is mainly divided into two strategies for the application of metal ions for imaging. The first part is about the establishment of in-liquid TEM measurements. The experiments were performed in close collaboration with Prof. RJ Dwayne Miller's group at the MPI for structure and dynamics of matter (Hamburg, Germany). Here, DNA coated AuNPs were used, that gave the required contrast for TEM, while the DNA was used to create multimers via hybridization. The DNA hybridization driven AuNP-multimers consisted of at least 3 different AuNPs and exhibit both used sizes (DNA1-AuNPs 60 nm and DNA2-AuNPs 20 nm). These multimers were allowed to form *in vitro* and imaged afterwards with in-liquid TEM using custom-made nanofluidic sample cells made of silicon nitride. The electron dose for imaging was  $110 \text{ e}^- \cdot \text{nm}^2 \cdot \text{s}^{-1}$ . Electron doses above this value led to further multimerization of smaller multimers to big clusters. This was not observed for the controls lacking Hyb-DNA or plain citrate AuNPs. The experiments on DNA-AuNPs showed the low impact of the electron beam according to electron damages of the DNA. The biomolecule proved robustness in the experiments. Based on these good results mammalian PC3 cells were tested. It was possible to visualize subcellular components of the cell such as nucleus, nucleoli, and membranes without any additional staining just by the natural z-contrast of the sample. The cells were maintained without any noticeable damage up to 2 h within the TEM and electron beam. As a follow up live cell imaging was shown. Here, the PC3 cells were not fixed and used directly for in-liquid TEM. In addition, in this samples nucleus, nucleoli, and cell membranes were visible. In fact a certain time point (4 h) during cell settlement on the silicon nitride was chosen in order to image possibly dynamics within the cell. This is why the cell membrane was not observed as distinct line, but showed a mesh-like structure. This observation is in good agreement with the literature. Furthermore, it was possible to detect dynamics of a vesicle or body that moved towards the center of the cell.

The second part shown in this thesis is the engineering of aequorin based on a thermostabilized variant (AQ TS) towards higher  $\text{Sm}^{3+}$  affinity and use as a bimodal probe for fluorescence light and electron microscopy.

Two different approaches were described for the engineering. On the one hand, saturation mutagenesis was performed for each of the 6 ion coordinating amino acid residues of EF-hand motif 2 and one additional position 11 that are normally not essential for ion coordination. The additional position was selected due to the bigger ion diameter of  $\text{Sm}^{3+}$  (122 pm) and trivalency compared to  $\text{Ca}^{2+}$  (114 pm). Saturation mutagenesis yielded in the new variant TS D127R with 3-times improved  $\text{Sm}^{3+}/\text{Ca}^{2+}$  luminescence ratio.

On the other hand, rational design based on lanthanide binding tags (LBT) was performed focusing on position 7 and 9 of the EF-hand motif. These positions were substituted to TS A123W S125E. The substitutions were adapted for each of the three active EF-hand motifs of AQ and combined with each other. The best variant was TS A123W S125E with 40 times higher  $\text{Sm}^{3+}$  affinity while the  $\text{Ca}^{2+}$  affinity dropped 30-fold. TS A123W S125E showed moreover structural changes compared to AQ TS. TS A123W S125E's binding of  $\text{Ca}^{2+}$  induced conformational changes that led to destabilization of the global structure recognized by CD spectroscopy. Binding of  $\text{Sm}^{3+}$  stabilized the enzyme.

The  $\text{Sm}^{3+}/\text{Ca}^{2+}$  luminescence ratio of TS A123W S125E was improved by factor 8. This could be even enhanced using a CTZ analog CTZ hcp (17-fold improved compared to AQ TS with hcp, and 270-fold compared to AQ TS with native CTZ).

TS A123W S125E was tested for contrasting ability in conventional TEM. Therefore, it was immobilized on AuNPs. The samples containing TS A123W S125E and  $\text{Sm}^{3+}$  were the only samples showing additional contrast in the area of AuNPs. This indicated samarium accumulation. To verify the existence of protein in this area and thus binding of  $\text{Sm}^{3+}$  to TS A123W S125E, EDX analysis was used. The signal for samarium and sulphur for the TS A123W S125E was matching in an overlay of the scans, suggesting that there was enzyme near to the  $\text{Sm}^{3+}$ . The control with a non- $\text{Sm}^{3+}$ -binding protein did not show any additional contrast.

After the TEM experiments TS A123W S125E was used in cell culture experiments with prostate cancer cells (PC3). The cells were transfected and protein production verified by immunoblotting. Next, the luminescence ability with  $\text{Sm}^{3+}$  and  $\text{Ca}^{2+}$  was tested with a positive control, AQ wt. CTZ and the enhancing analog hcp were used for luminescence tests and resulted in detectable luminescence for either variant with each CTZ or hcp and  $\text{Sm}^{3+}$  or  $\text{Ca}^{2+}$ .

The aim of an improved AQ variant according to  $\text{Sm}^{3+}$  affinity and contrasting ability in TEM was achieved with the variant named TS A123W S125E.



## 7 Zusammenfassung

In dieser Arbeit wurden zwei verschiedene Strategien für die Anwendung von Metallionen als Sonden für die Mikroskopie beschrieben. Der erste Teil handelt von der Etablierung der In-liquid TEM-Technologie. Die Experimente für diesen Teil wurden in enger Zusammenarbeit mit der Gruppe von Prof. RJ Dwayne Miller am MPI für die Struktur und Dynamic der Materie in Hamburg durchgeführt. Es wurden DNA-umhüllte Gold Nanopartikel (AuNPs) verwendet. Die AuNPs gaben den Kontrast für die Elektronenmikroskopie, während die DNA genutzt wurde um Multimere über DNA-Hybridisierung zu realisieren. Um die einzelnen DNA-AuNPs zu unterscheiden wurden zwei verschiedene Größen verwendet. DNA1-AuNP (60 nm) und DNA2-AuNP (20 nm) trugen zwei verschiedenen einzelsträngige (ss) DNA-Moleküle auf der gesamten Oberfläche, welche nicht miteinander hybridisieren konnten. Nur mit Hilfe einer weiteren ssDNA, der Hyb-DNA, mit komplementären Einheiten für DNA1 und DNA2 war eine Hybridisierung und somit Multimerisierung möglich. Als Multimere wurden nur Gebilde aus mindestens 3 AuNPs gewertet, die unterschiedlicher Größenzusammensetzung waren. Die Hybridisierung wurde *in vitro* durchgeführt und die Proben nachfolgend mittels in-liquid TEM analysiert. Nur in der Probe mit allen nötigen Bestandteilen für die Hybridisierung konnten Multimere in den speziell angefertigten Siliziumnitrit nanofluidischen Zellen detektiert werden. Für die Untersuchungen wurde eine Elektronendosis von  $110 \text{ e}^- \cdot \text{nm}^{-2} \cdot \text{s}^{-1}$  verwendet. Unter dieser Dosis konnte keine Strahlungsschäden der DNA festgestellt werden. Eine höhere Elektronendosis veranlasste weitere Multimerisierung von kleineren Clustern zu größeren Strukturen ausschließlich in der Probe mit allen Komponenten. Das lässt darauf schließen, dass die Bildung von größeren Strukturen ebenfalls auf DNA-Hybridisierung zurückzuführen ist.

Auf Basis der guten Robustheit der DNA wurden mammalische Prostatakarzinomzellen der Linie PC3 auf die Siliziumnitritflächen gesät, fixiert und ohne weitere Probenbehandlung, wie sonst für Elektronenmikroskopie üblich, mittels in-liquid TEM analysiert. Hier waren subzelluläre Strukturen wie Nukleus, Nukleoli und distinkte Membranen sichtbar. Diese Strukturen haben gemeinsam, dass sie einen relative hohen Phosphatanteil durch die Biomoleküle DNA/RNA bzw. Phospholipide aufweisen. Der natürliche Kontrast konnte daher auf z-Kontrast zurückgeführt werden. Die fixierten Zellen zeigten keine strukturellen Veränderungen und konnten bis zu 2 h im TEM analysiert werden. Als nächstes wurden lebende nicht fixierte PC3 Zellen untersucht. Diese zeigten ebenfalls die bereits beschriebenen subzellulären Strukturen. Außerdem wurde als Zeitpunkt die Adhäsionsphase der Zellen nach 4 h gewählt. Daher zeigte die Zellmembran nicht die distinkten Strukturen, sondern ein maschenähnliches Auftreten, das während der Adhäsion wohl bekannt ist. Dieser Zeitpunkt wurde gewählt, um

Dynamiken in der Zelle zu zeigen. Es konnte sogar ein Vesikel oder Körperchen ausgemacht werden, das sich zur Zellmitte hin bewegte.

Der zweite Teil der Arbeit handelt von der Konstruktion einer Aequorin (AQ)-variante basierend auf einer thermostabilisierten Variante (AQ TS) für verbesserte  $\text{Sm}^{3+}$ -Affinität zum Einsatz als bimodale Sonde für Fluoreszenz- und Elektronenmikroskopie.

Zwei verschiedene Herangehensweisen wurden durchgeführt. Auf der einen Seite wurde Sättigungsmutagenese an den einzelnen sechs beteiligten Aminosäure-Positionen für die Metallionenkoordination des konservierten EF-Hand-Motivs 2 von AQ TS durchgeführt. Eine zusätzliche Position wurden ebenfalls analysiert. Position 11 der 12 Aminosäure-langen Schleife wurden vor dem Hintergrund getestet, dass das etwas größere und trivalente Samariumion (122 pm) im Gegensatz zum bivalenten kleineren Calciumion (114 pm) eine erweiterte bzw. andere Koordination innerhalb der Schleife benötigt. Aus der Sättigungsmutagenese aller getesteten Positionen ging nur eine verbesserte Variante hervor. Diese war TS D127R und stammte von Position 11 ab. Sie zeigte ein dreifach verbessertes  $\text{Sm}^{3+}/\text{Ca}^{2+}$  Lumineszenzratio.

Auf der anderen Seite wurde ein rationaler Ansatz basierend auf Lanthanoid-bindenden-tags (LBT) durchgeführt. Dieser Ansatz fokussierte sich auf Position 7 und 9 des EF-Hand Motivs. Für EF-Hand 2 des AQ TS wurden die Substitutionen TS A123W S125E adaptiert. Diese Substitutionen wurden ebenfalls auf die zwei weiteren aktiven EF-Hand-Motive des AQ TS im Einzelnen sowie als Kombinationen übertragen. Dennoch war die beste aller getesteten Varianten TS A123W S125E mit einer 40-fach erhöhten Affinität zu  $\text{Sm}^{3+}$  und gleichzeitiger Verringerung der  $\text{Ca}^{2+}$ -Affinität um Faktor 30. Außerdem zeigte TS A123W S125E strukturelle Veränderungen im Vergleich zu AQ TS. Besonders stark waren diese bei der Bindung von  $\text{Ca}^{2+}$  mittels CD-Spektroskopie zu sehen. Die  $\text{Ca}^{2+}$ -Bindung schien TS A123W S125E zu destabilisieren, während  $\text{Sm}^{3+}$ -Bindung das Enzym stabilisierte.

Das  $\text{Sm}^{3+}/\text{Ca}^{2+}$  Lumineszenzratio konnte für TS A123W S125E im Vergleich zu AQ TS verachtfacht werden. Darüber hinaus verhalf die Rekonstitution mit dem CTZ-Analagon hcp zu einer weiteren Verstärkung des  $\text{Sm}^{3+}/\text{Ca}^{2+}$  Lumineszenzratios um Faktor 17 im Vergleich zu AQ TS mit hcp bzw. um das 270-fache im Vergleich zu AQ TS mit nativem CTZ.

Diese verbesserte Variante TS A123W S125E wurde daraufhin auf ihre beabsichtigte kontrastgebende Eigenschaft für die Elektronenmikroskopie getestet. Hierfür wurde das Enzym auf AuNPs immobilisiert. Die Proben mit TS A123W S125E und  $\text{Sm}^{3+}$  waren die einzigen im Test, die neben den stark kontrastgebenden AuNPs noch weitere kontrastrierte Bereiche zeigten. Die Kontrollen mit  $\text{Ca}^{2+}$ , ohne Salzzugabe oder das Kontrollprotein versetzt mit  $\text{Sm}^{3+}$  zeigten

keinerlei weiteren kontrastreichen Bereiche. Die kontrastreichen Bereiche konnten mittels EDX-Analyse auf die  $\text{Sm}^{3+}$ -Ionen zurückgeführt werden. Um die Bindung des  $\text{Sm}^{3+}$  an TS A123W S125E zu bestätigen, wurde ein EDX-Scan für Schwefel durchgeführt. Die Signale für Schwefel und Samarium aus dem EDX-Scans waren überlappend, sodass davon ausgegangen werden kann, dass die  $\text{Sm}^{3+}$ -Ionen am TS A123W S125E gebunden waren.

Auf die TEM-Experimente aufbauend wurden Zellkulturexperimente mit Prostatakarzinomzellen, PC3, durchgeführt. Die Zellen wurden mit dem Gen für TS A123W S125E transfiziert und die Proteinproduktion mittels Immunoblot und einem Antikörper gegen AQ verifiziert. Die Lumineszenz der Zellen wurde mit  $\text{Sm}^{3+}$  und  $\text{Ca}^{2+}$ , sowie dem nativen CTZ und das verbessernde Analogon hcp getestet. Als Positivkontrolle diente der Wildtyp AQ wt. Lumineszenz war sowohl für TS A123W S125E als auch für AQ wt mit  $\text{Sm}^{3+}$  und  $\text{Ca}^{2+}$  und jeweils CTZ und hcp detektierbar.

Das Ziel eine verbesserte AQ-Variante zu konstruieren, die kontrastgebend in der Elektronenmikroskopie ist und für die Lichtmikroskopie verwendet werden kann, wurde mit der neuen Variante TS A123W S125E realisiert.



## 8 Materials

Consumables used in this work were purchased from Sarstedt (Nümbrecht, Germany) and VWR (Darmstadt, Germany).

### 8.1 Chemicals

All chemical used in this work were purchased from AppliChem (Darmstadt, Germany), Carl Roth (Karlsruhe, Germany) or Life Technologies (Carlsbad, USA). Samarium salts were purchased from Alfa Aesar (Karlsruhe, Germany). Coelenterazine was purchased from NanoLights (Pinetop, USA) and the CTZ analoges from Biotium (Hayward, USA).

### 8.2 Buffer, Media and Solutions

Buffer, media and solutions were dissolved in Millipore water. Buffer for microbiological methods were steril filtered or autoclaved for 20 min at 1.4 bar for sterilization.

Table 7: buffer, media and solutions for microbiological methods.

Buffer	Compounds
<b>Ampicillin stock solution</b>	100 g/L ampicillin in 70 % (v/v) ethanol
<b>Chloramphenicol stock solution</b>	34 g/L chloramphenicol in 100 % ethanol
<b>Kanamycin stock solution</b>	25 g/L kanamycin in ddH <sub>2</sub> O
<b>IPTG stock solution</b>	0.1 M IPTG in ddH <sub>2</sub> O
<b>LB-Agar</b>	25 g/L LB-Medium, 15 g/L Agar
<b>SOC medium</b>	20 g/L tryptone, 5 g/L yeast extract, 0,5 g/L NaCl, 2,5 mM KCl, 10 mM MgCl <sub>2</sub> , 20 mM glucose, pH 7,0
<b>2YT medium</b>	8 g/L tryptone, 5 g/L yeast extract, 2,5 g/L NaCl, pH 7.0
<b>LB media</b>	5 g/L yeast extract, 10 g/L tryptone, 1 g/L NaCl
<b>SOB/TB</b>	20 g/L tryptone, 5 g/L yeast extract, 0.5 g NaCl, 0.186 g KCl, 5g/L glycerol, ad ddH <sub>2</sub> O to 0.9 L. After sterilization: 0.952 g anhydrous MgCl <sub>2</sub> and 2.467 g MgSO <sub>4</sub> (heptahydrate) and 1x phosphate buffer (2.31 g/L KH <sub>2</sub> PO <sub>4</sub> , 12.5 g/L K <sub>2</sub> HPO <sub>4</sub> )

In the following table all buffers and solution used for molecular biological experiments are listed.

**Table 8: Buffers and solutions for molecular biological experiments**

Buffer	Compounds
<b>Ethidium bromide staining solution</b>	4 µg/mL ethidium bromide in 1x TAE
<b>DNA loading dye (6x)</b>	3 mL glycerol (30%), 25 mg bromophenol blue (0.25%), 25 mg xylene cyanol, ad ddH <sub>2</sub> O to 10 mL
<b>RNA loading dye (2x)</b>	95 % ( <i>v/v</i> ) formamide, 0.025 % ( <i>w/v</i> ) SDS, 0.025 % ( <i>w/v</i> ) bromophenol blue, 0.025 % ( <i>w/v</i> ) xylene cyanol, 0.5 mM EDTA
<b>TAE buffer (50x)</b>	2 M Tris-HCl (pH 7.8), 0.25 M sodium acetate, 5mM EDTA
<b>Roti@Hybri-Quick</b>	Carl Roth (Karlsruhe, Germany)
<b>In vitro transcription buffer (3x)</b>	120 mM Tris-HCl (pH 8.1), 15 mM DTT, 6 mM spermidine, 0.03 % ( <i>v/v</i> ) Triton-X-100, 4.5 % ( <i>w/v</i> ) PEG 6000

Buffer used for protein biochemical methods were solved in Millipore water and filtered for sterilization (0.2 µm filter).

**Table 9: buffers and solutions used for protein biochemical methods**

Buffer	Compound
<b>Lysis buffer AQ</b>	100 mM Tris-HCl pH 8, 90 mM NaCl
<b>IMAC buffer AQ A</b>	100 mM Tris HCl pH 8, 5 mM EGTA, 5 mM DTT
<b>IMAC buffer AQ B</b>	100 mM Tris HCl pH 8, 5 mM DTT, 5 mM EGTA and 300 mM imidazole
<b>AEX buffer AQ A</b>	100 mM Tris HCl pH 8, 5 mM DTT, 5 mM EGTA and 20 mM NaCl.
<b>AEX buffer AQ B</b>	100 mM Tris HCl pH 8, 5 mM DTT, 5 mM EGTA and 1 M NaCl
<b>Storage buffer AQ</b>	100 mM Tris HCl pH 8, 5 mM EGTA, 5 mM DTT. Glycerol was added to 50 % ( <i>v/v</i> ) before storage at -20 °C.
<b>Luminescence activity test buffer AQ</b>	100 mM Tris-HCl pH 8, 90 mM NaCl, 1 mM DTT, 5 µM CTZ
<b>HTS lysis buffer</b>	100 mM Tris-HCl pH 8, 90 mM NaCl, 1 mM DTT, 0.1 % Triton-X 100
<b>ITC buffer AQ</b>	50 mM Hepes, 100 mM NaCl, 20 µM TCEP
<b>Tris Tricine gels</b>	
<b>Cathode buffer</b>	100 mM Tris-HCl (pH 8.6), 100 mM tricine, 0.1 % ( <i>w/v</i> ) SDS
<b>Anode buffer</b>	40 mM Tris-HCl (pH 8.9)

<b>Gel buffer (3x)</b>	3 M Tris-HCl, 0.3 % (v/v) SDS, adjust pH to 8.45, add ddH <sub>2</sub> O 250 mL
<b>Protein loading dye (3x)</b>	187.5 mM Tris-HCl (pH 6.8), 30 % (v/v) glycerol, 6 % (v/v) SDS, 0.03 % (w/v) bromophenol blue
<b>Coomassie staining solution</b>	45 % (v/v) ethanol, 10 % (v/v) acetic acid, 0.25 % (w/v) coomassie Brilliant Blue R-250
<b>Coomassie destaining solution</b>	20 % (v/v) acetic acid
<b>Immunoblot</b>	
<b>Transfer buffer</b>	25 mM Tris-HCl (pH 8.3), 192 mM glycine, 20 % (v/v) isopropanol
<b>Block buffer</b>	4 % (w/v) BSA in 1x PBS
<b>PBS (1x)</b>	140 mM NaCl, 2 mM KCl, 10 mM Na <sub>2</sub> HPO <sub>4</sub> , 1 mM KH <sub>2</sub> PO <sub>4</sub>
<b>PBST (1x)</b>	0.1 % (v/v) TWEEN®20 in 1x PBS
<b>Alkaline phosphatase reaction buffer</b>	100 mM Tris (pH 9.5), 4 mM MgCl <sub>2</sub>
<b>NBT stock solution</b>	50 mg/mL in 70 % (v/v) DMF
<b>BCIP stock solution</b>	0.5 % (w/v) in 70 % (v/v) DMF
<b>Additional solutions</b>	
<b>EGTA stock solution</b>	0.5 M EGTA pH 8 dissolved in ddH <sub>2</sub> O
<b>MgCl<sub>2</sub></b>	100 μM in ddH <sub>2</sub> O
<b>CaCl<sub>2</sub></b>	100 μM in ddH <sub>2</sub> O
<b>SmCl<sub>3</sub></b>	100 μM in ddH <sub>2</sub> O

The following table shows the media used for mammalian cell culture methods

**Table 10: Media and solutions for cell culture experiments**

<b>Media</b>	<b>Compounds</b>
<b>PC3 media</b>	1:1 RPMI1640 and Ham's F12 media (Gibco, Carlsbad, USA) supplemented with 10 % FCS and 1% P/S
<b>LNCaP media</b>	RPMI 1640 media (Gibco, Carlsbad, USA) supplemented with 20 % FCS and 1% P/S
<b>Internalization media</b>	RPMI 1640, 10 % HEPES, 1% P/S
<b>Fixation buffer</b>	4 % paraformaldehyde in 1xPBS
<b>PBS</b>	Lonza (Basel, Swiss)
<b>Pencillin streptomycin (P/S)</b>	Gibco (Carlsbad, USA)
<b>Fetal calf serum (FCS)</b>	Lonza (Basel, Swiss)
<b>HEPES stock solution</b>	Gibco (Carlsbad, USA)

### 8.3 Gold Nanoparticles

Gold nanoparticles were a kind gift of Centrum für angewandte Nanotechnologie (CAN, Hamburg, Germany).

Citrate stabilized AuNPs with diameters of 10, 14, 20 and 60 nm were used in this work.

### 8.4 Oligonucleotides

All used oligonucleotides used in this work are listed in the following table.

Table 11: Oligonucleotides used in this work.

Name	Sequence 5'-3'
<b>In-liquid TEM experiments</b>	
<b>DNA1</b>	<b>TAA GTC TAC GTT GCC AGA CGA</b> AAA AAA AAA-SH
<b>DNA2</b>	HS-AAA AAA AAA AT CGG GCG AGT CGT CTG <u>TCG TCG</u> <u>TCG TCG TCG TCG TCG</u>
<b>Control DNA</b>	GCG TTT TCG CTT TTG CGT TTT GGG TCA TCT GCT TAC GAT AGC AAT GCT CGG CTT TTT TTT TTT TTT TTG CCG
<b>Hyb-DNA</b>	TCG GGC GAG <b>TCG TCT GGG AAC GTA GAC TTA</b> GTA TAG AAG TCA GGT CTT TTT CGG TCC GCA TCG TCC <u>TCC CGA CGA CGA CGA CGA CGA CGA</u>
<b>Anti-PSMA A9</b>	GGG AGG ACG AUG CGG ACC GAA AAA GAC CUG ACU UCU AUA CUA AGU CUA CGU UCC CAG ACG ACU CGC CCG ACG ACG ACG ACG ACG ACG ACG A
<b>Scrambled Anti-PSMA A9</b>	GGG AGG ACG AUG CGG CAG GCA UGC CUA GCU AAG CAG CCC AUG GCU UAU GCG CGG ACA GAC GAC UCG CCC <u>GAC GAC GAC GAC GAC GAC GAC GA</u>
<b>5'-thiol modified capture DNA</b>	5-HS-CC-AAA AAA AAA A- <u>TCG TCG TCG TCG TCG TCG</u> <u>TCG</u>
<b>T7 RNA Pol Primer</b>	TAA TAC GAC TCA CTA TAG GGA GGA CGA TGC GG
<b>Anti-PSMA back</b>	TCG TCG TCG TCG TCG TCG TCG TCG GGC GAG TCG TCT G
<b>Anti PSMA middle</b>	TCG GGC GAG TCG TCT GGG AAC GTA GAC TTA GTA TAG AAG TCA GGT CTT TTT CGG TCC GCA TCG TCC TCC C
<b>Scrambled PSMA middle</b>	TCG GGC GAG TCG TCT GTC CGC GCA TAA GCC ATG GGC TGC TTA GCT AGG CAT GCC TGC CGC ATC GTC CTC CC
<b>Engineering of Aequorin</b>	
<b>T7 prom seq fw</b>	TAA TAC GAC TCA CTA TAG GG
<b>AQ fw Xho I</b>	CGA GCT <u>CGA GAA CAA</u> TGC TTA CA
<b>AQ rev Eco RI</b>	AGC TTC <u>GAA TTC</u> CAT GGT ACC AC
<b>NNK libraries</b>	
<b>D117X</b>	GTT <u>NNK</u> AAA GCC CAA AAT GG
<b>D119X</b>	ATT GAC AAA <u>NNK</u> CAA AAT GGA
<b>N121X</b>	AAA GAC CAA <u>NNK</u> GGA GCT ATT
<b>A123X</b>	CAA AAT GGA <u>NNK</u> ATT TCA CTG
<b>S125X</b>	GGA GCT ATT <u>NNK</u> CTG GAT GAA



<b>D127X</b>	GCT ATT TCA CTG <u>NNK</u> GAA TGG AAA G
<b>E128X</b>	ATT TCA CTG GAT <u>NNK</u> TGG AAA G
<b>CASTing 117/128</b>	GTT <u>NNK</u> AAA GCC CAA AAT GGA GCC ATT TCA CTG GAT <u>NNK</u> TGG
<b>Rational Design</b>	
<b>D119A fw</b>	GAT ATC ATT GAC AAA <u>GCC</u> CAA AAT GGA
<b>A123W fw</b>	AAA GAC CAA AAT GGA <u>TGG</u> ATT
<b>A123F fw</b>	AAA GAC CAA AAT GGA <u>TTT</u> ATT
<b>S125E fw</b>	GGA GCT ATT <u>GAA</u> CTG GAT
<b>S125D fw</b>	GGA GCT ATT <u>GAC</u> CTG GAT
<b>S125G fw</b>	GGA GCC ATT <u>GGA</u> CTG GAT
<b>S125R fw</b>	GGA GCC ATT <u>AGA</u> CTG GAT
<b>D127R fw</b>	GCT ATT TCA CTG <u>CGG</u> GAA TGG AAA G
<b>E128G fw</b>	GCT ATT TCA CTG GAT <u>GGA</u> TGG AAA G
<b>Q168R L171I fw</b>	TGA GAT GAC <u>AAG</u> <u>ACG</u> ACA TAT <u>AGG</u> ATT T
<b>D119A A123F fw</b>	GAC AAA <u>GCC</u> CAA AAT GGA <u>TTT</u> ATT TCA
<b>A123F S125D fw</b>	CAA AAT GGA <u>TTT</u> ATT <u>GAC</u> CTG GAT
<b>D119A A123F S125E fw</b>	AAA <u>GCC</u> CAA AAT GGA <u>TTT</u> ATT <u>GAA</u> CTG
<b>A123F S125E D127R fw</b>	AAT GGA <u>TTT</u> ATT <u>GAA</u> CTG <u>CGG</u> GAA
<b>D119A A123F S125E D127R fw</b>	AAA <u>GCC</u> CAA AAT GGA <u>TTT</u> ATT <u>GAA</u> CTG <u>CGG</u> GAA
<b>D119A A123W S125E fw</b>	AAA <u>GCC</u> CAA AAT GGA <u>TGG</u> ATT <u>GAA</u> CTG
<b>D119A A123W S125E D127R fw</b>	AAA <u>GCC</u> CAA AAT GGA <u>TGG</u> ATT <u>GAA</u> CTG <u>CGG</u> GAA
<b>A123W S125E D127R fw</b>	AAT GGA <u>TGG</u> ATT <u>GAA</u> CTG <u>CGG</u> GAA
<b>Q158W D160E D162R fw</b>	GAA AGT GGA <u>TGG</u> CTC GAA GTT
<b>R30W S32E fw</b>	AAT GGA <u>TGG</u> ATC <u>GAA</u> CTT GAC
<b>R30F S32D fw</b>	AAT GGA <u>TTT</u> ATC <u>GAT</u> CTT GAC
<b>Cloning of TS A123W S125E into VR 1012</b>	
<b>NheI fw</b>	CCG AGC <u>GCT</u> AGC CTC <u>AAA</u> CTT ACA CCA
<b>PstI rev compl</b>	TGG TAC CGC GGC CGC <u>TCA</u> GTC

## 8.5 Enzymes and Proteins

All enzymes were purchased from Thermo Scientific (Schwerte, Germany). Enzymes were supplied with reactions buffers. Proteins were purchased from AppliChem (Darmstadt, Germany). Enzymes and proteins used in this work are listed in the following table.

Table 12: Enzymes and proteins used in this work.

Enzyme/Protein	Manufacturer
<b>BSA</b>	AppliChem (Darmstadt, Germany)
<b>Lysozyme</b>	AppliChem (Darmstadt, Germany)
<b>FIREPol® DNA Polymerase [5 U/ <math>\mu</math> L]</b>	Solis BioDyne (Nivelles, Belgium)
<b>Phusion DNA Polymerase</b>	Thermo Scientific (Schwerte, Germany)
<b>EcoRI Fast Digest</b>	Thermo Scientific (Schwerte, Germany)
<b>NdeI Fast Digest</b>	Thermo Scientific (Schwerte, Germany)
<b>XhoI Fast Digest</b>	Thermo Scientific (Schwerte, Germany)
<b>NheI Fast Digest</b>	Thermo Scientific (Schwerte, Germany)
<b>PstI Fast Digest</b>	Thermo Scientific (Schwerte, Germany)
<b>DpnI</b>	Thermo Scientific (Schwerte, Germany)
<b>FastAP</b>	Thermo Scientific (Schwerte, Germany)
<b>T4 DNA Ligase</b>	Thermo Scientific (Schwerte, Germany)
<b>T7 RNA polymerase</b>	Own production
<b>T7 Y639F RNA polymerase</b>	Own production
<b>DNaseI</b>	AppliChem (Darmstadt, Germany)
<b>AQ variants</b>	Listed separately in the Appendix, own production

## 8.6 Commercially Available Kits and Columns

The following table lists all used commercially available kits and columns used for the described experiments.

Table 13: Commercially available kits and columns

Kit	Manufacturer
<b>HiYield® Plasmid Mini Kit</b>	Süd-Laborbedarf (Gauting, Germany)
<b>HiYield® Gel/PCR DNA Fragment Extraction Kits</b>	Süd-Laborbedarf (Gauting, Germany)
<b>HiTrap™ FF 1 mL column</b>	GE Healthcare (Munich, Germany)
<b>HiTrap DEAE FF 1 mL column</b>	GE Healthcare (Munich, Germany)
<b>Superdex 200</b>	GE Healthcare (Munich, Germany)

## 8.7 Nucleotides

Nucleotides used in this work are listed below. dNTPs were used in a mixture (25 mM). NTPs were mixed to 10 mM solutions.

Table 14: Nucleotides used in this work.

Nucleotide	Manufacturer
<b>Desoxyribonukleosidtriphosphate (dNTP)</b>	Thermo Scientific (Schwerte, Germany)
<b>Ribonukleosidtriphosphate (NTP)</b>	Thermo Scientific (Schwerte, Germany)
<b>2'-Fluoro-2'-dCTP</b>	TriLink BioTechnologies (San Diego, USA)
<b>2'-Fluoro-2'-dUTP</b>	TriLink BioTechnologies (San Diego, USA)

## 8.8 Antibodies

Antibodies used for immunoblotting and immobilization are given in table below.

Table 15: Antibodies used in the experiments.

Antibodies	Manufacturer	Solution
<b>Anti-His<sub>6</sub> IgG mouse</b>	5-PRIME (Hamburg, Germany)	1:20,000 ( <i>v/v</i> ) in 1% BSA in PBS
<b>Anti-mouse IgG goat AP</b>	Sigma Aldrich (Munich, Germany)	1:50,000 ( <i>v/v</i> ) in 1% BSA in PBS
<b>Anti-AQ IgG mouse</b>	Genetex	1:10,000 ( <i>v/v</i> ) in 1% BSA in PBS
<b>Anti-GFP IgG mouse</b>	Roche Diagnostics (Indianapolis, USA)	1:10,000 ( <i>v/v</i> ) in 1% BSA in PBS

## 8.9 Bacteria

For this thesis following bacteria were used and listed in the following table.

Table 16: All bacteria used in the work

Strain	Genotype
<b>BL21(DE3)</b>	F <sup>-</sup> omp <sup>T</sup> gal dcm lon hsdS <sub>B</sub> (r <sub>B</sub> <sup>-</sup> m <sub>B</sub> <sup>-</sup> ) λ(DE3 [lacI lacUV5-T7 gene 1 ind1 sam7 nin5])
<b>BL21(DE3)pLysS</b>	F <sup>-</sup> omp <sup>T</sup> gal dcm lon hsdS <sub>B</sub> (r <sub>B</sub> <sup>-</sup> m <sub>B</sub> <sup>-</sup> ) λ (DE3) pLysS(cm <sup>R</sup> )
<b>BL21(AI)</b>	F <sup>-</sup> omp <sup>T</sup> gal dcm lon hsdS <sub>B</sub> (r <sub>B</sub> <sup>-</sup> m <sub>B</sub> <sup>-</sup> ) araB::T7RNAP-tetA
<b>TOP10</b>	F <sup>-</sup> mcrA Δ(mrr-hsdRMS-mcrBC) ϕ80lacZΔM15 ΔlacX74 nupG recA1 araD139 Δ(ara-leu)7697 galE15 galK16 rpsL(Str <sup>R</sup> ) endA1 λ <sup>-</sup>

## 8.10 Plasmids

The list of used Plasmids is given in Table 17.

**Table 17: List of used plasmids in this work**

<b>Name</b>	<b>Important elements</b>
<b>pRSET::AQ wt</b>	Generous gift of PD Dr. Plieth (CAU Kiel, Germany) Gene for wildtype AQ, N-terminal His-tag
<b>pRSET::LAAQ</b>	Generous gift of PD Dr. Plieth (CAU Kiel, Germany) Gene for low Ca <sup>2+</sup> affinity AQ, N-terminal His-tag
<b>VR1012::AQ wt</b>	Generous gift of Prof. Rizzuto (Padua, Italy) Viral vector for transfection of mammalian cells with the gene for AQ wt. N-terminal HA-tag extension.

Plasmids carrying the genes for AQ generated during this work are not listed. All variants are given in an overview table in the appendix.

## 8.11 Mammalian Cells

The mammalian cells used for this work are listed in the table below.

**Table 18: Mammalian cells used for cell experiments.**

<b>Strain</b>	<b>Genotype</b>
<b>PC3</b>	Human prostate cancer cells, PSMA negative
<b>LNCaP</b>	Human prostate cancer cells, PSMA positive
<b>HEK293T</b>	Human embryonic kidney cells

## 8.12 Software

For data processing, different softwares were used. Table shows a list of the used software.

**Table 19: Software used in this work for data processing and analysis.**

<b>Name</b>	<b>Manufacturer</b>
<b>Origin® 8.5 OG SR1</b>	OriginLab Corporation (Northampton, USA)
<b>Adobe Illustrator ®</b>	Adobe systems (Delaware, USA)
<b>LabImage 1D</b>	Kapelan (Leipzig, Germany)
<b>i-control™ v. 1.7</b>	TECAN Group Ltd (Männedorf, Swiss)
<b>OligoCalc web server v. 3.26</b>	W. A. Kibbe (Northwestern University, Chicago, USA)
<b>PyMOL v. 1.5.0.4</b>	Schrödinger, LLC
<b>Unicorn v. 6.3.2</b>	GE Healthcare (Munich, Germany)
<b>ImageJ</b>	NIH (Bethesda, USA)
<b>Vector NTI</b>	Invitrogen (Carlsbad, USA)

## 9 Methods

### 9.1 General Molecular Biological Methods

#### 9.1.1 Polymerase Chain Reaction

Polymerase chain reaction (PCR) after Mullis *et al.* (Mullis et al., 1986) was performed to produce multiple copies of a desired DNA section. For the reaction thermostable Phusion DNA polymerase (Thermo Scientific, Germany) was used. Reactions were mixed according to the manufacturer's protocol. The annealing temperature was calculated for each primer using oligo calc. The reaction volume differed between 20-100  $\mu\text{L}$ . A schematic reaction mix for 50  $\mu\text{L}$  is shown in Table 20

**Table 20: Schematic reaction mix for PCR with Phusion Polymerase**

Component	Volume ( $\mu\text{L}$ )	End concentration
5x High Fidelity buffer	10	1x
5' Primer (10 $\mu\text{M}$ )	2.5	25 pmol
3' Primer (10 $\mu\text{M}$ )	2.5	25 pmol
Template (10 ng/ $\mu\text{L}$ )	5	50 ng
dNTPs (25 mM)	1	25 pmol
Phusion	0.5	
ddH <sub>2</sub> O ad 50 $\mu\text{L}$	28.5	

The elongation duration was calculated to the product length. The number of cycles varied between 20-30 repetitions. A typical PCR program is listed in Table 21.

**Table 21: Schematic temperature program for a PCR with Phusion**

PCR step	Temperature ( $^{\circ}\text{C}$ )	Time (s)
Initial denaturation	98	90
Denaturation	98	10
Annealing	55-70	30
Elongation	72	30
Final elongation	72	300

#### 9.1.1.1 MEGAWHOP PCR

MEGAWHOP (Mega primer whole plasmid) PCR was used for cloning of new variants and libraries without ligation. A short PCR product is first synthesized with a normal PCR reaction (50-3000 bp). This PCR product is designated as megaprimer. In a second PCR, the MEGAWHOP PCR, the whole plasmid is amplified with the megaprimer.

**Table 22: Schematic reaction mix for PCR with Phusion Polymerase**

Component	Volume ( $\mu\text{L}$ )	End concentration
5x High Fidelity buffer	20	1x
megaprimer	15	25 pmol
Template (10 ng/ $\mu\text{L}$ )	5	50 ng
dNTPs (25 mM)	2	25 pmol
Phusion	1	
ddH <sub>2</sub> O ad 100 $\mu\text{L}$	57	

The elongation duration was calculated to the product length which depends on the used vector.

**Table 23: Schematic temperature program for a PCR with Phusion**

PCR step	Temperature ( $^{\circ}\text{C}$ )	Time (s)	
Initial denaturation	98	90	
Denaturation	98	10	30 x
Annealing	45	60	
Elongation	72	300	
Final elongation	72	420	

After amplification of the new nicked circular DNA the template plasmid is removed via digestion with DpnI, a dam-methylated DNA-specific restriction enzyme for 1 h at 37 $^{\circ}\text{C}$ . The mixture was cleaned via isopropanol precipitation at -20  $^{\circ}\text{C}$  for 1 h. The mixture of isopropanol and reaction mixture was 1:1. The DNA was pelleted at 4 $^{\circ}\text{C}$  21,000 xg for 20 min. The supernatant was removed, pellet dried at RT and resuspended in 30  $\mu\text{L}$  ddH<sub>2</sub>O.

### 9.1.1.2 Colony PCR

Colony PCR is a common procedure to identify colonies after transformation of E.coli that contain the new genetic information. To do so the colonies are mixed with in 20  $\mu\text{L}$  water to a suspension. A PCR master mix is prepared (Table 24) and the colony suspension mixed with the PCR master mix for reaction. The plasmid DNA in the bacteria cells get into the reaction upon heating of the bacteria cells.

**Table 24: Schematic reaction mix for a colony PCR (6 samples) with FirePol**

Component	Volume ( $\mu\text{L}$ )	End concentration
10x PCR buffer	12	1x
MgCl <sub>2</sub> 25 mM	12	1x
5' primer 10 $\mu\text{M}$	2.4	2.5 $\mu\text{M}$
3' primer 10 $\mu\text{M}$	2.4	2.5 $\mu\text{M}$
dNTPs (25 mM)	0.96	6.25 mM
FirePol (5 U/ $\mu\text{L}$ )	0.6	1 U
ddH <sub>2</sub> O (ad 120 $\mu\text{L}$ )	71.5	

3  $\mu\text{L}$  of colony water as template mixed with 17  $\mu\text{L}$  PCR reaction mix

The elongation duration was calculated to the product length.

**Table 25: Schematic temperature program for a colony PCR with FirePol**

PCR step	Temperature ( $^{\circ}\text{C}$ )	Time (s)	
Initial denaturation	95	60	
Denaturation	95	10	20 x
Annealing	53	30	
Elongation	72	30	
Final elongation	72	300	

The product is analyzed on a 1% agarose gel afterwards.

## 9.1.2 Sequencing

To verify cloning of a new construct the samples were sequenced at GATC Biotech (Konstanz, Germany). The protocol used for sequencing follows Sanger et al. 100 ng of DNA were mixed with 5 ng priming oligonucleotides and sent to GATC Biotech for sequencing.

## 9.1.3 Gel Electrophoresis

### 9.1.3.1 Agarose gel Electrophoresis

Agarose gels were used to separate DNA with a size range of 200-8000 bp. Melted agarose forms a mesh during the cooling process which serves as a matrix for the separation of DNA molecules according to their length. As DNA is negatively charged due to the phosphate backbone, the molecules will migrate towards the cathode. Typically, a 1% *w/v* agarose gel in 1x TAE buffer was used for analysis of PCR or restriction reactions.



### 9.1.3.2 PAA gel Electrophoresis

DNA or RNA oligonucleotides beyond 100 nt/bp were analyzed on denaturing or native polyacrylamide (PAA) gels. Denaturing PAA gels, for analysis of length, were poured with 8M urea. Urea is the detergent that allows separation to single stranded DNA or RNA. Native PAA gels without urea were used to analyze hybridization of two strands. Here, the hybridization is not prohibited. According to the length of the molecules different percentages of gels can be chosen. Typically, 10% (*v/v*) denaturing and native PAA gels were used.

Table 26: Composition of an denat. PAA

Component	End concentration
Acrylamid/ <i>N,N</i> '-Methylenbisacrylamid (19:1)	10 % ( <i>v/v</i> ) in 1x TAE
Urea	8 M
TEMED	0.1 % ( <i>v/v</i> )
APS	0.07% ( <i>v/v</i> )

### 9.1.4 Detection of DNA or RNA in gel Electrophoresis

For visualization of DNA and RNA in a gel matrix intercalating ethidium bromide followed by UV light excitation at 255 nm was used.

### 9.1.5 Second Strand Synthesis

Single stranded DNA was turned into double stranded DNA by enzymatic reaction of the Klenow exo- fragment. For reaction the manufacturer's protocol was used.

### 9.1.6 *In vitro* Synthesis of RNA

RNA can be transcribed *in vitro* from a DNA template with a T7 RNA Polymerase. For this reaction a double stranded priming section on the template is necessary for binding of the T7 RNA polymerase. Furthermore the reaction requires Mg<sup>2+</sup> ions and NTPs. Optimal reaction temperature is 37°C.

A schematic reaction mix is listed in Table 27.

**Table 27: Schematic reaction mix for a colony PCR (100  $\mu$ L) with FirePol**

<b>Component</b>	<b>Volume (<math>\mu</math>L)</b>	<b>End concentration</b>
Transcription buffer 3x	33	1x
MgOAc 300 mM	3	9 mM
DNA template	5	10 ng/ $\mu$ L
NTPs (25 mM)	10	0.25 mM
T7 DNA polymerase	10	
ddH <sub>2</sub> O (ad 120 $\mu$ L)	39	

Reaction was carried out for 4 h at 37°C. DNA was digested with DNase I incubation for 10 min at 37 °C followed by inactivation for 10 min at 70 °C.

## 9.2 Protein Biochemistry Methods

### 9.2.1 Discontinuous Tris Tricine PAA gel Electrophoresis

Next to RNA or DNA proteins were analyzed on 10% discontinuous tris tricine PAA gels according to their molecular weight. The gel consists of two units, a resolving unit at the bottom and a stacking unit on top to focus the samples. The discontinuous buffer system uses two different pH values (cathode buffer pH 8.6, anode buffer pH 8.9) which results in higher separation resolution. The gel matrix is built by polymerization of acrylamide initiated with TEMED and APS.

Table 28: discontinuous 10% tris tricine PAA gels for protein analysis

	component	Volume	component	Volume
<b>Resolving gel</b>	Acrylamid (37%)	10 mL	Acrylamid (37%)	3.2 mL
	Gel buffer (3x)	10 mL	Gel buffer (3x)	6.2 mL
	ddH <sub>2</sub> O	6.3 mL	ddH <sub>2</sub> O	15.6 mL
	Glycerol (87%)	3.65 mL		
	APS (10%)	150 $\mu$ L		
	TEMED	15 $\mu$ L	TEMED	15 $\mu$ L
<b>Stacking gel</b>				

The protein samples are overload with negatively SDS using a 3x sample buffer and denatured by heating to 95°C for 5 min prior to separation. Typically for focusing in the stacking gel 100V are used, while separation in the resolving gel is done with 140 V.

### 9.2.2 Visualization of Proteins in Tris Tricine Gels with Coomassie Blue

After separation using TT gels the proteins can be stained with coomassie blue. The chromophor binds unspecific to the protein. Excess of coomassie in the gel matrix can be washed out with a 20% acetic acid solution until only the protein bands remain.

### 9.2.3 Immunoblot

Immunoblotting was used to verify proteins. Samples were separated in 10% TT PAA gels and immobilized on a nitrocellulose membrane by semi-dry blotting for 45 min with 80 mA/blot. To reduce unspecific binding, proteins were blocked with 4% BSA in PBS solution for 45 min at RT prior to primary antibody reaction.

Typically, an anti-His<sub>6</sub> antibody produced in mouse was used to detect purified His-tagged protein. Detection occurred via a secondary anti-mouse antibody conjugated to alkaline

phosphatase. Alkaline phosphatase was used for colorimetric detection with BCIP and NBT that react to an indigo chromophor.

#### **9.2.4 Protein Concentration Determination Using Bradford Assay**

Protein concentration was determined using the colorimetric Bradford assay in 96-multiwell plates. A commercially Bradford solution was used (RotiQuant, Roth, Germany). The samples were tested along a BSA standard with known concentration. Read out occurred at 595 nm in a TECAN infinite multiplate reader (M200 Pro, Tecan, Swiss). The concentration of the sample was calculated using linear regression of the BSA standard.

### **9.3 General Microbiological Methods**

#### **9.3.1 Transformation of *E. coli* Cells**

Electro competent Bl21(DE3)pLysS cells were transformed with plasmid DNA via electroporation (Electroporator, Eppendorf, Germany). For purified plasmids 10 ng DNA was used, while approximately 30 ng DNA used for megawhop constructs. Cells were mixed with DNA in an ice-cold electroporation cuvette and XY mA used. Pre-warmed SOC media was applied immediately after electroporation to the cells and these incubated for 30 min at 37°C and 300 rpm for recovery. Cells were then pelleted at 700 xg for 3 min for plating on LB agar plates or direct inoculation in 2YT media for overnight culture.

#### **9.3.2 Overnight Culture**

Overnight cultures were grown for preparation of plasmid DNA or protein production. In a volume of 2 mL 2YT media with selection antibiotics freshly transformed cells or a clone of a LB agar plate was inoculated and the culture incubated for 18h at 37°C and 180 rpm.

#### **9.3.3 Preparation of Plasmid DNA**

For plasmid DNA preparation a commercially available Kit (Südlabor) was used. Plasmid DNA was extracted of Bl21(DE3)pLysS cells. A yield of 120-380 ng/ $\mu$ L was achieved.

## 9.4 Cell culture

### 9.4.1 Cultivation of Prostate Cancer 3 Cells

Prostate cancer 3 cells (PC3) were cultivated in 1:1 RPMI1640 and Ham's F12 media (Gibco) supplemented with 10 % FCS and 1% P/S at 37°C and 5% CO<sub>2</sub>.

### 9.4.2 Cultivation of LNCaP Cells

LNCaP cells were cultivated in RPMI1640 media (Gibco) supplemented with 20 % FCS and 1% P/S at 37°C and 5% CO<sub>2</sub>.

### 9.4.3 Transfection of PC3 Cells

For the transfection of PC3 cells the cells were trypsinized. The cells in solution were counted and divided in aliquots (10<sup>5</sup> cells/750 µL for one well on a 6 well plate). The vector DNA VR1012::TS A123W S125E or VR1012::AQ wt were diluted to 1 µg in Opti-MEM (Gibco) with a final volume of 250 µL. The vector Opti-MEM solution was preincubated with 9 µL Fugene HD for 10 min at RT. Next, the mixture was carefully mixed by pipetting and pipetted dropwise to the cell aliquots and incubated for 5 min.

After the incubation step, the cells were seeded into the 6-well plate and cultivated as usual.

### 9.4.4 Immunofluorescence Sample Preparation

Cells were washed twice with PBS (1x) and fixed on coverslides with a 4% paraformaldehyde / PBS solution for 10 min at room temperature. Afterwards, cells were washed twice with PBS (1x) and stored in ddH<sub>2</sub>O until permeabilization. To permeabilize the cells a PBS Triton X-100 (0.3%) solution was used. Cells were incubated 30 min at room temperature with the permeabilization solution. To minimize unspecific binding the cells were washed with PBS-Tween (PBST, 0.01%) twice for 2 min on an elliptical incubator and treated with 1% BSA in PBST for 30 min on the elliptical incubator. Next, the cells were washed again twice for 1 min with PBST. Antibody treatment with the primary antibody occurred at room temperature for 30 min (1:1000 in PBST). Before treatment with the secondary labeled antibody, the cells were washed twice with PBST for 1 min. Incubation duration with the secondary antibody solution (1:2000) was 30 min at room temperature, followed by two washing steps with PBST for 1 min. Cells were either stored in PBS until microscopy analysis, or treated with Hoechst 33258 (1:10000 in PBST) for 5 min for counterstaining of the nucleus.

#### **9.4.5 Sample Preparation for GF-AAS Elemental Analysis for Samarium**

Cells were seeded at the desired density 24h before addition of  $\text{SmCl}_3$ . After incubation with  $\text{SmCl}_3$  the cells were washed twice with PBS and kept in media after washing. The cells were detached with trypsin-EDTA in order to count the cell density. The final cell solutions had a concentration of  $10^5$  cells/100  $\mu\text{L}$ . These were lysed using 50  $\mu\text{L}$  0.1 % Triton-X 100 solution dissolved in Tris-HCl pH 10. The lysis was checked via light microscopy.

Graphite furnace atomic absorption spectrometry (GF-AAS) requires an acidic matrix, preferable  $\text{HNO}_3$ , so that the cell lysate was diluted to 1 M  $\text{HNO}_3$  and a final volume of 500  $\mu\text{L}$ . This solution was supplied to Tuborg Krugmann (Central element analysis, Institute for inorganic chemistry, University of Hamburg) for analysis.

### **9.5 Microscopy**

#### **9.5.1 Fluorescence Confocal Light Microscopy**

Point scanning and confocal laser scanning microscopy of cells were achieved with an Olympus FluoView™ FV1000 microscope.

#### **9.5.2 Electron Microscopy**

Electron microscopy was carried out in cooperation with Prof. Dr. RJ Dwayne Miller at CFEL with an JEOL 2000 and a custommade liquid cell holder.

## 9.6 Gold Nanoparticles for Imaging

### 9.6.1 Coupling of Oligonucleotides to Gold Nanoparticles

Thiol modified DNA oligonucleotides were used for DNA-AuNP hybrids. The reaction was modified from Mirkin et al. For coupling approximately 176 oligonucleotides per AuNP was calculated in a volume of 2 mL. The calculated volume of thiol modified DNA was added to the AuNP solution and incubated under gently shaking for 18 hours. Free surface was stabilized with stepwise addition of NaCl (1 M stock solution, final concentration 0.1 M) and sodium phosphate buffer (pH 8.0, 1 M stock solution, final concentration 0.1 M) over 10 hours and further incubation for 18 h under gently shaking.

Unbound DNA was removed via centrifugation for 10 min with 21,000  $\times g$  at RT. Supernatant was discarded and DNA-AuNP hybrids resuspended in water. This washing steps was repeated two times and DNA-AuNP hybrids were stored afterwards at 4 °C in ddH<sub>2</sub>O or 1x PBS.

Hybridization of oligonucleotides to gold nanoparticle oligonucleotide hybrids

A three time- to five-time excess of DNA with a complementary sequence to the oligonucleotide bound to the AuNP surface was used for hybridization. The hybridization oligonucleotide was mixed with the AuNPs and heated to 90 °C for 5 min. The temperature was decreased in a gradient ranging from 90 °C to 20 °C with the velocity of 1°C per minute. Excess of hybridization oligonucleotide was removed by centrifugation for 20 min at 21,000  $\times g$  and 20 °C and discard of the supernatant, followed by to washing steps with PBS.

### 9.6.2 Dynamic Light Scattering

Analysis of nanoparticles was carried out in a Malvern Zetasizer Nano ZS system (Malvern Instruments Ltd, Malvern, UK) with a 173° backscattering system using He-Ne laser illumination at 633 nm. Each measurement was the average of 15 runs of autocorrelation function.

### 9.6.3 Surface Plasmon Resonance Scan

For characterization of the maximal surface plasmon absorption of nanoparticles a TECAN Infinite ® Pro M200 was used. The absorption from 400-700 nm was detected. The data was plotted in Microsoft Excel <sup>TM</sup>.



#### 9.6.4 Dot Blot and Northern Blot

For the Dot Blot 1  $\mu\text{L}$  RNA or DNA of increasing concentrations were spotted on a positively charged nylon membrane and allowed to dry. For Northern Blot increasing concentrations of *in vitro* transcribed RNA (cRNA or Ctrl. RNA) were separated on a 10 % denaturing PAA gel. The RNA was transferred on a positively charged nylon membrane using semi-dry blot. In both cases, the oligonucleotides were cross-linked to the surface with 154  $\text{kJ}/\text{cm}^2$ . To avoid unspecific signals the membrane was pre-incubated for 60-90 min at 53 °C in 10 mL blocking buffer (Roti<sup>®</sup>-Hybriquick supplemented with 1 mg sheared salmon sperm DNA). For detection with the gold particles 2 pmol DNA-AuNP probe were added and the membrane was incubated for 5 min at 80 °C and 25 min at 53 °C. No additional washing steps were necessary. For detection of the RNA with the radioactively labeled probes, the membrane was incubated with 10 pmol of the radioactively labeled DNA-probe at 53 °C for one hour or overnight. The membrane was washed with SSC buffers with decreasing concentrations (2x, 1x, 0.5x) containing 0.5 % SDS for 10 min each time at 53 °C. The signal was detected by autoradiography after overnight exposition for total RNA or 1 h exposition for *in vitro* transcribed RNA.

#### 9.6.5 Preparing the Nanofluidic Cell Samples and TEM Acquisition

The nanofluidic cell is custom made in house with a silicon nitride window size of 200 x 50 x 0.05  $\mu\text{m}$ . For the spacer, 200-400 nm silicon oxide film is sputtered on Silicon nitride and patterned as a rectangular micro-chamber for the live cells. The nanofluidic cells are cleaned with 98 %  $\text{H}_2\text{SO}_4$  and hydrogen peroxide (30%). This is crucial for live cell adhesion.

Mammalian cell attachment on the silicon nitride windows is verified by light microscopy. Subsequently, two identical components of the nanofluidic cell are overlapped in the holder and hermetically sealed with soft O-rings. The ultra-thin and flexible silicon nitride windows encapsulate the live cells.

The dimensions of the nanocell are adapted to fit a custom made liquid specimen holder for a JEOL JEM-2100 transmission electron microscope, equipped with a thermionic  $\text{LaB}_6$  emitter, and a CMOS detector (TVIPS TemCam-F216). The microscope is operated at 200 keV in bright field mode at a very low electron dose rate of approximately 10  $\text{e}/\text{nm}^2\text{s}$ . The magnification varied between 1200 to 5000 for all the measurements.

## **9.7 Aequirin as a Bimodal Probe for Electron and Fluorescence Light Microscopy**

### **9.7.1 Cloning of Amino Acid libraries using MEGAWHOP PCR**

All mutants and libraries were cloned using MEGAWHOP mutagenesis. Mutations were introduced using mutagenesis primers and checked via sequencing.

### **9.7.2 High-Throughput Screening for Luminescence Activity**

Clones of the libraries were picked from LB-Agar plates and inoculated in 400 mL TB/SOB media supplemented with 100 µg/mL Amp and 34 µg/mL Cam in 96 deep well plates. Plates were incubated in an orbital shaker at 37°C and 200 rpm for 18 h. For expression 550 µL 2YT media with 100 µg/mL Amp and 34 µg/mL Cam per well were mixed with 50 µL of the same well of the preculture plate using a Liquidator (Steinbrenner Laborsysteme, Wiesebach, Germany). Cells were incubated for 4 hours at 37°C and 200 rpm to reach an OD<sub>600</sub> of 1.8, cooled down to room temperature and protein production induced with additional 400 µL 2YT media supplemented with IPTG (final concentration 0.1 mM). After 18 hours 50 µL of the cell suspension were mixed with 50 µL reconstitution buffer and incubated for 4 hours in the dark at 4°C before luminescence assay.

### **9.7.3 Site-directed Mutagenesis**

Site-directed mutagenesis of the desired product was carried out using primer oligonucleotides with exchanged bases at the needed position. PCR was performed with Phusion due to proofreading ability. The PCR Product was used as megaprimer for MEGAWHOP. Parental plasmid DNA was digested with DpnI and PCR product precipitated with isopropanol and resuspended in water.

### **9.7.4 Protein Production**

E.coli Bl21(DE3)pLysS cells were transformed with plasmids carrying mutated aequirin cDNA in a pRSET vector via electroporation. Bacteria were incubated in SOC media at 37°C and 300 rpm over 30 min for recovery and plated afterwards to LB-Agar Amp/Cam plates. For expression the overnight culture was inoculated in 500 mL 2YT media supplemented with 100 µg/mL Amp and 34 µg/mL Cam. Bacteria were cultivated to an OD<sub>600</sub> of 0.6 at 37°C and 180 rpm and allowed to cool to room temperature before induction with 0.1 mM and protein

production for 18h at 17°C and 180 rpm. Cells were harvested by centrifugation at 4000 rpm for 15 min and pellets stored at -20°C until purification.

### **9.7.5 Protein Purification using ÄKTA**

For purification cells were resuspended in 15 mL Luminescence buffer and sonified for lysis. Cell debris was removed via centrifugation and filtrated lysate applied to a Ni-NTA FF His-tag column (GE healthcare) for purification with an ÄKTA purifier. Fractions containing the aequorin were tested on a dSDS PAGE and coomassie staining, pooled and further purified using anion exchange with a DEAE column and the ÄKTA system (GE healthcare). Fractions of this second step were analyzed using dSDS PAGE and coomassie staining, pooled and dialyzed against storage buffer using Millipore Amlicon centrifugation units and Vivaspins. For storage the enzyme solution was mixed with glycerol to 1:1 v/v% and aliquots stored at -20°C until used in further assays.

### **9.7.6 Luminescence Activity Assay**

Purified AQ was allowed to warm up to room temperature prior to the measurements. For luminescence activity tests (reaction volume per well 50 µL) in a 384 well plate 2.5 µM enzyme was mixed with 1 mM DTT, 5 µM CTZ (all final concentrations) and buffer ad 47.5 µL. Reconstitution of the apoenzyme was monitored for 20 min in 60 s intervals using the Tecan plate reader (luminescence mode, channels blue 1 (370-480 nm) and green 1 (520-570 nm)). For metal ion induced luminescence, 2.5 µL of various stock solutions of CaCl<sub>2</sub> or SmCl<sub>3</sub> were mixed and luminescence was immediately monitored with the Tecan reader in 10 s intervals.

### **9.7.7 Determination of EC<sub>50</sub> Values**

For determination of EC<sub>50</sub> values luminescence was measured as described above for purified proteins at different concentration of metal ions. Luminescence values were plotted against ion concentration and the EC<sub>50</sub> value calculated using logistic fit in Origin because each of the three EF-hand motifs bind metal ions with different affinities and thus each binding site needs to be saturated.

### 9.7.8 Determination of Half-lives

For each variant luminescence values were obtained over 20 min in 1 min intervals after induction with 100  $\mu\text{M}$   $\text{CaCl}_2$  or  $\text{SmCl}_3$  using a Tecan multiplate reader (Swiss) and plotted against time. The half-life was calculated with exponential fit in Origin.

### 9.7.9 Emission Wavelength Scan

The emission wavelength was determined using a Cary UV-Vis Eclipse fluorescence spectrophotometer (Varian, USA) in Bio-Luminescence mode with 5 repetitions with an interval of 100  $\mu\text{s}$  between each measurement. Luminescence reaction occurred in a cuvette and a total volume of 1000  $\mu\text{L}$ . For the reaction 2.5  $\mu\text{M}$  enzyme was mixed with 1 mM DTT, 5  $\mu\text{M}$  CTZ (all final concentrations) and buffer to the final volume. After 20 min of reconstitution the mixture was analyzed upon background luminescence followed by triggered luminescence with either  $\text{CaCl}_2$  or  $\text{SmCl}_3$  (100  $\mu\text{M}$ ). Emission wavelengths of the triggered luminescence was collected and read out for the maximum peak.

### 9.7.10 CD Spectroscopy

Structural analysis of all variants according to folding and thermo stability was performed in a JASCO CD spectrometer. Enzyme concentration for CD and melting curves was 1  $\mu\text{M}$  diluted in water. For melting curves the temperature increased 1 $^\circ\text{C}/\text{min}$  and temperature hold for 10 s before each measurement. Measurements were recorded from 20-80 $^\circ\text{C}$ . The melting temperature was calculated of the data at 220 nm using Boltzmann fit in Origin.

The molar ellipticity per amino acid was calculated using the equation

$$\theta[\text{deg} \cdot \text{cm}^2 \cdot \text{dmol}^{-1}] = \frac{\theta \cdot 10^5}{c \cdot d \cdot N_A}$$

For the equation  $\theta$  is given in [mdeg] as raw data of the spectrometer,  $c$  is the concentration of AQ [ $\mu\text{M}$ ] and  $d$  as distance of the light [cm], while  $N_A$  is the number of amino acids of the protein.

### 9.7.11 MALDI-MS

The enzymes were dialyzed against water for 60 min on a Millipore filter membrane VSWP (Millipore, Darmstadt, Germany) to avoid high salt concentrations. All samples were analyzed via MalDI TOF MS with DHAP matrix in a Bruker UltrafleXtreme Smartbeam II Laser.

### 9.7.12 Isothermal Titration Calorimetry

Isothermal titration calorimetry (ITC) was performed using a MicroCal ITC200 (Malvern, UK). TS and TS A123W S125E were purified and dialyzed against an ITC buffer (50 mM Hepes, 100 mM NaCl, 20  $\mu$ M TCEP) for 1 h using WSWP filters (0.025  $\mu$ m, Millipore, USA) because Tris-HCl and DTT interfere with the signals during measurement. For titration 20  $\mu$ M enzyme solution (200  $\mu$ L) was titrated with 1  $\mu$ L steps of 0.1 mM CaCl<sub>2</sub> or 0.5 mM SmCl<sub>3</sub>. K<sub>d</sub> values were calculated using Origin and the sequential binding model with 4 steps, one for each EF-hand motif in AQ.

### 9.7.13 Conventional TEM of Immobilized TS A123W S125E

For conventional TEM imaging TS A123W S125E was immobilized on anti-His<sub>6</sub>-AuNPs (14 nm AuNP core). The concentration of TS A123W S125E was approximately 10-fold of the AuNP core concentration due to 10 binding sites on the AuNP.

The TS A123W S125E-AuNPs were incubated with either Sm<sup>3+</sup> or Ca<sup>2+</sup> for 3 h. Excess of salt was removed via centrifugation and resuspension.

The samples were prepared on carbon film coated copper grids and analyzed by Daniela Weinert (University of Hamburg, Institute for Physical Chemistry, Group of Prof. Weller).

## 10 References

- Abcam (2014) 325.
- Adrian, M., Dubochet, J., Lepault, J. and McDowell, a W. (1984) *Nature*,**308** 32–36.
- Alivisatos, A. P. (1996) *J. Phys. Chem.*,**100** 13226–13239.
- Allen, D. G., Blinks, J. R. and Prendergast, F. G. (1977) *Science (80- )*,**195** 996–998.
- Ambrose, E. J. (1956) *Nature*,**178** 1194–1194.
- Anilkumar, G., Rajasekaran, S. A., Wang, S., Hankinson, O., Bander, N. H. and Rajasekaran, A. K. (2003) *Cancer Res*,**63** 2645–2648.
- Ardenne, M. von (1938) *Zeitschrift Für Phys.*,**109** 553–572.
- Aseyev, S. a. (2013) *J. Anal. Sci. Methods Instrum.*,**03** 30–53.
- Axelrod, D. (1981) *J. Cell Biol.*,**89** 141–145.
- Bakshi, M. S., Possmayer, F. and Petersen, N. O. (2007) *J. Phys. Chem. C*,**111** 14113–14124.
- Ballard, C., Gauthier, S., Corbett, A., Brayne, C., Aarsland, D. and Jones, E. (2011) *Lancet*,**377** 1019–31.
- Barinka, C., Sába, P., Sklenár, J., Man, P., Bezouska, K., Slusher, B. S. and Konvalinka, J. (2004) *Protein Sci.*,**13** 1627–1635.
- Bartesaghi, A., Merk, A., Banerjee, S., Matthies, D., Wu, X., Milne, J. L. S. and Subramaniam, S. (2015) *Science*,**348** 1147–1151.
- Blinks, J. R., Wier, W. G., Hess, P. and Prendergast, F. G. (1982) *Prog Biophys Mol Biol*,**40** 1–114.
- Bloomfield, V. A., Crothers, D. M. and Tinoco, I. (1999) *Nucleic Acids: Structures, Properties and Functions* Sausalito, CA: University Science Books.
- Bonora, M., Giorgi, C., Bononi, A., Marchi, S., Patergnani, S., Rimessi, A., Rizzuto, R. and Pinton, P. (2013) *Nat. Protoc.*,**8** 2105–18.
- Braun, R., Sarikaya, M. and Schulten, K. (2002) *J. Biomater. Sci. Ed.*,**13** 747–757.
- Brini, M., Murgia, M., Pasti, L., Picard, D., Pozzan, T. and Rizzuto, R. (1993) *EMBO J*,**12** 4813–4819.
- Brini, M., Pasti, L., Bastianutto, C., Murgia, M., Pozzan, T. and Rizzuto, R. (1994) *J. Biolumin. Chemilumin.*,**9** 177–84.
- Brini, M., Pinton, P., Pozzan, T. and Rizzuto, R. (1999) *Microsc. Res. Tech.*,**46** 380–9.
- Cabantous, S. and Waldo, G. S. (2006) *Nat. Methods*,**3** 845–854.
- Cameron Varano, A., Rahimi, A., Dukes, M. J., Poelzing, S., M. McDonald, S. and Kelly, D. F. (2015) *Chem. Commun.*,**51** 16176–16179.
- Campbell, N.A., & Reece, J. B. (2008) *Biology* (8th Edition).
- Cates, M. S., Berry, M. B., Ho, E. L., Li, Q., Potter, J. D. and Phillips, G. N. (1999) *Struct. with Fold. Des.*,**7** 1269–1278.
- Chang, S. S. (2004) *Rev. Urol.*,**6 Suppl 10** S13–S18.
- Charbonneau, H., Walsh, K. A., Mccann, R. O., Prendergast, F. G., Cormier, M. J. and Vanaman, T. C. (1985) *Biochemistry*,**24** 6762–6771.
- Chi, Q. J., Yin, T. Y., Gregersen, H., Deng, X. Y., Fan, Y. B., Zhao, J. B., Liao, D. H. and Wang, G. X. (2014) *J. R. Soc. Interface*,**11**.
- Chuang, Y. J. J., Zhou, X., Pan, Z. and Turchi, C. (2009) *Biochem Biophys Res Commun*,**389** 22–27.

- Cirino, P. C., Mayer, K. M. and Umeno, D. (2003) *Methods Mol. Biol.*,**231** 3–9.
- Cline, J., Braman, J. and Hogrefe, H. (1996) *Nucl. Acids Res.*,**24** 3546–51.
- Coling, D. and Kachar, B. (2001) *Curr. Protoc. Mol. Biol.*,**Chapter 14** Unit 14.10.
- Collatz, M. B., Rüdell, R. and Brinkmeier, H. (1997) *Cell Calcium*,**21** 453–459.
- Connor, E. E., Mwamuka, J., Gole, A., Murphy, C. J. and Wyatt, M. D. (2005) *Small*,**1** 325–7.
- Cormack, B. P., Valdivia, R. H. and Falkow, S. (1996) *Gene*,**173** 33–38.
- Cox, J. C. and Ellington, A. D. (2001) *Bioorg Med Chem*,**9** 2525–2531.
- Cramer, L. P. (1997) *Front Biosci*,**2** d260–70.
- Cremer, C. and Cremer, T. (1978) *Microsc. Acta*,**81** 31–44.
- Das, K., Groof, A. De, Jauniaux, T. and Bouquegneau, J. M. (2006) *BMC Ecol*,**6** 2.
- Daughtry, K. D., Martin, L. J., Sarraju, A., Imperiali, B. and Allen, K. N. (2012) *Chembiochem*,**13** 2567–2574.
- Deka, J., M??ch, R., Ianeselli, L., Amenitsch, H., Cacho-Nerin, F., Parisse, P. and Casalis, L. (2015) *ACS Appl. Mater. Interfaces*,**7** 7033–7040.
- Deng, L., Vysotski, E. S., Markova, S. V, Liu, Z. J., Lee, J., Rose, J. and Wang, B. C. (2005) *Protein Sci.*,**14** 663–675.
- Denk, W., Strickler, J. H. and Webb, W. W. (1990) *Science*,**248** 73–76.
- Derichs, N. (2013) *Eur. Respir. Rev.*,**22** 58–65.
- Diao, J., Ishitsuka, Y., Lee, H., Joo, C., Su, Z., Syed, S., Shin, Y. K., Yoon, T. Y. and Ha, T. (2012) *Nat. Protoc.*,**7** 921–934.
- Dikici, E., Qu, X., Rowe, L., Millner, L., Logue, C., Deo, S. K., Ensor, M. and Daunert, S. (2009) *Protein Eng. Des. Sel.*,**22** 243–8.
- Doherty, G. J. and McMahon, H. T. (2009) *Annu. Rev. Biochem.*,**78** 857–902.
- Drake, S. K., Lee, K. L. and Falke, J. J. (1996) *Biochemistry*,**35** 6697–705.
- Drake, S. K., Zimmer, M. A., Miller, C. L. and Falke, J. J. (1997) *Biochemistry*,**36** 9917–9926.
- Dröge, M. J., Boersma, Y. L., Pouderoyen, G. Van, Vrenken, T. E., Rüggeberg, C. J., Reetz, M. T., Dijkstra, B. W. and Quax, W. J. (2006) *ChemBioChem*,**7** 149–157.
- Drummond, D. A., Iverson, B. L., Georgiou, G. and Arnold, F. H. (2005) *J. Mol. Biol.*,**350** 806–816.
- Dubochet, J., Adrian, M., Lepault, J. and McDowell, A. (1985) *Trends Biochem. Sci.* 143–146.
- Egerton, R. F. (2005) Physical principles of electron microscopy: An introduction to TEM, SEM, and AEM.
- El-Sayed, I. H., Huang, X. and El-Sayed, M. a. (2005) *Nano Lett.*,**5** 829–834.
- European Nuclear Society (2016) Radiation exposure, dose limits, Germany.
- Evans, J. E. and Browning, N. D. (2013) *Microscopy*,**62** 147–156.
- Evans, J. E., Jungjohann, K. L., Browning, N. D. and Arslan, I. (2011) *Nano Lett.*,**11** 2809–2813.
- Faraday, M. (1857) *Philos. Trans. R. Soc. London*,**147** 145–181.
- Farinha, C. M. and Amaral, M. D. (2005) *Mol. Cell. Biol.*,**25** 5242–52.
- Farokhzad, O. C., Cheng, J., Teply, B. a, Sherifi, I., Jon, S., Kantoff, P. W., Richie, J. P. and Langer, R. (2006) *Proc Natl Acad Sci U S A*,**103** 6315–6320.

- Farokhzad, O. C., Jon, S., Khademhosseini, A., Tran, T. N., Lavan, D. A. and Langer, R. (2004) *Cancer Res*,**64** 7668–7672.
- Faulk, W. P. and Taylor, G. M. (1971) *Immunochemistry*,**8** 1081–1083.
- Fernandez-Suarez, M., Ting, A. Y., Fernández-Suárez, M. and Ting, A. Y. (2008) *Nat Rev Mol Cell Biol*,**9** 929–943.
- Flaherty, K. M., Zozulya, S., Stryer, L. and McKay, D. B. (1993) *Cell*,**75** 709–716.
- Foucault-Collet, A. et al. (2013) *Proc. Natl. Acad. Sci. U. S. A.*,**110** 17199–204.
- Franz, K. J., Nitz, M. and Imperiali, B. (2003) *ChemBiochem*,**4** 265–271.
- Frens, G. (1973) *Nature-Physical Sci.*,**241** 20–22.
- Fromant, M., Blanquet, S. and Plateau, P. (1995) *Anal. Biochem.*,**224** 347–353.
- Fukunaga, Y., Hirase, A., Kim, H., Wada, N., Nishino, Y. and Miyazawa, A. (2007) *J Electron Microsc.*,**56** 119–129.
- Garcia-Blanco, M. a, Baraniak, A. P. and Lasda, E. L. (2004) *Nat. Biotechnol.*,**22** 535–546.
- Gauthier, N. C., Masters, T. A. and Sheetz, M. P. (2012) *Trends Cell Biol.*,**22** 527–535.
- Gealageas, R., Malikova, N. P., Picaud, S., Borgdorff, A. J., Burakova, L. P., Brulet, P., Vysotski, E. S. and Dodd, R. H. (2014) *Anal Bioanal Chem.*
- Giepmans, B. N. G., Adams, S. R., Ellisman, M. H. and Tsien, R. Y. (2006) *Science*,**312** 217–24.
- Gifford, J. L., Walsh, M. P. and Vogel, H. J. (2007) *Biochem J*,**405** 199–221.
- Goodman Jr., O. B. et al. (2007) *Int J Oncol*,**31** 1199–1203.
- Griffin, B. a, Adams, S. R. and Tsien, R. Y. (1998) *Science*,**281** 269–272.
- Grogan, J. M. and Bau, H. H. (2010) *J. Microelectromechanical Syst.*,**19** 885–894.
- Gumbiner, B. M. (1993) *Neuron*,**11** 551–564.
- Gumbiner, B. M. (1996) *Cell*,**84** 345–357.
- Häkkinen, H. (2012) *Nat. Chem.*,**4** 443–455.
- Han, R., Li, Z., Fan, Y. and Jiang, Y. (2013) *J. Genet. Genomics*,**40** 583–595.
- Hao, L. K., Li, J. L., Kappler, A. and Obst, M. (2013) *Appl. Environ. Microbiol.*,**79** 6524–6534.
- Hastings, J. W. W., Mitchell, G., Mattingly, P. H. H., Blinks, J. R. R. and Leeuwen, M. van (1969) *Nature*,**222** 1047–1050.
- Head, J. F., Inouye, S., Teranishi, K. and Shimomura, O. (2000) *Nature*,**405** 372–6.
- Heim, R., Prasher, D. C. and Tsien, R. Y. (1994) *Proc Natl Acad Sci U S A*,**91** 12501–12504.
- Hell, S. W. and Wichman, J. (1994) *Opt. Lett.*,**19** 780 – 782.
- Hitachi (2015) Development of an with the World ' s Highest Point Resolution ( 43 picometers ).
- Hoenger, A. and McIntosh, J. R. (2009) *Curr Opin Cell Biol*,**21** 89–96.
- Hogue, C. W. V, Macmanus, J. P., Banville, D. and Szabo, A. G. (1992) *J. Biol. Chem.*,**267** 13340–13347.
- Holstein, J. M., Schulz, D. and Rentmeister, A. (2014) *Chem. Commun. (Camb)*,**50** 4478–81.
- Holt, C. E. and Schuman, E. M. (2013) *Neuron*,**80** 648–657.
- Humphries, A. C. and Way, M. (2013) *Nat Rev Microbiol*,**11** 551–560.
- Inouye, S. and Hosoya, T. (2009) *Biochem. Biophys. Res. Commun.*,**386** 617–22.



- Inouye, S., Noguchi, M., Sakaki, Y., Takagi, Y., Miyata, T., Iwanaga, S. and Tsuji, F. I. (1985) *Proc. Natl. Acad. Sci. U. S. A.*, **82** 3154–8.
- Jafarian, V., Sariri, R., Hosseinkhani, S., Aghamaali, M. R. R., Sajedi, R. H., Taghdir, M. and Hassannia, S. (2011) *Biochem. Biophys. Res. Commun.*, **413** 164–70.
- Javier, D. J., Nitin, N., Levy, M., Ellington, A. and Richards-Kortum, R. (2008) *Bioconjug. Chem.*, **19** 1309–1312.
- Jones, S. A., Shim, S. H., He, J. and Zhuang, X. (2011) *Nat Methods*, **8** 499–508.
- Jonge, N. de, Peckys, D. B., Kremers, G. J. and Piston, D. W. (2009) *Proc Natl Acad Sci U S A*, **106** 2159–2164.
- Kass, G. E. N. and Orrenius, S. (1999) *Environ. Health Perspect.*, **107** 25–35.
- Kastner, B., Bach, M. and Luhrmann, R. (1990) *Proc Natl Acad Sci U S A*, **87** 1710–1714.
- Kemple, M. D., Lovejoy, M. L., Ray, B. D., Prendergast, F. G. and Rao, B. D. N. (1990) *Eur. J. Biochem.*, **187** 131–135.
- Kendall, J. M., Salanewby, G., Ghalaut, V., Dormer, R. L. and Campbell, A. K. (1992) *Biochem Biophys Res Commun*, **187** 1091–1097.
- Keskin, S., Besztejan, S., Kassier, G., Manz, S., Bücken, R., Riekeberg, S., Trieu, H. K., Rentmeister, A. and Miller, R. J. D. (2015) *J Phys Chem Lett.*
- Kim, D., Jeong, Y. Y. and Jon, S. (2010b) *ACS Nano*, **4** 3689–3696.
- Kirk, S. E., Skepper, J. N. and Donald, A. M. (2009) *J Microsc.*, **233** 205–224.
- Knoll, M. and Ruska, E. (1932) *Zeitschrift F??r Phys.*, **79** 699.
- Köhler, A. and Hurt, E. (2007) *Nat. Rev. Mol. Cell Biol.*, **8** 761–773.
- Kraft, O. and Volkert, C. A. (2001) *Adv. Eng. Mater.*, **3** 99–110.
- Kukulski, W., Schorb, M., Welsch, S., Picco, A., Kaksonen, M. and Briggs, J. A. G. (2011) *J. Cell Biol.*, **192** 111–119.
- Kulic, L. et al. (2012) *Transl. Psychiatry*, **2** e183.
- la Fuente, J. M. de and Penadés, S. (2006) *Biochim. Biophys. Acta - Gen. Subj.*, **1760** 636–651.
- la Fuente, S. de, Fonteriz, R. I., la Cruz, P. J. de, Montero, M. and Alvarez, J. (2012) *Biochem. J.*, **445** 371–376.
- Lakowicz, J. R. (2006) *Principles of fluorescence spectroscopy.*
- Lévy, R., Thanh, N. T. K., Christopher Doty, R., Hussain, I., Nichols, R. J., Schiffrin, D. J., Brust, M. and Fernig, D. G. (2004) *J. Am. Chem. Soc.*, **126** 10076–10084.
- Li, H. X. and Rothberg, L. (2004) *Proc Natl Acad Sci U S A*, **101** 14036–14039.
- Liao, J. H., Zhang, Y., Yu, W., Xu, L. N., Ge, C. W., Liu, J. H. and Gu, N. (2003) *Colloids Surfaces a-Physicochemical Eng. Asp.*, **223** 177–183.
- Liao, M., Cao, E., Julius, D. and Cheng, Y. (2013) *Nature*, **504** 107–12.
- Lichtman, J. W. and Conchello, J. A. (2005) *Nat Methods*, **2** 910–919.
- Lieske, J. C., Walsh-Reitz, M. M. and Toback, F. G. (1992) *Am. J. Physiol.*, **262** F622–F630.
- Liu, H., Rajasekaran, A. K., Moy, P., Xia, Y., Kim, S., Navarro, V., Rahmati, R. and Bander, N. H. (1998) *Cancer Res.*, **58** 4055–4060.
- Liu, Y., Shipton, M. K., Ryan, J., Kaufman, E. D., Franzen, S. and Feldheim, D. L. (2007) *Anal. Chem.*, **78** 2221–2229.

- Liu, Y. Z., Lin, X. M., Sun, Y. G. and Rajh, T. (2013) *J. Am. Chem. Soc.*, **135** 3764–3767.
- Lodish, H., Berk, A., Zipursky, S. L., Matsudaira, P., Baltimore, D. and Darnell, J. (2000) *Molecular Cell Biology*. 4th edition.
- Lupold, S. E., Hicke, B. J., Lin, Y. and Coffey, D. S. (2002) *Cancer Res*, **62** 4029–4033.
- Luthey-Schulten, Z. and Wolynes, P. G. (1997) 545–600.
- Lytton, J., Westlin, M. and Hanley, M. R. (1991) *J. Biol. Chem.*, **266** 17067–17071.
- Machleidt, T., Robers, M. and Hanson, G. T. (2007) *Methods Mol. Biol.*, **356** 209–220.
- Marchand, S. and Roux, B. (1998) *Proteins Struct. Funct. Genet.*, **33** 265–284.
- Marsault, R., Murgia, M., Pozzan, T. and Rizzuto, R. (1997) *EMBO J.*, **16** 1575–1581.
- Massover, W. H. (2008) *Microsc. Microanal.*, **14** 126–137.
- Mayer, M. and Meyer, B. (1999) *Angew. Chemie - Int. Ed.*, **38** 1784–1788.
- McDowall, A. W., Chang, J. J., Freeman, R., Lepault, J., Walter, C. A. and Dubochet, J. (1983) *J Microsc.*, **131** 1–9.
- Mercogliano, C. P. and DeRosier, D. J. (2006) *J. Mol. Biol.*, **355** 211–223.
- Michelangeli, F. and East, J. M. (2011) *Biochem. Soc. Trans.*, **39** 789–797.
- Minsky, M. (1957) *US Pat. 3013467*, **3013467** 5.
- Mirkin, C. A., Letsinger, R. L., Mucic, R. C. and Storhoff, J. J. (1996) *Nature*, **382** 607–609.
- Missiaen, L. et al. (2004) *Cell Calcium*, **36** 479–487.
- Miyazaki, K. (2011) *Methods Enzym.*, **498** 399–406.
- Miyazaki, K. and Takenouchi, M. (2002) *Biotechniques*, **33** 1033–+.
- Mueller, C., Harb, M., Dwyer, J. R. and Miller, R. J. D. (2013) *J. Phys. Chem. Lett.*, **4** 2339–2347.
- Mukherjee, S., Ghosh, R. N. and Maxfield, F. R. (1997) *Physiol Rev*, **77** 759–803.
- Muller, D. J. and Dufrene, Y. F. (2011) *Trends Cell Biol.*, **21** 461–469.
- Mullis, K., Faloona, F., Scharf, S., Saiki, R., Horn, G. and Erlich, H. (1986) *Cold Spring Harb. Symp. Quant. Biol.*, **51** 263–273.
- Muscariello, L., Rosso, F., Marino, G., Giordano, A., Barbarisi, M., Cafiero, G. and Barbarisi, A. (2005) *J Cell Physiol*, **205** 328–334.
- Nakakoshi, M., Nishioka, H. and Katayama, E. (2011) *J Electron Microsc.*, **60** 401–407.
- New England Biolabs Inc. NEB-Phusion Polymerase Product Page.
- Nitz, M., Franz, K. J., Maglathlin, R. L. and Imperiali, B. (2003) *Chembiochem*, **4** 272–276.
- Nitz, M., Sherawat, M., Franz, K. J., Peisach, E., Allen, K. N. and Imperiali, B. (2004) *Angew. Chemie-International Ed.*, **43** 3682–3685.
- Nomura, M., Inouye, S., Ohmiya, Y. and Tsuji, F. I. (1991) *FEBS Lett*, **295** 63–66.
- Ohashi, W., Inouye, S., Yamazaki, T. and Hirota, H. (2005) *J Biochem*, **138** 613–620.
- Ormö, M., Cubitt, a B., Kallio, K., Gross, L. a, Tsien, R. Y. and Remington, S. J. (1996) *Science*, **273** 1392–1395.
- Pal, A., Severin, F., Hopfner, S. and Zerial, M. (2008) *Small Gtpases Dis. Part A*, **438** 239–257.
- Pardoux, R., Sauge-Merle, S., Lemaire, D., Delangle, P., Guilloreau, L., Adriano, J. M. M. and Berthomieu, C. (2012) *PLoS One*, **7** e41922.

- Park, J., Park, H., Ercius, P., Pegoraro, A. F., Xu, C., Kim, J. W., Han, S. H. and Weitz, D. A. (2015) *Nano Lett.*,**15** 4737–4744.
- Park, J., Zheng, H. M., Lee, W. C., Geissler, P. L., Rabani, E. and Alivisatos, A. P. (2012) *ACS Nano*,**6** 2078–2085.
- Pearse, B. M. F. (1976) *Proc Natl Acad Sci U S A*,**73** 1255–1259.
- Peckys, D. B. and Jonge, N. de (2014) *Microsc. Microanal.*,**20** 346–365.
- Permyakov, S. E. et al. (2000) *Protein Eng*,**13** 783–790.
- Pinton, P., Rimessi, A., Romagnoli, A., Prandini, A. and Rizzuto, R. (2007) *Methods Cell Biol*,**80** 297–325.
- Platt, F. M., Boland, B. and Spoel, A. C. van der (2012) *J. Cell Biol.*,**199** 723–734.
- Plieth, C. (2006) *Methods Mol Biol*,**323** 307–327.
- Prendergast, F. G. and Mann, K. G. (1978) *Biochemistry*,**17** 3448–3453.
- Querfurth, H. W. and LaFerla, F. M. (2010) *N. Engl. J. Med.*,**362** 329–344.
- Querido, E. and Chartrand, P. (2008) *Methods Cell Biol.*,**85** 273–292.
- Rajasekaran, A. K., Anilkumar, G. and Christiansen, J. J. (2005) *Am J Physiol Cell Physiol*,**288** C975–81.
- Rao, B. D. N., Kemple, M. D. and Prendergast, F. G. (1980) *Biophys. J.*,**32** 630–632.
- Rappoport, J. Z. (2008) *Biochem. J.*,**412** 415–423.
- Rappoport, J. Z. and Simon, S. M. (2003) *J Cell Sci*,**116** 847–855.
- Ray, B. D., Ho, S., Kemple, M. D., Prendergast, F. G. and Rao, B. D. N. (1985) *Biochemistry*,**24** 4280–4287.
- Reed, M. A., Randall, J. N., Aggarwal, R. J., Matyi, R. J., Moore, T. M. and Wetsel, A. E. (1988) *Phys. Rev. Lett.*,**60** 535–537.
- Reetz, M. T. and Carballeira, J. D. (2007) *Nat. Protoc.*,**2** 891–903.
- Reetz, M. T., Kahakeaw, D. and Lohmer, R. (2008) *ChemBioChem*,**9** 1797–1804.
- Reetz, M. T., Wang, L. W. and Bocola, M. (2006) *Angew. Chemie-International Ed.*,**45** 1236–1241.
- Resch-Genger, U., Grabolle, M., Cavaliere-Jaricot, S., Nitschke, R. and Nann, T. (2008) *Nat. Methods*,**5** 763–775.
- Rizzuto, R., Simpson, A. W. M., Brini, M. and Pozzan, T. (1992) *Nature*,**358** 325–327.
- Robert, V., Pinton, P., Tosello, V., Rizzuto, R. and Pozzan, T. (2000) *Methods Enzym.*,**327** 440–456.
- Rothmund, P. W. (2006) *Nature*,**440** 297–302.
- Rubinsztein, D. C. and Carmichael, J. (2003) *Expert Rev. Mol. Med.*,**5** 1–21.
- Rust, M. J., Bates, M. and Zhuang, X. W. (2006) *Nat Methods*,**3** 793–795.
- Ryou, S. M. M., Kim, S., Jang, H. H., Kim, J. H. H., Yeom, J. H. H., Eom, M. S., Bae, J., Han, M. S. and Lee, K. (2010) *Biochem Biophys Res Commun*,**398** 542–546.
- Saffarian, S., Cocucci, E. and Kirchhausen, T. (2009) *PLoS Biol*,**7** e1000191.
- Schmidt-Dannert, C. and Arnold, F. H. (1999) *Trends Biotechnol.*,**7799**.
- Schneider, N. M., Norton, M. M., Mendel, B. J., Grogan, J. M., Ross, F. M. and Bau, H. H. (2014) *J. Phys. Chem. C*,**118** 22373–22382.

- Schulz, D., Holstein, J. M. and Rentmeister, A. (2013) *Angew. Chemie - Int. Ed.*, **52** 7874–7878.
- Scita, G. and Fiore, P. P. Di (2010) *Nature*, **463** 464–473.
- Shafaq-Zadah, M. et al. (2016) *Nat Cell Biol*, **18** 54–64.
- Shao, L., Kner, P., Rego, E. H. and Gustafsson, M. G. L. (2011) *Nat. Methods*, **8** 1044–1046.
- Shi, H. Y., Yuan, L., Wu, Y. F. and Liu, S. Q. (2011) *Biosens. Bioelectron.*, **26** 3788–3793.
- Shimomura, O. (1991) *Cell Calcium*, **12** 635–643.
- Shimomura, O., Inouye, S., Musicki, B. and Kishi, Y. (1990) *Biochem J*, **270** 309–312.
- Shimomura, O. and Johnson, F. H. (1969) *Biochemistry*, **8** 3991–3997.
- Shimomura, O. and Johnson, F. H. (1970) *Nature*, **227** 1356–1357.
- Shimomura, O. and Johnson, F. H. (1975) *Nature*, **256** 236–238.
- Shimomura, O. and Johnson, F. H. (1978) *Proc Natl Acad Sci U S A*, **75** 2611–2615.
- Shimomura, O., Johnson, F. H. and Morise, H. (1974) *Biochemistry*, **13** 3278–3286.
- Shimomura, O., Johnson, F. H. and Saiga, Y. (1962a) *J Cell Comp Physiol*, **59** 223–&.
- Shimomura, O., Musicki, B. and Kishi, Y. (1988) *Biochem J*, **251** 405–410.
- Shimomura, O., Musicki, B., Kishi, Y. and Inouye, S. (1993) *Cell Calcium*, **14** 373–378.
- Shimomura, O., Saiga, Y. and Johnson, F. H. (1962b) *Fed. Proc.*, **21** 401–&.
- Shimomura, O. and Shimomura, a (1984) *Biochem. J.*, **221** 907–10.
- Shu, X., Lev-Ram, V., Deerinck, T. J., Qi, Y., Ramko, E. B., Davidson, M. W., Jin, Y., Ellisman, M. H. and Tsien, R. Y. (2011) *PLoS Biol*, **9** e1001041.
- Snyder, E. E., Buoscio, B. W. and Falke, J. J. (1990) *Biochemistry*, **29** 3937–3943.
- Speese, S. D. et al. (2012) *Cell*, **149** 832–846.
- Sperling, R. A., Rivera Gil, P., Zhang, F., Zanella, M. and Parak, W. J. (2008) *Chem Soc Rev*, **37** 1896–1908.
- Stokes, D. J. (2003) *Philos. Trans. R. Soc. London Ser. a-Mathematical Phys. Eng. Sci.*, **361** 2771–2787.
- Stokes, D. J., Rea, S. M., Best, S. M. and Bonfield, W. (2003) *Scanning*, **25** 181–184.
- Stratagene (2007) *QuikChange® Site-Directed Mutagen. Kit*, **200518**.
- Strynadka, N. C. and James, M. N. (1989) *Annu Rev Biochem*, **58** 951–998.
- Suzuki, E. (2002) *J. Microsc.*, **208** 153–157.
- Tazi, J., Bakkour, N. and Stamm, S. (2009) *Biochim. Biophys. Acta - Mol. Basis Dis.*, **1792** 14–26.
- The Univesity of Utah Electron Microscopy Tutorial.
- Toma, S., Chong, K. T. E. E., Nakagawa, A., Teranishi, K., Inouye, S. and Shimomura, O. (2005) *Protein Sci.*, **14** 409–416.
- Torrecilla, I., Leganes, F., Bonilla, I. and Fernandez-Pinas, F. (2000) *Plant Physiol.*, **123** 161–175.
- Tricoire, L., Tsuzuki, K., Courjean, O., Gibelin, N., Bourout, G., Rossier, J. and Lambolez, B. (2006) *Proc. Natl. Acad. Sci. U. S. A.*, **103** 9500–5.
- Tsien, R. Y. (2008) Nobel talk 2008 Roger Tsien.
- Tsien, R. Y., Ernst, L. and Waggoner, A. (2006) *Handb. Biol. Confocal Microsc. Third Ed.* 338–352.
- Tsuji, F. I., Inouye, S., Goto, T. and Sakaki, Y. (1986) *Proc. Natl. Acad. Sci. U. S. A.*, **83** 8107–11.

- Tsuzuki, K., Tricoire, L., Courjean, O., Gibelin, N., Rossier, J. and Lambolez, B. (2005) *J. Biol. Chem.*,**280** 34324–31.
- Turkevich, J., Stevenson, P. C. and Hillier, J. (1951) *Discuss. Faraday Soc.* 55–&.
- Urban, A., Neukirchen, S. and Jaeger, K. E. (1997) *Nucleic Acids Res.*,**25** 2227–2228.
- Valeur, B. (2002) *Molecular fluorescence: principles and applications.*
- Venkitakrishnan, R. P., Benard, O., Max, M., Markley, J. L. and Assadi-Porter, F. M. (2012) *Methods Mol. Biol.*,**914** 47–63.
- Vijayakumar, S. and Ganesan, S. (2012) *J. Nanomater.*,**2012** 1–9.
- Vlassak, J. J. and Nix, W. D. (1992) *J. Mater. Res.*,**7** 3242–3249.
- Wang, C. G., Chen, J., Talavage, T. and Irudayaraj, J. (2009) *Angew. Chemie-International Ed.*,**48** 2759–2763.
- Wang, D. O., Martin, K. C. and Zukin, R. S. (2010) *Trends Neurosci.*,**33** 173–182.
- Wang, Q., Mercogliano, C. P., Lowe, J. and Löwe, J. (2011) *Structure*,**19** 147–154.
- Wang, R. Y. R., Kudryashev, M., Li, X., Egelman, E. H., Basler, M., Cheng, Y., Baker, D. and DiMaio, F. (2015) *Nat. Methods*,**12** 335–8.
- Watson, J. D. (1968) *The Double Helix: A Personal Account of the Discovery of the Structure of DNA* London.
- Webb, S. E. and Miller, A. L. (2012) *Biochim. Biophys. Acta*,**1820** 1160–8.
- Westphal, V., Rizzoli, S. O., Lauterbach, M. A., Kamin, D., Jahn, R. and Hell, S. W. (2008) *Science*,**320** 246–9.
- Wilhelm, J. E. and Vale, R. D. (1993) *J. Cell Biol.*,**123** 269–274.
- Willig, K. I., Rizzoli, S. O., Westphal, V., Jahn, R. and Hell, S. W. (2006) *Nature*,**440** 935–939.
- Wilson, D. S. and Keefe, a D. (2001) *Curr. Protoc. Mol. Biol.*,**Chapter 8** Unit8.3.
- Wu, W. Y., Schulman, J. N., Hsu, T. Y. and Efron, U. (1987) *Appl. Phys. Lett.*,**51** 710–712.
- Yang, D. S. S., Mohammed, O. F. and Zewail, A. H. (2012) *Angew Chem Int Ed Engl*,**52** 2897–901.
- Yang, F., Moss, L. G. and Phillips, G. N. (1996) *Nat. Biotechnol.*,**14** 1246–1251.
- Zanacchi, F. C., Lavagnino, Z., Donnorso, M. P., Bue, a Del, Furia, L., Faretta, M. and Diaspro, a (2011) *Nat Methods*,**8** 1047–+.
- Zhang, J., Campbell, R. E., Ting, A. Y. and Tsien, R. Y. (2002) *Nat. Rev. Mol. Cell Biol.*,**3** 906–918.
- Zhang, J., Reedy, M. C., Hannun, Y. A. and Obeid, L. M. (1999) *J. Cell Biol.*,**145** 99–108.
- Zhang, X., Ge, P., Yu, X., Brannan, J. M., Bi, G., Zhang, Q., Schein, S. and Zhou, Z. H. (2013) *Nat. Struct. Mol. Biol.*,**20** 105–10.
- Zhao, J., Zhang, J., Jiang, C., Bohnenberger, J., Basché, T. and Mews, A. (2004) *J. Appl. Phys.*,**96** 3206–3210.
- Zheng, H. M., Mirsaidov, U. M., Wang, L. W. and Matsudaira, P. (2012) *Nano Lett.*,**12** 5644–5648.
- Zhou, Q., Sun, S., Tai, P. and Sui, S. F. F. (2012) *PLoS One*,**7** e47015.



## **11 Appendix**

### **11.1 Disposal**

All chemicals used during the experimental phase were handled and disposed according to their H and P-Sentences (See Table 29).














Solvents and contaminated waste was stored in the specific boxes and disposed according to the safety instructions.

Genetically modified organisms and related waste were autoclaved according to the “Gentechnikgesetz” before disposal for 20 min at 121°C and 5 bar.

## 11.2 List of used Chemicals according to GHS

In the following table all reagents and solvents used in this work and marked with hazard warnings and safety recommendations according to §6 of the Ordinance of Hazardous substances are listed.

**Table 29: List of used Chemical according to GHS**

Substance	Pictogramme	H-Sentences	P-Sentences
Acrylamide		301-312-315-317- 319- 332-340-350- 361f-372	201-280-302+352- 305+ 351 +338
Ampicillin		315-317-319-334- 335	261-280- 305+351+338- 342-311
APS		272-302-315-317- 319- 334-335	280-305+351+338- 302+352-304+341- 342+311
Bisacrylamide		302	
DTT		302-315-319	302+352-305+351+338
EDTA		319	305-351-338
Ethanol		225	210
Ethidium bromide		332-341	281-308+313
Formaldehyde		301-311-314-317-351	301+310-303+361+353- 305+351+338-361-405- 505
Imidazole		302-314-361d	280-301+330+331-305+ 351+338
Isopropanol		225-319-326	210-233- 305+351+338
Kanamycin sulfate		360	201-308+313
NaOH		314-290	280-301+330+331- 305+ 351+338



Nickel sulfate		350i-341360D-372-332- 302-315-334-317-410	201-280-273- 308+313- 342+311- 302+352
Ni-NTA-Agarose		226-317-373	210-233-261-272- 280- 302+352- 333+313-363- 403+ 235
HCl		290-314-335	280-301+330+331- 305+351+338
SDS		228-311-302-335-315- 319	210-280-304+340- 305+351+338- 309+310
TEMED		225-302-314-332	210-233-280- 301+330+331- 305+351+338
TRIS		315-319-335	261-305+351+338

---

### 11.3 Plasmid sequences

In this chapter the sequences of the plasmid generated in this work are listed. The coding unit for the enzyme is underlined for pRSET::AQ. The sequence for the vector is only given once. The coding units for the single genes for each AQ variant are given in the following.

#### pRSET::AQ wt

```

1 gatctcgatc ccgcgaaatt aatacgaactc actatagggg gaccacaacg gtttccctct
61 agaaataatt ttgtttaact ttaagaagga gatatacata tgcgggggtc tcatcatcat
121 catcatcatg gtatggctag catgactggg ggacagcaaa tgggtcggga tctgtacgac
181 gatgacgata aggatcggat ccgagctcga gaacaatgct tacaccagac ttcgacaacc
241 caaaatggat tggacgacac aagcacatgt ttaattttct tgatgtcaac cacaatggaa
301 ggatctctct tgacgagatg gtctacaagg cgtccgatat tgttataaac aatcttggag
361 caacacctga acaagccaaa cgtcacaaa agtctgtaga agccttcttc ggaggagctg
421 gaatgaataa tgggttagaa actgaatggc ctgaatacat cgaaggatgg aaaagactgg
481 cttccgagga attgaaaagg tattcaaaaa accaaatcac acttattcgt ttatgggggtg
541 atgcattggt cgatatcatt gacaaagacc aaaaatggagc tatttctactg gatgaatgga
601 aagcatacac caaatctgct ggcatcatcc aatcgtcaga agattgagag gaaacattca
661 gagtgtgcca tattgacgaa agtggacagc tcgatgttga tgagatgaca agacaacatt
721 taggattttg gtacaccatg gatcctgctt gcgaaaagct ctacgggtgga gctgtcccct
781 aactgactga ctgactgcag ctggtaccat ggaattcgaa gcttgatccg gctgtaaca
841 aagcccgaaa ggaagctgag ttgggtgctg ccaccgctga gcaataacta gcataacccc
901 ttggggcctc taaacgggtc ttgaggggtt ttttctgaa aggaggaact atatccggat
961 ctggcgaat agcgaagagg cccgcaccga tcgccttcc caacagttgc gcagcctgaa
1021 tggcgaatgg gacgcgccct gtagcggcgc attaagcgcg gcggtgtggt tggttacgcg
1081 cagcgtgacc gctacacttg ccagcgcctc agcgcctcgt ccttctgctt tcttcccttc
1141 ctttctgcgc acgttcgccc gcttccccc tcaagctcta aatcgggggc tccctttagg
1201 gttccgattt agtgcctttt ggcacctcga ccccaaaaaa cttgattagg gtgatgggtc
1261 acgtagtggg ccatcgcctc gatagacggt ttttgcctc ttgacgttgg agtccacggt
1321 ctttaaatag ggactcctgt tccaactgga aacaacactc aacctatctc cggctctattc
1381 ttttgattta taagggattt tgccgatttc ggcctattgg ttaaaaaatg agctgattta
1441 acaaaaaatt aacgcgaatt ttaacaaaaa attaacgctt acaatttagg tggcactttt
1501 cgggaaatg tgcgcggaac ccctatttct ttattttctc aaatacattc aaatatgtat
1561 ccgctcatga gacaataacc ctgataaatg cttcaataat attgaaaaag gaagagtatg
1621 agtattcaac atttccgtgt cgccttatt cccttttttg cggcattttg ccttctctgtt
1681 tttgctcacc cagaacgctt ggtgaaagta aaagatgctg aagatcagtt ggggtcacga
1741 gtgggttaca tcgaactgga tctcaacagc ggtaagatcc ttgagagttt tcgccccgaa
1801 gaactgtttc caatgatgag cacttttaaa gttctgctat gtggcgcggt attatccgtt
1861 attgacgccc ggcaagagca actcggctgc cgcatacact attctcagaa tgacttgggtt
1921 gagtactcac cagtcacaga aaagcatctt acggatggca tgacagtaag agaattatgc
1981 agtgctgcca taaccatgag tgataacact gcggccaact tacttctgac aacgatcggg
2041 ggaccgaagg agctaaccgc ttttttgcac aacatggggg atcatgtaac tcgccttgat
2101 cgttgggaac cggagctgaa tgaagccata ccaaacgacg agcgtgacac cagatgcctc
2161 gttagcaatg caacaacggt gcgcaacta ttaactggcg aactacttac tctagcttcc
2221 cggcaacaat taatagactg gatggaggcg gataaagttg caggaccact tctgcgctcg
2281 gcccttccgg ctggctggtt tattgctgat aaatctggag ccggtgagcg tgggtctcgc
2341 ggtatcattg cagcactggg gccagatggt aagcctccc gtatcgtagt tatctacacg
2401 acggggagtc aggcaactat ggatgaacga aatagacaga tcgctgagat aggtgcctca
2461 ctgattaagc attggttaact gtcagacca gtttactcat atatacttta gattgattta
2521 aaacttcatt tttaatttaa aaggatctag gtgaagatcc tttttgataa tctcatgacc
2581 aaaatccctt aacgtgagtt ttcgttccac tgagcgtcag acccgtaga aaagatcaaa
2641 ggatcttctt gagatccttt ttttctgccc gtaatctgct gcttgcaaac aaaaaacca
2701 ccgctaccag cgggtggtttg tttgccggat caagagctac caactctttt tccgaaggta
2761 actggcttca gcagagcgcg gataccaaat actgttcttc tagttagacc gtagttaggc
2821 caccacttca agaactctgt agcaccgctc acatacctcg ctctgctaact cctgttacca
2881 gtggctgctg ccagtggcga taagtctgtt cttaccgggt tggactcaag cagatagtta
2941 ccgataaagg cgcagcggtc gggctgaacg ggggttctgt gcacacagcc cagcttggag
3001 cgaacgacct acaccgaact gagataccta cagcgtgagc tatgagaaag cgcacgctt
3061 cccgaaggga gaaagcggg caggtatocg gtaagcggca gggtcggaac aggagagcgc
3121 acgagggagc ttccaggggg aaacgcctg gttctttata gtctctgctg gtttcgccac
3181 ctctgacttg agcgtcgatt tttgtgagc tcgtcagggg ggcggagcct atgaaaaaac
3241 gccagcaacg cggccttttt acggttctct gccttttctt ggccttttgc tccatggtc
3301 tttctgctg tatcccctga ttctgtggat aaccgtatta ccgcctttga gtgagctgat
3361 accgctcgc gcagccgaac gaccgagcgc agcagtcag tgagcgagga agcgggaag
3421 cgccaatac gcaaacgcgc tctcccgcg cgttggccga ttcattaatg cag

```

**pRSET::AQ TS**

ATGCTTACACCAGACTTCGACAACCCAAAATGGATTGGACGACACAAGCACATGTT  
TAATTTCTTGATGTCAACCACAATGGAAGGATCTCTCTTGACGAGATGGTCTACA  
AGGCGTCCGATATTGTTATAAACAATCTTGGAGCAACACCTGAACAAGCCAAACGT  
CACAAAGATGCTGTAGAAGCCTTCTTCGGAGGAGCTGGAATGAAATATGGTGTAG  
AACTGAATGGCCTGAATACATCGAAGGATGGAAAAGACTGGCTTCCGAGGAATT  
GAAAAGGTATTCAAAAAACCAAATCACACTTATTCGTTTATGGGGTGATGCATTGT  
TCGATATCATTGACAAAAGACCAAAAATGGAGCTATTTCACTGGATGAATGGAAAAGC  
ATACACCAAATCTGCTGGCATCATCCAATCGTCAGAAGATTGCGAGGAAACATTCA  
GAGTGTGCGATATTGACGAAAGTGGACAGCTCGATGTTGATGAGATGACAAGAC  
GACATATAGGATTTTGGTACACCATGGATCCTGCTTGCGAAAAGCTCTACGGTGG  
AGCTGTCCCCTAA

**pRSET::LAAQ**

ATGCTTACACCAGACTTCGACAACCCAAAATGGATTGGACGACACAAGCACATGTT  
TAATTTCTTGATGTCAACCACAATGGAAGGATCTCTCTTGACGAGATGGTCTACA  
AGGCGTCCGATATTGTTATAAACAATCTTGGAGCAACACCTGAACAAGCCAAACGT  
CACAAAGATGCTGTAGAAGCCTTCTTCGGAGGAGCTGGAATGAAATATGGTGTAG  
AACTGAATGGCCTGAATACATCGAAGGATGGAAAAGACTGGCTTCCGAGGAATT  
GAAAAGGTATTCAAAAAACCAAATCACACTTATTCGTTTATGGGGTGATGCATTGT  
TCGATATCATTGACAAAAGACCAAAAATGGATGGATTGAACTGGATGAATGGAAAAGC  
ATACACCAAATCTGCTGGCATCATCCAATCGTCAGAAGATTGCGAGGAAACATTCA  
GAGTGTGCGATATTGACGAAAGTGGATTTCTCGATGTTGATGAGATGACAAGACG  
ACATATAGGATTTTGGTACACCATGGATCCTGCTTGCGAAAAGCTCTACGGTGG  
GCTGTCCCCTAA

**pRSET::D119A**

ATGCTTACACCAGACTTCGACAACCCAAAATGGATTGGACGACACAAGCACATGTT  
TAATTTCTTGATGTCAACCACAATGGAAGGATCTCTCTTGACGAGATGGTCTACA  
AGGCGTCCGATATTGTTATAAACAATCTTGGAGCAACACCTGAACAAGCCAAACGT  
CACAAAGATGCTGTAGAAGCCTTCTTCGGAGGAGCTGGAATGAAATATGGTGTAG  
AACTGAATGGCCTGAATACATCGAAGGATGGAAAAGACTGGCTTCCGAGGAATT  
GAAAAGGTATTCAAAAAACCAAATCACACTTATTCGTTTATGGGGTGATGCATTGT  
TCGATATCATTGACAAAAGCCAAAATGGAGCTATTTCACTGGATGAATGGAAAAGC

ATACACCAAATCTGCTGGCATCATCCAATCGTCAGAAGATTGCGAGGAAACATTCA  
 GAGTGTGCGATATTGACGAAAGTGGACAGCTCGATGTTGATGAGATGACAAGAC  
 AACATTTAGGATTTTGGTACACCATGGATCCTGCTTGC~~G~~AAAAGCTCTACGGTGG  
 AGCTGTCCCCTAA

**pRSET::TS D119A**

ATGCTTACACCAGACTTCGACAACCCAAAATGGATTGGACGACACAAGCACATGTT  
 TAATTTTCTTGATGTCAACCACAATGGAAGGATCTCTCTTGACGAGATGGTCTACA  
 AGGCGTCCGATATTGTTATAAACAATCTTGGAGCAACACCTGAACAAGCCAAACGT  
 CACAAAGATGCTGTAGAAGCCTTCTTCGGAGGAGCTGGAATGAAATATGGTGTAG  
 AAACCTGAATGGCCTGAATACATCGAAGGATGGAAAAGACTGGCTTCCGAGGAATT  
 GAAAAGGTATTCAAAAAACCAAATCACACTTATTCGTTTATGGGGTGATGCATGT  
 TCGATATCATTGACAAAGCCCAAATGGAGCTATTCACTGGATGAATGGAAAGC  
 ATACACCAAATCTGCTGGCATCATCCAATCGTCAGAAGATTGCGAGGAAACATTCA  
 GAGTGTGCGATATTGACGAAAGTGGACAGCTCGATGTTGATGAGATGACAAGAC  
GACATATAGGATTTTGGTACACCATGGATCCTGCTTGCGAAAAGCTCTACGGTGG  
 AGCTGTCCCCTAA

**pRSET::LAAQ D119G**

ATGCTTACACCAGACTTCGACAACCCAAAATGGATTGGACGACACAAGCACATGTT  
 TAATTTTCTTGATGTCAACCACAATGGAAGGATCTCTCTTGACGAGATGGTCTACA  
 AGGCGTCCGATATTGTTATAAACAATCTTGGAGCAACACCTGAACAAGCCAAACGT  
 CACAAAGATGCTGTAGAAGCCTTCTTCGGAGGAGCTGGAATGAAATATGGTGTAG  
 AAACCTGAATGGCCTGAATACATCGAAGGATGGAAAAGACTGGCTTCCGAGGAATT  
 GAAAAGGTATTCAAAAAACCAAATCACACTTATTCGTTTATGGGGTGATGCATGT  
 TCGATATCATTGACAAAGACCAAATGGATGGATTGAACTGGATGAATGGAAAGC  
 ATACACCAAATCTGCTGGCATCATCCAATCGTCAGAAGATTGCGAGGAAACATTCA  
 GAGTGTGCGATATTGACGAAAGTGGATTTCTCGATGTTGATGAGATGACAAGACG  
 ACATATAGGATTTTGGTACACCATGGATCCTGCTTGC~~G~~AAAAGCTCTACGGTGG  
 GCTGTCCCCTAA

**pRSET::TS D119A/A123F**

ATGCTTACACCAGACTTCGACAACCCAAAATGGATTGGACGACACAAGCACATGTT  
 TAATTTCTTGATGTCAACCACAATGGAAGGATCTCTCTTGACGAGATGGTCTACA  
 AGGCGTCCGATATTGTTATAAACAATCTTGGAGCAACACCTGAACAAGCCAAACGT  
 CACAAAGATGCTGTAGAAGCCTTCTTCGGAGGAGCTGGAATGAAATATGGTGTAG  
 AAAGTGAATGGCCTGAATACATCGAAGGATGGAAAAGACTGGCTTCCGAGGAATT  
 GAAAAGGTATTCAAAAAACCAAATCACACTTATTCGTTTATGGGGTGATGCATTGT  
 TCGATATCATTGACAAAGCCAAAATGGATTATTTCACTGGATGAATGGAAAGCA  
 TACACCAAATCTGCTGGCATCATCCAATCGTCAGAAGATTGCGAGGAAACATTAG  
 AGTGTGCGATATTGACGAAAGTGGACAGCTCGATGTTGATGAGATGACAAGACG  
 ACATATAGGATTTTGGTACACCATGGATCCTGCTTGCGAAAAGCTCTACGGTGGA  
 GCTGTCCCCTAA

**pRSET::TS D119A/A123W**

ATGCTTACACCAGACTTCGACAACCCAAAATGGATTGGACGACACAAGCATATGTT  
 CAATTTCTTGATGTCAACCACAATGGAAAAATCTCTCTTGACGAGATGGTCTACA  
 AGGCATCTGATATTGTCATCAATAACCTTGGAGCAACACCTGAGCAAGCCAAACGA  
 CACAAAGATGCTGTAGAAGCCTTCTTCGGAGGAGCTGGAATGAAATATGGTGTG  
 GAAACTGATTGGCCTGCATATATTGAAGGATGGAAAAAATTGGCTACTGATGAAT  
 TGGAGAAATACGCCAAAAACGAACCAACGCTCATCCGTATATGGGGTGATGCTTT  
 GTTTGATATCGTTGACAAAGCCAAAATGGATGGATTTCCTGGATGAATGGAAA  
 GCATACACCAAATCTGCTGGCATCATCCAATCGTCAGAAGACTGCGAGGAAACATT  
 CAGAGTGTGCGATATTGATGAAAGTGGACAACCTCGATGTTGATGAGATGACAAG  
 ACAACATTTAGGATTTTGGTACACCATGGATCCTGCTTGTGAAAAGCTCTACGGTG  
 GAGCTGTCCCCTAA

**pRSET::TS D119A/S125A**

ATGCTTACACCAGACTTCGACAACCCAAAATGGATTGGACGACACAAGCACATGTT  
 TAATTTCTTGATGTCAACCACAATGGAAGGATCTCTCTTGACGAGATGGTCTACA  
 AGGCGTCCGATATTGTTATAAACAATCTTGGAGCAACACCTGAACAAGCCAAACGT  
 CACAAAGATGCTGTAGAAGCCTTCTTCGGAGGAGCTGGAATGAAATATGGTGTAG  
 AAAGTGAATGGCCTGAATACATCGAAGGATGGAAAAGACTGGCTTCCGAGGAATT  
 GAAAAGGTATTCAAAAAACCAAATCACACTTATTCGTTTATGGGGTGATGCATTGT  
 TCGATATCATTGACAAAGCCAAAATGGAGCTATTGCACTGGATGAATGGAAAGC

ATACACCAAATCTGCTGGCATCATCCAATCGTCAGAAGATTGCGAGGAAACATTCA  
 GAGTGTGCGATATTGACGAAAGTGGACAGCTCGATGTTGATGAGATGACAAGAC  
 GACATATAGGATTTTGGTACACCATGGATCCTGCTTGCAGAAAAGCTCTACGGTGG  
 AGCTGTCCCCTAA

**pRSET::TS D119A/S125G**

ATGCTTACACCAGACTTCGACAACCCAAAATGGATTGGACGACACAAGCACATGTT  
 TAATTTTCTTGATGTCAACCACAATGGAAGGATCTCTCTTGACGAGATGGTCTACA  
 AGGCGTCCGATATTGTTATAAACAATCTTGGAGCAACACCTGAACAAGCCAAACGT  
 CACAAAGATGCTGTAGAAGCCTTCTTCGGAGGAGCTGGAATGAAATATGGTGTAG  
 AAACCTGAATGGCCTGAATACATCGAAGGATGGAAAAGACTGGCTTCCGAGGAATT  
 GAAAAGGTATTCAAAAAACCAAATCACACTTATTCGTTTATGGGGTGATGCATGT  
 TCGATATCATTGACAAAAGCCAAAATGGAGCCATTGGACTGGATGAATGGAAAGC  
 ATACACCAAATCTGCTGGCATCATCCAATCGTCAGAAGATTGCGAGGAAACATTCA  
 GAGTGTGCGATATTGACGAAAGTGGACAGCTCGATGTTGATGAGATGACAAGAC  
 GACATATAGGATTTTGGTACACCATGGATCCTGCTTGCAGAAAAGCTCTACGGTGG  
 AGCTGTCCCCTAA

**pRSET::TS D119A/S125D**

ATGCTTACACCAGACTTCGACAACCCAAAATGGATTGGACGACACAAGCACATGTT  
 TAATTTTCTTGATGTCAACCACAATGGAAGGATCTCTCTTGACGAGATGGTCTACA  
 AGGCGTCCGATATTGTTATAAACAATCTTGGAGCAACACCTGAACAAGCCAAACGT  
 CACAAAGATGCTGTAGAAGCCTTCTTCGGAGGAGCTGGAATGAAATATGGTGTAG  
 AAACCTGAATGGCCTGAATACATCGAAGGATGGAAAAGACTGGCTTCCGAGGAATT  
 GAAAAGGTATTCAAAAAACCAAATCACACTTATTCGTTTATGGGGTGATGCATGT  
 TCGATATCATTGACAAAAGCCAAAATGGAGCCATTGACCTGGATGAATGGAAAGC  
 ATACACCAAATCTGCTGGCATCATCCAATCGTCAGAAGATTGCGAGGAAACATTCA  
 GAGTGTGCGATATTGACGAAAGTGGACAGCTCGATGTTGATGAGATGACAAGAC  
 GACATATAGGATTTTGGTACACCATGGATCCTGCTTGCAGAAAAGCTCTACGGTGG  
 AGCTGTCCCCTAA

**pRSET::TS D119A/S125E**

ATGCTTACACCAGACTTCGACAACCCAAAATGGATTGGACGACACAAGCACATGTT  
 TAATTTTCTTGATGTCAACCACAATGGAAGGATCTCTCTTGACGAGATGGTCTACA  
 AGGCGTCCGATATTGTTATAAACAATCTTGGAGCAACACCTGAACAAGCCAAACGT  
 CACAAAGATGCTGTAGAAGCCTTCTTCGGAGGAGCTGGAATGAAATATGGTGTAG  
 AAATGAATGGCCTGAATACATCGAAGGATGGAAAAGACTGGCTTCCGAGGAATT  
 GAAAAGGTATTCAAAAAACCAAATCACACTTATTCGTTTATGGGGTGATGCATTGT  
 TCGATATCATTGACAAAGCCAAAATGGAGCCATTGAACTGGATGAATGGAAAGC  
 ATACACCAAATCTGCTGGCATCATCCAATCGTCAGAAGATTGCGAGGAAACATTCA  
 GAGTGTGCGATATTGACGAAAGTGGACAGCTCGATGTTGATGAGATGACAAGAC  
 GACATATAGGATTTTGGTACACCATGGATCCTGCTTGCGAAAAGCTCTACGGTGG  
 AGCTGTCCCCTAA

**pRSET::TS A123F**

ATGCTTACACCAGACTTCGACAACCCAAAATGGATTGGACGACACAAGCACATGTT  
 TAATTTTCTTGATGTCAACCACAATGGAAGGATCTCTCTTGACGAGATGGTCTACA  
 AGGCGTCCGATATTGTTATAAACAATCTTGGAGCAACACCTGAACAAGCCAAACGT  
 CACAAAGATGCTGTAGAAGCCTTCTTCGGAGGAGCTGGAATGAAATATGGTGTAG  
 AAATGAATGGCCTGAATACATCGAAGGATGGAAAAGACTGGCTTCCGAGGAATT  
 GAAAAGGTATTCAAAAAACCAAATCACACTTATTCGTTTATGGGGTGATGCATTGT  
 TCGATATCATTGACAAAGACCAAAAATGGATTTATTTCACTGGATGAATGGAAAGCA  
 TACACCAAATCTGCTGGCATCATCCAATCGTCAGAAGATTGCGAGGAAACATTTCAG  
 AGTGTGCGATATTGACGAAAGTGGACAGCTCGATGTTGATGAGATGACAAGACG  
 ACATATAGGATTTTGGTACACCATGGATCCTGCTTGCGAAAAGCTCTACGGTGG  
 GCTGTCCCCTAA

**pRSET::TS A123F/S125E**

ATGCTTACACCAGACTTCGACAACCCAAAATGGATTGGACGACACAAGCACATGTT  
 TAATTTTCTTGATGTCAACCACAATGGAAGGATCTCTCTTGACGAGATGGTCTACA  
 AGGCGTCCGATATTGTTATAAACAATCTTGGAGCAACACCTGAACAAGCCAAACGT  
 CACAAAGATGCTGTAGAAGCCTTCTTCGGAGGAGCTGGAATGAAATATGGTGTAG  
 AAATGAATGGCCTGAATACATCGAAGGATGGAAAAGACTGGCTTCCGAGGAATT  
 GAAAAGGTATTCAAAAAACCAAATCACACTTATTCGTTTATGGGGTGATGCATTGT  
 TCGATATCATTGACAAAGACCAAAAATGGATTTATTTGAACTGGATGAATGGAAAGC

ATACACCAAATCTGCTGGCATCATCCAATCGTCAGAAGATTGCGAGGAAACATTCA  
 GAGTGTGCGATATTGACGAAAGTGGACAGCTCGATGTTGATGAGATGACAAGAC  
 GACATATAGGATTTTGGTACACCATGGATCCTGCTTGCGAAAAGCTCTACGGTGG  
 AGCTGTCCCCTAA

**pRSET::TS A123F/S125D**

ATGCTTACACCAGACTTCGACAACCCAAAATGGATTGGACGACACAAGCACATGTT  
 TAATTTTCTTGATGTCAACCACAATGGAAGGATCTCTCTTGACGAGATGGTCTACA  
 AGGCGTCCGATATTGTTATAAACAATCTTGGAGCAACACCTGAACAAGCCAAACGT  
 CACAAAGATGCTGTAGAAGCCTTCTTCGGAGGAGCTGGAATGAAATATGGTGTAG  
 AAACCTGAATGGCCTGAATACATCGAAGGATGGAAAAGACTGGCTTCCGAGGAATT  
 GAAAAGGTATTCAAAAAACCAAATCACACTTATTCGTTTATGGGGTGATGCATTTGT  
 TCGATATCATTGACAAAAGACCAAAAATGGATTTATTTGACCTGGATGAATGGAAAAGC  
 ATACACCAAATCTGCTGGCATCATCCAATCGTCAGAAGATTGCGAGGAAACATTCA  
 GAGTGTGCGATATTGACGAAAGTGGACAGCTCGATGTTGATGAGATGACAAGAC  
 GACATATAGGATTTTGGTACACCATGGATCCTGCTTGCGAAAAGCTCTACGGTGG  
 AGCTGTCCCCTAA

**pRSET::TS A123F/E128G**

ATGCTTACACCAGACTTCGACAACCCAAAATGGATTGGACGACACAAGCACATGTT  
 TAATTTTCTTGATGTCAACCACAATGGAAGGATCTCTCTTGACGAGATGGTCTACA  
 AGGCGTCCGATATTGTTATAAACAATCTTGGAGCAACACCTGAACAAGCCAAACGT  
 CACAAAGATGCTGTAGAAGCCTTCTTCGGAGGAGCTGGAATGAAATATGGTGTAG  
 AAACCTGAATGGCCTGAATACATCGAAGGATGGAAAAGACTGGCTTCCGAGGAATT  
 GAAAAGGTATTCAAAAAACCAAATCACACTTATTCGTTTATGGGGTGATGCATTTGT  
 TCGATATCATTGACAAAAGACCAAAAATGGATTTATTTCACTGGATGGATGGAAAAGC  
 ATACACCAAATCTGCTGGCATCATCCAATCGTCAGAAGATTGCGAGGAAACATTCA  
 GAGTGTGCGATATTGACGAAAGTGGACAGCTCGATGTTGATGAGATGACAAGAC  
 GACATATAGGATTTTGGTACACCATGGATCCTGCTTGCGAAAAGCTCTACGGTGG  
 AGCTGTCCCCTAA



**pRSET::TS A123W (A111G)**

ATGCTTACACCAGACTTCGACAACCCAAAATGGATTGGACGACACAAGCACATGTT  
 TAATTTTCTTGATGTCAACCACAATGGAAGGATCTCTCTTGACGAGATGGTCTACA  
 AGGCGTCCGATATTGTTATAAACAATCTTGGAGCAACACCTGAACAAGCCAAACGT  
 CACAAAGATGCTGTAGAAGCCTTCTTCGGAGGAGCTGGAATGAAATATGGTGTAG  
 AAATGAATGGCCTGAATACATCGAAGGATGGAAAAGACTGGCTTCCGAGGAATT  
 GAAAAGGTATTCAAAAAACCAAATCACACTTATTCGTTTATGGGGTGATGGATTGT  
 TCGATATCATTGACAAAAGACCAAAAATGGATGGATTTCACTGGATGAATGGAAAGC  
 ATACACCAAATCTGCTGGCATCATCCAATCGTCAGAAGATTGCGAGGAAACATTCA  
 GAGTGTGCGATATTGACGAAAGTGGACAGCTCGATGTTGATGAGATGACAAGAC  
 GACATATAGGATTTTGGTACACCATGGATCCTGCTTGCGAAAAGCTCTACGGTGG  
 AGCTGTCCCCTAA

**pRSET::TS A123W/S125D**

ATGCTTACACCAGACTTCGACAACCCAAAATGGATTGGACGACACAAGCACATGTT  
 TAATTTTCTTGATGTCAACCACAATGGAAGGATCTCTCTTGACGAGATGGTCTACA  
 AGGCGTCCGATATTGTTATAAACAATCTTGGAGCAACACCTGAACAAGCCAAACGT  
 CACAAAGATGCTGTAGAAGCCTTCTTCGGAGGAGCTGGAATGAAATATGGTGTAG  
 AAATGAATGGCCTGAATACATCGAAGGATGGAAAAGACTGGCTTCCGAGGAATT  
 GAAAAGGTATTCAAAAAACCAAATCACACTTATTCGTTTATGGGGTGATGCATTGT  
 TCGATATCATTGACAAAAGACCAAAAATGGATGGATTGACCTGGATGAATGGAAAGC  
 ATACACCAAATCTGCTGGCATCATCCAATCGTCAGAAGATTGCGAGGAAACATTCA  
 GAGTGTGCGATATTGACGAAAGTGGACAGCTCGATGTTGATGAGATGACAAGAC  
 GACATATAGGATTTTGGTACACCATGGATCCTGCTTGCGAAAAGCTCTACGGTGG  
 AGCTGTCCCCTAA

**pSRET::TS A123W/S125E**

ATGCTTACACCAGACTTCGACAACCCAAAATGGATTGGACGACACAAGCACATGTT  
 TAATTTTCTTGATGTCAACCACAATGGAAGGATCTCTCTTGACGAGATGGTCTACA  
 AGGCGTCCGATATTGTTATAAACAATCTTGGAGCAACACCTGAACAAGCCAAACGT  
 CACAAAGATGCTGTAGAAGCCTTCTTCGGAGGAGCTGGAATGAAATATGGTGTAG  
 AAATGAATGGCCTGAATACATCGAAGGATGGAAAAGACTGGCTTCCGAGGAATT  
 GAAAAGGTATTCAAAAAACCAAATCACACTTATTCGTTTATGGGGTGATGCATTGT  
 TCGATATCATTGACAAAAGACCAAAAATGGATGGATTGAACTGGATGAATGGAAAGC

ATACACCAAATCTGCTGGCATCATCCAATCGTCAGAAGATTGCGAGGAAACATTCA  
 GAGTGTGCGATATTGACGAAAGTGGACAGCTCGATGTTGATGAGATGACAAGAC  
 GACATATAGGATTTTGGTACACCATGGATCCTGCTTGCGAAAAGCTCTACGGTGG  
 AGCTGTCCCCTAA

**pRSET::TS A123W/E128G**

ATGCTTACACCAGACTTCGACAACCCAAAATGGATTGGACGACACAAGCACATGTT  
 TAATTTTCTTGATGTCAACCACAATGGAAGGATCTCTCTTGACGAGATGGTCTACA  
 AGGCGTCCGATATTGTTATAAACAATCTTGGAGCAACACCTGAACAAGCCAAACGT  
 CACAAAGATGCTGTAGAAGCCTTCTTCGGAGGAGCTGGAATGAAATATGGTGTAG  
 AAACCTGAATGGCCTGAATACATCGAAGGATGGAAAAGACTGGCTTCCGAGGAATT  
 GAAAAGGTATTCAAAAAACCAAATCACACTTATTCGTTTATGGGGTGATGCATTTGT  
 TCGATATCATTGACAAAAGACCAAAAATGGATGGATTTCACTGGATGGATGGAAAGC  
 ATACACCAAATCTGCTGGCATCATCCAATCGTCAGAAGATTGCGAGGAAACATTCA  
 GAGTGTGCGATATTGACGAAAGTGGACAGCTCGATGTTGATGAGATGACAAGAC  
 GACATATAGGATTTTGGTACACCATGGATCCTGCTTGCGAAAAGCTCTACGGTGG  
 AGCTGTCCCCTAA

**pRSET::TS S125D**

ATGCTTACACCAGACTTCGACAACCCAAAATGGATTGGACGACACAAGCACATGTT  
 TAATTTTCTTGATGTCAACCACAATGGAAGGATCTCTCTTGACGAGATGGTCTACA  
 AGGCGTCCGATATTGTTATAAACAATCTTGGAGCAACACCTGAACAAGCCAAACGT  
 CACAAAGATGCTGTAGAAGCCTTCTTCGGAGGAGCTGGAATGAAATATGGTGTAG  
 AAACCTGAATGGCCTGAATACATCGAAGGATGGAAAAGACTGGCTTCCGAGGAATT  
 GAAAAGGTATTCAAAAAACCAAATCACACTTATTCGTTTATGGGGTGATGCATTTGT  
 TCGATATCATTGACAAAAGACCAAAAATGGAGCCATTGACCTGGATGAATGGAAAGC  
 ATACACCAAATCTGCTGGCATCATCCAATCGTCAGAAGATTGCGAGGAAACATTCA  
 GAGTGTGCGATATTGACGAAAGTGGACAGCTCGATGTTGATGAGATGACAAGAC  
 GACATATAGGATTTTGGTACACCATGGATCCTGCTTGCGAAAAGCTCTACGGTGG  
 AGCTGTCCCCTAA

**pRSET::TS S125E**

ATGCTTACACCAGACTTCGACAACCCAAAATGGATTGGACGACACAAGCACATGTT  
 TAATTTTCTTGATGTCAACCACAATGGAAGGATCTCTCTTGACGAGATGGTCTACA  
 AGGCGTCCGATATTGTTATAAACAATCTTGGAGCAACACCTGAACAAGCCAAACGT  
 CACAAAGATGCTGTAGAAGCCTTCTTCGGAGGAGCTGGAATGAAATATGGTGTAG  
 AAATGAATGGCCTGAATACATCGAAGGATGGAAAAGACTGGCTTCCGAGGAATT  
 GAAAAGGTATTCAAAAAACCAAATCACACTTATTCGTTTATGGGGTGATGCATTGT  
 TCGATATCATTGACAAAAGACCAAAATGGAGCCATTGAACTGGATGAATGGAAAGC  
 ATACACCAAATCTGCTGGCATCATCCAATCGTCAGAAGATTGCGAGGAAACATTCA  
 GAGTGTGCGATATTGACGAAAGTGGACAGCTCGATGTTGATGAGATGACAAGAC  
 GACATATAGGATTTTGGTACACCATGGATCCTGCTTGCGAAAAGCTCTACGGTGG  
 AGCTGTCCCCTAA

**pRSET::TS S125G**

ATGCTTACACCAGACTTCGACAACCCAAAATGGATTGGACGACACAAGCACATGTT  
 TAATTTTCTTGATGTCAACCACAATGGAAGGATCTCTCTTGACGAGATGGTCTACA  
 AGGCGTCCGATATTGTTATAAACAATCTTGGAGCAACACCTGAACAAGCCAAACGT  
 CACAAAGATGCTGTAGAAGCCTTCTTCGGAGGAGCTGGAATGAAATATGGTGTAG  
 AAATGAATGGCCTGAATACATCGAAGGATGGAAAAGACTGGCTTCCGAGGAATT  
 GAAAAGGTATTCAAAAAACCAAATCACACTTATTCGTTTATGGGGTGATGCATTGT  
 TCGATATCATTGACAAAAGACCAAAATGGAGCCATTGGACTGGATGAATGGAAAGC  
 ATACACCAAATCTGCTGGCATCATCCAATCGTCAGAAGATTGCGAGGAAACATTCA  
 GAGTGTGCGATATTGACGAAAGTGGACAGCTCGATGTTGATGAGATGACAAGAC  
 GACATATAGGATTTTGGTACACCATGGATCCTGCTTGCGAAAAGCTCTACGGTGG  
 AGCTGTCCCCTAA

**pRSET::TS S125R**

ATGCTTACACCAGACTTCGACAACCCAAAATGGATTGGACGACACAAGCACATGTT  
 TAATTTTCTTGATGTCAACCACAATGGAAGGATCTCTCTTGACGAGATGGTCTACA  
 AGGCGTCCGATATTGTTATAAACAATCTTGGAGCAACACCTGAACAAGCCAAACGT  
 CACAAAGATGCTGTAGAAGCCTTCTTCGGAGGAGCTGGAATGAAATATGGTGTAG  
 AAATGAATGGCCTGAATACATCGAAGGATGGAAAAGACTGGCTTCCGAGGAATT  
 GAAAAGGTATTCAAAAAACCAAATCACACTTATTCGTTTATGGGGTGATGCATTGT  
 TCGATATCATTGACAAAAGACCAAAATGGAGCCATTAGACTAGATGAATGGAAAGC

ATACACCAAATCTGCTGGCATCATCCAATCGTCAGAAGATTGCGAGGAAACATTCA  
 GAGTGTGCGATATTGACGAAAGTGGACAGCTCGATGTTGATGAGATGACAAGAC  
 GACATATAGGATTTTGGTACACCATGGATCCTGCTTGCGAAAAGCTCTACGGTGG  
 AGCTGTCCCCTAA

**pRSET::TS D127G**

ATGCTTACACCAGACTTCGACAACCCAAAATGGATTGGACGACACAAGCACATGTT  
 TAATTTTCTTGATGTCAACCACAATGGAAGGATCTCTCTTGACGAGATGGTCTACA  
 AGGCGTCCGATATTGTTATAAACAATCTTGGAGCAACACCTGAACAAGCCAAACGT  
 CACAAAGATGCTGTAGAAGCCTTCTTCGGAGGAGCTGGAATGAAATATGGTGTAG  
 AAACCTGAATGGCCTGAATACATCGAAGGATGGAAAAGACTGGCTTCCGAGGAATT  
 GAAAAGGTATTCAAAAAACCAAATCACACTTATTCGTTTATGGGGTGATGCATGT  
 TCGATATCATTGACAAAAGACCAAAAATGGAGCTATTTCACTGGGGGAATGGAAAGC  
 ATACACCAAATCTGCTGGCATCATCCAATCGTCAGAAGATTGCGAGGAAACATTCA  
 GAGTGTGCGATATTGACGAAAGTGGACAGCTCGATGTTGATGAGATGACAAGAC  
 GACATATAGGATTTTGGTACACCATGGATCCTGCTTGCGAAAAGCTCTACGGTGG  
 AGCTGTCCCCTAA

**pRSET::TS D127R**

ATGCTTACACCAGACTTCGACAACCCAAAATGGATTGGACGACACAAGCACATGTT  
 TAATTTTCTTGATGTCAACCACAATGGAAGGATCTCTCTTGACGAGATGGTCTACA  
 AGGCGTCCGATATTGTTATAAACAATCTTGGAGCAACACCTGAACAAGCCAAACGT  
 CACAAAGATGCTGTAGAAGCCTTCTTCGGAGGAGCTGGAATGAAATATGGTGTAG  
 AAACCTGAATGGCCTGAATACATCGAAGGATGGAAAAGACTGGCTTCCGAGGAATT  
 GAAAAGGTATTCAAAAAACCAAATCACACTTATTCGTTTATGGGGTGATGCATGT  
 TCGATATCATTGACAAAAGACCAAAAATGGAGCTATTTCACTGAGGGGAATGGAAAGC  
 ATACACCAAATCTGCTGGCATCATCCAATCGTCAGAAGATTGCGAGGAAACATTCA  
 GAGTGTGCGATATTGACGAAAGTGGACAGCTCGATGTTGATGAGATGACAAGAC  
 GACATATAGGATTTTGGTACACCATGGATCCTGCTTGCGAAAAGCTCTACGGTGG  
 AGCTGTCCCCTAA

**pRSET::TS E128G**

ATGCTTACACCAGACTTCGACAACCCAAAATGGATTGGACGACACAAGCACATGTT  
 TAATTTTCTTGATGTCAACCACAATGGAAGGATCTCTCTTGACGAGATGGTCTACA  
 AGGCGTCCGATATTGTTATAAACAATCTTGGAGCAACACCTGAACAAGCCAAACGT  
 CACAAAGATGCTGTAGAAGCCTTCTTTCGGAGGAGCTGGAATGAAATATGGTGTAG  
 AAACCTGAATGGCCTGAATACATCGAAGGATGGAAAAGACTGGCTTCCGAGGAATT  
 GAAAAGGTATTCAAAAAACCAAATCACACTTATTCGTTTATGGGGTGATGCATTGT  
 TCGATATCATTGACAAAGACCAAAAATGGAGCTATTTCACTGGATGGATGGAAAGC  
 ATACACCAAATCTGCTGGCATCATCCAATCGTCAGAAGATTGCGAGGAAACATTCA  
 GAGTGTGCGATATTGACGAAAGTGGACAGCTCGATGTTGATGAGATGACAAGAC  
 GACATATAGGATTTTGGTACACCATGGATCCTGCTTTCGAAAAGCTCTACGGTGG  
 AGCTGTCCCCTAA

**pRSET::TS I116V/D117A/D119A**

ATGCTTACACCAGACTTCGACAACCCAAAATGGATTGGACGACACAAGCACATGTT  
 TAATTTTCTTGATGTCAACCACAATGGAAGGATCTCTCTTGACGAGATGGTCTACA  
 AGGCGTCCGATATTGTTATAAACAATCTTGGAGCAACACCTGAACAAGCCAAACGT  
 CACAAAGATGCTGTAGAAGCCTTCTTTCGGAGGAGCTGGAATGAAATATGGTGTAG  
 AAACCTGAATGGCCTGAATACATCGAAGGATGGAAAAGACTGGCTTCCGAGGAATT  
 GAAAAGGTATTCAAAAAACCAAATCACACTTATTCGTTTATGGGGTGATGCATTGT  
 TTGATATCGTTGCCAAAAGCCAAAATGGAGCCATTTCACTGGATGAATGGAAAGC  
 ATACACCAAATCTGCTGGCATCATCCAATCGTCAGAAGATTGCGAGGAAACATTCA  
 GAGTGTGCGATATTGACGAAAGTGGACAGCTCGATGTTGATGAGATGACAAGAC  
 GACATATAGGATTTTGGTACACCATGGATCCTGCTTTCGAAAAGCTCTACGGTGG  
 AGCTGTCCCCTAA

**pRSET::TS D127R**

ATGCTTACACCAGACTTCGACAACCCAAAATGGATTGGACGACACAAGCACATGTT  
 TAATTTTCTTGATGTCAACCACAATGGAAGGATCTCTCTTGACGAGATGGTCTACA  
 AGGCGTCCGATATTGTTATAAACAATCTTGGAGCAACACCTGAACAAGCCAAACGT  
 CACAAAGATGCTGTAGAAGCCTTCTTTCGGAGGAGCTGGAATGAAATATGGTGTAG  
 AAACCTGAATGGCCTGAATACATCGAAGGATGGAAAAGACTGGCTTCCGAGGAATT  
 GAAAAGGTATTCAAAAAACCAAATCACACTTATTCGTTTATGGGGTGATGCATTGT  
 TCGATATCATTGACAAAGACCAAAAATGGAGCTATTTCACTGCGGGAATGGAAAGC

ATACACCAAATCTGCTGGCATCATCCAATCGTCAGAAGATTGCGAGGAAACATTCA  
 GAGTGTGCGATATTGACGAAAGTGGACAGCTCGATGTTGATGAGATGACAAGAC  
 GACATATAGGATTTTGGTACACCATGGATCCTGCTTGCGAAAAGCTCTACGGTGG  
 AGCTGTCCCCTAA

**pRSET::TS D119A A123F S125E D127R**

ATGCTTACACCAGACTTCGACAACCCAAAATGGATTGGACGACACAAGCACATGTT  
 TAATTTTCTTGATGTCAACCACAATGGAAGGATCTCTCTTGACGAGATGGTCTACA  
 AGGCGTCCGATATTGTTATAAACAATCTTGGAGCAACACCTGAACAAGCCAAACGT  
 CACAAAGATGCTGTAGAAGCCTTCTTCGGAGGAGCTGGAATGAAATATGGTGTAG  
 AAACCTGAATGGCCTGAATACATCGAAGGATGGAAAAGACTGGCTTCCGAGGAATT  
 GAAAAGGTATTCAAAAAACCAAATCACACTTATTCGTTTATGGGGTGATGCATGT  
 TCGATATCATTGACAAAAGCCAAAATGGATTTATTTGAACCTGCGGGAAATGGAAAGC  
 ATACACCAAATCTGCTGGCATCATCCAATCGTCAGAAGATTGCGAGGAAACATTCA  
 GAGTGTGCGATATTGACGAAAGTGGACAGCTCGATGTTGATGAGATGACAAGAC  
 GACATATAGGATTTTGGTACACCATGGATCCTGCTTGCGAAAAGCTCTACGGTGG  
 AGCTGTCCCCTAA

**pRSET::TS A123W S125E D127R**

ATGCTTACACCAGACTTCGACAACCCAAAATGGATTGGACGACACAAGCACATGTT  
 TAATTTTCTTGATGTCAACCACAATGGAAGGATCTCTCTTGACGAGATGGTCTACA  
 AGGCGTCCGATATTGTTATAAACAATCTTGGAGCAACACCTGAACAAGCCAAACGT  
 CACAAAGATGCTGTAGAAGCCTTCTTCGGAGGAGCTGGAATGAAATATGGTGTAG  
 AAACCTGAATGGCCTGAATACATCGAAGGATGGAAAAGACTGGCTTCCGAGGAATT  
 GAAAAGGTATTCAAAAAACCAAATCACACTTATTCGTTTATGGGGTGATGCATGT  
 TCGATATCATTGACAAAAGACCAAAAATGGATGGATTGAACTGCGGGAAACCATGGA  
 TCCTGCTTGCGAAAAGCTCTACGGTGGAGCTGTCCCCTAA

**pRSET::TS A123F S125E D127R**

ATGCTTACACCAGACTTCGACAACCCAAAATGGATTGGACGACACAAGCACATGTT  
 TAATTTTCTTGATGTCAACCACAATGGAAGGATCTCTCTTGACGAGATGGTCTACA  
 AGGCGTCCGATATTGTTATAAACAATCTTGGAGCAACACCTGAACAAGCCAAACGT  
 CACAAAGATGCTGTAGAAGCCTTCTTCGGAGGAGCTGGAATGAAATATGGTGTAG

AAACTGAATGGCCTGAATACATCGAAGGATGGAAAAGACTGGCTTCCGAGGAATT  
 GAAAAGGTATTCAAAAAACCAAATCACACTTATTCGTTTATGGGGTGATGCATTTGT  
 TCGATATCATTGACAAAGACCAAAATGGATTTATTTGAACTGCGGGAATGGAAAGC  
 ATACACCAAATCTGCTGGCATCATCCAATCGTCAGAAGATTTGCGAGGAAACATTTCA  
 GAGTGTGCGATATTGACGAAAGTGGACAGCTCGATGTTGATGAGATGACAAGAC  
 GACATATAGGATTTTGGTACACCATGGATCCTGCTTTCGAAAAGCTCTACGGTGG  
 AGCTGTCCCCCTAA

**pRSET::TS D119A A123W S125E D127R**

ATGCTTACACCAGACTTCGACAACCCAAAATGGATTGGACGACACAAGCACATGTT  
 TAATTTTCTTGATGTCAACCACAATGGAAGGATCTCTCTTGACGAGATGGTCTACA  
 AGGCGTCCGATATTGTTATAAACAATCTTGGAGCAACACCTGAACAAGCCAAACGT  
 CACAAAGATGCTGTAGAAGCCTTCTTCGGAGGAGCTGGAATGAAATATGGTGTAG  
 AAACCTGAATGGCCTGAATACATCGAAGGATGGAAAAGACTGGCTTCCGAGGAATT  
 GAAAAGGTATTCAAAAAACCAAATCACACTTATTCGTTTATGGGGTGATGCATTTGT  
 TCGATATCATTGACAAAGCCCAAAATGGATGGATTTGAACTGCGGGGAAACATTTCA  
 GAGTGTGCGATATTGACGAAAGTGGACAGCTCGATGTTGATGAGATGACAAGAC  
 GACATATAGGATTTTGGTACACCATGGATCCTGCTTTCGAAAAGCTCTACGGTGG  
 AGCTGTCCCCCTAA

**pRSET::TS D119A A123W S125E**

ATGCTTACACCAGACTTCGACAACCCAAAATGGATTGGACGACACAAGCACATGTT  
 TAATTTTCTTGATGTCAACCACAATGGAAGGATCTCTCTTGACGAGATGGTCTACA  
 AGGCGTCCGATATTGTTATAAACAATCTTGGAGCAACACCTGAACAAGCCAAACGT  
 CACAAAGATGCTGTAGAAGCCTTCTTCGGAGGAGCTGGAATGAAATATGGTGTAG  
 AAACCTGAATGGCCTGAATACATCGAAGGATGGAAAAGACTGGCTTCCGAGGAATT  
 GAAAAGGTATTCAAAAAACCAAATCACACTTATTCGTTTATGGGGTGATGCATTTGT  
 TCGATATCATTGACAAAGCCCAAAATGGATGGATTTGAACTGGATGAATGGAAAGC  
 ATACACCAAATCTGCTGGCATCATCCAATCGTCAGAAGATTTGCGAGGAAACATTTCA  
 GAGTGTGCGATATTGACGAAAGTGGACAGCTCGATGTTGATGAGATGACAAGAC  
 GACATATAGGATTTTGGTACACCATGGATCCTGCTTTCGAAAAGCTCTACGGTGG  
 AGCTGTCCCCCTAA

**pRSET::TS D119A A123F S125E**

ATGCTTACACCAGACTTCGACAACCCAAAATGGATTGGACGACACAAGCACATGTT  
 TAATTTTCTTGATGTCAACCACAATGGAAGGATCTCTCTTGACGAGATGGTCTACA  
 AGGCGTCCGATATTGTTATAAACAATCTTGGAGCAACACCTGAACAAGCCAAACGT  
 CACAAAGATGCTGTAGAAGCCTTCTTTCGGAGGAGCTGGAATGAAATATGGTGTAG  
 AAACCTGAATGGCCTGAATACATCGAAGGATGGAAAAGACTGGCTTCCGAGGAATT  
 GAAAAGGTATTCAAAAAACCAAATCACACTTATTCGTTTATGGGGTGATGCATTGT  
 TCGATATCATTGACAAAAGCCAAAATGGATTATTTGAACTGGATGAATGGAAAAGC  
 ATACACCAAATCTGCTGGCATCATCCAATCGTCAGAAGATTGCGAGGAAACATTCA  
 GAGTGTGCGATATTGACGAAAGTGGACAGCTCGATGTTGATGAGATGACAAGAC  
 GACATATAGGATTTTGGTACACCATGGATCCTGCTTGCGAAAAGCTCTACGGTGG  
 AGCTGTCCCCTAA

**pRSET::TS A123W S125E Q159F**

ATGCTTACACCAGACTTCGACAACCCAAAATGGATTGGACGACACAAGCACATGTT  
 TAATTTTCTTGATGTCAACCACAATGGAAGGATCTCTCTTGACGAGATGGTCTACA  
 AGGCGTCCGATATTGTTATAAACAATCTTGGAGCAACACCTGAACAAGCCAAACGT  
 CACAAAGATGCTGTAGAAGCCTTCTTTCGGAGGAGCTGGAATGAAATATGGTGTAG  
 AAACCTGAATGGCCTGAATACATCGAAGGATGGAAAAGACTGGCTTCCGAGGAATT  
 GAAAAGGTATTCAAAAAACCAAATCACACTTATTCGTTTATGGGGTGATGCATTGT  
 TCGATATCATTGACAAAAGACCAAAAATGGATGGATTGAACTGGATGAATGGAAAAGC  
 ATACACCAAATCTGCTGGCATCATCCAATCGTCAGAAGATTGCGAGGAAACATTCA  
 GAGTGTGCGATATTGACGAAAGTGGATTTCTCGATGTTGATGAGATGACAAGACG  
 ACATATAGGATTTTGGTACACCATGGATCCTGCTTGCGAAAAGCTCTACGGTGG  
 GCTGTCCCCTAA

**pRSET::TS A123W S125E D161E**

ATGCTTACACCAGACTTCGACAACCCAAAATGGATTGGACGACACAAGCACATGTT  
 TAATTTTCTTGATGTCAACCACAATGGAAGGATCTCTCTTGACGAGATGGTCTACA  
 AGGCGTCCGATATTGTTATAAACAATCTTGGAGCAACACCTGAACAAGCCAAACGT  
 CACAAAGATGCTGTAGAAGCCTTCTTTCGGAGGAGCTGGAATGAAATATGGTGTAG  
 AAACCTGAATGGCCTGAATACATCGAAGGATGGAAAAGACTGGCTTCCGAGGAATT  
 GAAAAGGTATTCAAAAAACCAAATCACACTTATTCGTTTATGGGGTGATGCATTGT  
 TCGATATCATTGACAAAAGACCAAAAATGGATGGATTGAACTGGATGAATGGAAAAGC



ATACACCAAATCTGCTGGCATCATCCAATCGTCAGAAGATTGCGAGGAAACATTCA  
GAGTGTGCGATATTGACGAAAGTGGACAGCTCGAAGTTGATGAGATGACAAGAC  
GACATATAGGATTTTGGTACACCATGGATCCTGCTTGCAGAAAAGCTCTACGGTGG  
AGCTGTCCCCTAA

**pRSET::TS A123W S125E Q159W D161E**

ATGCTTACACCAGACTTCGACAACCCAAAATGGATTGGACGACACAAGCACATGTT  
TAATTTTCTTGATGTCAACCACAATGGAAGGATCTCTCTTGACGAGATGGTCTACA  
AGGCGTCCGATATTGTTATAAACAATCTTGGAGCAACACCTGAACAAGCCAAACGT  
CACAAAGATGCTGTAGAAGCCTTCTTCGGAGGAGCTGGAATGAAATATGGTGTAG  
AAACTGAATGGCCTGAATACATCGAAGGATGGAAAAGACTGGCTTCCGAGGAATT  
GAAAAGGTATTCAAAAAACCAAATCACACTTATTCGTTTATGGGGTGATGCATTTGT  
TCGATATCATTGACAAAAGACCAAAAATGGATGGATTGAACTGGATGAATGGAAAGC  
ATACACCAAATCTGCTGGCATCATCCAATCGTCAGAAGATTGCGAGGAAACATTCA  
GAGTGTGCGATATTGACGAAAGTGGATGGCTCGAAGTTGATGAGATGACAAGAC  
GACATATAGGATTTTGGTACACCATGGATCCTGCTTGCAGAAAAGCTCTACGGTGG  
AGCTGTCCCCTAA

**pRSET::TS R30W S32E A123W S125E Q159W D161E**

ATGCTTACACCAGACTTCGACAACCCAAAATGGATTGGACGACACAAGCACATGTT  
TAATTTTCTTGATGTCAACCACAATGGATGGATCGAACTTGACGAGATGGTCTACA  
AGGCGTCCGATATTGTTATAAACAATCTTGGAGCAACACCTGAACAAGCCAAACGT  
CACAAAGATGCTGTAGAAGCCTTCTTCGGAGGAGCTGGAATGAAATATGGTGTAG  
AAACTGAATGGCCTGAATACATCGAAGGATGGAAAAGACTGGCTTCCGAGGAATT  
GAAAAGGTATTCAAAAAACCAAATCACACTTATTCGTTTATGGGGTGATGCATTTGT  
TCGATATCATTGACAAAAGACCAAAAATGGATGGATTGAACTGGATGAATGGAAAGC  
ATACACCAAATCTGCTGGCATCATCCAATCGTCAGAAGATTGCGAGGAAACATTCA  
GAGTGTGCGATATTGACGAAAGTGGATGGATCGAACTTGACGAGATGACAAGAC  
GACATATAGGATTTTGGTACACCATGGATCCTGCTTGCAGAAAAGCTCTACGGTGG  
AGCTGTCCCCTAA

**TS EF1/3 P3 N EF1/2/3 WE**

ATGCTTACACCAGACTTCGACAACCCAAAATGGATTGGACGACACAAGCACATGTT  
 TAATTTTCTTGATGTCAACCACAATGGATGGATCGAACTTGACGAGATGGTCTACA  
 AGGCGTCCGATATTGTTATAAACAATCTTGGAGCAACACCTGAACAAGCCAAACGT  
 CACAAAGATGCTGTAGAAGCCTTCTTTCGGAGGAGCTGGAATGAAATATGGTGTAG  
 AAATGAATGGCCTGAATACATCGAAGGATAGAAAAGACTGGCTTCCGAGGAATT  
 GAAAAGGTATTCAAAAAACCAAATCACACTTATTCGTTTATGGGGTGATGCATTGT  
 TCGATATCATTGACAAAAGACCAAAAATGGATGGATTGAACTGGATGAATGGAAAGC  
 ATACACCAAATCTGCTGGCATCATCCAATCGTCAGAAGATTGCGAGGAAACATTCA  
 GAGTGTGCGATATTGACGAAAGTGGATGGATCGAACTTGACGAGATGACAAGAC  
 GACATATAGGATTTTGGTACACCATGGATCCTGCTTGCGAAAAGCTCTACGGTGG  
 AGCTGTCCCCTAA

**pRSET::TS Q159W D161E**

ATGCTTACACCAGACTTCGACAACCCAAAATGGATTGGACGACACAAGCACATGTT  
 TAATTTTCTTGATGTCAACCACAATGGAAGGATCTCTCTTGACGAGATGGTCTACA  
 AGGCGTCCGATATTGTTATAAACAATCTTGGAGCAACACCTGAACAAGCCAAACGT  
 CACAAAGATGCTGTAGAAGCCTTCTTTCGGAGGAGCTGGAATGAAATATGGTGTAG  
 AAATGAATGGCCTGAATACATCGAAGGATGGAAAAGACTGGCTTCCGAGGAATT  
 GAAAAGGTATTCAAAAAACCAAATCACACTTATTCGTTTATGGGGTGATGCATTGT  
 TCGATATCATTGACAAAAGACCAAAAATGGAGCTATTTCACTGGATGAATGGAAAGC  
 ATACACCAAATCTGCTGGCATCATCCAATCGTCAGAAGATTGCGAGGAAACATTCA  
 GAGTGTGCGATATTAACGAAAGTGGATGGCTCGAGGTTGATGAGATGACAAGAC  
 GACATATAGGATTTTGGTACACCATGGATCCTGCTTGCGAAAAGCTCTACGGTGG  
 AGCTGTCCCCTAA

**pRSET::TS R30W S32E**

ATGCTTACACCAGACTTCGACAACCCAAAATGGATTGGACGACACAAGCACATGTT  
 TAATTTTCTTGATGTCAACCACAATGGATGGATCGAACTTGACGAGATGGTCTACA  
 AGGCGTCCGATATTGTTATAAACAATCTTGGAGCAACACCTGAACAAGCCAAACGT  
 CACAAAGATGCTGTAGAAGCCTTCTTTCGGAGGAGCTGGAATGAAATATGGTGTAG  
 AAATGAATGGCCTGAATACATCGAAGGATGGAAAAGACTGGCTTCCGAGGAATT  
 GAAAAGGTATTCAAAAAACCAAATCACACTTATTCGTTTATGGGGTGATGCATTGT  
 TCGATATCATTGACAAAAGACCAAAAATGGAGCTATTTCACTGGATGAATGGAAAGC

ATACACCAAATCTGCTGGCATCATCCAATCGTCAGAAGATTGCGAGGAAACATTCA  
GAGTGTGCGATATTGACGAAAGTGGACAGCTCGATGTTGATGAGATGACAAGAC  
GACATATAGGATTTTGGTACACCATGGATCCTGCTTGCAGAAAAGCTCTACGGTGG  
AGCTGTCCCCTAA

**pRSET::TS R30W S32E A123W S125E**

ATGCTTACACCAGACTTCGACAACCCAAAATGGATTGGACGACACAAGCACATGTT  
TAATTTTCTTGATGTCAACCACAATGGATGGATCGAACTTGACGAGATGGTCTACA  
AGGCGTCCGATATTGTTATAAACAATCTTGGAGCAACACCTGAACAAGCCAAACGT  
CACAAAGATGCTGTAGAAGCCTTCTTCGGAGGAGCTGGAATGAAATATGGTGTAG  
AACTGAATGGCCTGAATACATCGAAGGATGGAAAAGACTGGCTTCCGAGGAATT  
GAAAAGGTATTCAAAAAACCAAATCACACTTATTCGTTTATGGGGTGATGCATGT  
TCGATATCATTGACAAAAGACCAAAATGGATGGATTGAACTGGATGAATGGAAAGC  
ATACACCAAATCTGCTGGCATCATCCAATCGTCAGAAGATTGCGAGGAAACATTCA  
GAGTGTGCGATATTGACGAAAGTGGACAGCTCGATGTTGATGAGATGACAAGAC  
GACATATAGGATTTTGGTACACCATGGATCCTGCTTGCAGAAAAGCTCTACGGTGG  
AGCTGTCCCCTAA

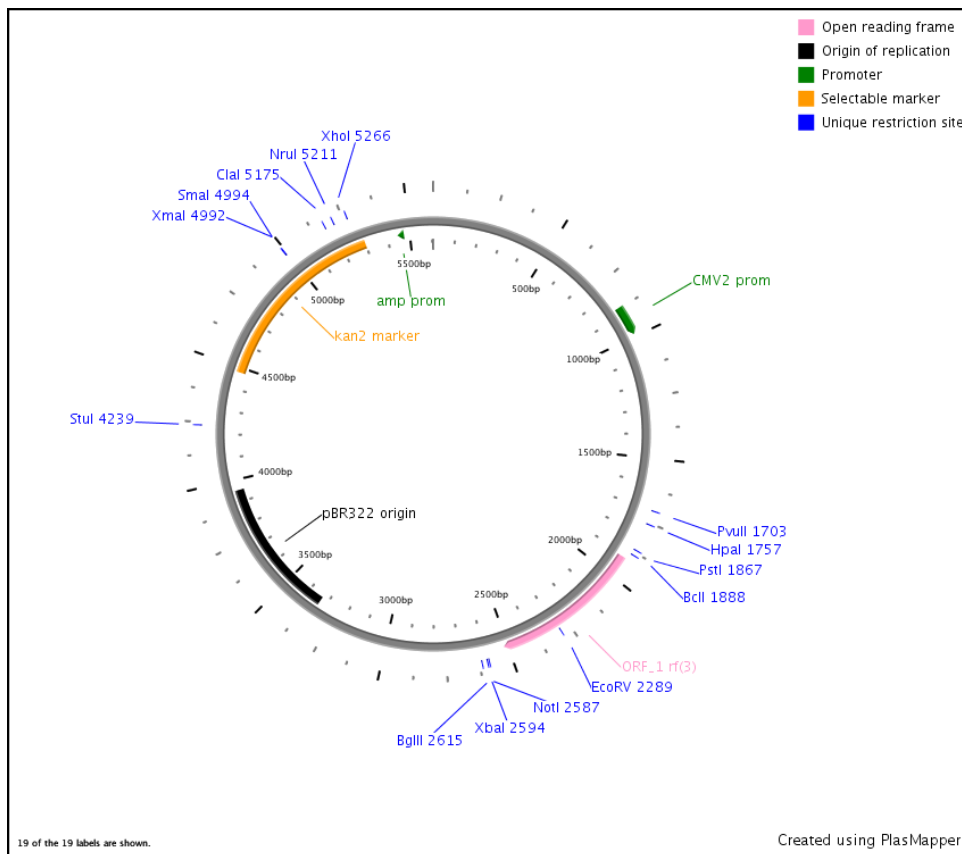
## VR1012::HA-AQ

1 tcgcgcggtt cggatgatgac ggtgaaaacc tctgacacat gcagctcccg gagacgggtca  
 61 cagcttgtct gtaagcggat gccgggagca gacaagcccg tcagggcgcg tcagcgggtg  
 121 ttggcgggtg tcggggctgg cttactatg cggcatcaga gcagattgta ctgagagtgc  
 181 accatatgcg gtgtgaaata ccgcacagat gcgtaaggag aaaataccgc atcagattgg  
 241 ctattggcca ttgcatacgt tgtatccata tcataaatg tacatttata ttggctcatg  
 301 tccaacatta ccgcatggtt gacattgatt attgactagt tattaatagt aatcaattac  
 361 ggggtcatta gttcatagcc catatatgga gttccgcgtt acataactta cggtaaatgg  
 421 cccgcctggc tgaccgcccc acgacccccg cccattgacg tcaataatga cgtatgttcc  
 481 catagtaacg ccaatagggg ctttccattg acgtcaatgg gtggagtatt tacggtaaac  
 541 tgcccacttg gcagtacatc aagtgtatca tatgccaagt acgcccccta ttgacgtcaa  
 601 tgacggtaaa tggcccgcct ggcattatgc ccagtacatg accttatggg acgttcccta  
 661 cttggcagta catctacgta ttagtcatcg ctattacat ggtgatgctg ttttggcagt  
 721 acatcaatgg gcgtggatag cggtttgact cacggggatt tccaagtctc cacccttctg  
 781 acgtcaatgg gagtttgttt tggcaccaaa atcaacggga ctttccaaaa tgtcgttaaca  
 841 actccgcccc attgacgcaa atgggcggta ggcgtgtacg gtgggaggtc tatataagca  
 901 gagctcggtt agtgaaccgg tcagatcgcc tggagacgcc atccacgctg ttttgacctc  
 961 catagaagac accgggaccg atccagcctc cgcggccggg aacgggtgcat tggaacgctg  
 1021 attccccgtg ccaagagtga cgtaagtacc gcctatagac tctataggca cacccttctg  
 1081 gctcttatgc atgctatact gtttttggct tggggcctat acacccccgc ttcccttatgc  
 1141 tataggtgat ggtatagctt agcctatag tgtgggttat tgaccattat tgaccactcc  
 1201 cctattgggt acgatacttt ccattactaa tccataacat ggctctttgc cacaactatc  
 1261 tctattggct atatgccaat actctgtcct tcagagactg acacggactc tgtattttta  
 1321 caggatgggg tcccatttat tatttcaaaa ttcacatata caacaacgcc gtccccctg  
 1381 cccgcagttt ttattaaaca tagcgtggga tctccacgcg aatctcgggt acgtgttccg  
 1441 gacatgggct cttctccggt agcggcggag cttccacatc cgagccctgg tcccatgcct  
 1501 ccagcggctc atggctgctc ggcagctcct tgctcctaac agtggaggcc agacttaggc  
 1561 acagcacaat gccaccacc accagtgtgc cgcacaaggc cgtggcggta gggatgtgt  
 1621 ctgaaaatga gcgtggagat tgggctcgca cggctgacgc agatggaaga cttaaggcag  
 1681 cggcagaaga agatgcaggc agctgagttg ttgtattctg ataagagtca gaggtaactc  
 1741 ccgttgcggt gctgttaacg gtggaggcca gtgtagtctg agcagtactc gttgctgccc  
 1801 cgcgcgccac cagacataat agctgacaga ctaacagact gttcctttcc atgggtcctt  
 1861 tctgcagtca ccgtcgtcga cacgtgtgat cagataattc gagctcggta cccatgaagc  
 1921 tttatgatgt tcttgattat gctagcctca aacttacatc agacttcgac aaccacaagt  
 1981 ggattggacg acacaagcat atgttcaatt tccttgatgt caaccacat ggaaaaatct  
 2041 ctcttgacga gatggtctac aaggcatctg atattgtcat caataacctt ggagcaaac  
 2101 ctgagcaagc caaacgacac aaagatgctg tagaagcctt cttcggaggga gctggaatga  
 2161 aatatggtgt ggaactgat tggcctgcat atattgaagg atggaaaaaa ttggctactg  
 2221 atgaattgga gaaatagcc aaaaacgaac caacgctcat ccgtatatgg ggtgatgctt  
 2281 tgtttgatat cgttgacaaa gatcaaatg gagccattac actggatgaa tggaaagcat  
 2341 acaccaaagc tgctggatc atccaatcat cagaagattg cgaggaaaca ttcagagtgt  
 2401 gcatattgaa tgaagtggg caactcgatg ttgatgagat gacaagacaa catttaggat  
 2461 tttggtagac catggatcct gcttgcgaaa agctctacgg tggagctgct ccctaagaag  
 2521 ctctacggtg gtgatgcacc cttaggaagat gatgtgattt tgaataaaaac actgatgaat  
 2581 tatcgcggcc gctctagacc aggccctgga tccagatctg ctgtgccttc tagttgccag  
 2641 ccactctgtt tttgcccctc ccccgctgct tccttgacc tggaaagggtc cactcccact  
 2701 gtcctttcct aataaaatga ggaattgca tcgcattgtc tgagttaggtc tcattctatt  
 2761 ctgggggggt ggggtggggca ggcagcaag ggggaggatt ggaagacaa tagcagcat  
 2821 gctgggggat cgggtgggctc tatgggtacc cagggtgctga agaattgacc cgttccctc  
 2881 tgggccagaa agaagcaggc acatccccct ctctgtgaca caccctgtcc acgcccctg  
 2941 ttcttagttc cagccccact cataggacac tcatagctca ggagggtcc gccttcaatc  
 3001 ccaccgccta aagtacttgg agcggctctc ccctccctca tcagcccacc aaaccaaacc  
 3061 tagcctccaa gagtgggaag aaattaaagc aagataggct attaagtga gagggagaga  
 3121 aatgcctcc aacatgtgag gaagtaatga gagaaatcat agaatttctt ccgcttccctc  
 3181 gctcactgac tcgctgcgct cggctgctcg gctgcggcga gcggtatcag ctactcaaa  
 3241 ggcggttaata cggttatcca cagaatcagg ggataacgca ggaagaaca tgtgagcaaa  
 3301 aggccagcaa aaggccagga accgtaaaaa ggccgcgttg ctggcgttt tccataggct  
 3361 ccgccccctc gacgagcatc acaaaaatcg acgctcaagt cagagggtgc gaaacccgac  
 3421 aggactataa agataccagg cgtttccccg tggaaagctc ctctgtgctc ctctgttcc  
 3481 gacctgcgc cttaccggat acctgctcgc ctttctccct tcgggaagctc tggcgtctt  
 3541 tcatagctca cgctgtaggt atctcagttc ggtgtaggct gttcgtcca agctgggctg  
 3601 tgtgcacgaa cccccgttc agcccagccg ctgcgcctta tccggtaact atcgtcttga  
 3661 gtccaaccgc gtaagacaag acttatcgcc actggcagca gccactggta acaggattag  
 3721 cagagcgagg tatgtaggcg gtgctacaga gttcttgaag tgggtggccta actacggcta

```

3781 cactagaaga acagtatttg gtatctgcmc tctgctgaag ccagttacct tcggaaaaag
3841 agttggtagc tcttgatccg gcaaacaac caccgctggt agcggtggtt tttttgtttg
3901 caagcagcag attacgcgca gaaaaaaagg atctcaagaa gatcctttga tcttttctac
3961 ggggtctgac gctcagtgga acgaaaactc acgттаaggg атттттггтса тгаааттатс
4021 aaaaaggatc ttcacctaaa tcctttttaa ttaaaaatga агтттттаат саатсгааг
4081 tatatatgag taaacttggt ctgacagtta ccaatgctta атсagtгagg сасататстс
4141 agcgatctgt ctatttcggt catccatagt tgcctgactc gggggggggg ggcgctgagg
4201 tctgcctcgt gaagaaggтg ttgtgactc атaccaggcc тгаатсagcc сатсатссag
4261 ccagaaagtг agggagccac ggttgatgag агctttgttg таgгтggacc агттггтgat
4321 tttgaaactt тgctttgcca сggaacggтс тgcgттgtсg ггаagатгсg тgatсtгatс
4381 cttcaactca gcaaaagttc gatttattca аcaaaгссгс сgtcccгтса агтсagсгта
4441 атgctctгсс агтгттaсaa сcaаттаacc аattctгatt агaaaaactc атсgagсатс
4501 ааатгааact гcaатттatt саататсagga тtatcaatac саататтттг аaaaгссгт
4561 тtctгтаатg аaggagaaaa сtcaccgagg саgtтссата гgatггсaaг атсctггтат
4621 сggтсtгсga тtссgactсg тccaacatca атаcaaccta ттаатттссс сtсгтсaaaa
4681 атаaggттat саagtгagaa атсaccatга гtgacгactг аatссггтга гаатггсaaa
4741 агctтатgca тttcttttсca гactтгттса асaggссagс саттacгстс гтсатсaaaa
4801 тсactсгсат саaccaaaacc гттattсatt сgtгattгсg сctгagсgag асgaaатacг
4861 сgатсгсгтг таaaaggaca атtacaaac aggaatсgaa тgcaaccггс гсaggaacac
4921 тgсссagсгс атcaacaata тttttсact gaatссagat аattctттtс аатacттгга
4981 атgctгтттt ссгgggгatс гсagtггтга гтаaccatгс атсатсagga гtacггатаa
5041 аатгctтgat гgtсggaaga гgcataaatt ссгтсagсca гттtagтсгг accatсtсat
5101 сtгтаacatс аттггсaaсg сtacctттгс сагттттсag ааacaactсt ггсгсатсгг
5161 гctтсссата саатсгатаg аттгтсгсac сtgattгссс гacattатсг сgagсссатт
5221 татаccсата таaatсagca тсcatгттгг аатттаатсг сggсctсgag саagacгттt
5281 ссггттгаат атггстсата асaccсctгг тattactгтт таtgтаagca гacagттtta
5341 тtгттсатга тgatататтт тtatctгтг саатгтаaca тсagagаттт тgagacacaa
5401 сgtггсctтtс сccccсссс саттаттгаа гсатттатса гggттаттгт сtсатгagсg
5461 гатасататт тгаатгтат таgaaaaata аacaaатagг гgtтссгсгс асатттсссс
5521 гаааagtгсс асctгacгтс таagaaacca тtattатсат гacаттаacc татаaaaaata
5581 гgcгtatсac гaggссctтт сgtс

```





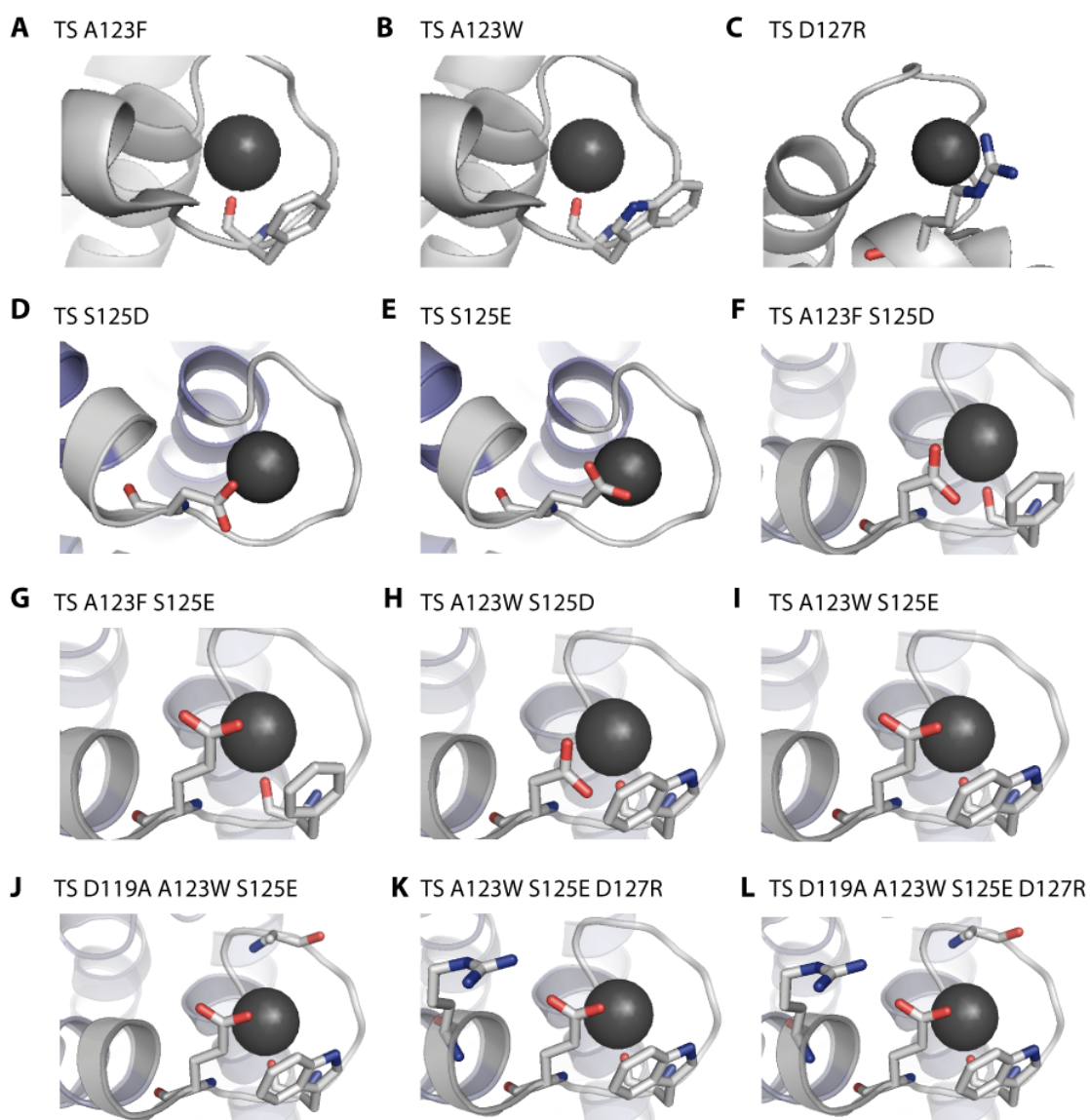
## 11.4 Table of all tested AQ variants

No.	Variant	$L_{\max} \text{Ca}^{2+}$ (100 $\mu\text{M}$ )	$L_{\max} \text{Sm}^{3+}$ (100 $\mu\text{M}$ )	$\text{Sm}^{3+}/\text{Ca}^{2+}$ + (100 $\mu\text{M}$ )	$T_{1/2}$ (Ca)/s	$T_{1/2}$ (Sm)/s	$T_M / ^\circ\text{C}$	Ca $\lambda_{\text{Em}}/\text{nm}$	Sm $\lambda_{\text{Em}}/\text{nm}$	$\text{EC}_{50}$ ( $\text{Ca}^{2+}$ )/ $\mu\text{M}$	$\text{EC}_{50}$ ( $\text{Sm}^{3+}$ )/ $\mu\text{M}$	yield mg/L culture	Source
1	AQ wt	469536.7	268480.0	0.57	23 $\pm$ 0.7	81.7 $\pm$ 5.9	38.45 $\pm$ 1.6	467	462	20.8 $\pm$ 2.8	33.2 $\pm$ 1.9		Shimomura 1962. J Cell Comp Physiol
2	LAAQ	53112.0	46573.7	0.88	312 $\pm$ 18	333 $\pm$ 24	39.2 $\pm$ 7.4	467	n.d.	19.5 $\pm$ 0.2	23.0 $\pm$ 2.0	0.84	Isoform, Inouye 1985, PNAS
3	<b>AQ TS (Q168R/L170I)</b>	<b>266899.3</b>	<b>27961.0</b>	<b>0.10</b>	<b>30<math>\pm</math>3.5</b>	<b>96.86<math>\pm</math>5.5</b>	<b>43.35<math>\pm</math>0.7</b>	<b>459</b>	<b>450</b>	<b>82.0<math>\pm</math> 6.6</b>	<b>265.7<math>\pm</math> 28</b>	<b>2.16</b>	<b>Tsuzuki 2005. J of Biological Chemistry</b>
4	<b>D119A</b>	<b>263182.7</b>	<b>114338.2</b>	<b>0.43</b>	<b>13.7<math>\pm</math>0.5</b>	<b>104<math>\pm</math>5.2</b>	<b>45.66<math>\pm</math>1.6</b>	<b>448</b>	<b>n.d.</b>	<b>60.3<math>\pm</math> 0.5</b>	<b>223<math>\pm</math>30</b>	<b>1.6</b>	<b>Plieth 2006, Methods Mol Biol</b>
5	TS D119A	509534.0	2200.3	0.00	37.6 $\pm$ 1.6	44.2 $\pm$ 4.5	45.35 $\pm$ 1.5	473	n.d.	42.4 $\pm$ 10	188.8 $\pm$ 13		Rational design
6	LAAQ D119G	105784.7	12471.7	0.12	48.2 $\pm$ 6.9	88.0 $\pm$ 15	42.63 $\pm$ 1.7	n.d.	n.d.	n.d.	n.d.	0.68	Screening
7	TS D119A/A123F	164025.0	596.0	0.00	24.3 $\pm$ 1.9	n.d.	n.d.	--	--	--	--	0.58	Rational design
8	TS D119A/A123W	1378390.0	40553.0	0.03	39.0 $\pm$ 2.7	104 $\pm$ 1.7	47.45 $\pm$ 0.8	452	n.d.	94.0 $\pm$ 6.4	325.8 $\pm$ 14	0.56	Rational design
9	TS D119A/S125A	107.8	55.0	0.51	n.d.	n.d.	49.7 $\pm$ 1.8	456	n.d.	n.d.	n.d.		Rational design SB, characterization Franziska Böwer
10	TS D119A/S125G	2658.6	99.0	0.04	353.7 $\pm$ 40	n.d.	39.9 $\pm$ 9.4	n.d.	n.d.	n.d.	n.d.		Rational design SB, characterization Franziska Böwer
11	TS D119A/S125D	152838.4	1664.0	0.01	50.5 $\pm$ 7.7	n.d.	48.2 $\pm$ 1.1	466	n.d.	n.d.	n.d.		Rational design SB, characterization Franziska Böwer
12	TS D119A/S125E	151977.2	3195.0	0.02	87.6 $\pm$ 0.5	n.d.	42.2 $\pm$ 1.3	464	442	n.d.	n.d.		Rational design SB, characterization Franziska Böwer
13	LAAQ N121V	100330.0	5075.7	0.05	31.1 $\pm$ 2.4	9.7 $\pm$ 9.3	50.21 $\pm$ 2.3	451	n.d.	66.6 $\pm$ 0.3	188.8 $\pm$ 13	1.92	Screening
14	<b>TS A123F</b>	<b>682050.6</b>	<b>202160.3</b>	<b>0.30</b>	<b>34.2<math>\pm</math>3.6</b>	<b>85.2<math>\pm</math>4.0</b>	<b>47.43<math>\pm</math>0.3</b>	<b>471</b>	<b>461</b>	<b>29.8<math>\pm</math> 7</b>	<b>158.2<math>\pm</math>64</b>	<b>1.70</b>	<b>Rational design</b>
15	TS A123F/S125E	4355670	376032	0.08	42.2 $\pm$ 4.5	330 $\pm$ 9.4	43.29 $\pm$ 0.2	437	459	44.3 $\pm$ 3.5	147.3 $\pm$ 20	2.23	Rational design
16	TS A123F/S125D	10000000	1084020	0.11	23.6 $\pm$ 1.4	135.3 $\pm$ 2.4	49.6 $\pm$ 2.0	480	n.d.	6.8 $\pm$ n.d.	105.4 $\pm$ n.d.	1.47	Rational design
17	<i>TS A123F/E128G</i>	<i>364702.0</i>	<i>19328.0</i>	<i>0.05</i>	<i>32.0<math>\pm</math>2.0</i>	<i>95.2<math>\pm</math>5.6</i>	<i>42.6<math>\pm</math>1.4</i>	<i>462</i>	<i>n.d.</i>	<i>311.7<math>\pm</math> 39</i>	<i>212<math>\pm</math>1.4</i>	2.7	Rational design
18	<b>TS A123W</b>	<b>663360.0</b>	<b>208175.7</b>	<b>0.31</b>	<b>33.6<math>\pm</math>3.2</b>	<b>153.6<math>\pm</math>22</b>	<b>33.42<math>\pm</math>1.6</b>	<b>466</b>	<b>455</b>	<b>130</b>	<b>137<math>\pm</math>19</b>	<b>2.06</b>	<b>Rational Design und LAAQ/TS Scceing</b>
19	<i>TS A123W/S125D</i>	<i>4355670</i>	<i>5557</i>	<i>0.00</i>	<i>110<math>\pm</math>1.6</i>	<i>72.5<math>\pm</math>2.6</i>	<i>43.60<math>\pm</math>0.7</i>	<i>465</i>	<i>444</i>	<i>181.3<math>\pm</math>46</i>	<i>171.3<math>\pm</math>16</i>	1.07	Rational design
20	<b><i>TS A123W/S125E</i></b>	<b><i>2206670</i></b>	<b><i>1744690</i></b>	<b><i>0.79</i></b>	<b><i>42.3<math>\pm</math>1.3</i></b>	<b><i>257<math>\pm</math>7.0</i></b>	<b><i>43.05<math>\pm</math>1.0</i></b>	<b><i>485</i></b>	<b><i>458</i></b>	<b><i>1022<math>\pm</math>31</i></b>	<b><i>148.3<math>\pm</math>0.0</i></b>	<b><i>2.96</i></b>	<b>Rational design</b>
21	TS A123W/E128G	205517.3	17428.0	0.08	19.0 $\pm$ 1.6	2498 $\pm$ 867	44.95 $\pm$ 0.3	468	n.d.	51.5 $\pm$ 5.2	202.0 $\pm$ 10		Rational design
22	TS S125D	2745520	156650	0.05	32.7 $\pm$ 2.3	1173 $\pm$ 295	56.02 $\pm$ 0.7	468	452	19.4 $\pm$ 1.0	268 $\pm$ 0	2.1	Rational design

23	TS S125E	102637.5	10558.6	0.10	82.0±10	114.6±14	49.35±0.6	451	451	23.1± 3.6	163.2±28	0.06	Rational design
24	TS S125G	2354.7	56.2	0.02	9.5±16	306.5±56	n.d.	434	445	n.d.	n.d.		Rational design SB, characterization Franziska Böwer
25	TS S125R	314478.2	3336.3	0.01	124.8±20	n.d.	44.1±1.9	466	n.d.	n.d.	n.d.		Rational design SB, characterization Franziska Böwer
26	TS D127G	78833.0	7031.0	0.09	33.9±4.3	1867±10	46.2±5.2	466	461	73.8±19	159±17	5.66	Screening
27	<b>TS E128G</b>	<b>10043.0</b>	<b>1899.0</b>	<b>0.19</b>	<b>465.5±36</b>	<b>226.2±28.8</b>	<b>48.1±2.7</b>	<b>466</b>	<b>410</b>	<b>133.65±17</b>	<b>249±0.12</b>	<b>3.7</b>	<b>Screening</b>
28	TS I116V/D117A/D1 19A	3352.7	71.9	0.02	399±96	n.d.	n.d.	n.d.	n.d.	n.d.	n.d.		Rational design SB, characterization Franziska Böwer
29	<b>TS D127R</b>	<b>304656.0</b>	<b>98767.0</b>	<b>0.32</b>	<b>54.2±6.0</b>	<b>370.9±23.4</b>	<b>47.5±0.8</b>	<b>461</b>	<b>460</b>	22.0± 0.2	198.5±40	<b>2.8</b>	<b>Screening</b>
30	TS D119A A123F S125E D127R	42581.7	6781.0	0.16	29.6±2.3	46.1±9.1	n.d.	466	n.d.	66.9	560	1.33	Combination Screening and Rational Design
31	TS A123W S125E D127R	1558850	22649	0.01	18.9±1.3	296.4±34	n.d.	450	450	25.4± 0.03	139.5±0	3.58	Combination Screening and Rational Design
32	TS A123F S125E D127R	1288465.7	411257.3	0.32	8.3±0.6	321.7±22.7	45.5±0.6	n.d.	n.d.	13.9	546	<b>2.4</b>	Combination Screening and Rational Design
33	TS D119A A123W S125E D127R	248758.0	2580.0	0.01	37.7±2.4	251±230	n.d.	443	n.d.	<b>62.5± 0</b>	<b>126.8±0</b>	0.67	Combination Screening and Rational Design
34	TS D119A A123W S125E	1570951.3	91843.3	0.06	23.8±0.8	n.d.	36.5±1.7	463	462	71.7	504	1.29	Combination Screening and Rational Design
35	TS D119A A123F S125E	665225.7	18915.7	0.03	26.4±0.3	47.3±2.5	46.9±2.7	n.d.	n.d.	18.4± 0.0	149.3±0	0.43	Combination Screening and Rational Design
36	<b>TS A123W S125E Q159F</b>	<b>5235947.2</b>	<b>988993.2</b>	<b>0.19</b>	<b>26.9±2.9</b>	<b>457±98</b>	<b>42.5±0.1</b>	<b>460</b>	<b>464</b>	n.d.	n.d.	<b>3.51</b>	Rational Design
37	<b>TS A123W S125E D161E</b>	<b>4415832.3</b>	<b>1097859.0</b>	<b>0.25</b>	<b>22.6±1.5</b>	<b>358±33</b>	<b>34.0±1.5</b>	<b>459</b>	<b>453</b>	n.d.	n.d.	<b>3</b>	Rational Design
38	<b>TS A123W S125E Q159W D161E</b>	<b>119857.4</b>	<b>43298.5</b>	<b>0.36</b>	<b>22.6±1.8</b>	<b>1276±176</b>	<b>24.3±7.8</b>	<b>458</b>	<b>455</b>	<b>119.5± 27</b>	<b>232.4±38</b>	<b>0.75</b>	Rational Design
39	<b>TS R30W S32E A123W S125E Q159W D161E</b>	<b>4554487</b>	<b>518120.5</b>	<b>0.11</b>	<b>17.5±1.8</b>	<b>6270±145</b>	<b>50.4±2.5</b>	<b>458</b>	<b>456</b>	<b>117.0± 4.1</b>	<b>62.7±30</b>	<b>2.2</b>	Rational Design
40	TS EF1/3 P3 N EF1/2/3 WE	99701.7	240.0	0.00	13.7±1.2	40.3±n.d.	41.7±3.3	473	n.d.	32.2± 2.5	296.4± 0	0.13	Rational Design
41	TS Q159W D161E	28878.0	6117.0	0.21	28.0±1.9	750±19	40.1±0.9	n.d.	n.d.	10.4± 2.2	61.6±n.d.	<b>1.7</b>	Rational Design
42	TS R30W S32E	3384904.7	37282.5	0.01	48.8±4.0	plateau	46.3±1.1	n.d.	n.d.	34.1± 0.4	138.8±49	<b>1</b>	Rational Design
43	TS R30W S32E A123W S125E	3944561.3	83064.3	0.02	39.3±2.3	plateau	43.3±0.5	n.d.	n.d.	20.0± 1.9	47.7±21	<b>0.9</b>	Rational Design



## 11.5 Overview of the Modeled Variant Structures



Suppl. Figure 2: PyMol modeled structures based on 1SL8 of the combinations of TS A123W S125E (rational design) and the best variant of iterative saturation mutagenesis together with the known low affinity substitution D119A.

## 12 Acknowledgements

Firstly, I would like to express my sincere gratitude to my advisor Prof. Dr. Andrea Rentmeister for the continuous support of my Ph.D study and related research, for her patience, motivation, and encouraging hands on mentality. I am thankful for your trust during this journey to a completely new field. Andrea, I hope your courage to explore new fields will always lead you to success, as it did before.

I was honored with three excellent advisors that helped me to grow with my research.

Besides my advisor, I would like to thank the rest of my thesis advisory panel: Prof. Dr. RJ Dwayne Miller for your very motivating and inspiring words and ideas that helped me to overcome every hurdle, Prof. Dr. Uli Hahn, who gave me access to the laboratory and research facilities of his labs after the Rentmeister group moved to Münster and his good and hard questions that incited me to widen my research.

My sincere thanks also goes to Prof. Dr. Alf Mews for the preparation of the second opinion.

Moreover, I would like to express my sincere gratitude to my lab fellows: Dr. Daniela Stummer, Dr. Anna Rath, Josephin Holstein, Stefanie Kellermann, Dénes Haase and our extraordinary technician Julia Sandberg-Meinhardt. You always supported me no matter what and made every cloudy or rainy day to a sunny day. Thank you for allowing me to be part of the Care Bears Crew. I wish you all the best!

I would also like to thank the “Münster-Part” of the AG Rentmeister for your support in every possible way.

And also to my “host family”, AG Hahn, I say thank you, for your tremendous help and support. Especially, Dr. Katrin Seelhorst, Dr. Eileen Magbanua, Dr. Patrick Ziegelmüller, Dr. Katharina Berg, Joanna Fafinska and Kristina Szameit. Katrin, thank you for the coffee breaks, many discussions and your helpful thoughts. Eileen, thank you for believing in me and encouraging me. Patrick, thank you for your excellent technical know-how and your support. Kati and Joanna, you helped with your kindness and sometimes crazy ideas and Kristina, thank you for sharing the long bus rides to the MPI and the question marks whenever theoretical physics appeared or whenever we were asked, if our research is just fun or real research!

Furthermore, I would like to thank the „TEM-Society“ Dr. Günther Kassier, Dr. Stephanie Manz, Dr. Robert Bückler and Sercan Keskin for your hard work and companionship to create a common scientific language during our in-liquid TEM journey. It was my honor to work with you and learn from you.

Moreover, I am grateful for the support of Katja Werner for her mentoring and delightful brain stormings as well as her team to advise me to any gold nanoparticle related question and their lab facilities. In particular, Charis Rabea Schlundt who shared many hours in the cell culture lab with me, and Christian Supej for the gold nanoparticles.

I would further like to thank JProf. Dr. Henning Tidow for the inspiring discussions and his group for the technical support for the ITC measurements and staying with me the lab until late. Thank you Katha and Julius, for your endless support also beside the lab. Furthermore, I thank Dr. Marco Klinge and Dr. Madeleine Künz. DJ Marco, you did not only support my lab work by assisting the CD measurements, you also enlightened many days beside the lab. May the Burger Society find many further burgers. Madeleine, thank you for the long discussions about career possibilities and wedding locations.

This work would not have been possible without the doctoral fellowship of the International Max Planck Research School UFAST and funding of the Centre for Ultrafast Imaging (CUI).

For this research many collaborations were created. So I would like to use this opportunity to thank Prof. Dr. Duchstein and Dr. Uli Riederer and their Team for working with their capillary electrophoresis. Next, I would like to thank the AG Weller for allowing me to use their DLS and technical support and imaging conventional TEM. In particular: Daniela Weinert and Andreas Kornowski. Thank you for testing my physical knowledge and preparing the TEM images. Moreover, I thank Dr. Florian Schulz for his knowledge on the field of gold nanoparticles and PD Dr. Christoph Plieth for the generous gift of my first batch CTZ and the vectors containing LAAQ and AQ wt.

Beside all my lab fellows I need to express my tremendous gratitude to my family and friends. I know, you waited a long time to have me back and you have all been very understanding whenever I missed a family date, birthday or anything related. However, I need to mention some people in particular: Julia and Sherin, you have been inspiring distraction in the moments when I needed it most. Your trust in me and the huge amount of Kinder Schokobons helped me to survive even the longest night shifts, especially in the end. Daniela, Katrin and Anna, thank you so much for reading this thesis between child care, protocols and wedding preparations, you are awesome. Bianca and Sven even between diapers you always cheered me up and supported me, our friendship means a lot to me and I am very happy for you that the „Chaos“-Family is growing. Thank you very much for your love and care. I hope I can pay back some time.

Last but not the least, I would like to thank my family: my mom and my brother for your endless love and strength you shared with me during this time. Ini juga untuk kami. Terima kasih untuk

memiliki kesabaran. Herzlichen Dank an meine Schwiegerfamilie für Rat und Tat und Gulasch und Meeresbrise, sowie viele schöne Abende mit den Kindern, die einen immer aufheitern konnten.

And to the most important person in my life: René, I do not know, if I had made it without you. You took care of mostly everything in the last month. I truly hope, I can make this up some time. Your love helped me to overcome any obstacle on my way.

### **13 Curriculum vitae**

Entfällt aus Datenschutzgründen

## **14 Eidesstattliche Erklärung**

*Hiermit versichere ich an Eides statt, die vorliegende Dissertation selbst verfasst und keine anderen als die angegebenen Hilfsmittel benutzt zu haben. Ich versichere, dass diese Dissertation nicht in einem früheren Promotionsverfahren eingereicht wurde.*

Hamburg, März 2016